



**HAL**  
open science

# Matricial approach for field correlation and temporal control of light propagation through strongly scattering media

Louisiane Devaud

► **To cite this version:**

Louisiane Devaud. Matricial approach for field correlation and temporal control of light propagation through strongly scattering media. Optics [physics.optics]. Sorbonne Université, 2021. English. NNT: 2021SORUS311 . tel-03587603

**HAL Id: tel-03587603**

**<https://theses.hal.science/tel-03587603>**

Submitted on 24 Feb 2022

**HAL** is a multi-disciplinary open access archive for the deposit and dissemination of scientific research documents, whether they are published or not. The documents may come from teaching and research institutions in France or abroad, or from public or private research centers.

L'archive ouverte pluridisciplinaire **HAL**, est destinée au dépôt et à la diffusion de documents scientifiques de niveau recherche, publiés ou non, émanant des établissements d'enseignement et de recherche français ou étrangers, des laboratoires publics ou privés.



SORBONNE  
UNIVERSITÉ



COLLÈGE  
DE FRANCE  
—1530—



Laboratoire Kastler Brossel  
Physique quantique et applications

# THÈSE DE DOCTORAT DE SORBONNE UNIVERSITÉ

ÉCOLE DOCTORALE : “PHYSIQUE EN ÎLE-DE-FRANCE”

RÉALISÉE AU : LABORATOIRE KASTLER BROSSEL

---

## Matricial approach for field correlation and temporal control of light propagation through strongly scattering media

---

Par :  
Louisiane DEVAUD

Dirigée par :  
Sylvain GIGAN

Pour obtenir le grade de **Docteur en Physique**

Présentée et soutenue publiquement le 17 décembre 2021,  
devant le jury composé de :

Mme. Hui CAO	Professeur à l’université de Yale, États-Unis	<i>Rapporteur</i>
M. Allard MOSK	Professeur à l’université d’Utrecht, Pays-Bas	<i>Rapporteur</i>
Mme. Agnès MAÎTRE	Professeur à Sorbonne Université, France	<i>Examineur</i>
Mme. Rachel GRANGE	Professeur à l’ETH Zürich, Suisse	<i>Examineur</i>
M. Sébastien POPOFF	Chargé de recherche à l’Institut Langevin, France	<i>Examineur</i>
M. Rémi CARMINATI	Professeur à l’Institut Langevin, France	<i>Invité</i>
M. Stefan ROTTER	Professeur à TU Wien, Autriche	<i>Invité</i>
M. Sylvain GIGAN	Professeur à Sorbonne Université, France	<i>Directeur de thèse</i>



# Remerciements

## Voyage au bout de la thèse

*Ça s'est terminé comme ça.*

Terminé un vendredi après-midi d'hiver, pour beaucoup dernier jour de travail avant l'accalmie attendue pour les fêtes de Noël.

Terminé dans une salle exigüe, perdue sous les toits du département de mathématiques du 45 rue d'Ulm – travaux obligeant.

Terminé dans un climat d'incertitude sous une demi-organisation – restrictions sanitaires exigent. Mais pourtant terminé, en présence d'un public, certes restreint mais attentif et bienveillant, doublé, par écran interposé, des autres acteurs de cette petite pièce de théâtre, mi-drame, mi-comédie, qu'à constitué pour moi cette thèse qui s'achève et dont se jouait la dernière scène. Et puis cette clémence météorologique exceptionnelle pour un 17 décembre, qui nous a permis un moment convivial dans la cour auprès des Ernests. À tous les protagonistes je voudrais dire merci !

## Remerciements

Ça s'est donc terminé par une soutenance.

Grand merci à vous, membres de mon jury, pour votre participation. Merci d'avoir en amont accepté de m'accorder de votre temps, de m'avoir lue et écoutée, ce malgré vos emplois du temps bien chargés. Mais en creux de cette soutenance, sachez que vous m'avez été d'une grande inspiration, sur les plans tant scientifique qu'humain : mon travail a été bercé par la lecture de vos articles et travaux et j'ai eu la chance de pouvoir interagir avec vous tous, à différents degrés, lors de ma préparation. Travailler entourée de chercheurs comme vous fut une aubaine incroyable. Thus thank you Hui Cao, Sylvain Gigan, Rémi Carminati, Rachel Grange, Agnès Maître, Allard Mosk, Sébastien Popoff and Stefan Rotter for accepting to be part of my jury comity despite the time it represents in your busy schedules. Thank you for the scientific and human inspiration you all were to me along my preparation!

Parmi les membres de mon jury, Sylvain, tu as joué un rôle bien particulier : tu as dirigé mes pas. Tu m'as donné l'opportunité de travailler sur un sujet passionnant avec des outils de pointe. Bride sur le cou mais jamais sans filet de sécurité, c'est ainsi que tu guides tes poulains, suivant l'adage selon lequel *la liberté est pour la science ce que l'air est pour l'animal*. Je ne pouvais pas rêver meilleur environnement de travail que celui que tu as su créer au laboratoire au sein d'un groupe soudé, voire familial. Merci pour ta bienveillance à l'égard de tous et pour tes efforts à accommoder au mieux la vie d'équipe dans une période troublée.

Stefan, you also played a particular role all along my PhD preparation. Thank you for welcoming me in Vienna and for your constant support on many projects. The theoretical assistance you brought with Matthias Kühmayer and Jakob Melchard was of high value. I really enjoyed our numerous visio-discussions during the lockdown, which enabled us, deprived experimentalists, to keep on working. Thank you all of you.

Merci également à Marc Guillon et Ivan Gusachenko. J'ai beaucoup aimé notre collaboration sur l'effet chromato-axial dans les fibres. Ivan, tu m'as marquée par la mise en place, en un temps record, d'une manip, dont j'ai mesuré au fur et à mesure à quel point tu l'avais pensée de fond en comble. Спасибо! Marc, ton travail sur les milieux diffusants a doté notre projet d'une résonance toute particulière, dont tu nous as fait grandement bénéficier. Et que de temps passé au téléphone avec toi, quand les réunions n'étaient pas possibles, pour discuter aspects expérimentaux, modèle analytique ou simulations !

C'est incontestablement avec Bernhard Rauer que j'ai le plus travaillé. Je ne pourrai jamais dire combien je lui dois pour ma thèse. Une aide permanente, des heures innombrables de discussion autour de différents projets, des idées fantastiques à foison et un entrain contagieux. Travailler avec toi, Bernhard, c'est oser tenter avec l'impression sereine que tout est possible, car *in fine* même si on bloque un instant, tu trouves la solution. Je peine à imaginer la recherche sans notre collaboration, je vais être un peu perdue... Alors pour tout, danke!

Au chapitre de l'entraide, tout le monde est au rendez-vous. Quel que soit le souci – question administrative ou de physique, problème d'alignement ou juste de matériel – chacun est sur le pont. Savoir prendre du temps les uns pour les autres, c'est une institution ici, un *credo*, un *confiteor*. Et quand je parle d'équipe, c'est au sens large, car l'équipe ne cesse d'évoluer et se réinventer. À tel point que je commence à faire figure de dinosaure, ou juste partie des meubles – question de point de vue. Merci d'abord aux anciens : Hugo, Saroch avec qui j'ai travaillé lors de mon stage de M2. Mickaël qui m'a fourni une manip très riche et dont le manuscrit de thèse m'a fait office de bible pendant ces trois dernières années. Tom, Antoine, Jonathan (mais es-tu vraiment parti ?!), Mushegh, Michal, Baptiste, Ivan, Claudio, Bingxin, Lorenzo, Zen... Merci à mon "jumeau" de thèse Julien pour, entre autres, toutes ces longues discussions où nous refaisions le monde à notre façon. Cela va me manquer. Merci à toute l'équipe du "bureau des chaises musicales" (alias de l'ambiance), Alexandra (que de bons moments passés à discuter avec toi aussi !), Gianni, Julien, Léa et Louis ainsi qu'à toutes les personnes de l'équipe présente : Bernhard, Shupeng, Hilton (la mémoire vivante des salles de manip), Lei (le meilleur élève), Raj, Fei, Fernando, Lorenzo (il primo), YonSeok, Sylvain, Francesco, Marc, Payvand. Se rendre au labo est, grâce à vous, un plaisir quotidien. Une grosse équipe somme toute, unie dans les bons moments (pique-niques, bières hebdomadaires, raclettes et galettes) ; dans les tourmentes aussi. Merci, thank you, grazie – *mon gosier de thésarde doit parler toutes les langues* – danke, gracias, dziękuję, obrigada, ขอบคุณ, תודה, טַהַרְרַהַרְr

Notre équipe s'épanouit au sein du laboratoire Kastler Brossel. Bien que spatialement réparti en trois sites parisiens, ce laboratoire est convivial et sa vie agréablement rythmée de rencontres diverses. C'est ainsi que j'ai pu découvrir le travail réalisé dans d'autres groupes. Merci à Tom Bienaimé et Murad Abuzarli tout particulièrement, pour nos discussions et réflexions sur des travaux communs éventuels. Je voudrais également dire ma gratitude à toutes les personnes qui, via le comité de suivi de thèse, se sont intéressées à mon travail et ont été attentives au bon déroulement de mon doctorat : Antoine Heidmann, Pierre-Jean Nacher et Serge Reynaud. Le laboratoire ne serait pas ce qu'il est sans tous les membres des équipes techniques et administratives. Merci à tous et tout particulièrement à mes voisins de palier, Thierry, Stéphanie, Audrey, Christelle et Valérie : le plaisir que j'ai pris à passer vous voir a largement adouci ma phobie administrative !

Ma vie de doctorante ne s'est pas bornée aux portes du 24 rue Lhomond. Pendant mes trois ans de thèse, j'ai eu la chance de pouvoir enseigner un peu à la préparation à l'agrégation de Montrouge. Changement d'air salvateur et nécessaire. Merci à toute l'équipe enseignante pour son accueil chaleureux, et tout particulièrement à Agnès Maître, Arnaud Raoux, André Salou et Éric Guineveu ! Merci aussi à Tom Bienaimé, Clément Sayrin et Agnès Maître pour notre petit travail sur la manip SLM.

Je voudrais également mentionner ici toutes les personnes dont la rencontre, bien avant ma thèse, à été déterminante. Mes divers enseignants, en commençant par M. Bonamy, l'instituteur qui m'a réconciliée avec l'école (ça n'était pourtant pas bien parti), MM. Putois et Rivière au Lycée, mes enseignants en prépa et à l'ENS de Lyon ainsi que Christine Leygnac, qui m'a consacré tant de temps...

Un grand merci également à tout le "groupe Jolidon" pour ces années passées ensemble à l'ENS et notre beau projet de livre: Éric, Benjamin C., Camille, Antoine, Christopher, Benjamin G., Louis, David, Théo, Alexandre, Jérémy. À mes amis lyonnais et tout particulièrement à Antoine, binôme de toujours qui, à défaut de montagne, soulèverait un électro-aimant pour une petite manip de supra de dernier moment en fin de TP !

Je voudrais également remercier les membres de ma famille dont certains, bien que non-scientifiques, ont pris la peine de regarder ma soutenance (ce malgré parfois un décalage horaire les faisant se lever aux aurores !). À mes parents et ma soeur, je sais gré de m'avoir toujours soutenue et encouragée dans mes études. À mon père, amoureux authentique et prosélyte d'une physique qu'il partage si généreusement, d'avoir su capter mon intérêt. Que d'anecdotes et expéditions au Palais de la Découverte pour s'extasier devant le manège de Coriolis ou la cage de Faraday ! À ma mère, modèle de volonté et de dynamisme, d'avoir su toujours me rassurer dans l'angoisse du choix et de m'avoir montré que si on veut, on peut. Ça paraît si simple ! Merci également aux miens d'avoir su adoucir le confinement de mars 2020 en réussissant à extraire, de cette période inédite et difficile, le bon grain de l'ivraie. Un grand merci aussi à mon grand-père Emmanuel, mon presque voisin de palier pendant ces années de doctorat parisien, pour nos plus fréquents déjeuners partagés et son intérêt pour mes lectures.

Merci enfin à Simon qui m'a quotidiennement supportée sans trop râler pendant toute cette période, d'autant plus méritant à cet égard qu'il n'avait pas signé pour le télétravail... Merci pour ta bonne humeur et ton dynamisme, qui ont été précieux pour nous changer les idées et sortir de la morosité ambiante. Mais tu ne t'en es pas tenu à cela et ton aide dans ma thèse a été immense. Vif, tu saisis toujours les problèmes que je te soumetts, ce même lorsque je ne me comprends pas bien moi-même. Tu m'a sortie d'affaire à presque tout propos : calculs, modèles, etc. ; si bien qu'à l'issue de ces trois ans, tu connais presque aussi bien ma thèse que moi. Pour finir, merci surtout d'avoir su venir à bout, par la simple évocation de tes problèmes d'algorithmique, de mes insomnies passagères !

**Que la thèse en vaut la peine<sup>1</sup>**

C'est une chose étrange à la fin que la thèse  
 Aujourd'hui je la clos sans en avoir tout dit  
 Ces moments de bonheur ces midis d'incendie  
 Les nuits immenses et noires en mal d'hypothèse

Rien n'est si abouti peut-être qu'on le croit  
 D'autres viennent Ils ont le cœur que j'ai moi-même  
 Ils aiment retourner torturer le problème  
 Et passer leurs soirées à chercher d'autres voies

D'autres qui referont comme moi le voyage  
 D'autres qui souriront d'un effet retrouvé  
 Qui s'émerveilleront d'un résultat prouvé  
 D'autres qui lèveront les yeux vers les nuages

Il y aura toujours un thésard frémissant  
 Pour qui une soutenance sera l'aube première  
 Il y aura toujours l'eau le vent la lumière  
 Rien ne passe après tout si ce n'est le passant

C'est une chose au fond que je ne puis entendre  
 Cette peur de conclure que les gens ont en eux  
 Comme si ce n'était pas assez merveilleux  
 D'avoir passé trois ans dans la soif de comprendre

Oui je sais cela peut sembler court un moment  
 Nous sommes ainsi faits que la joie et la peine  
 Furent comme un vin menteur de la coupe trop pleine  
 Et la mer à nos soifs n'est qu'un commencement

Mais pourtant malgré tout malgré les temps austères  
 Malgré les jours maudits qui sont des puits sans fond  
 Malgré ces nuits sans fin où plus d'un se morfond  
 Jamais l'abattement n'atteint le volontaire

Malgré tout je vous dis que ces années furent telles  
 Qu'à qui voudra m'entendre à qui je parle ici  
 N'ayant plus sur la lèvre un seul mot que merci  
 Je dirai malgré tout que ces années furent belles

---

<sup>1</sup>Adaptation d'Aragon *Que la vie en vaut la peine*, 1954.

# Résumé

Sauf à se placer dans le vide intégral – source incluse – la lumière que capte tout détecteur est diffusée. Celle qui parvient à la rétine d'un observateur n'échappe pas à la règle : simple diffusion cohérente donnant une image nette pour un œil emmétrope ou diffusion complexe donnant une image dégradée en cas de cataracte... La lumière que nous observons est du reste déjà diffusée en amont de notre cornée. Diffusion à l'origine de magnifiques phénomènes comme les couleurs du ciel, des nuages, de certains insectes ; diffusion parfois responsable de notre mauvaise vision, même avec une vue parfaite : quand les gouttelettes d'eau qui constituent le brouillard se retrouvent partout entre nos yeux et l'objet observé, par exemple ; ou bien quand des turbulences atmosphériques, en distordant les fronts d'onde entrants, floutent les images des étoiles que nous tentons de regarder.

C'est du reste pour faciliter l'observation astronomique qu'une technique d'optique adaptative a été développée : compenser ces distorsions d'origine atmosphérique par des contre-distorsions dûment provoquées en amont du télescope – des "lunettes" adaptatives en quelque sorte – permet de retrouver des images nettes. Dans le même ordre d'idée, des techniques de contrôle du front d'onde sont développées pour les milieux diffusants : le front d'onde entrant dans le milieu est façonné à volonté grâce à des modulateurs spatiaux de lumière, dans le but de contrôler le front sortant. Plusieurs méthodes sont aujourd'hui utilisées pour réaliser le façonnage optimal du front entrant dans le cadre de l'optique linéaire. Parmi elles, les optimisations via la mesure de la matrice de transmission. Cette matrice, reliant le champ incident et le champ sortant, contient l'information nécessaire sur le milieu diffusant. Sa connaissance permet par exemple de focaliser la lumière en sortie du milieu. On peut lui appliquer les traitements standard de l'algèbre linéaire, entre autres s'intéresser à ses vecteurs propres (ou vecteurs singuliers) en déterminant son spectre.

Dans cette thèse, je présente mes travaux sur le contrôle du champ via la décomposition en valeurs singulières de la matrice de transmission. Le contrôle du champ comprend, entre autres, la modification de la taille des grains de speckle et des corrélations ainsi que la variation de la transmission. Ces aspects sont traités d'abord en régime monochromatique, puis étendus temporellement en éclairant le milieu en régime pulsé.

Ce manuscrit de thèse est organisé comme suit:

- Dans le **Chap. 1**, j'illustre le phénomène de diffusion de la lumière sur des exemples du quotidien ; j'en explique brièvement l'origine, donne quelques définitions, introduis et caractérise les principales quantités physiques pour le décrire. La nature diffusante du milieu en est une caractéristique essentielle. Je travaille exclusivement avec des milieux induisant une diffusion multiple. L'intensité lumineuse suit alors une équation de diffusion, a priori annonciatrice d'irréversibilité. Cependant, à la différence de la diffusion de la chaleur par exemple, la phase du champ électromagnétique n'est pas perdue lors des diffusions successives, ce qui conduit à des interférences multiples : contrôler le champ diffusé devient possible. Je montre que ce contrôle, utilisant la technique de façonnage du front d'onde inspirée de l'astronomie, est extrêmement précis. À l'aide des modulateurs spatiaux de lumière, la phase du champ peut être

localement modulée pour un front d'onde incident donné, ce qui déforme ce dernier. Différentes approches permettent de déterminer la déformation adéquate.

Je m'appuie essentiellement dans ce travail sur le concept de matrice de transmission. Rappelons que l'existence d'une telle matrice repose sur la linéarité de la transformation du champ. La mesure dudit champ avant et après le milieu d'intérêt permet donc de construire une matrice entrée-sortie de la transformation, appelée matrice de transmission. Le niveau de contrôle expérimental influe sur les caractéristiques de la matrice. Deux régimes extrêmes sont à signaler : le contrôle total permettant l'accès à des modes de transmission dits ouverts (transmission totale) ou fermés (transmission nulle) ; le contrôle très partiel pour lequel les matrices de transmission se comportent comme des matrices aléatoires. Je présente enfin certains opérateurs construits à partir de la matrice de transmission et visant un contrôle spécifique du champ sortant.

- Le **Chap. 2** est dédié à la présentation du montage expérimental, les différentes méthodes d'acquisition et certains détails techniques. Je commence par présenter individuellement les composants du montage : laser pulsé, caméra, modulateur spatial de lumière etc., puis j'explique le fonctionnement global du système permettant des mesures de champ résolues en temps. Les détails techniques portent essentiellement sur la méthode de mesure du champ électrique, la détermination de la matrice de transmission et la méthode de fixation de l'origine temporelle du délai dans le pulse lumineux.
- Dans le **Chap. 3**, une étude monochromatique de la figure de speckle, distribution d'intensité obtenue par diffusion multiple d'une lumière cohérente, est présentée.

La statistique du champ, qui suit une loi de Rayleigh, est discutée tant sur ses conséquences que sur son origine. Dans cette lignée, je présente brièvement différents travaux montrant la possibilité d'influencer, légèrement ou drastiquement, la statistique de speckle. Je présente également des résultats expérimentaux sur la modification de la statistique par le biais de la matrice de transmission. Focaliser la lumière transmise sur toute une surface de sortie transforme le speckle et sa statistique de Rayleigh en une illumination plus homogène associée à une statistique de Ricin. Je présente pour finir une technique, fondée sur la décomposition en valeurs singulières de la matrice de transmission, permettant de contrôler à souhait les tailles et formes des grains de speckle, jouant ainsi sur les corrélations à courte et plus longues portées. L'ingrédient phare de cette technique consiste en un filtrage spatial de Fourier, naturel ou numérique, du champ de sortie. Les résultats expérimentaux proposés sont en accord avec le modèle simple qui est proposé.

- Dans le **Chap. 4** j'étends au domaine temporel les concepts et techniques introduits dans le **Chap. 3**. Pour cela, de courts pulses lumineux ( $\sim 100$  fs) sont envoyés sur le milieu et une mesure résolue en temps permet d'accéder à l'évolution temporelle du champ sortant.

Je montre que la puissance délivrée à la sortie du milieu diffusant peut être ajustée tant spatialement que temporellement en choisissant le front d'onde incident adéquat, déterminé grâce à la connaissance des vecteurs singuliers de la matrice de transmission résolue en temps. Il est à noter que le contrôle spatio-temporel est obtenu uniquement par une modification statique du front d'onde incident. En plus des résultats expérimentaux obtenus dans un régime de contrôle très partiel, des résultats de simulations dans un guide d'onde sont présentés, confirmant les conclusions dressées. Ces simulations montrent la robustesse de la technique et permettent en outre de sonder un régime de plus fort contrôle.

- Le **Chap. 5** est consacré à la création de corrélations entre différentes figures de speckle. Pour

cela, une méthode fondée sur la décomposition en valeurs singulières d'une somme de matrices de transmission est proposée. Les vecteurs singuliers d'une telle somme de matrices ont la propriété de générer des champs corrélés et ce quelles que soient les matrices en question. Je montre par exemple qu'il est possible de corrélérer les champs issus de la propagation à travers un milieu diffusant pour différentes longueurs d'onde d'illumination, différentes positions spatiales à la sortie ou encore pour différents délais dans un pulse lorsque l'illumination est polychromatique. Les natures des matrices sommées peuvent être diverses, ce que nous illustrons en travaillant simultanément avec une matrice monochromatique et une matrice résolue en temps. La valeur de la corrélation obtenue peut être contrôlée et prédite grâce à un modèle fondé sur les propriétés des matrices aléatoires. J'utilise également la relation de Fourier entre temps et fréquence pour manipuler encore plus les corrélations et créer des peignes (temporels ou fréquentiels) de corrélation.

- Dans le [Chap. 6](#) je présente les fibres optiques et discute certaines de leurs propriétés, notamment leurs similitudes et différences avec les milieux diffusants usuels. Ainsi par exemple l'existence de nombreux modes (pour les fibres optiques multimodes), qui peuvent se mélanger lorsque les fibres sont tordues ou présentent des défauts, est à l'origine de la similarité avec les milieux diffusants.

Les fibres optiques sont des outils prometteurs, parce qu'elles représentent une alternative aux circuits photoniques actuels et peuvent ainsi bénéficier des avancées obtenues en contrôle de front d'onde pour les milieux diffusants tout en conservant une forte transmission. L'absence de pertes et le nombre limité de modes de propagation permettent de plus facilement s'approcher expérimentalement d'un régime de fort contrôle. Les fibres constituent donc un outil idéal pour étendre et tester les modèles établis dans les milieux diffusants. La technique présentée au [Chap. 5](#) est appliquée, en simulation, aux fibres optiques. De plus, un effet mémoire chromato-axial observé dans les milieux diffusants vers l'avant [[Zhu et al. 2020](#)] est retrouvé pour les courtes fibres optiques à saut d'indice.



# Introduction

If the sun suddenly died, assume for example that all nuclear reactions just stop, how long would it keep lighting?

A quick answer would be to consider the time photons take to travel from the sun to the earth: 150 million km at  $c = 3 \times 10^8 \text{ m s}^{-1}$ , takes approximately 8 min. But is that answer correct?

It would be forgetting that photons are created at the sun's core and first need to travel through the sun to escape. This journey is much longer [NASA 2007]. Photons are scattered inside the sun and thus, to evaluate their traveling time, one needs to know the sun's radius ( $R_s \approx 700\,000 \text{ km}$ ) and the distance between two collisions called the photon mean free path. The latter distance is hard to estimate as it varies radially together with the sun's density. A rough estimate is  $l_s \sim 0.1 \text{ cm}$  [Mitalas et al. 1992; Shu 1982]. Due to scattering events, photons follow a random walk inside the sun. From these distances and the random walk model, it is possible to evaluate the time it takes for photons to exit the sun. The maximal distance achieved with a random walk scales as the square root of the number of steps  $N$ , which gives<sup>2</sup>  $3R_s^2 \simeq Nl_s^2$  and thus a travel distance of  $L = N \times l_s$ . An estimation of the travel time  $\tau$  is then,

$$\tau = \frac{L}{c} = \frac{Nl_s}{c} = \frac{3R_s^2}{cl_s} \simeq 4.9 \times 10^{12} \text{ s}, \quad (0.1)$$

that is **150 000 years**. It is estimated in [Mitalas et al. 1992] to be 170 000 years. The precise value does not matter and is subject to various abusive approximations (even the order of magnitude does not reach a consensus). The keypoint here is only to realize the impressive role of scattering in the sun. Some of the photons that we see today were created in the middle Paleolithic, at the epoch of Neanderthals!

The time evaluated above is a well known characteristic of scattering phenomena, called the **Thouless time**. Each scattering material, for a given illumination, has its own Thouless time. In most scattering materials encountered in daily life, Thouless times are quite short and not noticeable. As a point of comparison, it is of the order of the picosecond for white paint slabs used in the experiments of this thesis.

The journey of the sun's photons mentioned above is only an example of the consequences of light scattering. Indeed, scattering phenomena are not specific to electromagnetic waves, but affect acoustic waves as well. In the elastic regime, scattering results in dephasings. Historically, acoustic scattering was initially more studied than light scattering, due to the accessible time and length scales. However the recent development of new devices to control electromagnetic wavefronts was a turning point for light scattering research. In this work, we will solely concentrate on light scattering while drawing inspiration from works realized in acoustics.

Light scattering is a major drawback when it comes to imaging, especially in biological media. To reduce or compensate for this effect, understanding the light-matter interaction and more specifically

---

<sup>2</sup>The factor of 3 comes from the 3D dimension of the random walk.

light propagation in complex media is crucial. Taking advantage of spatial light modulators on the experimental level and of the transmission matrix formalism on the conceptual level, this work presents results about the control of speckles, well known patterns which result from complex interferences of the scattered field. The main objective pursued by this thesis consists in understanding and predicting speckle patterns and their correlations, as well as being able to design them at will. This last part is realized both in the monochromatic and temporal regimes, using the so-called singular modes of the system's transmission matrix.

This thesis is organized as follows:

- In **Chap. 1** we introduce the scattering phenomenon, together with related terms, definitions and properties. We present the emergence of the idea of wavefront shaping in astronomy, as well as its current application in the study of complex media. From an experimental standpoint, we discuss the main tools enabling wavefront shaping. From several available approaches to implement wavefront shaping I mainly discuss the transmission matrix, which is extracted from the scattering matrix. The study of the transmission matrix through its singular modes allows to highlight different regimes of control. These regimes determine the transmission characteristics and the appropriate model: from full control to a random matrix model. Finally, we discuss several operators based on the transmission matrix that have been engineered to address specific problems. In this first chapter, we do not dive into concepts that will be discussed in detail in the corresponding chapters.
- In **Chap. 2** we describe the experimental setup and technical aspects of our work. First, we present the main components individually, and then discuss the operation of the whole setup. Technical details include the time-gated measurement, the field extraction techniques, the measurement of the transmission matrix, the definition of the zero delay in the pulse etc..
- In **Chap. 3**, we examine speckle statistics, when working with monochromatic light. Analyzing its origin, it is possible to create deviations or even completely modify it. We discuss an example of drastic modification using the transmission matrix to globally focus light. The correlations among the speckle grains and the grains shape itself are shown to be precisely controllable using the singular modes of the transmission matrix.
- In **Chap. 4** we extend the concepts and techniques introduced in **Chap. 3** to the temporal domain by sending short pulses into the medium and performing time-gated measurements to access the temporal field information. We show that the energy delivery behind a scattering medium can be locally (both temporally and spatially) tuned with an adequate input wavefront determined using the singular vectors of a measured time-gated transmission matrix. Simulations realized in a waveguide geometry confirm these results and enable to reach more important degrees of control using a small number of modes. This enhancement control is compared to the global-focus technique. It is noteworthy that this temporal control is solely achieved exploiting spatial degrees of freedom.
- In **Chap. 5** we apply the singular value decomposition to sums of transmission matrices to engineer input states having the property of generating correlated interference patterns behind a complex medium. These correlations can be obtained for different propagating frequencies, for different targeted delays in a pulse and even for different disorders. The amount of correlation as well as the relative phase between the fields is fully controllable and predictable with the random matrix theory. Finally, we use the Fourier relation between time and frequency to further manipulate the correlations and create correlation combs.

- In [Chap. 6](#) we present and discuss multimode fibers. They represent a good alternative to existing photonic platforms as they can benefit both from high transmission and the complex media mixing properties. Because their transmission matrices are unitary and one can reach full control, they constitute ideal models to test wavefront shaping techniques in a regime that is not experimentally accessible. For instance, techniques presented in [Chap. 5](#) are extended in simulations to multimode fibers, and the chromato-axial memory effect observed in forward scattering media [[Zhu et al. 2020](#)] is observed and characterized for short step-index multimode fibers.

Throughout this thesis, some comments and illustration boxes appear. Their content is usually not required to understand the results but corresponds to small derivations and definitions that are not often detailed in the literature (or not in the present form). I consider them useful to fix ideas and provide some details.



# Contents

<b>Remerciements</b>	<b>iii</b>
<b>Résumé</b>	<b>xiii</b>
<b>1 Complex media and light propagation</b>	<b>3</b>
1.1 Scattering is ubiquitous	6
1.1.1 Observation of scattering	6
1.1.2 From scattering to light diffusion	10
1.1.2.1 Dipole scattering	10
1.1.2.2 Diffusion equation for multiple scattering	11
1.1.3 A consequence of coherent scattering: the speckle pattern	16
1.1.3.1 Speckle pattern	16
1.1.3.2 Correlations in the speckle pattern	20
1.1.4 Dependencies of the speckle pattern	22
1.1.4.1 Illumination scheme and the memory effect speckle resilience	22
1.1.4.2 Spectral dependence	23
1.1.4.3 Temporal dependence	25
1.2 How to fight diffusion: wavefront shaping and optimization	28
1.2.1 Motivation	28
1.2.2 Principle of wavefront shaping and its tools	31
1.2.2.1 Origin and principle of wavefront shaping	31
1.2.2.2 Different tools for wavefront shaping	33
1.2.3 Time reversal operator and phase conjugation	34
1.2.4 Optimization	36
1.2.4.1 Phase alignment and seminal works	36
1.2.4.2 Different methods	38
1.2.4.3 Inside biological samples	39
1.2.5 Approaches extended to pulses of light	40
1.3 Transmission matrix	41
1.3.1 From the scattering matrix to the transmission matrix	41
1.3.2 The monochromatic transmission matrix and its characteristics	44
1.3.2.1 The monochromatic transmission matrix	44
1.3.2.2 Focusing achievements of the transmission matrix	45
1.3.2.3 Access to the medium modes	46
1.3.3 A concept extended to light pulses	49
1.3.3.1 Multispectral transmission matrix	49
1.3.3.2 Time resolved transmission matrix	51
1.3.3.3 Broadband transmission matrix	53

1.4	Between limited control and mesoscopic effects . . . . .	54
1.4.1	Complete measurements . . . . .	54
1.4.2	Scattering slab and partial control . . . . .	58
1.4.2.1	Physical origin . . . . .	58
1.4.2.2	Marchenko-Pastur distribution for random matrices . . . . .	59
1.4.2.3	RM model for simulations . . . . .	63
1.4.3	Intermediate regime of control . . . . .	63
1.5	Scattering approach with operators . . . . .	65
1.5.1	The Wigner-Smith time-delay operator . . . . .	65
1.5.2	Other operators . . . . .	67
1.6	Scattering: always detrimental? . . . . .	67
1.7	Take home message . . . . .	70
<b>2</b>	<b>Presentation of the experimental setup</b>	<b>71</b>
2.1	General principle of the setup . . . . .	73
2.2	Presentation of the different elements . . . . .	74
2.2.1	LASER source . . . . .	74
2.2.2	Spatial light modulator . . . . .	75
2.2.2.1	Functioning . . . . .	75
2.2.2.2	SLM active area . . . . .	76
2.2.2.3	Phase-only constraint . . . . .	78
2.2.3	Scattering samples . . . . .	82
2.2.3.1	Sample Fabrication . . . . .	82
2.2.3.2	Sample characterization . . . . .	82
2.2.4	Camera . . . . .	84
2.2.5	Stage . . . . .	84
2.3	All elements working together, operation of the setup . . . . .	85
2.3.1	Polarization considerations . . . . .	85
2.3.2	Field extraction . . . . .	86
2.3.2.1	Phase-stepping . . . . .	87
2.3.2.2	Delay-line scan . . . . .	89
2.3.2.3	When to use which? . . . . .	90
2.3.3	Experimental determination of the optical path equalization between two arms	91
2.3.4	Measurement of TMs . . . . .	93
2.3.4.1	Canonical <i>vs.</i> Hadamard basis . . . . .	94
2.3.4.2	Internal <i>vs.</i> external reference . . . . .	95
2.3.4.3	TM measurement . . . . .	96
2.3.5	TM characterization and level of control . . . . .	97
2.3.5.1	Speckle grain size and binning of the camera pixels . . . . .	97
2.3.5.2	Different SLM modes addressing . . . . .	98
2.3.5.3	Level of control . . . . .	99
2.3.5.4	Illumination scheme . . . . .	99
2.4	Take home message . . . . .	100
<b>3</b>	<b>Monochromatic speckle and its manipulation with the transmission matrix</b>	<b>109</b>
3.1	Speckle statistics . . . . .	111
3.1.1	Fully developed speckle and Rayleigh statistics . . . . .	111
3.1.2	Non-Rayleigh statistics . . . . .	114
3.1.2.1	Natural non-Rayleigh speckles . . . . .	114

3.1.2.2	Artificial non-Rayleigh speckles . . . . .	117
3.2	The transmission matrix beyond the transmission control . . . . .	123
3.2.1	Fourier filtering for correlation engineering . . . . .	124
3.2.2	An axial extend of the correlation control . . . . .	126
3.2.3	Simple control over the speckle grain size . . . . .	128
3.2.3.1	Illumination and collection microscope objectives positions . . . . .	128
3.2.3.2	Speckle grain size control . . . . .	129
3.3	Take home message . . . . .	131
<b>4</b>	<b>From monochromatic to temporal aspects</b>	<b>139</b>
4.1	Measurement of time-gated transmission matrices . . . . .	141
4.1.1	Measurement techniques . . . . .	141
4.1.1.1	Indirect measurement via the multi-spectral transmission matrix . . . . .	141
4.1.1.2	Direct measurement . . . . .	142
4.1.2	How to use a time-gated transmission matrix? . . . . .	143
4.2	Spatio-temporal focusing . . . . .	143
4.2.1	Focusing on one speckle grain . . . . .	144
4.2.2	Multi-time and multi-speckle focusing . . . . .	145
4.2.3	Extension to a temporal global-focus . . . . .	147
4.3	Singular value decomposition to control the energy delivery . . . . .	149
4.3.1	Singular value decomposition and pulse shape . . . . .	149
4.3.2	Comparison to the global-focusing . . . . .	152
4.3.3	Enhancement for different delays with a single phase mask . . . . .	154
4.3.4	Evolution of the control over the pulse . . . . .	155
4.3.5	Shift of the enhanced delay . . . . .	158
4.4	Temporal speckle grain size control . . . . .	160
4.5	Time gated transmission matrix on a waveguide . . . . .	161
4.5.1	Simulated geometry and protocol . . . . .	162
4.5.1.1	Geometry . . . . .	162
4.5.1.2	From spectral to temporal information . . . . .	162
4.5.1.3	Definition of $\tau = 0$ . . . . .	163
4.5.1.4	Calculation of the output field . . . . .	163
4.5.2	Results . . . . .	164
4.6	Take home message . . . . .	165
<b>5</b>	<b>SVD as a correlation generator tool</b>	<b>169</b>
5.1	Speckle correlations, a valuable tool . . . . .	171
5.1.1	Importance of the correlations . . . . .	171
5.1.2	TM-based operators to engineer field correlations . . . . .	172
5.1.3	An idea along the same lines . . . . .	173
5.2	SVD-based correlations and temporal illustration . . . . .	175
5.2.1	Modifications to the experimental geometry . . . . .	175
5.2.2	Observation of the effect . . . . .	176
5.2.3	Playing with the effect . . . . .	178
5.2.3.1	Controlling correlations for varied spaced matrices . . . . .	178
5.2.3.2	Extension to more than two matrices . . . . .	179
5.2.4	Importance of the transmission matrices coupling . . . . .	179
5.2.5	Correlation variation with the singular vectors . . . . .	181
5.3	A general concept not restricted to temporal aspects . . . . .	184

5.3.1	Multi-wavelength correlation . . . . .	184
5.3.2	Spatial correlation . . . . .	185
5.3.3	Comparison of some TM-based operators . . . . .	186
5.4	Cross-effects . . . . .	187
5.4.1	Time and frequency two conjugated variables . . . . .	188
5.4.2	Global phase between the two transmission matrices . . . . .	189
5.4.3	Mixing transmission matrices measured in different regimes . . . . .	190
5.5	Take home message . . . . .	191
<b>6</b>	<b>What about optical fibres?</b>	<b>203</b>
6.1	Multimode optical fibers, a versatile tool . . . . .	205
6.1.1	An overview of optical fibers . . . . .	205
6.1.2	A mixing tool . . . . .	207
6.1.3	Complete measurement of the TM of a MMF . . . . .	210
6.2	$\chi$ -axial memory effect in SI-MMF . . . . .	212
6.2.1	An overview of memory effect and its application for MMF . . . . .	212
6.2.2	Observation of $\chi$ -axial memory effect in forward scattering complex media . . . . .	213
6.2.3	$\chi$ -axial memory effect in SI-MMF . . . . .	215
6.2.3.1	Observation of the effect . . . . .	215
6.2.3.2	Correlation widths . . . . .	219
6.2.3.3	Correlation slope . . . . .	220
6.2.3.4	Spectral and axial widths . . . . .	223
6.2.3.5	Some applications . . . . .	225
6.3	SVD induced correlations in multimode fibers . . . . .	225
6.3.1	MMF mode solver and fiber TM . . . . .	226
6.3.2	Correlation . . . . .	226
6.3.2.1	Abrupt correlation variations . . . . .	228
6.3.2.2	Full correlation control . . . . .	231
6.4	Take home message . . . . .	234
<b>A</b>	<b>Experimental complements</b>	<b>239</b>
A.1	Laser jitter . . . . .	239
A.2	Impact of phase-only control . . . . .	241
A.3	Zero-delay stage position . . . . .	244
A.3.1	Zero-delay position for very scattering media . . . . .	244
A.3.2	Implication for the time to frequency cross effect . . . . .	245
A.4	Evaluating the measurement quality of a transmission matrix . . . . .	246
A.5	Some information contained in the transmission matrix . . . . .	248
A.5.1	Speckle information . . . . .	248
A.5.2	SLM information . . . . .	250
<b>B</b>	<b>Theoretical complements and results</b>	<b>251</b>
B.1	Speckle grains dimensions . . . . .	251
B.2	Elongated speckle grains . . . . .	253
B.3	Intensity and field amplitude enhancements . . . . .	255
B.3.1	Intensity enhancement . . . . .	255
B.3.1.1	Transmitted field . . . . .	257
B.3.1.2	Intensity enhancement . . . . .	258
B.3.1.3	Scaling with $\gamma$ . . . . .	260

B.3.2	Field amplitude enhancement . . . . .	261
B.3.3	Enhancement simulations for the SVD and the global-focus . . . . .	263
B.4	Phase-only impact on the enhancement . . . . .	265
B.5	SVD-based correlations: derivations and results . . . . .	265
B.5.1	For random matrices . . . . .	266
B.5.2	For random unitary matrices . . . . .	270
B.6	Unitary random transmission matrices . . . . .	273
B.6.1	Matrix generation . . . . .	274
B.6.2	Impact of sub-unitary matrices size on the singular values . . . . .	275
B.6.2.1	Singular values range and bimodal law . . . . .	275
B.6.2.2	Singular values distribution and Marchenko-Pastur . . . . .	278



# Nomenclature

#	number	MMF	multimode fiber
$\chi$ -axial	chromato-axial	MP	Marchenko-Pastur
$\emptyset$	diameter	MRI	magnetic resonance imaging
BBTM	broadband transmission matrix	NA	numerical aperture
CCD	charged coupled device	PDF	probability density function
DMD	digital micromirror device	RM	random matrix
DMPK	Dorokhov-Mello-Pereyra-Kumar	RMT	random matrix theory
FT	Fourier transform	ROI	region of interest
$FT^{-1}$	inverse Fourier transform	SI	step-index
FWHM	full width at half maximum	SIM	structured illumination microscopy
GI	graded index	SLM	spatial light modulator
i.i.d	independent and identically distributed	SVD	singular value decomposition
IR	infra-red	TGTM	time-gated transmission matrix
LP	linearly polarized	TM	transmission matrix
LUT	look up table	WFS	wavefront shaping
ME	memory effect	WS	Wigner-Smith
MEMS	micro-electro mechanical system		



# 1 | Complex media and light propagation

---

1.1	Scattering is ubiquitous . . . . .	6
1.1.1	Observation of scattering . . . . .	6
1.1.2	From scattering to light diffusion . . . . .	10
1.1.2.1	Dipole scattering . . . . .	10
1.1.2.2	Diffusion equation for multiple scattering . . . . .	11
1.1.3	A consequence of coherent scattering: the speckle pattern . . . . .	16
1.1.3.1	Speckle pattern . . . . .	16
1.1.3.2	Correlations in the speckle pattern . . . . .	20
1.1.4	Dependencies of the speckle pattern . . . . .	22
1.1.4.1	Illumination scheme and the memory effect speckle resilience . . . . .	22
1.1.4.2	Spectral dependence . . . . .	23
1.1.4.3	Temporal dependence . . . . .	25
1.2	How to fight diffusion: wavefront shaping and optimization . . . . .	28
1.2.1	Motivation . . . . .	28
1.2.2	Principle of wavefront shaping and its tools . . . . .	31
1.2.2.1	Origin and principle of wavefront shaping . . . . .	31
1.2.2.2	Different tools for wavefront shaping . . . . .	33
1.2.3	Time reversal operator and phase conjugation . . . . .	34
1.2.4	Optimization . . . . .	36
1.2.4.1	Phase alignment and seminal works . . . . .	36
1.2.4.2	Different methods . . . . .	38
1.2.4.3	Inside biological samples . . . . .	39
1.2.5	Approaches extended to pulses of light . . . . .	40
1.3	Transmission matrix . . . . .	41
1.3.1	From the scattering matrix to the transmission matrix . . . . .	41
1.3.2	The monochromatic transmission matrix and its characteristics . . . . .	44
1.3.2.1	The monochromatic transmission matrix . . . . .	44
1.3.2.2	Focusing achievements of the transmission matrix . . . . .	45
1.3.2.3	Access to the medium modes . . . . .	46
1.3.3	A concept extended to light pulses . . . . .	49
1.3.3.1	Multispectral transmission matrix . . . . .	49
1.3.3.2	Time resolved transmission matrix . . . . .	51
1.3.3.3	Broadband transmission matrix . . . . .	53
1.4	Between limited control and mesoscopic effects . . . . .	54

1.4.1	Complete measurements . . . . .	54
1.4.2	Scattering slab and partial control . . . . .	58
1.4.2.1	Physical origin . . . . .	58
1.4.2.2	Marchenko-Pastur distribution for random matrices . . . . .	59
1.4.2.3	RM model for simulations . . . . .	63
1.4.3	Intermediate regime of control . . . . .	63
1.5	Scattering approach with operators . . . . .	65
1.5.1	The Wigner-Smith time-delay operator . . . . .	65
1.5.2	Other operators . . . . .	67
1.6	Scattering: always detrimental? . . . . .	67
1.7	Take home message . . . . .	70

This first chapter introduces all notions useful for the work presented in the present thesis: from the existence of light scattering to the introduction of the Wigner-Smith operator. All concepts which are closely related to contributions of this thesis will be detailed in the corresponding chapters, and will only be briefly mentioned in this preliminary chapter. In [Sec. 1.1](#) we present the (very) diverse aspects of scattering, and we express the relevant temporal and spatial quantities encountered. Whenever possible, we establish analogies, with their advantages and limits, to get the scaling of the introduced parameters. In [Sec. 1.2](#), we present the motivations, ideas and tools that enable counteracting scattering. [Sec. 1.3](#)) is entirely dedicated to the main tool used in all the experiments of this thesis: the transmission matrix. We present its basic form in the monochromatic domain, as well as its generalizations for broadband light. We raise the very important question of the degree of control in [Sec. 1.4](#), and we discuss the use of specific operators to control the output field in [Sec. 1.5](#).

## 1.1 Scattering is ubiquitous

Not necessarily noticed in everyday life, we are surrounded by scattering media. Their presence is so natural that their impact is automatically internalized and included in our vision and perception of the world. In this section we are going to review some clear observations of scattering ([Sec. 1.1.1](#)), detail its physical origin ([Sec. 1.1.2](#)) and focus on its concrete consequences ([Sec. 1.1.3](#)): such as the well known speckle pattern. Finally, we consider external factors impacting the scattering process and hence the speckle pattern ([Sec. 1.1.4](#)).

### 1.1.1 Observation of scattering

Light scattering is a natural process that can be simply illustrated by the altered vision in foggy weather<sup>1</sup>. The presence of very low clouds prevents the observation of distant objects otherwise visible. It is illustrated in [Fig. 1.1\(a\)](#) where cars and trees, despite their proximity, are hardly visible. It is noteworthy that the scattering elements (in this example water droplets) are present throughout the environment: moving to the blurred region, the blurring vanishes. This “easy experiment” illustrates an important parameter when studying scattering media: the medium thickness (in this example the distance between the observer and the object). We discuss how the transmission scales with the thickness in [Sec. 1.1.2](#). Another natural feature is the existence, for a macroscopic medium, of a refractive index: due to the scattering, any incident light is dephased, its overall phase velocity is no longer equal to its vacuum velocity. In the case of a non-homogeneous index, light rays no longer

<sup>1</sup>The same holds for sound in bubbly water [[Kafesaki et al. 2000](#)], but in this work we chiefly concentrate on light scattering.

follow straight lines. Moreover, at an interface between two media with different indices, they are split in a reflected and a refracted ray, the direction of the latter depending on the light frequency. A spectacular illustration of this color-dependent refraction is provided by the rainbow phenomenon, observed when the sun light undergoes backward coherent scattering by spherical water droplets, see Fig. 1.1(b). It illustrates another result of scattering: the chromatic aspect. In Fig. 1.1(b) the white color of the clouds and the blue color of the sky both result from light diffusion<sup>2</sup>. The Rayleigh scattering of small atmospheric polarizable particles, scaling as  $\omega^4$ , explains the blue color reaching the eye of an observer. The Mie scattering for larger particles (water droplets for the clouds), do not favor specific frequencies, which results in the white color of clouds<sup>3</sup>. From this difference one can draw another preliminary observation (as well further developed later) that scattering is frequency dependent. It is the very important scattering occurring in Beetle scales that is responsible for their important whiteness Fig. 1.1(c) [Burrese et al. 2014]. Structural scattering for instance paves the way to bio-inspired materials [Jacucci et al. 2021].

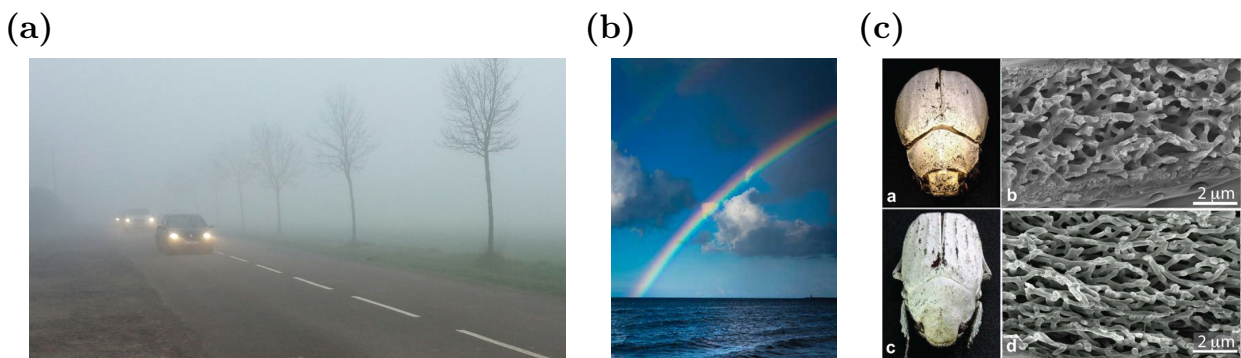


Figure 1.1: **Omnipresence of light scattering.** (a) Fog preventing vision of far trees and cars. (b) Rainbow and clouds. (c) Beetle images (left) and scanning electron micrographs of their scales (right). Image from [Burrese et al. 2014].

Most of the time one observes light scattering because it occurs between an object (a landscape for instance) and the receptor (the observer's eye). However sometimes the scattering is due to the receptor itself. This is for instance the case in cataract when the crystalline lens, usually acting as a convergent lens to focus light on the retina, becomes opaque as illustrated in Fig. 1.2. The eye no longer plays the role of a perfect lens. The healthy crystalline lens is not supposed to scatter light, such behavior resulting from damages. Nevertheless this transparency characteristic remains rare in biological media, most of them being naturally highly scattering<sup>4</sup>. The scattering properties of biological samples are extensively studied, due the major obstacle that scattering represents for imaging.

To conclude this little introduction, a general comment is the omnipresence of light scattering, from enjoyable consequences (colors) to detrimental ones (impaired vision). This ubiquity has long been well perceived, for instance by artists who introduced it in art. The Impressionist movement, see Fig. 1.3, explicitly accords light phenomena a particular attention and the sfumato technique of Leonardo da Vinci is also a good example.

Since scattering is so present, it has been explained and theorized. The next section will hence address the origin of light scattering and introduce the main parameters of interest.

<sup>2</sup>The distinction between scattering and diffusion is developed in Sec. 1.1.2.

<sup>3</sup>The white color actually results from a competition between the scattering of the different frequencies [Feynman et al. 1963].

<sup>4</sup>The cornea transparency for instance is due to structural partial order [Hart et al. 1969; Salameh et al. 2020]



Figure 1.2: **Tissue scattering.** Left: normal vision with a healthy eye. Right: blurred vision induced by scattering inside the eye due to an opacification of the crystalline lens called cataract.

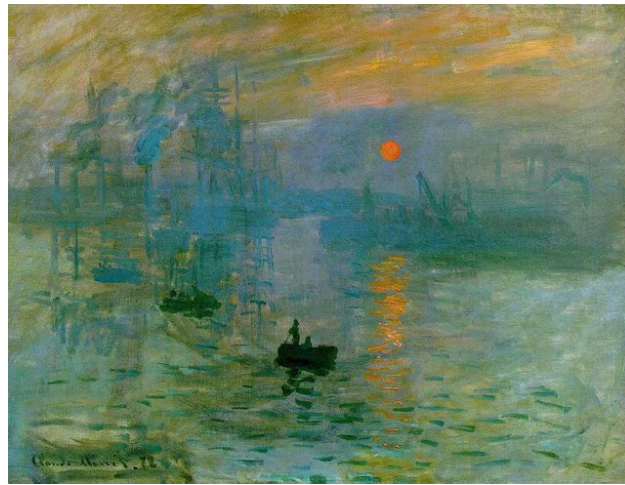


Figure 1.3: **Scattering in art.** Impressionist painting by Claude Monet *Impression, soleil levant*.

## 1.1.2 From scattering to light diffusion

### 1.1.2.1 Dipole scattering

As already perceived in the previous section, the physical origin of scattering is the interaction of light with particles [Hulst et al. 1981]. It is the high density of particles and the strength of the interaction that leads to observable phenomena. Let us first consider a single particle interacting with light through its electric dipole and assume an elastic scattering: the photon frequency remains unchanged in the process<sup>5</sup>. When light arrives on a dielectric medium, the electric field induces dipoles which themselves radiate a scattered field. For particles of size  $a \ll \lambda$ , the scattering in the electric dipolar approximation is given by Rayleigh's theory. The mean scattered power is given by

$$\langle P \rangle = \frac{\mu_0}{12\pi c} \omega^4 p_0^2, \quad (1.1)$$

where  $c$  is the speed of light,  $\mu_0$  the vacuum permeability,  $\omega$  the angular frequency and  $p_0$  the dipole moment. The radiated power, favoring short wavelengths in the visible spectrum, explains the blue color of the sky. For larger particles the scattering is no longer restricted to one dipole and results in

<sup>5</sup>In all this thesis we solely consider light elastic scattering. An example of inelastic scattering is Raman scattering where the incident photon is red-shifted (Stokes Raman scattering) or blue shifted (anti-Stokes Raman scattering).

a more complex field ruled by Mie's theory [Mie 1908]. The Mie theory gives the scattering equations for spherical particles, which involves the particle size  $a$  (the scattering efficiency scales as  $1/a^2$ ). It predicts a particle-dependent scattering directionality: large particles ( $a \gg \lambda$ ) experience forward scattering, whereas smaller ones ( $a \ll \lambda$ ) enjoys a more isotropic scattering. The size constraint detailed above explains why not all materials scatter light equivalently. This description is however complex and difficult to use for practical applications. A solution consists in working with averaged quantities, thus leaving the microscopic scale. For instance when one can define a refractive index, then geometrical optics is a very convenient way to describe light propagation.

### 1.1.2.2 Diffusion equation for multiple scattering

A way of tackling the problem is to write an energy balance on mesoscopic volumes, which leads to an equation of radiative transfer<sup>6</sup>. In larger dimensions, the latter equation can reduce to a diffusion equation<sup>7</sup>:

$$\left[ \frac{\partial}{\partial t} - \mathcal{D}\Delta_r + v_E\mu_a \right] u_d(r, t) = S(r, t), \quad (1.2)$$

where  $u_d$  is the scattered energy density,  $S$  is a source term,  $v_E$  is the energy velocity,  $\mu_a$  is the absorption coefficient<sup>8</sup> and  $\mathcal{D}$  is the diffusion constant [Carminati et al. 2021; Rossum et al. 1999]. In the following we will consider media without (or with very limited, see Sec. 1.2.1) absorption and no source term (e.g. no gain medium). The diffusion constant  $\mathcal{D}$  introduced is expressed as

$$\mathcal{D} = \frac{v_E l^*}{3}, \quad (1.3)$$

where length  $l^*$  stands for the transport mean free path. It physically corresponds to the distance after which a light beam has “forgotten” about its initial direction due to the succession of scattering events. It would seem logical that the transport mean free path should depend on the (averaged) distance between two scattering events, namely the scattering mean free path  $l_s$ . The latter can be estimated from the medium density. However the transport mean free path and the scattering mean free path do not necessarily coincide. The directionality of the scattering is involved through the anisotropy factor  $g_{\text{aniso.}}$ :

$$l^*(\omega) = \frac{l_s(\omega)}{1 - g_{\text{aniso.}}(\omega)}. \quad (1.4)$$

The factor  $g_{\text{aniso.}}$  is defined as the averaged cosine of the scattering angle. For forward scattering media the transport and the scattering mean free path are identical whereas, for biological samples (for instance), the anisotropy factor is close to 1 [Cheong et al. 1990; Ntziachristos 2010]).

The introduction of these diffusion length scales ( $l_s$  and  $l^*$ ) allows to classify the diffusion regimes by comparing the scattering medium size  $L$  to  $l_s$  (or  $l^*$ ):

- $L \ll l_s$ : most of the light is not scattered at all, it is the **ballistic regime**,
- $L \sim l_s, l^*$ : in average the light was subjected to a single scattering event, it is the **single scattering regime**,
- $L \gg l^*$ : several scattering events occur, it is the **multiple scattering regime**.

These regimes<sup>9</sup> are illustrated in Fig. 1.4. The theoretical highlight of these different regimes supports

<sup>6</sup>Equation that can also be derived from the field and radiative transport theory.

<sup>7</sup>Written as it is, the equation applies to a non absorbing medium.

<sup>8</sup>The absorption coefficient is the inverse of the absorption length.

<sup>9</sup>The distinction between  $l_s$  and  $l^*$  for defining the regimes ranges is not detailed.

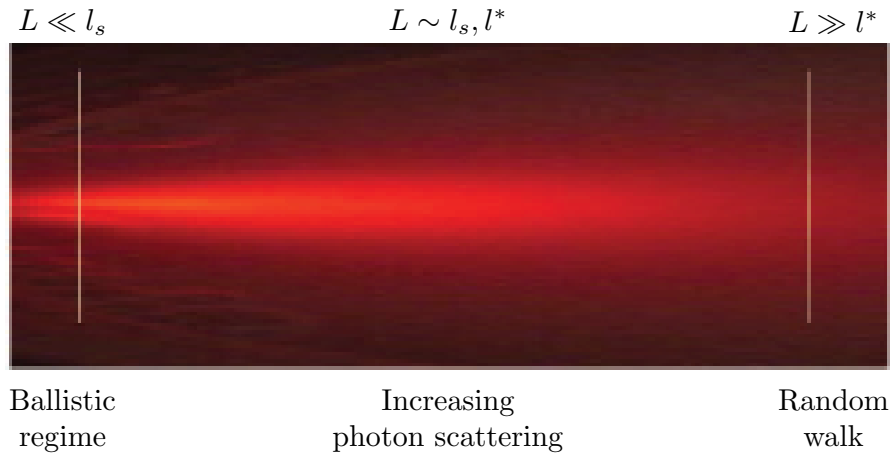


Figure 1.4: **Different regimes of for light propagation.** Light propagation and scattering sample thickness  $L$ . For  $L \ll l_s$  most photons do not experience scattering events and are ballistic. Increasing  $L$  increases the probability of photon scatterings. For  $L \gg l^*$ , due to the very numerous scattering events, the photons undergo a random walk. Figure from [Ntziachristos 2010].

the intuition obtained with the fog picture of Sec. 1.1.1.

Given some boundary conditions, Eq. 1.2 can be solved. The general geometry used is the one of a slab. In this case one gets for the transmission  $T$  [Rossum et al. 1999]

$$T \sim \frac{l^*}{L}. \quad (1.5)$$

This scaling of the scattered light transmission is interesting in two aspects. First it can be compared with the Beer-Lambert law predicting, for the ballistic light, an exponential decay along the medium. Second it is very reminiscent of Ohm's law observed in electrokinetics (Eq. 1.5 is for this reason called **Optical Ohm's law**<sup>10</sup>). This similarity is not fortuitous as both phenomena are driven by diffusion equations. A table summarizing the analogies is presented<sup>11</sup> Tab. 1.1. It is noteworthy that in all cases the macroscopic quantities (resistance, transmission, etc.) are linked to microscopic ones through the diffusion coefficient and the medium geometry.

Due to the first order time derivative in Eq. 1.2, diffusion is an irreversible process. However, this holds at the global intensity level. The field satisfies Maxwell equations and we will show that the coherent aspect of light scattering makes it possible to circumvent the apparent irreversibility of the process and achieve light control even in (or behind) very scattering media.

We will focus now on one striking consequence of coherent scattering: the speckle pattern, typically observed when coherent light propagates through scattering media.

### 1.1.3 A consequence of coherent scattering: the speckle pattern

#### 1.1.3.1 Speckle pattern

A diffusion equation highlights an irreversible process: the first order temporal derivative forbids time reversal. However the scattering description considering the intensity diffusion is incomplete

<sup>10</sup>It is noteworthy that  $T$  corresponds to the intensive writing of the "luminicent resistance", see Tab. 1.1.

<sup>11</sup>Viscosity diffusion also could be added to the table.

<sup>12</sup>No specific name at my knowledge linking the radiative vector to the energy density [Carminati et al. 2021].

	(a) Thermal	(b) Electric	(c) Particles	(d) Light
<b>Diffused quantity</b>	Heat (T, temperature)	charge density (V)	particle density (n)	energy density ( $u_d$ )
<b>Local law</b>	Fourier ( $\mathbf{j} = -\kappa \nabla T$ )	Local Ohm's law ( $\mathbf{j} = \sigma \mathbf{E} = -\sigma \nabla V$ )	Fick ( $\mathbf{j} = -\mathcal{D} \nabla n$ )	Fick <sup>12</sup> ( $\mathbf{j} = -l^* \nabla I_\nu$ )
<b>Diffusion coefficient</b>	$\mathcal{D} = \frac{\kappa}{C}$	$\mathcal{D} = \frac{\mu_e k_B T}{e}$	$\mathcal{D} = \frac{k_B T}{6\pi r \eta}$ (liquids) depends on the state	$\mathcal{D} = \frac{v_E l^*}{3}$
<b>Global law</b>	$R_{\text{th.}} = \frac{1}{\kappa} \frac{\ell}{S}$	$R_{\text{el.}} = \frac{1}{\sigma} \frac{\ell}{S}$	$R_{\text{part.}} = \frac{\ell}{\mathcal{D} S}$	$R_L = \frac{1}{l^*} \frac{\ell}{S}$

Table 1.1: **Analogy among diffusion equations for different quantities.** All four quantities follow a diffusion equation. Macroscopic geometric quantities are  $\ell$  (medium length) and  $S$  (medium section). (a) Heat transport,  $\kappa$  is the thermal conductivity,  $C$  the heat capacity per unit volume. (b) Electrokinetics,  $\sigma$  is the electrical conductivity,  $e$  the electron charge,  $k_B$  the Boltzmann constant and  $\mu_e$  the mobility. (c) Particles,  $k_B$  the Boltzmann constant,  $r$  the particle radius and  $\eta$  the dynamic viscosity. (d) Light,  $l^*$  is the transport mean free path and  $I_\nu$  the specific intensity. Using the equations analogy a “luminicent resistance”  $R_L$  (with the dimension of the inverse of a surface) is introduced.

as it disregards the phase information. This effect is somewhat reminiscent of the inhomogeneous transversal decay rate  $T_2^*$  observed for a collection of spins. Looking at the spins individually, their decay rate is slower ( $T_2 > T_2^*$ ) as illustrated when “reversing the time” (with a  $\pi$ -pulse in a spin echo sequence): the spins can be back aligned. Similarly with the scattering a phase information remains that makes the propagation deterministic, but it is not visible when describing only the intensity.

From now on we forget about the physical origin of the light scattering and just keep in mind that during a scattering process the phase is conserved thus involving an interference pattern. It is this pattern that will catch our attention. To describe it, we will take advantage of the particle-wave duality by either considering the light field as a wave (to compute the intensity profile and harness spectral and temporal aspects) or using photons. With the photon picture, performing a random walk in the medium, statistical quantities of the speckle pattern can be derived [Goodman 2007].

Let us consider a scattering medium illuminated by a coherent light (laser light for instance). Looking at the intensity distribution behind the medium one observes a complex structure composed of several bright and dark spots, see Fig. 1.5(a). This is a speckle pattern (the source coherence however is not the only constraint to observe a speckle pattern, see Comm. 1.1.1). One can interpret

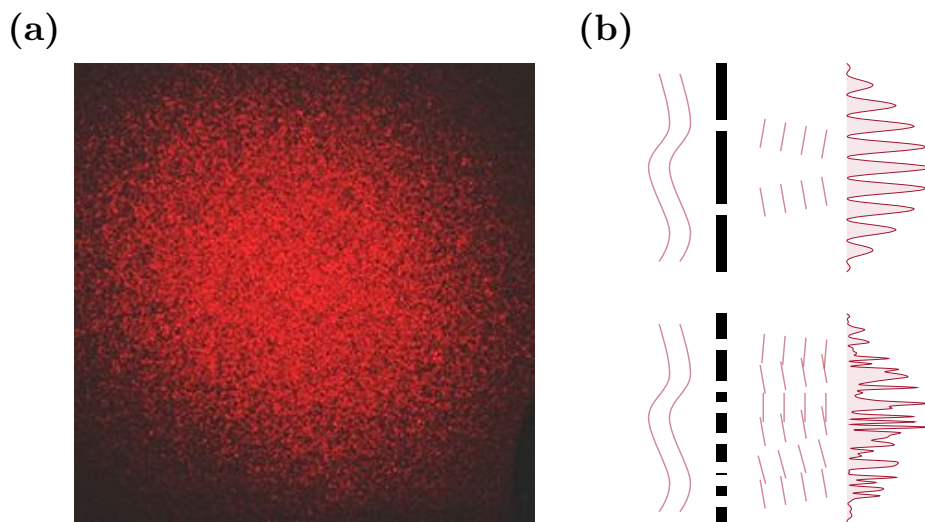


Figure 1.5: **Speckle pattern: result of a complex interference.** (a) Image of a speckle pattern obtained when illuminating a scattering medium with a laser light. (b) Top: Intensity pattern from the interference of two slits. Bottom: Speckle pattern or the interference from numerous arbitrarily positioned slits.

this pattern as the result of the diffraction by numerous particles randomly positioned, see Fig. 1.5(b).

#### Comment 1.1.1.

It is also noteworthy that the observation of a speckle pattern is however not automatic, even in coherent light. An important condition is the static behavior of the complex medium. If the medium changes faster than the acquisition time of the receptor (human eye or so), the different intensity patterns sum up (incoherently) so that the total intensity appears homogeneous. This is for instance what happens when illuminating liquids containing suspensions of scattering particles (diluted milk for instance).

Let us try to analyze the speckle pattern itself [Françon 2012]. From its mere observation some comments arise. It is a very contrasted pattern (Sec. 3.1.1) with two different length scales: a large scale forms the speckle blob (halo) and a shorter scale is related to the speckle grain. Let us consider

the illumination on an area of transverse characteristic size  $\Delta$  with particles of size  $a$ . Imaging a plane at a position  $z$  behind this area (far enough to be in the far field), both the blob size  $B$  and the transversal speckle grain  $b_{\perp}$  (extended version of the interfringe) are given by diffraction arguments [Ward et al. 2009; Goodman 2007].

$$B \approx \frac{\lambda z}{a} \quad \text{and} \quad b_{\perp} \approx \frac{\lambda z}{\Delta}. \quad (1.6)$$

As mentioned, the speckle pattern presented in Fig. 1.5(a) is captured on a single plane. However the interference is delocalized<sup>13</sup> and occurs in a volume. In the axial direction of the initial laser beam, the speckle grain size corresponds to the Rayleigh length [Halford et al. 1987b; Ward et al. 2009; Goodman 2007] such that the longitudinal grain  $b_{//}$  size is given by

$$b_{//} \approx \lambda \left( \frac{z}{\Delta} \right)^2. \quad (1.7)$$

Because no axial variation is expected in Fraunhofer diffraction, there is no straightforward handway explanation of Eq. 1.7 based on interfringe. However, the longitudinal speckle grain size expression (as well as the transverse one) can be retrieved with a small calculation presented in Appendix B.1. The main idea is to consider the speckle grain as a volume in which the optical path difference between two rays from the illuminated area does not exceed  $\lambda/2$ . These estimations are rough and an analysis of the speckle dimensions requires similar hypotheses on the imaged planed, as deeply discussed by [Gatti et al. 2008; Magatti et al. 2009] who investigate the three dimensional coherence of light speckle.

In addition to these geometrical characteristics, the speckle pattern is remarkable due to its universal statistics and its contrast reaching unity. Speckle statistics, follow a Rayleigh distribution, as extensively discussed in Sec. 3.1.

The interferential origin of the speckle pattern is just sketched above. A complete description of the speckle requires the knowledge of the pattern intensity. Within the framework of the diffraction theory the expected intensity of a constructive interference of  $N$  elements scales as  $N^2$ . It is thus important to understand what  $N$  stands for in a complex medium. It can be estimated by

$$N \equiv N_{\text{modes}} \propto \left( \frac{\Delta}{\lambda} \right)^2. \quad (1.8)$$

Such a scaling is not bizarre as it corresponds to the scaling of the number of modes in a waveguide with the same input surface size (see Sec. 6.1.1).

### 1.1.3.2 Correlations in the speckle pattern

Let us now consider correlations in the speckle pattern. From the modal approach (see Sec. 1.3.1) one can consider that an input field is linked to its output by a propagator depending on both input and output directions (or positions) [Carminati et al. 2021; Vesperinas 2006]. The question is the following: is there a correlation between a field the input of which propagates in a direction  $a$  and the output of which propagates in a direction  $b$ , with another field the input of which propagates in a direction  $a'$  and the output of which propagates in a direction  $b'$ ? The correlation between these two quantities is denoted  $C_{aba'b'}$ . There exists a general expression of  $C_{aba'b'}$  using the field propagator (computed from a Born series of the Lippman-Schwinger equation), but it will not be given here. From the expression of  $C_{aba'b'}$  some remarkable behaviors can be highlighted and they

<sup>13</sup>The interference results from a wavefront division.

are presented hereafter without details that can be found in the seminal paper [Feng et al. 1988a], in articles [Berkovits et al. 1994], in books [Carminati et al. 2021; Akkermans et al. 2007] or in a review [Rotter et al. 2017]. The full correlation  $C_{aba'b'}$  can be expanded in powers of  $1/(kl^*)$  with  $(1/(kl^*) \ll 1$  in the strong scattering regime). Three terms are worth mentioning:  $C_{aba'b'}^{(1)}$ ,  $C_{aba'b'}^{(2)}$  and  $C_{aba'b'}^{(3)}$ ; they are detailed in [Feng et al. 1988a].

- The first (and dominant) term represents the large local correlations responsible for the speckle grain size, called *short-range correlations*. Already discussed through mere diffraction arguments, both approaches lead to the same results. Nonetheless a novel feature appears: when tilting the input angle by  $\Delta\theta$ , the output speckle gets shifted by the same angle. This effect, called **memory effect** (ME), discussed in details in Sec. 1.1.4.1 and in Sec. 6.2.1, is however expected to be limited to a finite angle range with  $\Delta\theta \leq \lambda/L$ .
- The second term corresponds to the case of two similar inputs ( $a = a'$ ) leading to correlated outputs. The spatial decay of this term is slower than the grain size so that it can affect two output positions further apart than a grain size. One hence can refer to the correlation as a *long-range correlation*. However the magnitude of this term is smaller than for  $C_{aba'b'}^{(1)}$ . The weight reduction factor is called the conductance  $g$  referring to Landauer's formula for electrons conductance in a disordered medium [Fisher et al. 1981] and scales as  $N_{\text{modes}}/(l^*L)$  [Akkermans et al. 2007].
- The third term is expected to give a spatially unlimited uniform positive correlation and is hence called *infinite-range correlation*. Its magnitude is also reduced by a factor of  $1/g$  with respect to the long-range correlation term, making it hardly measurable despite an achievement by [Scheffold et al. 1998].

In all the experiments performed in this thesis, one has  $g \sim 10^5$ - $10^8$  only limiting us to  $C^{(1)}$  correlations, due to the high number of modes ( $N_{\text{modes}} \sim 10^6$ - $10^9$ ) and the limited transmission  $T = l^*/L \sim 0.2$ .

Hence, the speckle pattern mainly depends on external parameters that can be set. Some are discussed in the following section.

### 1.1.4 Dependencies of the speckle pattern

As detailed previously, the speckle pattern is the result of a complex interference. Slightly modifying the field at the output leads to a change in the speckle pattern. Thus, it is not surprising that completely changing the disorder changes the speckle, see Fig. 1.6(a). However, when changing continuously an illumination parameter, it is interesting to evaluate the range for which the speckle is still correlated to the initial one [Shapiro 1986]. We will discuss some frequently choices of parameters, that can be tuned experimentally.

#### 1.1.4.1 Illumination scheme and the memory effect speckle resilience

A modification that we already mentioned is the illumination angle itself. For relatively small tilts of the input wavefront, the speckle pattern gets shifted in the imaged plane (see Sec. 1.1.3). The theoretical prediction of [Feng et al. 1988a] was followed by an experimental observation [Freund et al. 1988] and several extensions, see Sec. 6.2.1. The ME is very helpful in imaging techniques and has been extensively used in this field as soon as 1990 [Freund 1990].

### 1.1.4.2 Spectral dependence

The reasoning applied in [Feng et al. 1988a] can be extended to include correlations between waves at different frequencies [Berkovits et al. 1994]. It is indeed straightforward that changing the input light frequency would change the speckle pattern. In addition to a homothetic scaling factor [Goodman 2007] expected from Eq. 1.6, the impact on the output phases of the different modes leads to a new speckle pattern<sup>14</sup>, see Fig. 1.6(b). The frequency shift required to uncorrelate the speckle pattern depends on the medium and it is referred to as the medium spectral bandwidth  $\delta\lambda_m$ . It somehow corresponds to the spectral grain size  $b_\lambda$  of the speckle,

$$b_\lambda \approx \delta\lambda_m. \quad (1.9)$$

Although [Shapiro 1986] gives a theoretical analysis, the spectral bandwidth can be determined experimentally by extracting the full width at half maximum (FWHM) of the correlation between speckle patterns measured varying the input wavelength, as performed in [Andreoli et al. 2015] and illustrated in Fig. 1.6(c). On the rightmost part of Fig. 1.6(c), one can see the effect of simultaneously

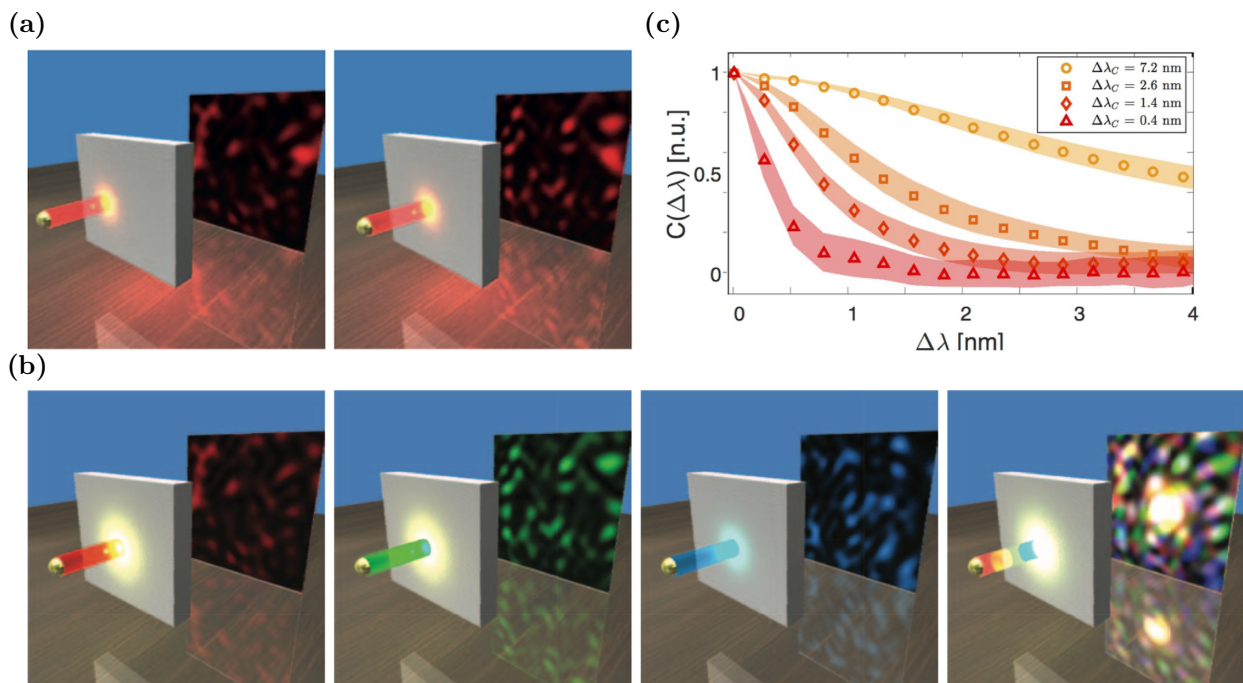


Figure 1.6: **Speckle pattern dependencies.** (a) The illumination of two different spatial spots of the medium with the same wavelength leads to different output speckle patterns. (b) The illumination of the same spatial spot of the medium with different wavelengths also leads to different speckle patterns. (c) Smoothly tuning the illuminating wavelength and computing the speckle correlations enables to obtain the decorrelation function. Measuring its FWHM experimentally gives access to  $\delta\lambda_m$  the value of which is medium dependent. Figures (a,b) are extracted from [Mosk et al. 2012] whereas (c) is taken from [Andreoli et al. 2015].

illuminating the sample with different wavelengths. The speckle results from the incoherent sum of the monochromatic speckles obtained for all the different wavelengths. The contrast  $C$  is hence reduced and is expected to be  $C = 1/\sqrt{N_\lambda}$ , where  $N_\lambda$  represents the number of independent speckle

<sup>14</sup>The phase changing faster than the amplitude with  $\lambda$ , in complex media no homothetic scaling with wavelength is usually observed.

patterns (here  $N_\lambda = 3$ ). When illuminating a medium with a source of spectral bandwidth  $\delta\lambda_s < \delta\lambda_m$  then the source can be considered monochromatic for the medium [Vellekoop 2015]. Otherwise the number of independent wavelengths is

$$N_\lambda = \frac{\delta\lambda_s}{\delta\lambda_m}. \quad (1.10)$$

This contrast dependence was proven useful to measure scattering properties of the medium [Curry et al. 2011; Thompson et al. 1997] or even to localize scattering particles [McKinney et al. 2000].

Due to the Fourier relation, it is noteworthy that illuminating the sample with a broadband source is equivalent to illuminating it with a temporal pulse. Hence, in the next section we will focus on temporal aspects of the speckle pattern.

### 1.1.4.3 Temporal dependence

Before considering broadband light, let us first recall that light propagation in highly scattering media follows a diffusion equation (see Eq. 1.2). From this equation emerges a timescale given by

$$\tau_D \sim \frac{L^2}{\mathcal{D}}, \quad (1.11)$$

and called the **Thouless time**. A closer study reveals two times with different physical interpretations following this scaling [Rotter et al. 2017]:  $\tau_T$  the transmission time and  $\tau_R$  the reflexion time.

- The Thouless<sup>15</sup> time  $\tau_D$  corresponds to the average time taken by light, initially in the medium, to exit. It is given by  $\tau_D \approx L^2/(\pi^2\mathcal{D})$  [Vellekoop et al. 2005]. The Thouless time can be extracted by fitting the exponential decay of an incoming short pulse. The intensity exponential decay is interesting as it allows to keep the electrical analogy: the medium acts as a low-pass RC filter (the luminicent equivalent of the resistance arising from the diffusion equation, see Tab. 1.1). The response to an impulsion is an exponential discharge of the medium (then seen as a capacitor). The medium thus smoothes input intensity variations.
- Conversely, the transmission time  $\tau_T$  represents the average time taken by light to diffuse through the medium; it is given by  $\tau_T \approx L^2/(6\mathcal{D})$  [Landauer et al. 1987]. It is measured by different techniques in [Vellekoop et al. 2005].
- The reflexion time represents the average time light takes to be reflected by the medium. Because it is more likely that light only travels a small path through the medium, it can be deduced from the diffusion time scaling by taking  $L \simeq l^*$ , leading to  $\tau_R \sim l^*/v_E$ .

The transmission time and reflexion time can be formally introduced and linked with the mean transmission time and the mean reflection time operators [Durand 2020] introduced in Sec. 1.5. Considering these three times, one has the ordering (valid in the multiple scattering regime)

$$\tau_R < \tau_D < \tau_T. \quad (1.12)$$

The contrast measurement performed in [Curry et al. 2011] also enables to extract  $\tau_T$  using Eq. 1.10 and sending an input light pulse of known bandwidth  $\delta\lambda_s$ , using the fact that  $\delta\lambda_m \propto 1/\tau_T$  for the medium.

Notice that the temporal aspect brings another degree of freedom for the speckle. It becomes time dependent if a light pulse is sent to the medium, see Fig. 1.7. In the spectral domain, the

<sup>15</sup>This name comes from the extraction by Thouless in [Thouless 1977] of a similar time for electrons to diffuse to the end of a wire. It is noteworthy that this similarity comes from the diffusion equation followed by both electrons and light.

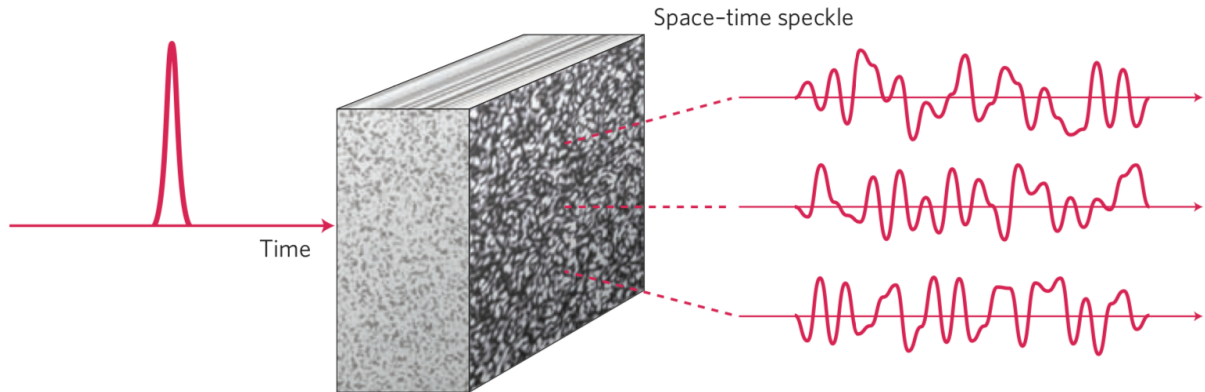


Figure 1.7: **Spatio-temporal speckle.** A short input pulse is sent into a scattering medium. A time-dependent speckle is observed at the output. The figure is taken from [Weiner 2011].

source bandwidth corresponds to the large spectral scale and the spectral grain size is related to the medium bandwidth. On the contrary, in the time domain the medium timescale (transmission time for instance) is related to the envelope whereas the source duration  $\delta t_s$  gives the temporal grain size which yields

$$b_t \approx \delta t_s. \quad (1.13)$$

In this section we have seen that, due to diffusion, light propagating through a complex medium is distorted both spatially and temporally. Since the pulse is Fourier limited, spectral and temporal aspects are two facets of the same phenomenon [Genack et al. 1990], aspect that we will extensively use all along this work. In the next section we will review the methods and tools harnessed to circumvent and even take advantage of this distortion.

## 1.2 How to fight diffusion: wavefront shaping and optimization

As seen previously, as soon as a medium scatters light and is not thin enough to avoid multiple scattering, the outgoing light is diffuse. Under coherent light, the speckle pattern, despite its intrinsic interest, seems to be of limited help to get information on the medium. So then why putting so much efforts in the study of light propagation through complex media? Can we even do something about it? The motivations of this work are presented in Sec. 1.2.1. The coherent aspect of the propagation provides a way to understand and control the propagation using **wavefront shaping** (WFS); we present its principle and main tools in Sec. 1.2.2 and two examples of applications in Sec. 1.2.3 and Sec. 1.2.4.

### 1.2.1 Motivation

All imaging techniques rely on the interaction between the probe wave and the object. Nowadays the most common non-invasive imaging techniques are radiology, scintigraphy, magnetic resonance imaging (MRI) and echography [Poirier-Quinot 2019].

- Radiology, for which Wilhelm Röntgen was awarded the Nobel prize in 1901, uses X-rays. The technique relies on the rays' different absorption by the tissues, leading to a transmission gray level anatomical image. Though rapid, it however suffers from a limited resolution ( $\sim 0.1$  mm) and subjects the patient to X-radiations.

- Scintigraphy uses a radioactive tracer linked to the target (cell for instance). The signal emitted by the tracer ( $\gamma$  rays) is collected by a  $\gamma$  camera. This technique enables functional imaging but is specific, with low spatial resolution ( $\sim 5$  mm), slow and subjects the patient to  $\gamma$ -radiations.
- MRI (the most recent technique) is based on the measurement of different relaxation times ( $T_1$  and  $T_2$ ) of the tissue water protons. It uses the nuclear magnetic resonance mechanism to rouse the hydrogen nuclei from their Boltzmann thermal equilibrium. Subtle imaging tricks are implemented to get a three dimensional map of the tissue water density. It is non-invasive (apart from the injection of contrast agents) but costly, long to perform and resolution-limited<sup>16</sup> ( $\sim 1$  mm).
- The echography technique uses ultrasonic waves. The tissue structure, modeled as a succession of acoustic impedances, is probed by measuring the return time of an input signal. The imaging is depth-limited (even though penetration reaches a few centimeters) with spatial resolution of  $\sim 0.2$  mm using conventional medical echographs.

All these techniques are complementary but a gap still needs to be filled [Sebbah 2001]. Optical light is a good candidate for non-invasive and radiation-free imaging as it could allow a kind of echography with an optical resolution. Moreover, the idea of seeing through tissues (or more generally through opaque media) is exciting. Among the wave-based electromagnetic imaging techniques described above, the frequency of the wave is dictated by the underlying physical principle. For optical imaging where scattering is the issue, the frequency remains fundamental (scattering is indeed frequency dependent). An idea would be to target frequencies for which the scattering is the lowest possible (i.e. longest wavelengths [Hong et al. 2014]). However scattering is not the only imaging limitation, and one should not forget absorption. A range of wavelengths, the **therapeutic window**, is defined and consists in the minimization of water absorption (shifted to the higher wavelengths region), see Fig. 1.8. Yet tissue absorption is not always avoided and sometimes it is an asset to improve the penetration depth by suppressing the multiple scattered photons which are more subjected to absorption [Carr et al. 2018].

To be able to use visible light for imaging, dealing with light scattering is thus fundamental. The next section presents a manner of doing so using wavefront shaping techniques.

## 1.2.2 Principle of wavefront shaping and its tools

### 1.2.2.1 Origin and principle of wavefront shaping

The idea of wavefront shaping comes from astronomy. Observation was impaired by atmospheric turbulence leading to refractive index inhomogeneities and hence aberrations: distorted wavefronts arriving on the telescope lead to a blurred image. The idea, developed in 1953 by H.W. Babcock, was to “un-distort” the wavefront by adding a compensation with the optical elements of the setup [Babcock 1953]. The need for this compensation to be reconfigurable led to the development of deformable mirrors at the root of **adaptive optics**. Now widely used [Roddier 1999; Tyson 2015; Hardy 1998] this technique extends to microscopy where similar issues call for similar remedies. An illustration of adaptive optics is presented in Fig. 1.9: an aberrated focus (Fig. 1.9(a)) is corrected thanks to a pre-aberrated wavefront (Fig. 1.9(b)). A reverse measurement (for instance using fluorescent particles in the sample) allows to determine the detection-induced aberrations (Fig. 1.9(c)). The latter example introduces the important notion of **guidestar**, also used in astronomy, required

<sup>16</sup>But very good regarding the used frequencies (64 MHz).

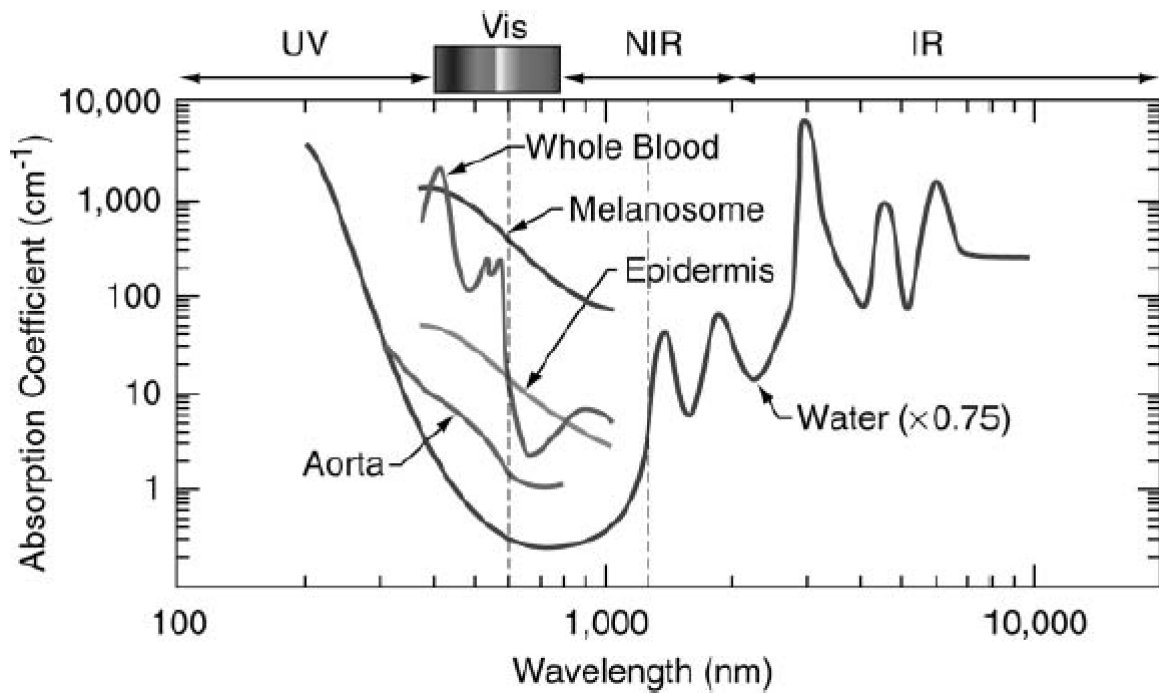


Figure 1.8: **Therapeutic window.** Dependence of the absorption of some tissues with the wavelength. The drop (especially for water) in absorption is observed in the upper-wavelength part of the visible spectrum and the near infra-red. The figure is taken from [Vo-Dinh 2014].

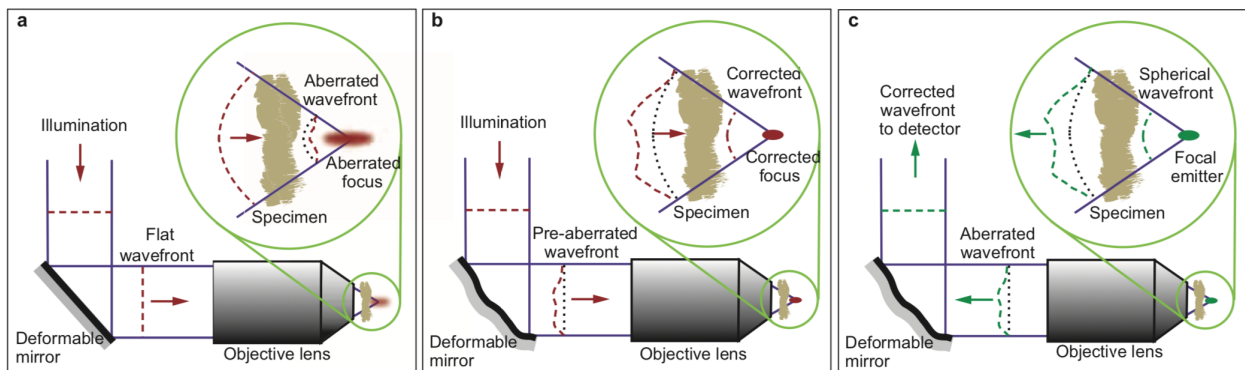


Figure 1.9: **Adaptive optics for microscopy.** (a) Aberrated focus induced by an incoming aberrated wavefront. (b) A deformable mirror compensates for the outgoing aberrated wavefront allowing the obtention of a corrected focus. (c) The use of a guidestar enables to determine the aberrations induced by the detection path. The figure is taken from [Booth 2014].

when light manipulation on both sides of a scattering material is not possible [Horstmeyer et al. 2015].

However the main restriction of adaptive optics is the limited correction. For higher scattering regimes a complete control over the incoming field is required, while keeping the adaptive optics spirit, it calls for the use of specific devices. Some are presented in the next section.

### 1.2.2.2 Different tools for wavefront shaping

The wavefront shaping is performed using **spatial light modulators** (SLMs). There are different types of SLMs differentiated by their operating mode, all bearing numerous pixels ( $\sim 10^3$  to  $10^6$ ). I introduce here three of them: the micro-electro mechanical system (MEMS), the digital micro-mirror device (DMD) and the liquid crystal SLM.

- The MEMS is the direct evolution of the deformable mirror used in adaptive optics [Bao 2005]. It is composed of a set of movable mirrors (of size in the range 10–100  $\mu\text{m}$ ). Their fast translation allows a phase modulation in the range  $[0, 2\pi]$  with a refresh rate between 10 and 100 kHz.
- The DMD belongs to the same category as MEMS as it also involves micro-mirrors. These mirrors are not translated but rotated. Two positions allow a fast (same order of speed magnitude as the MEMS) binary amplitude modulation by deflecting the incoming light.
- The liquid crystal SLM, that is detailed in Sec. 2.2.2 and abusively only referred to as SLM here, is composed of liquid crystal pixels. The refractive index change of the pixels allows a phase modulation in the range  $[0, 2\pi]$  but prevents any fast control (the refresh rate is 10–100 Hz). Moreover (liquid-crystal) SLMs can have the highest number of pixels among all SLMs. (Liquid-crystal) SLMs performances are compared to those of DMDs in [Turtaev et al. 2017].

A comparison summary is presented in Tab. 1.2.

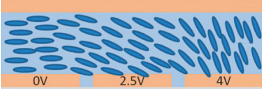
Technology	liquid crystal SLM	MEMS	DMD
Illustration			
Number of pixels	$\sim 10^6$	$\sim 10^3$	$\sim 10^{5-6}$
Diffraction efficiency	$\sim 90\%$	100 %	50 %
Modulation	Phase $[0, 2\pi]$	Phase $[0, 2\pi]$	Binary amplitude
Maximal speed	$\sim 100$ Hz	$\sim 10$ kHz	$< 100$ kHz
Cost	$\sim 10^4\text{€}$	$\sim 10^5\text{€}$	$\sim 10^3\text{€}$

Table 1.2: **Main spatial light modulator devices.** Comparison of the main characteristics of widely used SLMs. Table inspired from [Mounaix 2017].

With these tools allowing to shape at will the wavefront of an incoming beam, a guiding principle is now required for implementing the shaping. One not only needs the tools but also a goal and procedure idea. The same distinction as in [Horstmeyer et al. 2015] is followed here for the presentation: we present **conjugation** techniques in Sec. 1.2.3 and **feedback** ones in Sec. 1.2.4.

### 1.2.3 Time reversal operator and phase conjugation

The starting point of the use of phase conjugation is the **time-reversal** operator introduced [Fink 1997] in acoustics. To understand, one should recall that acoustic waves follow a d'Alembert equation having the property of being time reversal invariant due to the temporal second order derivative. Thus if a wave generated on some location propagates (even in a complex environment), applying

the time-reversal operation on it would make it refocus at its emission point. To do so, one needs a device that could conjugate the incoming wave and send it back, it is called a time-reversal mirror [Fink 1993]. It is noteworthy that it is very reminiscent of the deformable mirrors from adaptive optics [Hardy 1998]. Time reversal mirrors are used for acoustic waves [Fink et al. 2001]; their principle for electromagnetic waves, that also follow a d'Alembert equation, is presented in [De Rosny et al. 2010]. In optics, this procedure is called **optical phase conjugation** [Fisher 2012]. It can be performed by recording a hologram on a photographic plate [Leith et al. 1966] or using photorefractive crystals. This technique was proven to be powerful in thick scattering tissues [Yaqoob et al. 2008; McDowell et al. 2010] or to compensate for pulse dispersion by nonlinear phase conjugation [Yariv et al. 1979]. However the emergence of SLMs extends possibilities and favors **digital optical phase conjugation** expansion. The principle remains globally the same: (i) the field is recorded (in general using interference with a reference beam) see Fig. 1.10(a) (ii), a pattern is displayed on the SLM to form the phase conjugated wavefront that propagates back, see Fig. 1.10(b). Digital optical phase conjugation is interesting as it enables a single measurement

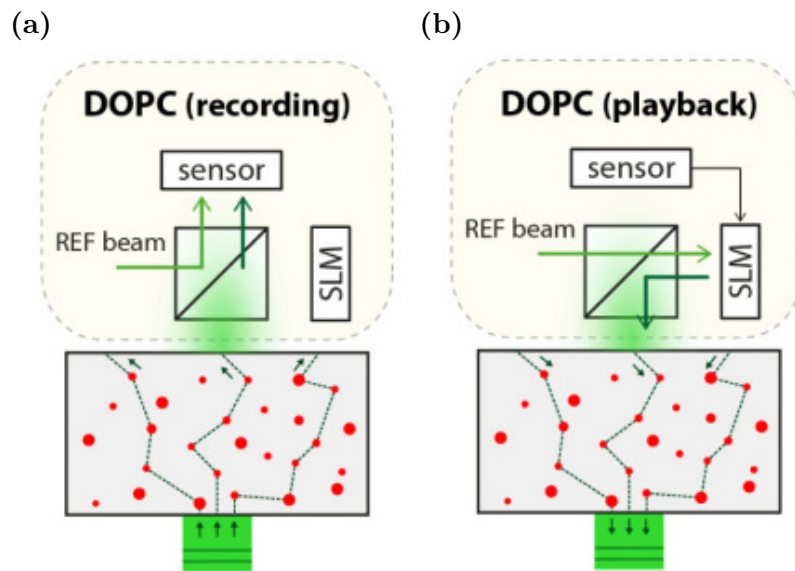


Figure 1.10: **Principle of the digital optical phase conjugation.** DOPC stands for digital optical phase conjugation. (a) Recording of the output scattered field (through its interference pattern with the reference beam). (b) Digital phase conjugation with the SLM (acting on the reference beam as a time-reversal mirror) to illuminate the sample and refocus light. Figure adapted from [Jang et al. 2015].

and can easily be applied to dynamic media (often the case for biological samples). However one of its limitations is the delicate alignment required [Jang et al. 2014].

In the next section we are going to discuss a similar approach relying on iterative optimization of the wavefront.

## 1.2.4 Optimization

### 1.2.4.1 Phase alignment and seminal works

To illustrate the idea of the optimization technique let us take the example of the seminal work by [Vellekoop et al. 2007]. A scattering medium (10  $\mu\text{m}$ -thick layer of  $\text{TiO}_2$ ) is illuminated by a

plane wave input and an output speckle pattern is measured on a camera behind it. This speckle is the coherent sum of random phasors [Goodman 2007]. This initial configuration is illustrated in Fig. 1.11(a). With a SLM set to have  $N_{\text{SLM}} \approx 3000$  degrees of freedom (modes), the wavefront is modulated. At the beginning of the optimization all SLM modes phases are set to 0. Then during the optimization process the phase of the mode is modulated from 0 to  $2\pi$  and the intensity on a target position is measured. The phase maximizing the output intensity is kept for this mode. We iterate over all the SLM modes. By doing so at every step, one aligns all phasors together. At the end of the process one displays a complex wavefront on the SLM that aligns all the phasors for the target position, resulting in a light focus, see Fig. 1.11(b).

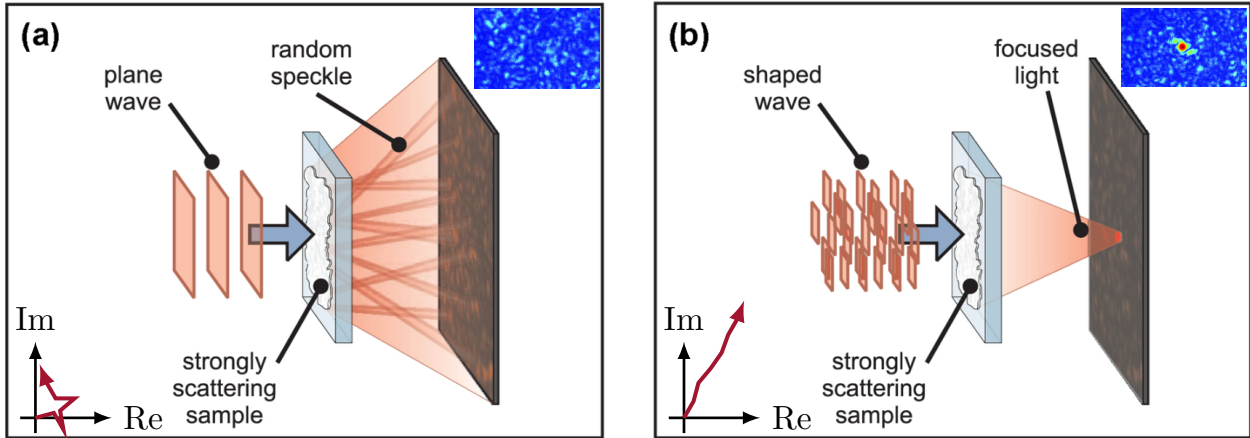


Figure 1.11: **Focusing behind a scattering medium with wavefront optimization.** (a) Non-optimized wavefront, a speckle pattern is observable behind the scattering medium, corresponding to the sum of random phasors. (b) Optimized wavefront that aligns all phasors at the target position and hence entails light focusing. Figure adapted from [Vellekoop et al. 2007].

The obtained focus bears some interesting properties. The reached intensity enhancement (with respect to a plane wave input wavefront)  $\eta_I$  is

$$\eta_I \simeq \frac{\pi}{4} N_{\text{SLM}}, \quad N_{\text{SLM}} \gg 1. \quad (1.14)$$

This value can be simply understood: the amplitude of the aligned phasors should scale as  $N_{\text{SLM}}$  whereas the background phasors, due to the random summing should scale as  $\sqrt{N_{\text{SLM}}}$ . The amplitude enhancement (ratio of both) hence scales as  $\sqrt{N_{\text{SLM}}}$  and one can obtain the intensity enhancement by simply squaring the value (it is only one spatial position). Another interesting property of the focus is its resilience to an incoming frequency shift that is given by the medium bandwidth [Van Beijnum et al. 2011]. Once a focus is formed it is also resilient in the range of the ME [Tran et al. 2019].

#### 1.2.4.2 Different methods

The previous optimization is the historical one. Several similar methods have been developed since, that we will briefly review; for a more complete description see [Vellekoop 2015].

First the optimization is not limited to one output target and the algorithm can be run optimizing simultaneously on several points as in [Vellekoop et al. 2007], the individual enhancement being reduced accordingly. Other algorithms have been proposed in [Conkey et al. 2012] or [Boniface et al. 2019a] where the optimization is performed on the speckle spatial variance.

When it comes to focus light on large areas (not being limited to a single or a couple of spatial positions), more complex behaviors arise. For instance in [Ojambati et al. 2016] a spread enhancement was reached due to the presence of long-range correlations (see Sec. 1.1.3.2).

One problem of this optimization scheme is its intrinsic iterative nature: the measurement takes some time and is not reconfigurable to focus in another position. Also, due to the choice of the parameter to optimize with, the focus result might not be optimal. It is optimal when optimizing with the intensity in one spatial position, but it is harder to conclude for a whole area. Then what is the best way to enhance the energy on a specific region? These questions will be addressed in Chap. 3 and Chap. 4.

Before discussing another approach for controlling the field behind a complex medium, let us make a small step aside by discussing temporal and spectral aspects and focusing with non-invasive imaging.

### 1.2.4.3 Inside biological samples

To perform the techniques detailed in Sec. 1.2.3 and in Sec. 1.2.4, and focus light inside a scattering medium, see Fig. 1.12, often the case when seeking at *in vivo* imaging, a guidestar is needed<sup>17</sup> [Horstmeyer et al. 2015]. The guidestar can take various forms: from fluorescence [Vellekoop

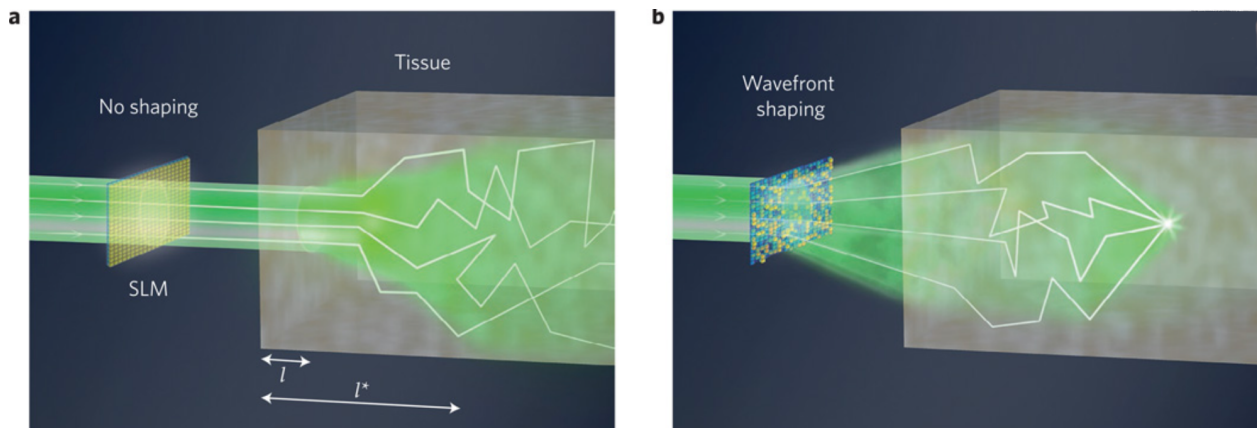


Figure 1.12: **Focusing inside a scattering sample.** (a) A coherent beam of light propagates through a scattering sample. Reaching one transport mean free path  $l^*$  the directionality is lost. (b) Wavefront shaping is applied on the incoming beam making it possible to focus light inside the scattering sample beyond  $l^*$ . Figure from [Horstmeyer et al. 2015].

et al. 2008a; Vellekoop et al. 2012] to second harmonic generation from nonlinear particles [Hsieh et al. 2010], but also ultrasounds and photoacoustics [Wang et al. 2012; Chaigne et al. 2014] and even taking advantage of the medium itself [Zhou et al. 2014]. For a review of the techniques see [Horstmeyer et al. 2015].

### 1.2.5 Approaches extended to pulses of light

The previous concepts (phase conjugation Sec. 1.2.3 and optimization Sec. 1.2.4), generally presented for monochromatic light can be extended to control pulses propagation. The feedback optimization is implemented in [Paudel et al. 2013] with polychromatic light and is associated with a narrow spectrum and hence a pulse recompression. The time-reversal analogue is presented in [McCabe et al.

<sup>17</sup>See [Ambichl et al. 2017a] for an atypical guidestar example.

2011], where the complex mixing of spatial and spectral degrees of freedom is emphasized [Wang et al. 2011]. A consequence of this spatio-temporal coupling is the conversion of spatiotemporal degrees of freedom to spatial ones [Lemoult et al. 2009]. It was done for instance with a time-gated feedback in [Aulbach et al. 2011] or with two-photon fluorescence in [Katz et al. 2011].

### 1.3 Transmission matrix

In this section we introduce the concept of the **transmission matrix** (TM), that we will extensively use all along this work. This tool proves to be both very practical and very informative about mechanisms governing light propagation in complex media. The TM is introduced via the **scattering matrix**, presented in Sec. 1.3.1. The TM main focusing characteristics are detailed in Sec. 1.3.2 and its extension to broadband light is discussed in Sec. 1.3.3.

#### 1.3.1 From the scattering matrix to the transmission matrix

In Sec. 1.1.3.2 the modes of the medium were mentioned. To understand what this term exactly refers to, it is convenient to extend the analogy with electron scattering. The latter is mainly developed by Landauer, Imry and Büttiker [Beenakker 1997]. They consider a mesoscopic conductor subjected to coherent scattering connected to electron reservoirs. This approach is extended to any scattering problem, for instance for electromagnetic waves [Saxon 1955]. This asymptotical description of scattering (the matrix globally describes the scattering with no near field information [Carminati et al. 2000]) is depicted in Fig. 1.13. All leads are connected together with the introduction of a

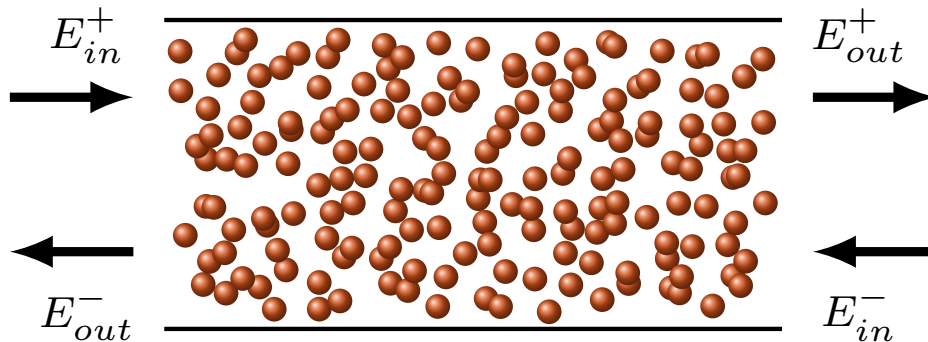


Figure 1.13: **Scattering matrix.** Information on light propagation is contained in the scattering matrix. On a slab geometry it links the input field  $E_{in}$  from both sides (left to right:  $E_{in}^+$  and right to left  $E_{in}^-$ ) to the output field  $E_{out}$  (left to right:  $E_{out}^+$  and right to left  $E_{out}^-$ ).

matrix [Imry 1986], called the **scattering matrix** and denoted  $S$ , such that

$$E_{out} = SE_{in}, \quad (1.15)$$

where  $E_{out}$  and  $E_{in}$  are respectively the waves exiting and entering the area. The same holds for photons [Beenakker 1997; Rotter et al. 2017]. In a 2D geometry (e.g. slab), to differentiate the field propagation from left to right ( $E^+$ ) from the field propagating from right to left ( $E^-$ ), the matrix is decomposed into four different sub-matrices:  $T$ ,  $T'$ ,  $R$ ,  $R'$ :

$$S = \begin{pmatrix} R & T' \\ T & R' \end{pmatrix}, \quad \text{with } E_{in} = \begin{pmatrix} E_{in}^+ \\ E_{in}^- \end{pmatrix} \text{ and } E_{out} = \begin{pmatrix} E_{out}^- \\ E_{out}^+ \end{pmatrix}. \quad (1.16)$$

Matrices  $R$  and  $R'$  are called **reflexion matrices** and matrices  $T$  and  $T'$  are called **transmission matrices**. It is noteworthy that the reflexion matrices are necessarily square whereas the transmission matrices are not.

In absence of absorption, energy conservation dictates that  $S$  is Hermitian ( $S^\dagger S = \mathbb{1}$ ), leading to relations between the sub-matrices. One has,

$$\begin{aligned} R^\dagger R + T^\dagger T &= T'^\dagger T' + R'^\dagger R' = \mathbb{1}, \\ R^\dagger T' + T^\dagger R' &= T'^\dagger R + R'^\dagger T = 0, \end{aligned} \tag{1.17}$$

with a similar set for  $SS^\dagger = \mathbb{1}$ . The link between all the quantities (e.g. Eq. 1.17) is very useful as it enables in some cases to access the required information without a full measurement of the scattering matrix as in [Davy et al. 2021]. The matrices  $R^\dagger R$  and  $T^\dagger T$  (and the two primed forms) play an important role in the scattering study. For instance they bear information on the total transmitted intensity and total reflected intensity given by  $T_1 = \text{Tr}(T^\dagger T)$  and  $R_1 = \text{Tr}(R^\dagger R)$ . These quantities ( $T^\dagger T$ ,  $R^\dagger R$ ,  $T_1$  and  $R_1$ ) also give access to the so-called conductance of the system. Introducing this conductance, we follow the line of the analogy with electron scattering [Fisher et al. 1981], where a dimensionless conductance is introduced and given by Landauer's formula:

$$g \equiv \frac{G}{e^2 h} = T_1, \tag{1.18}$$

where  $G$  is the conductance,  $e$  is the electron charge,  $h$  is the Planck constant and  $T_1$  is the transmitted intensity [Feng et al. 1988a; Berkovits et al. 1994]. The implications of the conductance value and its fluctuations in scattering experiments is discussed in Sec. 1.4.1.

It is noteworthy, from the scattering matrix description, that the scattering matrix is closely related to the Green functions of the system [Fisher et al. 1981]. The differences are discussed in [Rotter et al. 2017] and the near field effects are accounted in [Carminati et al. 2000].

Usually no complete measurements of the scattering matrix are performed, because of the very high level of information required. Such a measurement was however done in acoustics (with a limited number of modes) [Gérardin et al. 2014] but not in optics despite important efforts [Yu et al. 2013].

In this work we will solely measure the sub-matrix  $T$  that will be referred to as the transmission matrix (TM). Moreover even the measurement of the TM is very partial. The consequences of this partial control are discussed in Sec. 1.4. The purpose of the following section is only to introduce the different tools, putting apart the completeness of the measurement and its effect.

## 1.3.2 The monochromatic transmission matrix and its characteristics

### 1.3.2.1 The monochromatic transmission matrix

The simplest framework to introduce the transmission matrix is the monochromatic case, with a first measure by Popoff et al [Popoff et al. 2010]. Its principle follows the lines of the scattering matrix description: due to the linearity of the propagation it is possible to build up a matrix linking the input field to the output field (in the left to right propagation, it is the  $T$  sub-matrix of the scattering matrix  $S$ , see Eq. 1.16). To measure experimentally this matrix one needs to record the output fields for a basis of input vectors. The presentation of the field measurement as well as the choice of the basis are discussed in Sec. 2.3.4. Each input vector is generated using wavefront shaping that forms a 2D field sent to the medium of interest. The associated 2D output field is measured and reshaped as a vector to fill in a column of the TM. The field measurement is detailed

in [Sec. 2.3.2](#), and is based on the scattered field interference with a reference field. The reference field can either propagate through the sample (without any phase modulation with the SLM) or be an external plane wave.

It is noteworthy that, presented as it is, the measurement of a TM requires the access to both sides of the sample, a constraint incompatible with non-invasive *in vivo* imaging. However there exist methods to overcome this difficulty in obtaining non-invasive TM measurements [[Boniface et al. 2020](#); [Chaigne et al. 2014](#)].

### 1.3.2.2 Focusing achievements of the transmission matrix

Once a TM  $T$  is measured it can be used to focus light. It is possible to compute the input field  $E_{\text{in}}^{\text{target}}$  to send into the medium for a targeted output  $E_{\text{out}}^{\text{target}}$ .

$$E_{\text{out}} = TE_{\text{in}} \quad \rightarrow \quad E_{\text{in}}^{\text{target}} = T^{-1}E_{\text{out}}^{\text{target}}. \quad (1.19)$$

In practice, inverting the TM is not an easy and straightforward step due to computational and measurement errors being enhanced. To overcome this difficulty, we use the phase conjugation method<sup>18</sup> already employed in [Sec. 1.2.3](#). To focus light on one output pixel ( $i^{\text{th}}$  of the canonical basis for instance) the input is determined as follows:

$$E_{\text{in}}^{\text{target}} = T^\dagger e_i, \quad \text{where } e_i = \begin{pmatrix} \vdots \\ 0 \\ 1 \\ 0 \\ \vdots \end{pmatrix}. \quad (1.20)$$

This technique hence allows to spatially focus the light and has the advantage of being fully reconfigurable: as long as the TM is valid the targeted output field can be modified and a new input field calculated. This is a major advantage to optimization technique presented in [Sec. 1.2.4](#). It is noteworthy that these two techniques are not independent, indeed the optimized wavefront corresponds to a row of the TM (the row associated with the output spatial position of interest) [[Mosk et al. 2012](#)].

### 1.3.2.3 Access to the medium modes

In addition to focusing possibilities, the TM gives access to the medium's modes. Having measured a TM, the natural thing to do is try to diagonalize it. As mentioned earlier, a TM is not necessarily square, preventing a direct eigen-decomposition. A workaround consists in studying the eigen-decomposition of  $T^\dagger T$ , which is to the **singular value decomposition** (SVD) of  $T$ . The SVD is detailed below.

#### Singular value decomposition

The SVD of a matrix  $T_{(n,m)}$  (size  $n \times m$ ) consists in a decomposition such that

$$T_{(n,m)} = U_{(n,n)} \Sigma_{(n,m)} V_{(m,m)}^\dagger, \quad (1.21)$$

<sup>18</sup>The error is discussed in [[Defienne 2015](#)]. Moreover using the transpose conjugate instead of the inverse realises the constraint of decreasing the field at non-focusing positions and just bears information on the target position.

where  $U$  and  $V$ , both unitary, are the matrices containing the so-called left and right singular vectors and  $\Sigma$  is a diagonal matrix whose entries are the values  $s$ . Due to the origin of the SVD (eigen-decomposition of  $T^\dagger T$ ) all singular values are positive real numbers, usually sorted in a decreasing order. However it is important to keep in mind that the SVD returns the square root of the eigenvalues of  $T^\dagger T$ .

A very interesting point is that the SVD of a TM  $T$  corresponds to the study of the time-reversal operator given by  $T^\dagger T$  [Popoff et al. 2011; Prada et al. 1994].

### Interest

The access to the TM singular modes granted by the SVD is interesting. Due to the SVD definition, when illuminating the medium with an input singular vector (for instance the  $i^{\text{th}}$ ,  $V_i$ ), the transmission is driven by the associated singular value:  $TV_i = s_i U_i$ . Due to the singular vectors unitarity, the total intensity is given by

$$I = V_i^\dagger T^\dagger T V_i = s_i^2 U_i^\dagger U_i = s_i^2. \quad (1.22)$$

This technique can thus be used to control the transmitted output intensity behind a scattering medium as in [Kim et al. 2012]. They measure the total transmission on one ROI after a scattering medium when using the different singular vectors to shape the incoming wavefront (red circles) or when focusing spatially on one speckle grain (green line) and compare it to the mean transmittance (black line), see Fig. 1.14

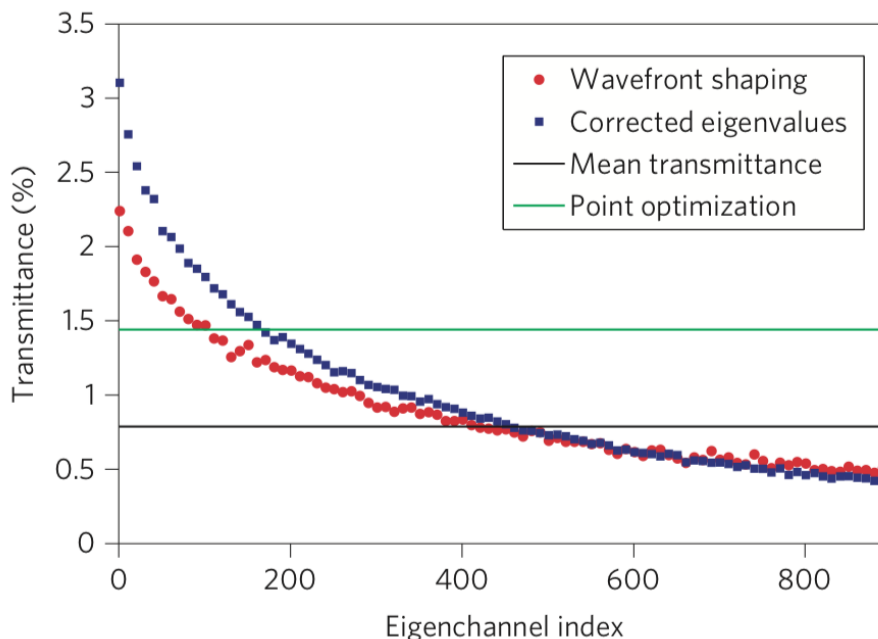


Figure 1.14: **Transmission control with the singular value decomposition of a monochromatic transmission matrix.** Transmission through a ZnO nanoparticles layer for different singular vectors (red dots) and associated singular values corrected for the sample transmission. The green line represents the global enhancement when optimization on one speckle grain is performed and the black line the mean transmittance measured for an input plane wave. Figure from [Kim et al. 2012].

Now that we introduced the TM tool and its use in monochromatic regime, we show that it can be extended to broadband light transmission.

### 1.3.3 A concept extended to light pulses

The approach of broadband transmission is presented below with three approaches: the spectral one using the **multi-spectral transmission matrix** (MSTM) in [Sec. 1.3.3.1](#), the temporal one using the **time-resolved transmission matrix** (TRTM) in [Sec. 1.3.3.2](#), both allowing spatio-temporal control, and another one relying on the measure of the so-called **broadband transmission matrix** (BBTM) in [Sec. 1.3.3.3](#).

#### 1.3.3.1 Multispectral transmission matrix

The idea of the MSTM is to gather a set of monochromatic TMs. For several wavelengths belonging to the pulse spectrum a monochromatic TM is measured, see [Fig. 1.15\(a\)](#). In the figure, an external reference is used to measure the field and corresponds to the second arm of the setup. To fully characterize the pulse propagation only a finite number of monochromatic TMs is required. This number depends on the ratio between the bandwidth of the input light  $\delta\lambda_s$  and the medium spectral bandwidth  $\delta\lambda_m$  (see [Eq. 1.10](#)) as illustrated in [Fig. 1.15\(b\)](#). The set of monochromatic TMs, that can be represented as a cube, see [Fig. 1.15\(b\)](#), forms the MSTM.

With the MSTM one can focus selectively one or several spectral components of the pulse, using the medium as a controllable dispersive element [[Andreoli et al. 2015](#)]. To go further and be able to introduce a temporal control, a phase relation between all the measured monochromatic TMs is required. It is reached thanks to a reference arm, see [Chap. 2](#) for more details on the TM technical measurement and the use of references. The phase relation opens the path to the full spatiotemporal control of the ultrashort pulse, allowing spatio-temporal focusing [[Mounaix et al. 2016b](#)].

However a major drawback of the MSTM is the long measurement time it requires (measuring  $N_\lambda$  TMs). To reduce this delay, a hyperspectral imaging system is used in [[Boniface et al. 2019b](#)] that allows measuring at once all spectral components acquiring both spatial and spectral data in a single array. It makes significant difference for thick scattering media (where  $N_\lambda$  is large). Its use however requires a calibration step and a compromise in the number of pixels.

Another method to reach temporal control with fast measurements is the introduction of temporally resolved measurements.

#### 1.3.3.2 Time resolved transmission matrix

A pulse of light can be considered from the spectral point of view, as done in the previous section, but also in the temporal domain; both being linked by a Fourier transform relation.

In the following we will call TRTM the Fourier equivalent of the MSTM, see [Fig. 1.16\(c\)](#). It hence holds direct temporal information. All individual matrices are measured for specific delays in the pulse thanks to a time-gated measurement, and are thus called **time-gated transmission matrices**<sup>19</sup> (TGTMs), see [Fig. 1.16\(a,b\)](#). For the purpose of a gated measurement an external reference with a delay-line is mandatory: the short reference pulse can selectively interfere with the elongated scattered pulse for different delays. The MSTM is based on  $N_\lambda$  monochromatic TMs similarly, to reach the full temporal information the TRTM needs the measurement of  $N_\tau$  TGTMs. The value of  $N_\tau$  is related to  $N_\lambda$  by

$$N_\tau = \frac{\tau_D}{\delta t_s} = \frac{\delta\lambda_s}{\delta\lambda_m} = N_\lambda. \quad (1.23)$$

<sup>19</sup>Time-gated reflexion matrices were also measured [[Choi et al. 2013](#)].

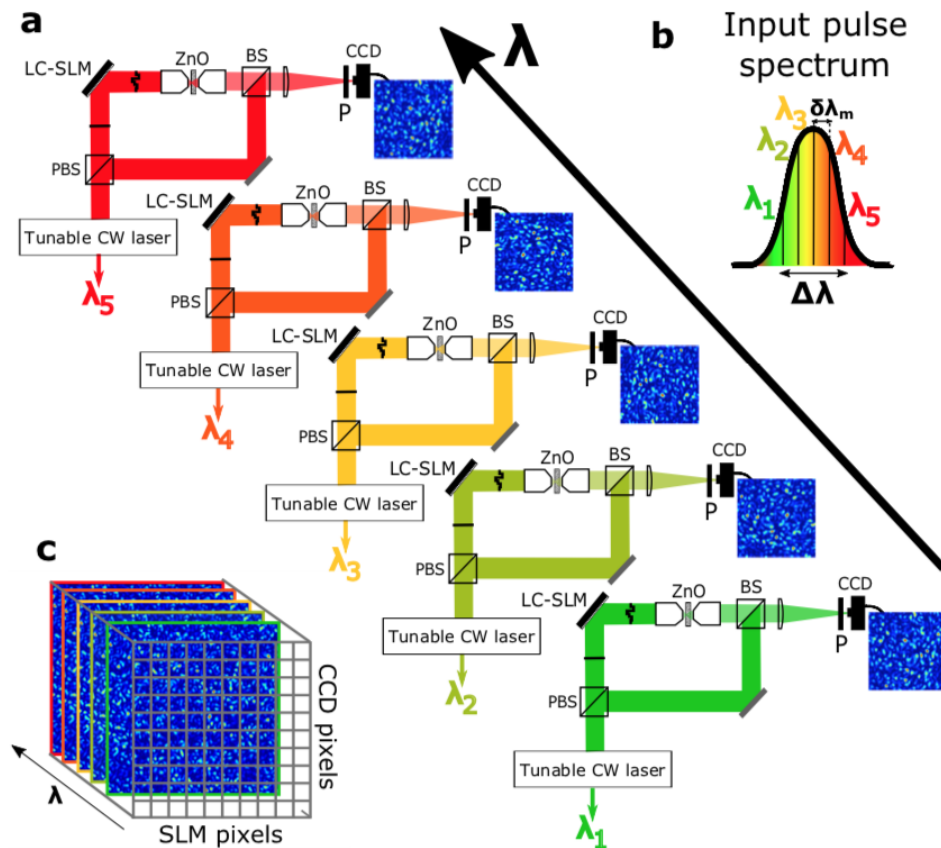


Figure 1.15: **Measurement of the multi-spectral transmission matrix.** (a) Measurement of several monochromatic TMs for a set of wavelengths, here  $\lambda_1 - \lambda_5$ . (b) Representation of the pulse spectrum. The considered medium (giving a  $\delta\lambda_m$ ) holds five independent spectral degrees of freedom. (c) The MSTM can be represented by a cube of size  $N_{\text{SLM}} \times N_{\text{CCD}} \times N_{\lambda}$ . Figure from [Mounaix 2017].

Hence to collect the full information both approaches (spectral and temporal) require approximatively the same measurement time. However for more specific usages both approaches are no longer equivalent. To control specific spectral degrees of freedom a MSTM is better suited; conversely to control specific delays the TGTm is recommended. The MSTM is nonetheless used for temporal experiments to compensate for the absence of pulse source and time-gated setups [Carpenter et al. 2016; Mounaix et al. 2019; Xiong et al. 2019]. The measurement of the TGTm, as well as several other achievements are presented in [Mounaix et al. 2016a]. The TGTm is more detailed in Chap. 4 where it is used experimentally for controlling the energy delivery.

However to measure a TGTm a gated measurement is needed. Another approach introducing a novel concept and relying on an internal reference is presented below.

### 1.3.3.3 Broadband transmission matrix

The idea of the BBTm is to control, for instance to focus, all the wavelengths of the incoming spectrum non-selectively. Already performed using a feedback [Paudel et al. 2013] or taking advantage of long-range correlations [Hsu et al. 2015] it is promising for biological media [Aguar et al. 2016].

The first characterization of a BBTm is presented in [Mounaix et al. 2017]. The measurement

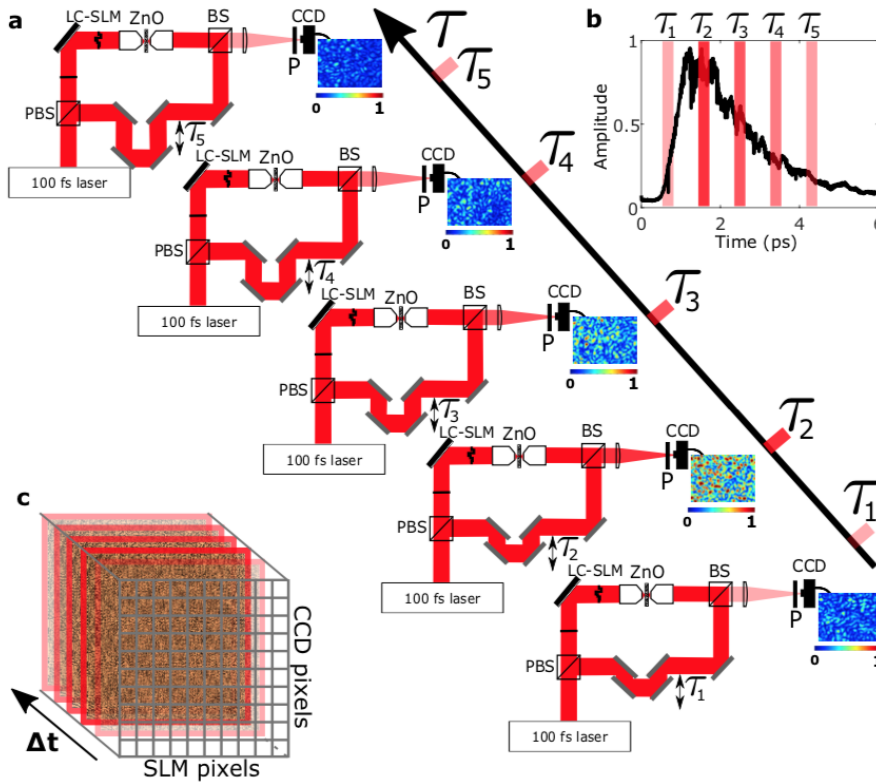


Figure 1.16: **Measurement of the time-resolved transmission matrix.** (a) Measurement of several TGTMs for a set of delays  $\tau_1 - \tau_5$ . (b) Presentation of the different delays together with the pulse shape. (c) The TRTM can be represented by a cube of size  $N_{\text{SLM}} \times N_{\text{CCD}} \times N_{\tau}$ . Figure from [Mounaix 2017].

of the BBTM is simple to perform as it corresponds to the measurement of a monochromatic TM with internal reference, but sending broadband light instead of monochromatic one. Thus all the information for the different wavelengths is gathered simultaneously. A major advantage is the need of only one measurement. Some remarkable results on the temporal behavior of pulses are pulse recompression and polarization recovery by the BBTM [Aguilar et al. 2017].

Now that the tools (TMs) have been presented we will focus in the next section on their properties. We will in particular examine the experimental level of control and the consequences of partial measurements.

## 1.4 Between limited control and mesoscopic effects

Theoretically all the scattering informations are contained in the scattering matrix. As seen in the previous section, interest is usually concentrated on the transmission matrix (or the reflection matrix). We will discuss in Sec. 1.4.1 the particularities of the transmission matrix when completely measured or when simulated. But because in optics TM measured experimentally are never complete due to the access to a limited number of modes, we discuss in Sec. 1.4.2 the impact of partial measurements.

Due to the very complex microscopic description of scattering, its statistical properties can be theorized using the random matrix theory. It is based on the assumption that sufficiently disordered

systems can well be described by an ensemble of random matrices [Wigner 1993]. This explains why random matrices are extensively used to model transmission matrices, see Sec. 1.4.2.3.

### 1.4.1 Complete measurements

The scattering matrix being unitary, all its singular values are equal to one. However the transmission matrix, as a subpart of the scattering matrix is not unitary and bears a richer spectrum. We discuss here the characteristics of complete TMs in the framework of the random matrix theory.

Using the random matrix theory the eigenchannels transmission of complex media were described and an analytical formula for their distribution was obtained by Dorokhov, Mello, Pereyra and Kumar, henceforth called the **DMPK** model whose probability density function is [Pendry et al. 1990; Dorokhov 1996; Beenakker 1997; Mello et al. 1988]

$$\rho(\tau) = \frac{l^*}{2L} \frac{1}{\tau\sqrt{1-\tau}}. \quad (1.24)$$

It is noteworthy that the PDF written above diverges in two points. The one at zero is not integrable such that the distribution does not start at zero but at a finite value  $\tau_0$  [Rotter et al. 2017]. The distribution of Eq. 1.24 is plotted Fig. 1.17. Its shape, with extreme transmission probability density

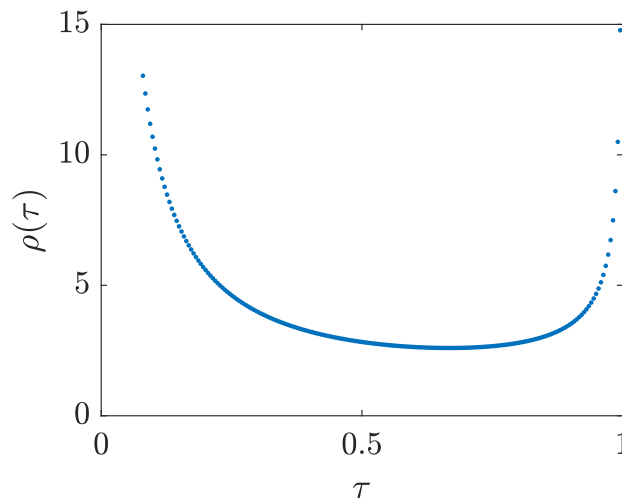


Figure 1.17: **Bimodal distribution.** PDF (Eq. 1.24) of the transmission eigenvalues of  $T^\dagger T$  under the DMPK model.

for  $\tau$  close to 1 and close to 0, motivate its denomination as **bimodal law**. These full transmission ( $\tau = 1$ ) and full reflexion ( $\tau = 0$ ) channels are respectively called **open** and **closed channels**. They are very exciting as coupling to them would allow any medium to act, for energy transmission, like a transparent one (full transmission) or a completely opaque one (full reflexion). These channels are however fragile [Goetschy et al. 2013] and only are accessible when the full transmission (or reflexion) matrix is measured. They have not been measured in optics for complex media<sup>20</sup>, but in acoustics [Gérardin et al. 2014].

However indication of coupling to open channels was experimentally measured in [Vellekoop et al. 2008c] through the expected universal transmission value of 2/3 for perfectly shaped wavefronts regardless of the thickness of the scattering material [Choi et al. 2011; Yu et al. 2013], see Comm. 1.4.1 for a rapid evaluation of this value.

<sup>20</sup>An equivalent involving polarization has been reach with multimode fibers, see Sec. 6.1.3

**Comment 1.4.1.**

The coefficient referred to for the transmission in [Vellekoop et al. 2008c; Choi et al. 2011] is  $C_{4,2}$ , corresponding to the ratio of the second and first moment of the distribution [Yu et al. 2013]. It is possible to evaluate it using the bimodal law, see Eq. 1.24 that gives  $\rho(\tau) = \frac{1}{\tau\sqrt{1-\tau}}$  (where  $\tau$  are the eigenvalues of  $T^\dagger T$ ). One has  $C_{4,2} = \frac{\langle \tau^2 \rangle}{\langle \tau \rangle}$ , leading to

$$C_{4,2} = \frac{\int_0^1 \tau^2 \frac{d\tau}{\tau\sqrt{1-\tau}}}{\int_0^1 \tau \frac{d\tau}{\tau\sqrt{1-\tau}}} = \frac{\int_0^1 \tau \frac{d\tau}{\sqrt{1-\tau}}}{\int_0^1 \frac{d\tau}{\sqrt{1-\tau}}}. \quad (1.25)$$

We perform an integration by substitution setting  $\tau = \sin^2 \theta$  then  $\sqrt{1-\tau} = \cos \theta$  and  $d\tau = 2 \sin \theta \cos \theta$ ,

$$C_{4,2} = \frac{\int_0^{\pi/2} \sin^2 \theta \frac{2 \sin \theta \cos \theta d\theta}{\cos \theta}}{\int_0^{\pi/2} \frac{2 \sin \theta \cos \theta d\theta}{\cos \theta}} = \frac{\int_0^{\pi/2} \sin^3 \theta d\theta}{\int_0^{\pi/2} \sin \theta d\theta}. \quad (1.26)$$

We have  $\sin^3 \theta = \frac{1}{4}(3 \sin \theta - \sin 3\theta)$ , hence  $\int_0^{\pi/2} \sin^3 \theta d\theta = \frac{2}{3}$ .

The spatial profiles of open and closed channels have also been studied and drastically differ from the spatial profile of a plane wave input which follows the optical Ohm's law (see Eq. 1.5) [Choi et al. 2011; Davy et al. 2015b; Sarma et al. 2016]. Another interesting behavior is the experimental

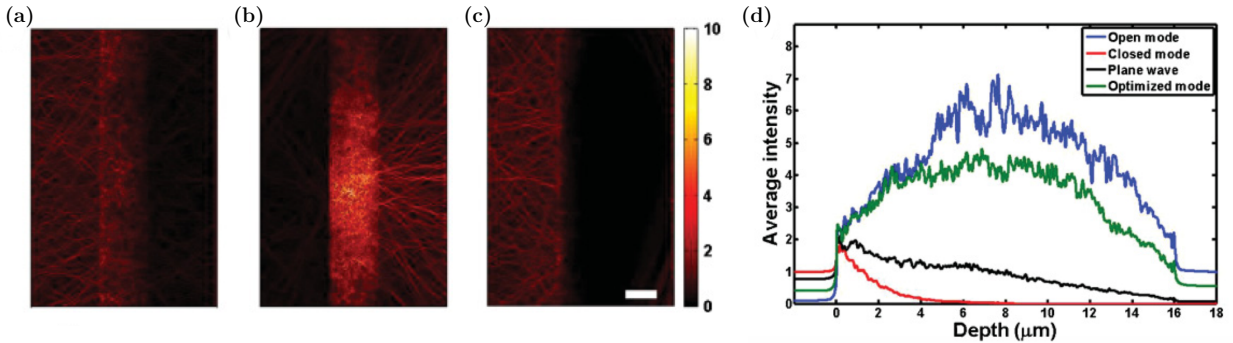


Figure 1.18: **Field distributions inside a scattering medium.** Simulations results for a plane wave input (a), an open channel (b), a closed channel (c). The white scale bar represents  $10 \mu\text{m}$ . (d) Averaged intensity along the  $z$  direction. Figure from [Choi et al. 2011].

observation of the transverse localization of eigenchannels [Yilmaz et al. 2019].

## 1.4.2 Scattering slab and partial control

### 1.4.2.1 Physical origin

Unlike in acoustics [Gérardin et al. 2014] where the bimodal law is observed, in optics for scattering media, no TM has been completely measured due to the experimental open geometry and the very high number of propagating modes. However, despite this knowledge and attempts to measure very large TM [Yu et al. 2013], where considering both polarizations, and a TM of 420 million of elements, the bimodal law was not reached. Thus with TMs of acceptable sizes<sup>21</sup> experimentalists are very far from the complete measurements. Therefore transmission and reflexion matrices both in optics and

<sup>21</sup>Acceptable in terms of computation time and size.

acoustics are well approximated by random matrices [Popoff et al. 2010; Sprik et al. 2008; Aubry et al. 2009].

With random matrices the number of modes is no longer a relevant parameter and the measured TM is characterized by the level of control it grants, evaluated through the ratio  $\gamma$  of the “constraints” ( $N_{\text{SLM}}$ ) and the degrees of freedom ( $N_{\text{CCD}}$ ),

$$\gamma = \frac{N_{\text{CCD}}}{N_{\text{SLM}}}. \quad (1.27)$$

Hence with this definition a very high level of control corresponds to very small values of  $\gamma$  whereas very large values of  $\gamma$  indicate a limited control. It is noteworthy that  $\gamma$  corresponds to the aspect ratio of the TM, hence a square matrix relates to  $\gamma = 1$ . However in experiments the value of  $\gamma$  is corrected to take into account, experimental constraints impacting the degree of control, see Sec. 2.3.5.3.

It is important to stress that some experimental constraints can induce correlations in the TM elements, this is for instance the case when several CCD pixels have similar values due to the measurement on these pixels of only one speckle grain (equivalent of one degree of freedom). These correlations modify the properties of the TM, which deviates from the random matrix model and leads to higher transmissions than the ones expected in absence of real mesoscopic (as the system conductance remains very high) effects [Popoff et al. 2014; Hsu et al. 2017].

If both the full TM and the random matrix regimes are well understood, the intermediate level of control is more complicated to describe. It can be done using an analytic prediction of the effect of incomplete channel control, based on filtered random matrices, and developed in [Goetschy et al. 2013].

#### 1.4.2.2 Marchenko-Pastur distribution for random matrices

Random matrices with **independent and identically distributed** (i.i.d.) coefficients bear some remarkable properties. V. Marchenko et L. Pastur proved that asymptotically the singular values of a random i.i.d. matrix<sup>23</sup> follow a specific distribution [Marčenko et al. 1967], called the **Marchenko-Pastur distribution** (MP).

Let us consider a random matrix  $M \in \mathcal{M}_{m,n}(\mathbb{C})$  ( $n > m$ , see Comm. 1.4.3 for a discussion on the case  $m > n$ ) with Gaussian i.i.d coefficients of mean 0 and standard deviation  $\sigma$ . The degree of control is given by  $\gamma = m/n$ . Its singular value decomposition gives a set of singular values  $s_i$  ( $1 \leq i \leq m$ ) such that  $s_i = \sqrt{\lambda_i}$ , where  $\lambda_i$  are the eigenvalues of  $MM^\dagger$ . The Marchenko-Pastur distribution describes the normalized singular values (it is a convergence theorem), with a normalization by  $\sigma\sqrt{n}$  ( $\tilde{s}_i = s_i/\sigma\sqrt{n}$ ). However it requires to know  $\sigma$  and an equivalent normalization is, see Comm. 1.4.2,

$$\tilde{s}_i = \frac{s_i}{\sqrt{\frac{1}{m} \sum_{j=1}^m s_j^2}}. \quad (1.28)$$

#### Comment 1.4.2.

Let us consider the spectra from two points of view.

- **Singular values of M and Marchenko-Pastur**

The singular values lie in  $[\sigma(\sqrt{n} - \sqrt{m}), \sigma(\sqrt{n} + \sqrt{m})]$ , they can be renormalized by  $\sigma\sqrt{n}$

<sup>22</sup>A more compelling definition of  $\gamma$  would have been the inverse:  $\gamma = \frac{N_{\text{SLM}}}{N_{\text{CCD}}}$ . However, as it is already defined in other papers, we do not change here the definition of  $\gamma$  to avoid confusions.

<sup>23</sup>There exist weaker hypotheses where the matrix does not need to be random i.i.d. but only have i.i.d. lines (resp. columns) and can afford “small” correlations among the columns (resp. lines) [Yaskov 2016].

( $\tilde{s} = s/(\sigma\sqrt{n})$ ) giving  $\tilde{s} \in [1 - \frac{\sqrt{m}}{\sqrt{n}}, 1 + \frac{\sqrt{m}}{\sqrt{n}}]$ .

• **Eigenvalues of  $MM^\dagger$**

Let us here start from the eigenvalues of  $MM^\dagger$ . One has  $\sum_{i=1}^m \lambda_i = \text{Tr}(MM^\dagger) = \sum_{i=1}^n \sum_{j=1}^m |m_{ij}|^2 \simeq m.n.\sigma^2$

Combining these two results enables to write

$$\sigma\sqrt{n} \simeq \sqrt{\frac{\text{Tr}(MM^\dagger)}{m}} = \sqrt{\frac{1}{m} \sum_{i=1}^m s_i^2} \quad (1.29)$$

This result is very interesting and useful as it shows that renormalizing the singular values may be done directly with the matrix spectrum with no need of computing the standard deviation of the matrix coefficients.

The probability density function of the normalized singular values  $\rho(\tilde{s})$  is given by

$$\rho(\tilde{s}) = \frac{1}{\pi\tilde{s}\gamma} \sqrt{(\tilde{s}^2 - \tilde{s}_{\min}^2)(\tilde{s}_{\max}^2 - \tilde{s}^2)}, \quad (1.30)$$

where, as seen in [Comm. 1.4.2](#),  $\tilde{s}_{\min} = 1 - \sqrt{\gamma}$  and  $\tilde{s}_{\max} = 1 + \sqrt{\gamma}$ .

In [Fig. 1.19](#), we illustrate variations in the singular values distribution, as a function of  $\gamma$ . In most of this thesis, we will have  $\gamma < 1$ , or more precisely the input dimension of the TM (number of columns  $n$ ) is larger than the output dimension (number of lines  $m$ ). It is noteworthy that for a square matrix ( $\gamma = 1$ ), as illustrated in [Fig. 1.19\(c\)](#), one recovers the so-called **quarter circle law**.

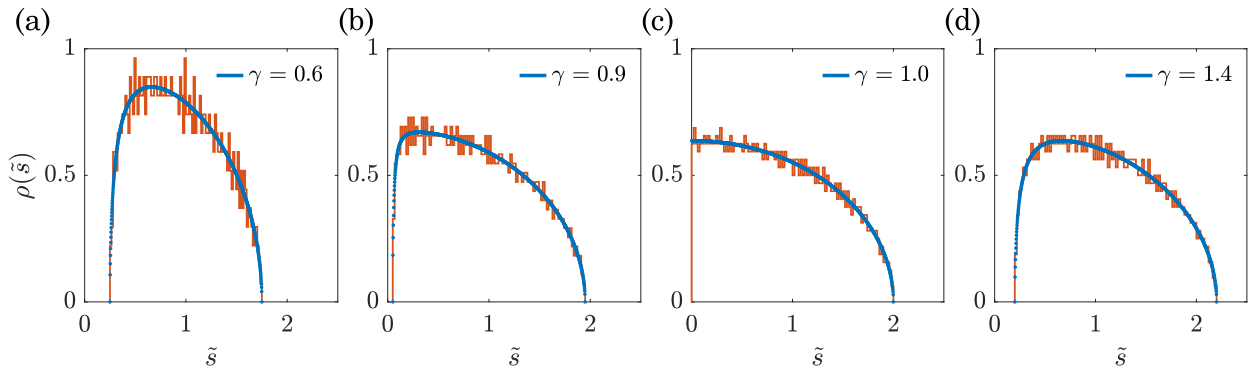


Figure 1.19: **Marchenko-Pastur law.** Marchenko-Pastur law for different values of  $\gamma$ . The simulated PDF is plotted in orange and the law from [Eq. 1.30](#) is presented with the blue dots for different values matrices aspect ratio:  $\gamma = 0.6$  (a),  $\gamma = 0.9$  (b),  $\gamma = 1$  (c) and  $\gamma = 1.4$  (d).

**Comment 1.4.3.**

From the SVD, one can show that  $M$  and  $M^\dagger$  have the same non-zero singular values. Thus, when  $\gamma > 1$  (that is when  $n < m$ ), one could (by symmetry) renormalize singular values by  $\sigma\sqrt{m}$  and obtain a Marchenko-Pastur distribution with normalized singular values in  $[1 - \frac{\sqrt{n}}{\sqrt{m}}, 1 + \frac{\sqrt{n}}{\sqrt{m}}]$ , which has the nice property of being included in  $[0, 2]$ . Henceforth, the Marchenko-Pastur normalization will stand for the normalization of singular values by  $\sigma\sqrt{\min(m, n)}$ . Following

the remark from [Comm. 1.4.2](#), it is equivalent with [Eq. 1.31](#):

$$\tilde{s}_i = \frac{s_i}{\sqrt{\frac{1}{\min(m,n)} \sum_{j=1}^{\min(m,n)} s_j^2}}. \quad (1.31)$$

However, some application might require to stick to the normalization by  $\sigma\sqrt{n}$ , because of the physical interpretation of  $m$  and  $n$ . In such a situation, singular values might be scaled by a factors  $\gamma$  when compared to the Marchenko-Pastur distribution, which explains why singular values in [Fig. 1.19\(d\)](#) lie in  $[\sqrt{\frac{m}{n}} - 1, \sqrt{\frac{m}{n}} + 1]$ .

### 1.4.2.3 RM model for simulations

Due to the strongly scattering properties of the medium used, the TM is well approximated by a random matrix [[Popoff et al. 2010](#)]. For instance an ideally measured TM follows the MP law given by [Eq. 1.30](#), see [Fig. 1.19](#). Hence generating a complex random Gaussian i.i.d. matrix well simulates the TM of a given medium. The field obtained after propagation through the medium is thus computed from this input field by multiplying the TM by the input vector field. The TM can be made more realistic by introducing spatial short-range correlations (e.g. speckle grain size) to mimic different levels of binning. This step is done by convolving each TM column (reshaped to form a CCD image) with a Gaussian the width of which depends on the targeted grain size. Some other features, as unitarity constraint, can also be added, see [Sec. 6.3.2.2](#) and [Appendix B.6](#).

Even though this approach is minimalist and heuristic, it can well reproduce the data obtained in different experiments and helps to predict some results, for instance in the case of the experimentally non-accessible phase and amplitude control.

### 1.4.3 Intermediate regime of control

Even though the full TM measurement is not experimentally accessible in optics, it is important to get an idea of how far we are from the full measurement. A good indicator is the value of the conductance  $g$  (see [Eq. 1.18](#)). As already mentioned in the experiments presented here  $g \gg 1$ , leading to a very partial control, see [Sec. 1.4.2](#). However when the value of  $g$  is relatively small, or when the number of controlled modes is large enough such that  $g \approx N_{\text{SLM}}$ , then some features of the bimodal distribution emerge [[Davy et al. 2015a](#); [Rotter et al. 2017](#)]. The filtered random matrix model developed in [[Goetschy et al. 2013](#)] describes well the cross-over between the bimodal distribution and the Marchenko-Pastur one, see [Fig. 1.20](#). For instance for very complete TM measurements as in [[Akbulut et al. 2016](#); [Yu et al. 2013](#)], deviations from the Marchenko-Pastur law were observed. Also a coupling to open channels is responsible for the observation of the long-range ( $C^{(2)}$ ) and infinite-range ( $C^{(3)}$ ) correlations discussed in [Sec. 1.1.3.2](#). It was realized experimentally in [[Vellekoop et al. 2008c](#)] where optimizing the intensity on one speckle grain also enhances the surrounding speckle. These long-range correlations play an important role in spatial enhancement increase [[Hsu et al. 2017](#)], but also when temporal aspects are present [[Xiong et al. 2019](#); [Hsu et al. 2015](#)]. Long-range transmission reflexion correlations predicted by [[Fayard et al. 2015](#)] have been observed by [[Ojambati et al. 2016](#)].

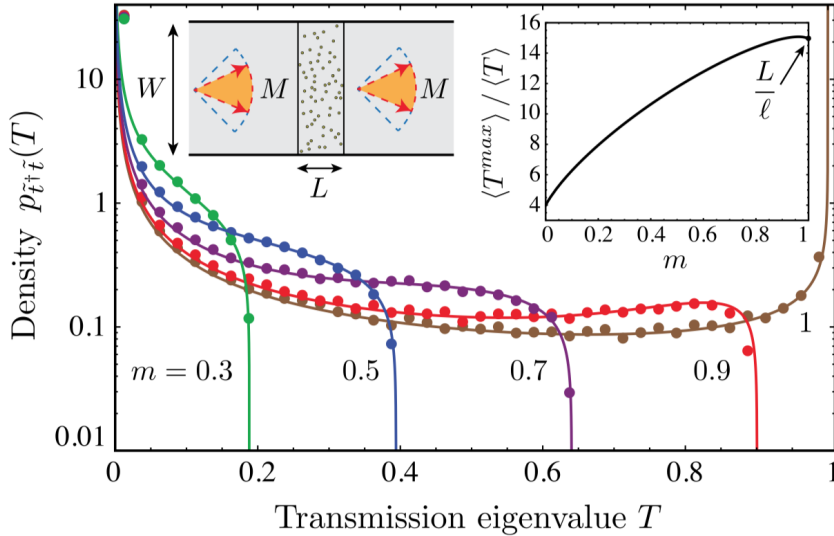


Figure 1.20: **Filtering of random matrices.** Simulation (dots) and analytical (solid line) results for transmission eigenvalue densities in a slab geometry for different fractions of controlled channels  $m$  ( $m = 1$  corresponds to the complete channel control). Figure from [Goetschy et al. 2013].

## 1.5 Scattering approach with operators

### 1.5.1 The Wigner-Smith time-delay operator

The Wigner-Smith operator is closely linked to the notion of **time-delay**. This notion was introduced by Eisenbud, Wigner and Smith [Wigner 1955; Smith 1960]. To consider the lifetime of metastable states Smith introduced the lifetime matrix. Interestingly the scope in this operator goes beyond the nuclear scattering context. Its expression  $Q$ , generally used for light scattering and referred to as the **Wigner-Smith time-delay operator** (or just the Wigner-Smith operator), is based on the scattering matrix and its derivative

$$Q(\omega_0) = -iS^\dagger(\omega_0) \left. \frac{dS}{d\omega} \right|_{\omega_0}. \quad (1.32)$$

With such a definition it is noteworthy that the eigenvalues of  $Q$  have the dimension of a time, and thus can be interpreted as time-delays (broadly studied, see [Van Tiggelen et al. 1999]). Applied to multimode fibers, its eigenstates, called principal modes, prove to be dispersion free at the first order [Fan et al. 2005], as observed in 100 m long multimode fibers [Carpenter et al. 2015]. This resilience to frequency change allows to broaden the field correlation between two neighboring frequencies [Xiong et al. 2016; Xiong et al. 2017] or even couples of frequencies that are further apart using a discretized version of the derivative [Ambichl et al. 2017b]. It is noteworthy that in case of multimode fibers, the scattering matrix can be replaced by the transmission matrix due to the very limited reflexion. In waveguides (or generally in slab geometries) the full scattering matrix may not be always available. To continue working with the transmission matrix some equivalences can be reached as in [Davy et al. 2021] where they show that the trace of  $Q$  is connected to the trace of the same operator, but is computed with the transmission matrix instead of the scattering matrix.

Initially linked to time-delays, the operator can be extended to different sets of coupled variables by performing the derivative with respect to another parameter than frequency, generalizing its use [Brouwer et al. 1997; Ambichl et al. 2017a]. For instance in [Ambichl et al. 2017a], measuring

the matrix for different positions of scatters enables to focus light inside a scattering medium, which generalizes the guidestar notion.

The Wigner-Smith operator also allows generating particle-like states [Rotter et al. 2011; Gérardin et al. 2016; Böhm et al. 2018]. It is also found in the dwell-time<sup>24</sup> operator [Durand et al. 2019; Durand 2020] and when maximizing the energy storage [Hougue et al. 2021].

The Wigner-Smith operator, is not the only operator that can be built on transmission matrices, even if it is the most famous. We review below some of them, recently introduced.

### 1.5.2 Other operators

Similarly to the dwell-time operator mentioned above, transmission and reflexion mean time operators are introduced in [Durand 2020] with the use of a polychromatic version of the Wigner Smith operator. They are designed to optimize a pulse temporal profile. They can reduce temporal dispersion at the cost of a small transmission, which is counterbalanced with an iterative optimization procedure. Their efficiency are compared with that of the singular modes of the TGTm. Other operators not directly built on the TM or the Wigner-Smith operator are designed to compensate distorsion (distorsion matrix) [Lambert et al. 2020; Badon et al. 2020] or to control the energy deposition in a scattering medium [Bender et al. 2021] as well as to determine the maximal information one can extract (Fisher information) [Bouchet et al. 2021a].

Other matricial operators defined for specific purposes are presented in Sec. 5.1.2 to introduce a method based on the singular value decomposition of transmission matrices (subject of the Chap. 5). The two of main operator of interest for this work are described in [Yilmaz et al. 2021] and in [Pai et al. 2021].

## 1.6 Scattering: always detrimental?

Before getting into the contribution of this thesis, an aspect of scattering is worth mentioning. Even though scattering is often perceived as detrimental and even though many tools have been developed to compensate and correct for it, this is not always the case. On the contrary, scattering and its complex mixing properties can turn into an asset. It will be visible in the field correlation control it allows (Chap. 3 and Chap. 5) and in the temporal targeted energy delivery (Chap. 4) discussed in this work. But benefits go even further. Still in the field of imaging, in [Vellekoop et al. 2010] a complex medium coupled to wavefront shaping techniques, improves rather than deteriorate the focus. The idea is that due to scattering, after some transport mean free paths, the effective numerical aperture of the system is increased, allowing for a thinner focus spot in the presence of a scattering medium Fig. 1.21(b) than without Fig. 1.21(a). The same observation was made for backscattering in acoustics [Tourin et al. 1999]. Along the same lines, using a thick biological sample in the near IR (dominated by scattering) a better image reconstruction was obtained with a lot of scattering [McDowell et al. 2010]. Moreover with wavefront shaping, a complex medium can be turned into any different optics: lens [Vellekoop et al. 2007; Popoff et al. 2010], phase plate [Guan et al. 2012; Park et al. 2012b], spectral filters [Park et al. 2012a; Small et al. 2012], high resolution spectrometer [Redding et al. 2014; Redding et al. 2013a] etc..

However numerous fields can take advantage of scattering [Wiersma 2013]. Scattering can prove useful for new generations of materials. As already mentioned, scattering of substrates are targeted to obtain whiteness [Jacucci et al. 2021; Syurik et al. 2018] and thus helps developing paints and coatings. Also the self-assembly of barium titanate nano-crystals was shown to enable tailored

<sup>24</sup>Interpreted as the mean time for the signal to leave the medium without loss.

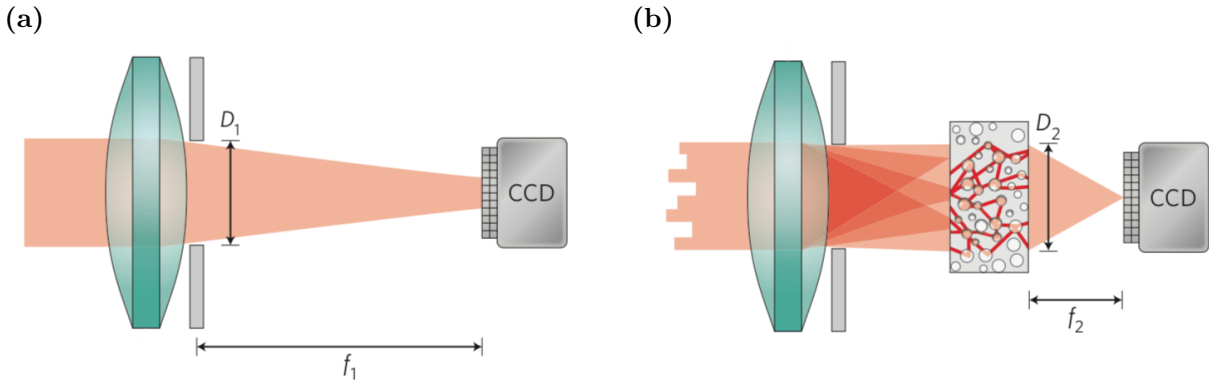


Figure 1.21: **Improved focus due to scattering.** (a) Focus obtained with a lens. (b) Thinner focus behind a scattering medium with wavefront shaping. Figure from [Mosk et al. 2012].

phase-matching at the micro-scale [Savo et al. 2020]. Moreover strong scattering enables alternative light trapping [John 1984; Anderson 1985; Sheng et al. 2007]. In [Sapienza et al. 2010], they observe strongly confined Anderson-localized cavity modes by adding disorder to photonic crystal waveguides, enhancing the interaction between single photons and single quantum emitters, paving the way for new platforms for quantum electrodynamics. Also the emergence of coherent feedback from scattering can enable creation of random lasers [Wiersma 2008; Cao et al. 2003; Cao et al. 1999] and tune them by controlling the pump [Bachelard et al. 2014].

In the field of information transfer, scattering also proves valuable. It allows transmitting error free information and which effectively increases the information transfer rate [Derode et al. 2003]. Scattering can also secure the transmitted information with the development of cryptography [Pappu et al. 2002] and the creation of quantum secure authentication [Goorden et al. 2014a], in which multimode fibers play an important role [Bromberg et al. 2019].

Last (of this non-exhaustive list) but not least, complex media are opening the way to optical computing, through the creation of optical scalable spin-glass simulator [Pierangeli et al. 2021; Pierangeli et al. 2019]. Its understanding allows compressive imaging [Liutkus et al. 2014] which is closely related to the link between multiple scattering and random matrices [Foucart et al. 2013].

## 1.7 Take home message

In this chapter we introduced main quantities of interest for this work: the scattering and transport mean free paths  $l_s$  and  $l^*$ , the Thouless time  $\tau_D$ , the speckle grain size  $b$ , the number of modes  $N_{\text{modes}}$  etc.. We also introduced the main tools and techniques to compensate for scattering: the SLM, the optimization and phase conjugation techniques, the transmission matrix and its SVD, the Wigner-Smith and related operators. We discussed the main consequences of the completeness of a TM measurement. Reaching a full control allows the emergence of open and closed channels whereas very partial measurements lead to a TM well described by a random matrix.

# 2 | Presentation of the experimental setup

---

2.1	General principle of the setup . . . . .	73
2.2	Presentation of the different elements . . . . .	74
2.2.1	LASER source . . . . .	74
2.2.2	Spatial light modulator . . . . .	75
2.2.2.1	Functioning . . . . .	75
2.2.2.2	SLM active area . . . . .	76
2.2.2.3	Phase-only constraint . . . . .	78
2.2.3	Scattering samples . . . . .	82
2.2.3.1	Sample Fabrication . . . . .	82
2.2.3.2	Sample characterization . . . . .	82
2.2.4	Camera . . . . .	84
2.2.5	Stage . . . . .	84
2.3	All elements working together, operation of the setup . . . . .	85
2.3.1	Polarization considerations . . . . .	85
2.3.2	Field extraction . . . . .	86
2.3.2.1	Phase-stepping . . . . .	87
2.3.2.2	Delay-line scan . . . . .	89
2.3.2.3	When to use which? . . . . .	90
2.3.3	Experimental determination of the optical path equalization between two arms . . . . .	91
2.3.4	Measurement of TMs . . . . .	93
2.3.4.1	Canonical <i>vs.</i> Hadamard basis . . . . .	94
2.3.4.2	Internal <i>vs.</i> external reference . . . . .	95
2.3.4.3	TM measurement . . . . .	96
2.3.5	TM characterization and level of control . . . . .	97
2.3.5.1	Speckle grain size and binning of the camera pixels . . . . .	97
2.3.5.2	Different SLM modes addressing . . . . .	98
2.3.5.3	Level of control . . . . .	99
2.3.5.4	Illumination scheme . . . . .	99
2.4	Take home message . . . . .	100

---

In this chapter I will present the setup used for all experimental results presented (except for the ones of [Chap. 6](#)). After giving a general idea of its principle in [Sec. 2.1](#), I will in [Sec. 2.2](#) present individually the different elements with the technical details omitted in [Chap. 1](#): the laser source

in Sec. 2.2.1, the SLM in Sec. 2.2.2, the scattering sample in Sec. 2.2.3, the camera in Sec. 2.2.4 and the translation stage in Sec. 2.2.5. I will finish in Sec. 2.3 by presenting how all these elements are combined to perform the experiments. For instance the techniques used to extract the field are detailed in Sec. 2.3.2, a method to set its temporal origin will be proposed in Sec. 2.3.3 and the general TM measurement will be presented in Sec. 2.3.4.

## 2.1 General principle of the setup

The experimental setup (presented Fig. 2.1) enables, in general, the measurement of TMs and more specifically of TGTMs and MSTMs. It hence involves all the elements required for wavefront shaping,

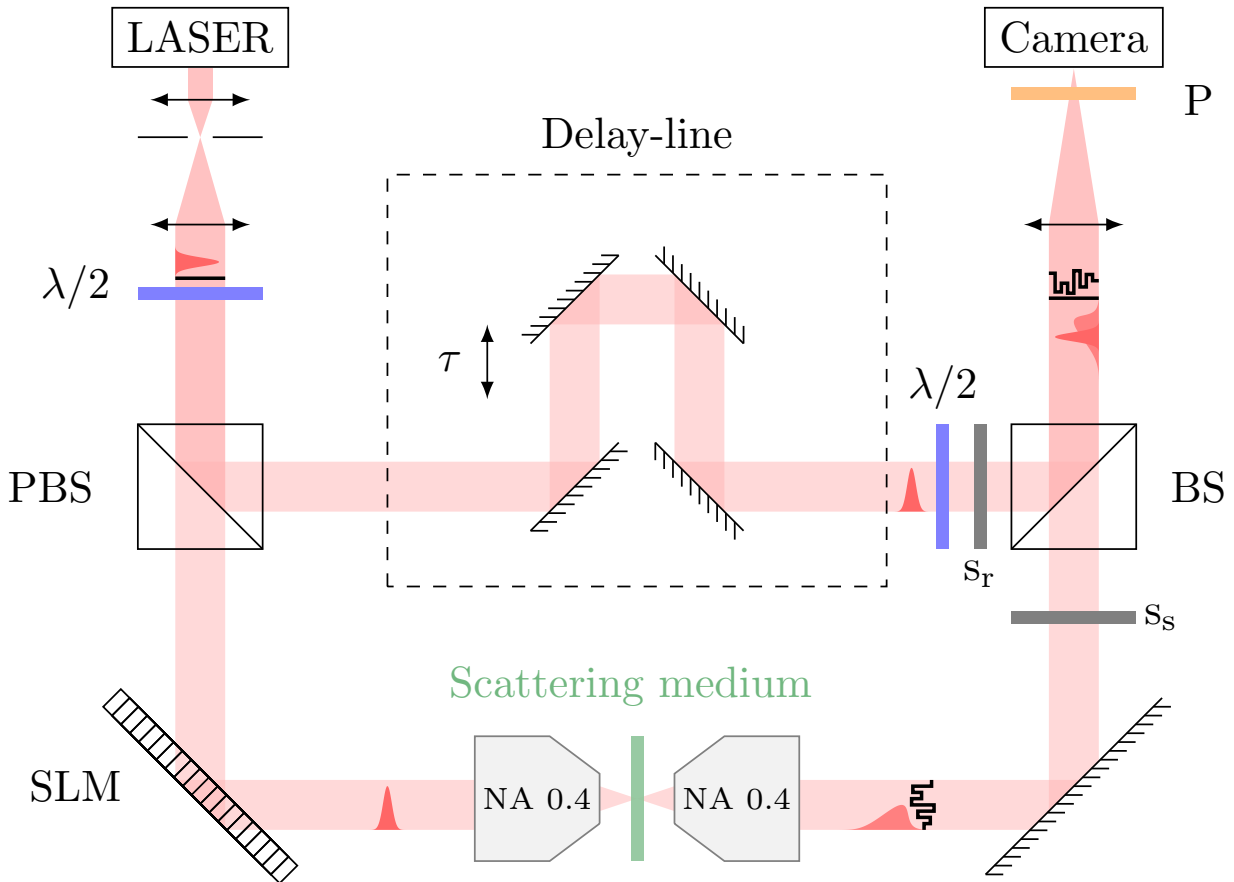


Figure 2.1: **Simplified scheme of the experimental setup.** An ultrashort pulse of light delivered from a Ti:sapphire pulsed laser (MaiTai HP, Spectra Physics,  $\approx 100$  fs pulse length) is divided upon two paths by a polarizing beam splitter (PBS). On one path the pulse wavefront is modulated by a reflective phase-only SLM (HSP512L-1064, Meadowlarks) and passes through a  $\text{TiO}_2$  layer (transmittance varying with the sample, suspended on a glass slide) where it gets spatially scattered (black distorted line represents the wavefront) and temporally elongated (pink pulse). On the second path, the pulse is sent on a controllable delay-line and acts as an interferometric temporal gate (probe pulse). Both pulses are recombined on a beam splitter (BS) that is imaged onto a CCD camera (Manta, G-046, Allied Vision). A polarizer (P) before the camera selects the desired polarization. Two shutters  $s_r$  (reference) and  $s_s$  (speckle) enable to block independently the light from each arm.

i.e. a light source, a wavefront shaping device (here a SLM more precisely), a scattering medium and a camera. However in addition to these elements, to probe temporal aspects, a reference arm with a delay-line is present. Indeed the camera is not able to resolve optical frequencies and the temporal averaged intensity measured. While not limiting in case of monochromatic illumination it becomes a restricting factor when it comes to pulses: an interferometric and temporally resolved measurement is required. Because an incoming short pulse is elongated in time due to scattering events, the same short pulse (non elongated) can be used as a temporal probe. Its delay is controllable with the delay-line. Once the probe delay fixed, it interferes solely with the scattered light that has accumulated the corresponding delay in the medium. This time-gated interference enables us to extract the field corresponding to this specific time delay.

All elements will be analyzed individually in [Sec. 2.2](#) and their symbiosis discussed in [Sec. 2.3](#) with in particular the presentation of the field extraction technique in [Sec. 2.3.2](#).

## 2.2 Presentation of the different elements

### 2.2.1 LASER source

The source used in all experiments is a mode-locked Ti:sapphire pulsed laser (MaiTai HP, Spectra Physics) of  $\sim 100$  fs pulse length and 80 MHz repetition rate. The pulse's central frequency is tunable in the 690–1040 nm range. The laser spectral range enables to perform experiments in the near-IR<sup>1</sup>, the precise value of the wavelength we chose is arbitrary. The laser optimal emission is situated around 800 nm (also corresponding to the SLM optimal reflectivity), but due to the optics constraints (the  $\lambda/2$  working wavelength being fixed) the selected central frequency is set to 808 nm. The laser may also be converted into a tunable monochromatic source when not used in the mode-locked regime. To do so a physical slit is placed after a dispersive element (in the cavity) and selects the targeted amplified wavelengths, filtering out the other ones and hence preventing the mode-locking. Translating the slit enables to define the frequency.

A spectrometer (HR 4000, Ocean Optics), collecting some light at the output of the laser enables to monitor in real time its spectrum. Predictably from the pulse temporal length, as the pulse is close to Fourier transform limited, its spectral full width at half maximum (FWHM) is of  $\sim 10$  nm. When operated as a monochromatic CW source (mode-unlocked), the measured laser spectral width is  $< 0.1$  nm (0.1 nm reaching the spectrometer resolution limit). This spectral width is much smaller than the medium spectral decorrelation width (see [Sec. 2.2.3.2](#) and [Sec. 1.1.4.2](#)): all wavelengths contained in the narrow band light will experience the same scattering<sup>2</sup>. Hence for the medium and the performed experiments, the source can be considered monochromatic, allowing us to use this term to refer to it.

However, since the laser is optimized for mode locked operation, the monochromatic mode is unstable: one observes a jitter. The characterization of this jitter, performed using the scattering media as a spectrometer is developed in [Appendix A.1](#). From this jitter measurement we estimated the relative wavelengths fluctuations (measured fluctuations over the input light bandwidth) at 0.01 for the pulse mode and 0.2 for the monochromatic mode. The jitter of the monochromatic source is not an issue for most of the experiments performed. It is however important to keep in mind that frequency resolved measurement may not be achievable below 0.1–0.2 nm. This experimental constraint however would be very important for the study of the Wigner-Smith operator defined, see [Sec. 1.5.1](#) where the derivative with respect to the frequency of the transmission matrix is computed.

<sup>1</sup>Which is convenient for further applications, see [Sec. 1.2.1](#).

<sup>2</sup>The laser is probably not single longitudinal mode, but with no effect on the studied media

## 2.2.2 Spatial light modulator

### 2.2.2.1 Functioning

The wavefront shaping device used on the setup is a reflective phase-only SLM (HSP512L-1064, Meadowlarks). It is a liquid crystal array (here of  $512 \times 512$  pixels) whose pixels may be individually addressed. A voltage is applied between the two sides of the pixels leading to the modification of their optical properties. The SLM pixels are filled with nematic liquid crystal (birefringent medium) aligned with the cover glass when no voltage is applied. Applying a voltage tilts the liquid crystal perpendicularly to the cover glasses hence modifying the effective refractive index and thus the local optical path. It is noteworthy that to obtain a pure voltage-dependent phase shift the incoming light polarization is important. A linearly polarized light along the extraordinary axis of the liquid crystal is required here.

Also to be able to conveniently set the phase delays a calibration of the look up table<sup>3</sup> (LUT) is needed. After this step the delay of each SLM pixel may be controlled: a 8-bits gray level (associated to a voltage) controls the phase delay between 0 and  $2\pi$ . The global control the wavefront after the SLM is thus obtained with a 8-bits matrix, whose size corresponds to the SLM.

### 2.2.2.2 SLM active area

We do not always use the full SLM. For instance when the beam illuminates a subpart of the SLM we need to localize this region, to only work with it. This region is called the “active region”, only in this zone the SLM masks will be displayed. It is noteworthy that the illuminated area depends on the beam size and profile. All the pixels of the active area may not be homogeneously illuminated in case of an input Gaussian profile. The effective aperture of the backfocal plane of the microscope objective (or other geometrical effect) also affects the effective active SLM area as discussed in [Comm. 2.2.1](#).

#### Comment 2.2.1.

In the configuration discussed previously it is noteworthy that all the SLM modes are not addressed homogeneously for mere geometrical reasons. Indeed here the SLM is imaged on the back aperture of the illumination microscope objective. Due to its circular shape the latter may cut a part of the incoming light from the SLM, even if the active part of the SLM have been carefully selected. There are then two options: under-fill or overfill the microscope objective backfocal aperture. Under-filling it consists in selecting an active area smaller than the illuminated beam and such that all the light passes through the SLM backfocal aperture as done in [\[Popoff et al. 2010\]](#). However this configuration leads to the transmission of unmodulated light which we want to avoid. We thus overfill the microscope objective backfocal aperture but with the price of having an effective number of modes smaller than the one set. The information of the effective number of modes is present on the TM and affects its rank. The effective number of modes can be evaluated and accounted for, see [Sec. 2.3.5.2](#). Another idea to circumvent this difficulty would be to adopt a circular active SLM region by shaping the basis. This circular SLM active region has been used in [\[Mastiani et al. 2021; Akbulut et al. 2011\]](#) when performing optimizations. This is also easy to imagine for the Canonical basis and has been extended to binary masks with the Hadamard basis [\[Ledesma-Carrillo et al. 2017\]](#).

In order to select the active region on the SLM one needs to determine where the laser beam hits the SLM (we assume here that for all experiments the laser beam is smaller than the the SLM). To do so one realizes horizontally (resp. vertically) a pixel line scan: all SLM pixels are addressed

<sup>3</sup>The look up table links a 16-bits voltage value to a 8-bits gray level.

to generate a 0 phase shift except for a column (resp. line) that is set to  $\pi$ . This line is moved along its full transverse dimension on the SLM while images are taken with the camera. When the pixels modify the phase of a region where there is no light the speckle pattern is not affected. In contrast, when the phase modification concerns illuminated areas the speckle pattern changes. Hence computing the speckle correlations with the initial one enables to map the illuminated region on the SLM and select an optimal area to work with.

On the active area the number of pixels independently controlled gives the maximal number of SLM modes. Since this number may be high and the learning of the TM too long, we select a number of modes and group the pixels into macropixels. The macropixel size thus depends on the SLM active area and the targeted number of modes. The use of macropixels also enables to avoid “cross talk” effects [Moser et al. 2019] between individual neighboring pixels.

### 2.2.2.3 Phase-only constraint

It is important to note that with this device only the phase of the field is controlled. The amplitude transmission remains uniform for all pixels. Despite the apparent limitation of phase-only control, this constraint does not drastically affect the experimental achievements. The enhancement decrease observed when focusing with phase-only instead of phase and amplitude is  $\pi/4$  ([Čižmár et al. 2011]). Indeed in a complex field the information is chiefly contained in the phase, the amplitude “just” weights it. This is very easy to see when considering the example of the information contained in an image as presented in III. 2.2.2.

#### Illustration 2.2.2.

Let’s consider two images, one of a cat (image A) and one of a landscape (image B), see Fig. 2.2 top part. For both images one can realize the Fourier transform and split the information on the phase  $\phi_A$  (resp.  $\phi_B$ ) and the information on the amplitude  $A_A$  (resp.  $A_B$ ). The Fourier transforms are modified by switching their phases and amplitudes. Then taking the inverse Fourier transform leads to new images presented in Fig. 2.2 bottom part. It appears that one still can distinguish the cat from the landscape. The cat appears on the reconstructed image whose Fourier transform phase is  $\phi_A$  (conversely for the landscape).

Another illustration, closer to experiments, is presented in Appendix A.2.

However, even if the phase-only constraint is not detrimental for most of the experiments, it is a conceptual and theoretical major difficulty. Indeed in most experiments performed the input states that one wants to generate after the SLM are vectors containing both phase and amplitude information. They usually are computed from the TM or another related operator. But linear algebra theorems no longer apply when disregarding the amplitude of the input vectors making it difficult to theoretically describe the experiment. Differences between phase and amplitude and phase-only control are observed in simulations and discussed all along the different studies (for instance in Sec. 3.2.3, Sec. 4.5.2 and Sec. 5.2.5)

For these reasons, implementing an experimental phase and amplitude control with a phase-only SLM is promising and, fortunately, not impossible. Several methods have been developed for that purpose. I will briefly present a non exhaustive list of them. A method, presented in [Zhu et al. 2014] uses two cascaded SLMs to achieve this goal. They illuminate the first SLM with a light polarized at  $45^\circ$  with respect to the extraordinary axis, hence only a part of the light is modulated, after a polarizer a second SLM modulates all the light leading to an independent control of the phase and amplitude. To circumvent the use of two different SLMs, sensitive to alignment, costly and space demanding, the same SLM is sometimes used twice [Chavali et al. 2007]. Otherwise necessary degrees of freedom may be taken from the SLM itself by encoding the information over neighboring SLM pixels [Bagnoud et al. 2004; Van Putten et al. 2008] and associated to a spatial filtering step.

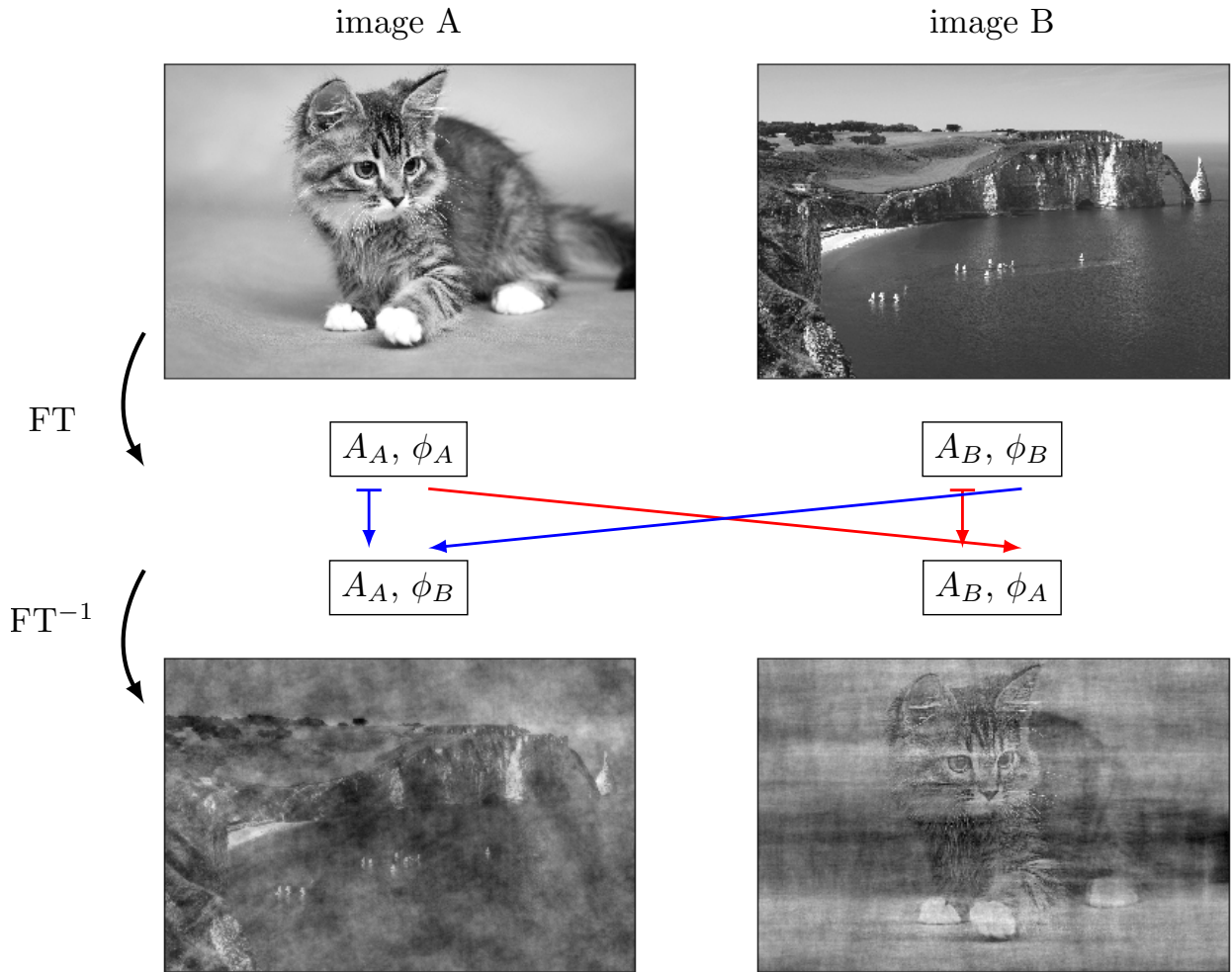


Figure 2.2: **Phase vs amplitude information.** The images of a cat (image  $A$ ) and of Étretat cliffs in Normandy (image  $B$ ) are Fourier transformed (FT); the respective phases ( $\phi_{A/B}$ ) and amplitudes ( $A_{A/B}$ ) of these FT are then exchanged. The inverse of the thus modified Fourier transforms are computed. On the bottom images one can recognize the cliff on the image containing  $\phi_B$  and the cat on the one containing  $\phi_A$ .

The spatial filtering is generally used in an off-axis geometry [Čižmár et al. 2011; Leach et al. 2005]. The idea relies on the properties of blazed gratings: by displaying on the SLM, on top of the mask, a grating, a controllable amount of light is sent on the first order of diffraction that can hence be selected by cutting the zero order with a pinhole. The blazed nature of the grating enables to send the maximum of light on the first order. Importantly, to be able to display gratings on top of the SLM mask, the SLM pixels should be grouped into macropixels. This constraint is not very limiting as in most cases the pixels are anyway grouped to fulfill the number of SLM modes constraint. The off-axis technique has the advantage of suppressing the contribution of the non modulated light (the light that reflects on the SLM glass front and hence whose wavefront is unshaped). It is nevertheless more delicate to align and less flexible. Indeed one needs to remain on the first diffraction order, whose position depends on the macropixel size. Changing the number of SLM controlled modes hence requires to modify the setup alignment.

A very similar technique, but this time exploiting the zero<sup>th</sup> order [Van Putten et al. 2008; Guillon et al. 2017], may also be used<sup>4</sup>. The SLM gratings (here checkerboards are used) instead of sending the desirable light to the first order keeps it in the zero order. The rest is cut with a pinhole. The advantages and drawbacks of this technique are complementary to those of the off-axis technique: flexibility and alignment are easier but the unmodulated light remains. This manner of going from phase-only to phase and amplitude control is easy to implement in several cases as it only requires coding. A schematic of its different steps is presented in [Appendix A.2](#).

For the rest of this manuscript the phase-only control is used. It makes experiments easier to carry with no major limitations in this work. The influence of the phase-only modulation will be discussed on each experiment individually.

## 2.2.3 Scattering samples

### 2.2.3.1 Sample Fabrication

The scattering samples used are layers of titanium dioxide ( $\text{TiO}_2$ ) or zinc oxide ( $\text{ZnO}$ ) suspended on a glass coverslip. They are fabricated in the lab by letting dry (about 5–10 h depending on the droplet size) a droplet of solution of particles on the glass cover. The droplet is deposited on a vertical cylinder lying on the glass coverslip to present its spreading during the water evaporation. The particles size used is 50 nm. An example of this medium is presented [Fig. 2.3](#). For a very detailed sample manufacturing technique see [[Putten 2011](#)].

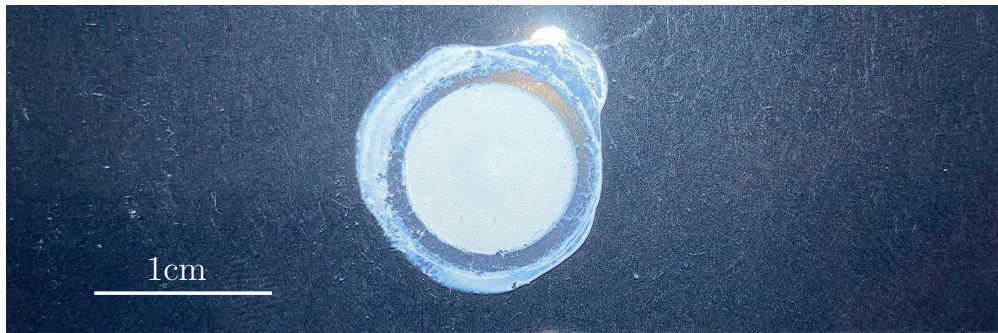


Figure 2.3: **Photo of one sample used for the experiments.** A droplet of  $\text{TiO}_2$  solution is deposited on a cover glass and left to dry forming a paint layer ( $\text{ZnO}$  also can be used). The white bar represents the scale (1 cm).

### 2.2.3.2 Sample characterization

The scattering properties of the sample used in the experiments are measured following the approach of [[Andreoli 2014](#); [Mounaix 2017](#)].

For instance the thickness  $L$  of the different media is measured with a microscope by focusing alternatively on the scattering surface and the glass slab. This method, relatively easy to implement, is however imprecision prone. Moreover the thickness is not uniform on the sample preventing anyway a more precise measurement. For the samples used the measured thickness ranges from 10–50  $\mu\text{m}$ . The transmittance  $T$  of the sample is measured independently using an integrating sphere. From both  $L$  and  $T$  measured one then can access the transport mean free path value [[Genack 1987](#);

<sup>4</sup>A similar approach is used for phase and amplitude control with a DMD [[Goorden et al. 2014b](#)].

Garcia et al. 1992; Sapienza et al. 2007] through the optical Ohm's law [Rossum et al. 1999]

$$T \simeq \frac{l^*}{L}. \quad (2.1)$$

The temporal response of the sample also may be probed measuring the Thouless time  $\tau_m$  [Thouless 1977]. It corresponds to the averaged time light already in the medium takes to reach its boundaries as discussed in [Rotter et al. 2017]. It is measured here (Fig. 2.4(a)) from the intensity pulse shape as in [Mounaix 2017; Johnson et al. 2003] but the setup enables to also measure it from the amplitude temporal evolution, see Comm. 2.2.3.

### Comment 2.2.3.

The Thouless time  $\tau_m$  is usually deduced from the intensity decay evolution given by  $I(t) = I_0 e^{-t/\tau_m}$ . One also can measure it from the amplitude  $A$  decay evolution:  $A(t) = A_0 e^{-t/\tau_m^A}$ , using  $I = |A|^2$  leads to  $\tau_m = \tau_m^A/2$ .

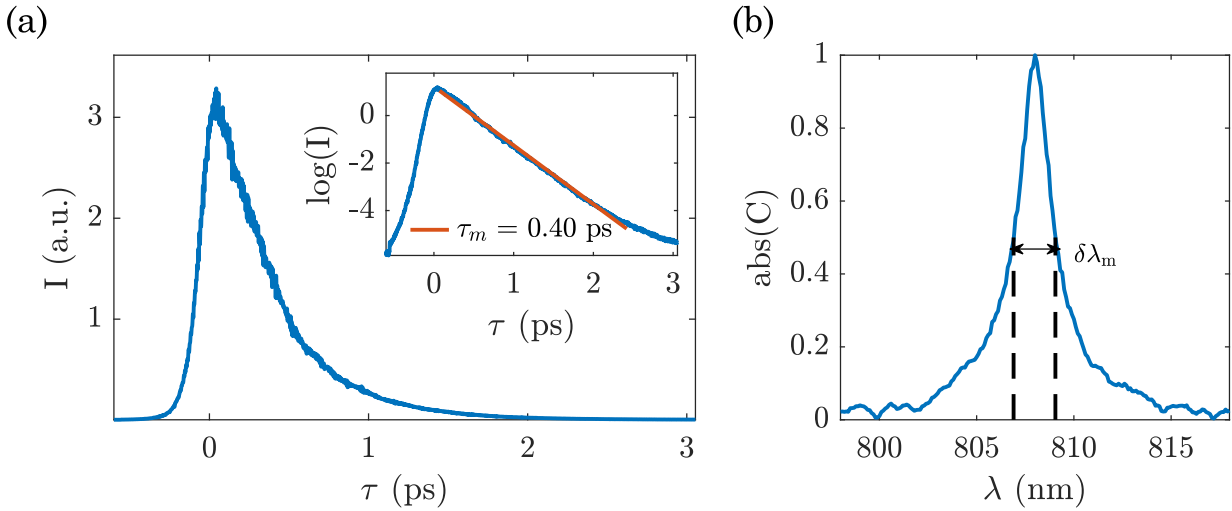


Figure 2.4: **Spectral and temporal characteristics of a typical  $\text{TiO}_2$  sample.** The sample presented here is a  $\text{TiO}_2$  layer of transmittance  $T \sim 0.3$  and of thickness  $L \sim 30 \mu\text{m}$ . (a) Spatially averaged transmitted intensity after the scattering medium when illuminating with the femtosecond pulse. The decay is exponential as visible when plotting it in log scale in the inset. The fit of the slope enables to extract a value for the Thouless time. For this sample  $\tau_m \simeq 0.4 \text{ ps}$ . (b) Spectral decorrelation of the medium. When tuning  $\lambda$  the field is measured and correlated to the one at 808 nm. The field spectral decorrelation width  $\delta\lambda_m \sim 2 \text{ nm}$  is measured as the FWHM of the curve.

Other techniques exist to access the scattering medium properties, for instance in [Curry et al. 2011] the speckle contrast is measured to recover the diffusion constant  $\mathcal{D}$ , see Chap. 1.

The spectral decorrelation width  $\delta\lambda_m$  is also easily accessible as follows. For different input wavelengths the field is measured and the obtained set of output fields are then all correlated to the central wavelength one. Plotting the absolute value of the correlation, Fig. 2.4(b), gives access to the FWHM; in this work we restrain ourselves to spectral decorrelation in the range of  $\delta\lambda_m \sim 1 \text{ nm}$ .

## 2.2.4 Camera

The camera used is a Manta, G-046, Allied Vision. It has a  $8.3 \mu\text{m} \times 8.3 \mu\text{m}$  pixel pitch and  $752 \times 582$  pixels. Its full frame framerate is 67.5 images per second and can be increased when less pixels are

addressed. For this reason, to increase the measurement speed, from one experiment to another the framerate is not fixed but set to its current maximal value. The lens after the collection microscope objective is selected such that the speckle is oversampled on the camera, i.e. the magnification is such that one speckle grain covers several camera pixels. When non-redundant information is required the images are “binned”: one pixel is made out of its  $N_{\text{bin}}$  neighbors. The choice of  $N_{\text{bin}}$  is fixed with the measured speckle grain size.

### 2.2.5 Stage

The stage of the delay-line is a Newport TRA25CC motorized actuator. It enables to adjust the delay between both arms of the setup. Its full scanning range (25 mm) is convenient, it allows to compensate small path length modification due to the insertion of optical elements (lens, beam splitters, optical densities, etc...). Its resolution (0.2  $\mu\text{m}$ ) enables to measure delays of 1.3 fs (the factor of 2 coming from the light return trip) and hence resolve the 100 fs pulse. Due to the motor mounted rotary encoder of 64 cts rev<sup>-1</sup> (counts per revolution) scanning the stage induces a 12.8  $\mu\text{m}$  modulation thus a experimentally visible 25.6  $\mu\text{m}$  modulation (return trip). It results in a frequency modulation, when extracting the pulse, of about 10 THz as presented in the inset of Fig. 2.5(d). This frequency modulation of the signal is however not detrimental to extract the field.

## 2.3 All elements working together, operation of the setup

The different elements presented in Sec. 2.2 are all controlled via Matlab. Before getting to the details of the operation in itself a comment on the polarizations all along the setup is interesting.

### 2.3.1 Polarization considerations

The laser emits linearly polarized light whose axis is controlled by a  $\lambda/2$  waveplate. The light is then separated with a polarized beam splitter such that the beam arriving on the SLM fulfills the polarization constraint (Sec. 2.2.2). With the  $\lambda/2$ , the amount of light passing through the sample and reference arm can be controlled. This is important as the field extraction (and the gated information) relies on the interference between the light traveling in both arms: the higher the contrast of the interferences the better the field extraction. To maximize the contrast the two sources need to have equal intensities, however the transmission of the scattering sample may vary from one sample to the other<sup>5</sup> and modifying the intensities with optical densities is not convenient since adding an optical density also modifies the optical delay. The best way to fulfill all constraints is to control upstream the injected light on both arms, hence the use of an initial  $\lambda/2$  waveplate.

In most experiments we aim at only detecting multiply scattered light (filtering all non-scattered light) to belong to the very scattering regime. Due to the numerous scattering events in the sample, the polarization after the sample is randomized. A polarizer is thus placed in front of the camera to select the same polarization as the reference arm. Indeed light beams on both arms are initially (before the scattering sample) orthogonally polarized. The  $\lambda/2$  waveplate placed on the reference arm is hence, most of the time, not affecting the polarization. It is however present just in case one wants to observe the non crossed polarized light. For this purpose it is turned by 90° as well as the polarizer in front of the camera.

---

<sup>5</sup>It also changes in time due to the temporal pulse shape, this effect is not compensated for.

### 2.3.2 Field extraction

Measuring the field of a light beam is paramount in many applications, but is a difficult task in optics. The detectors in the optical domain are indeed only sensitive to intensity, and the phase information is lost. There are several ways to recover the phase information that can be divided into two main categories: interferometric or non interferometric techniques [Kelly 2018].

A popular non interferometric technique relies on the so-called transport of intensity technique. It requires the acquisition of more than one intensity image. Two intensity images measured for different axial positions are acquired and the field propagation equation enables to extract the phase [Teague 1983; Sheppard 2002]. Another technique uses a thin diffuser close to the camera and extracts the phase from the speckle pattern translation [Berto et al. 2017]. Along the same line, phase retrieval algorithms, inspired by Gerschberg-Saxton (algorithm based on a numeric iterative field propagation between two planes, usually related by a Fourier transform, to retrieve the phase) use back and forth propagation to converge to the phase map of the initial intensity image [Fienup 1982].

On the list of non interferometric techniques, a device, the Shack-Hartmann [Shack 1971], is particularly useful to locally probe the wavefront, albeit at low resolution.

The second class of techniques for field extraction are interferometric techniques, among which the most widespread is digital holography [Gabor 1949; Goodman et al. 1967]. It consists in the measurement of holograms followed by a numeric post-processing. The operation of phase-stepping holography will be explained in details below. It is based on the acquisition of several interferograms (obtained by stepping the phase of one field) that gives access to the phase relationship between the two interfering fields. Usually several intensity images are required to extract the phase information, but off-axis holography enables to do so in one shot [Cucho et al. 2000].

On all the work that follows, two main complementary techniques are used to extract the field. Both rely on phase shifting interferometry, only the manner of shifting the phase differs. In one case the phase shifting is discrete (phase-stepping) as in the other case a delay-line scan enables to obtain a continuous phase shift. I will first present them individually and discuss their practical use afterward.

#### 2.3.2.1 Phase-stepping

The idea of the phase-stepping technique is as follows: one of the fields is fixed and the other one is globally phased-stepped (whatever the initial SLM mask applied on the SLM). In the present work we fixed the reference field and phase-stepped the one propagating through the scattering medium<sup>6</sup>. Due to the phase-stepping the interferences with the reference field vary. Hence the field can be extracted from the set of intensity images. Let's first develop the calculations in case of 4 steps. One can express the intensity measured on the camera  $I_n^\phi$ , where  $n$  is the number of camera pixels and  $\phi$  is the uniform phase value of one beam, from both interfering fields  $\mathbf{E}_n = E_n e^{i\theta_n}$  and  $\mathbf{E}_n^{\text{ref}} = E_n^{\text{ref}} e^{i\theta_n^{\text{ref}}}$  (bold symbol represents complex values),

$$\begin{aligned} I_{mn}^\phi &= |\mathbf{E}_n e^{i\phi} + \mathbf{E}_n^{\text{ref}}|^2 \\ &= E_n^2 + E_n^{\text{ref}2} + 2E_n E_n^{\text{ref}} \cos(\theta_n + \phi - \theta_n^{\text{ref}}). \end{aligned} \quad (2.2)$$

From intensity images measured for  $\phi = [0, \pi/2, \pi, 3\pi/2]$ , the field is computed as follows:

$$\mathbf{E}_n \mathbf{E}_{\text{ref}}^* = \frac{I_n^0 - I_n^\pi}{4} + i \frac{I_n^{3\pi/2} - I_n^{\pi/2}}{4}. \quad (2.3)$$

<sup>6</sup>Note that the phase-stepping can be performed on the signal, as presented here, as well as in the reference field. The choice is arbitrary as only the relative phase matters.

Measuring the reference amplitude (possible in case of an external reference) enables to recover, except for a global phase, the field of interest. However this step is not critical in this experiment: even if the reference prevents the exact access to the field, it is static and hence only acts as a fixed amplitude scaling and phase shift<sup>7</sup>. The field variations, which are the relevant informations, remain.

It is noteworthy that this procedure is the discrete version of a continuous phase shift and cosine fit of intensity to extract the phase. For an arbitrary number of phase steps  $N^\phi \geq 4$ , the field is retrieved with

$$\mathbf{E}_n \mathbf{E}_{\text{ref}}^* = \frac{1}{N_\phi} \sum_{\phi} I_n^\phi (\cos(\phi) - i \sin(\phi)) \quad (2.4)$$

In some experimental situation, to improve the phase extraction, the use of more than 4 phases is required. This is for instance the case when measuring TMs in the tail of the pulse where the signal over noise ratio is not sufficient, see [Sec. 4.3.4](#).

### 2.3.2.2 Delay-line scan

To measure the field of the whole pulse, the interferometric cross-correlation (ICC) technique presented in [[Mounaix 2017](#)] is employed. It consists in recording the interference of a probe pulse (laser pulse passing through the reference arm) with the unknown pulse (elongated pulse which propagated through the scattering sample). The cross-correlation is measured by scanning the delay-line of the reference arm (each stage position corresponds to a specific temporal delay). For a delay  $\tau$  the measured interference on the camera is:

$$\begin{aligned} I(x, y, \tau) &= \int |\mathbf{E}(x, y, t) + \mathbf{E}_{\text{ref}}(x, y, t - \tau)|^2 dt \\ &= \int |\mathbf{E}(x, y, t)|^2 + |\mathbf{E}_{\text{ref}}(x, y, t - \tau)|^2 dt + 2\text{Re} \int \mathbf{E}(x, y, t) \mathbf{E}_{\text{ref}}^*(x, y, t - \tau) dt, \end{aligned} \quad (2.5)$$

where the integral over time is due to the camera integration time.

When moving the stage, which corresponds to varying the delay  $\tau$ , the first term remains fixed (baseline). However the second term corresponds to an interferometric cross-correlation between the field of interest and the reference field around a time-gate  $\tau$ . From the set of intensity images acquired ([Fig. 2.5\(a\)](#)), to access the field ([Fig. 2.5\(f\)](#)), a computation step remains: removing the baseline ([Fig. 2.5\(b → c\)](#)) and filtering out the fast phase variations of the temporal speckle to only keep the envelop ([Fig. 2.5\(d\)](#)). The baseline may be removed by subtracting the intensity images taken by closing successively the shutters  $s_r$  (the intensity of the speckle is hence measured  $I$ ) and  $s_s$  (the intensity of the reference is hence measured  $I_{\text{ref}}$ ). The remaining cross correlation term is normalized dividing it by  $2\sqrt{I_{\text{ref}}I}$  to obtain the field<sup>8</sup>. To visualize the pulse mean amplitude for each delay all fields  $(x, y)$  absolute values are averaged (represented by the multiples arrows [Fig. 2.5\(e\)](#)).

### 2.3.2.3 When to use which?

As previously said, these two techniques are complementary, the delay-line scan being a continuous version of the phase-stepping technique. The delay-line scan only works when extracting the field of the pulse and is not practicably applicable for monochromatic operation. But this method has the advantage of being quite fast: it is technically limited by the camera framerate due to Shannon's criteria. The phase-stepping technique on the contrary applies for both pulsed and monochromatic

<sup>7</sup>This is especially true for a perfect flat reference where the amplitude scaling and phase shifts are homogeneous. Also, phases can always just be measured relative to others.

<sup>8</sup>Or divided by  $2\sqrt{I_{\text{ref}}I}$  to obtain a fully normalized and insensitive to global transmission variations field (see [Sec. 5.2.1](#)).

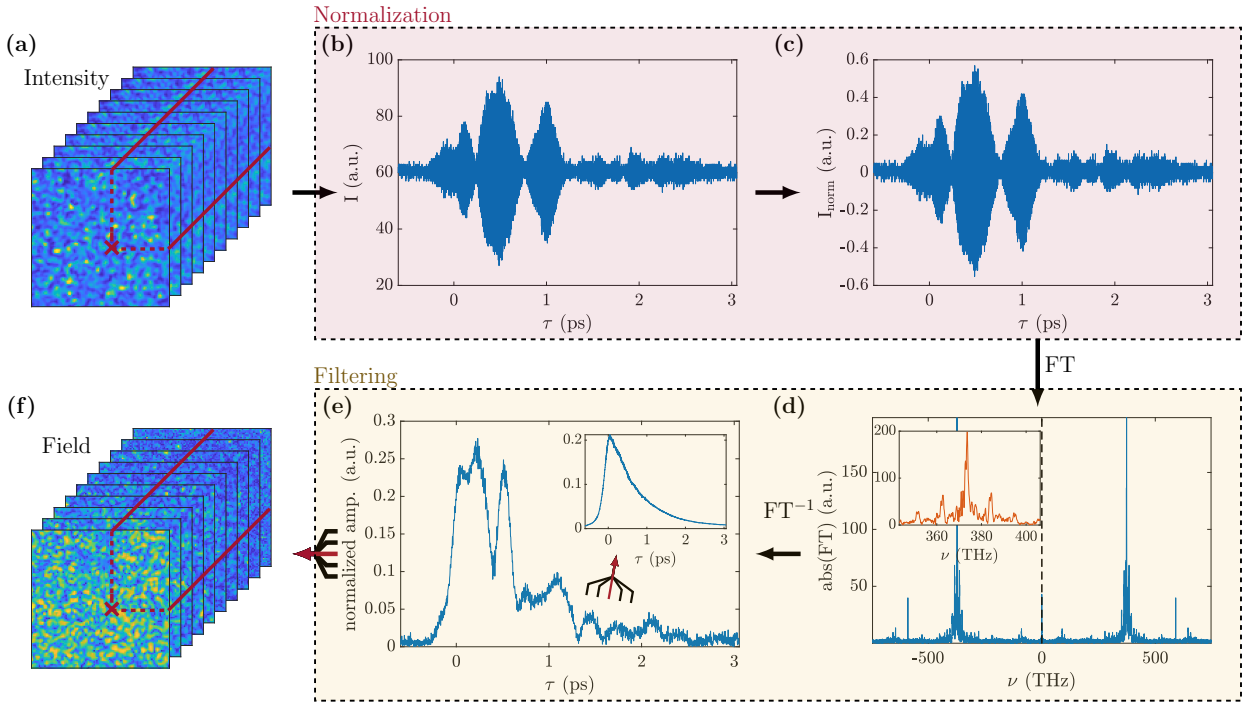


Figure 2.5: **Field extraction from interferometric cross-correlation.** (a) Set of intensity images measured when varying the delay  $\tau$ . (b) For each CCD pixel individually the intensity varies with  $\tau$ . (c) Fully normalized intensity (hence centered and between  $-0.5$  and  $0.5$ ): the baseline is subtracted and the intensity divided by the reference and signal amplitudes. (d) Absolute value of the Fourier transform (FT) of (c). The signal at the pulse frequency ( $\sim 400$  THz) is extracted with a numeric band-pass filter represented with the vertical dashed lines. The inset represents a zoom of the peak showing the sidebands due to a slight periodic modulation of the stage speed. (e) Signal amplitude obtained by inverse Fourier transform ( $\text{FT}^{-1}$ ) of (d). The inset represents the amplitude averaged (represented by the set of arrows) over all CCD pixels. (f) Set of retrieved fields values (the field amplitude is plotted).

lights. It is however temporally “local” (it is possible to extract the field for one delay only at once) and hence not very suited for measuring the field evolution all along the pulse. It is noteworthy that the temporal information retrieved when extracting the field of the pulse is relative: the temporal evolution is correct but the zero position is arbitrarily fixed. Hence experiments are not directly comparable to simulations as the zero position has no physical meaning. The experimental determination of  $t = 0$  requires an additional measurement that is developed in the following section.

### 2.3.3 Experimental determination of the optical path equalization between two arms

An important point is therefore to measure the position of the translation stage that equalizes the lengths of both optical paths. This determination goal is twofold: being able to compare experiments with each other (where an arbitrary definition is sufficient) and being able to compare the experiments to simulations results (for this end a more physical definition is required). In this regard some ideas could be the following:

- Removing the scattering sample. The stage position allowing the interference of the two non elongated pulses hence enables to determine the equal paths and to fix the origin of the

temporal axis. However this  $t = 0$  is not valid anymore when the sample, suspended on its glass cover, is introduced.

- A possible workaround is to perform the same experiment as before but with a glass cover. The  $t = 0$  position would be a better estimation but still missing the optical path introduced by the scattering sample itself. Considering the medium thickness and the mean refractive index of its constituent particles an estimate may be calculated (see [Sec. 4.5.1.3](#)).

I will present in this section a simple method I used to determine the stage position associated with  $t = 0$ .

Let's consider the experimental setup [Fig. 2.1](#) that may be regarded as a mere Mach-Zehnder interferometer. The laser emits monochromatic light at  $\lambda$  and hence the accumulated phase on both arms of the interferometer are:  $\varphi = 2\pi\ell/\lambda$  and  $\varphi^{\text{ref}} = 2\pi\ell^{\text{ref}}/\lambda$ , where  $\ell$  and  $\ell^{\text{ref}}$  are the optical lengths. The field interference results in a speckle intensity image on the camera, its phase is given by  $\delta\varphi = 2\pi\delta\ell/\lambda$  where  $\delta\ell$  ( $\delta\ell = \ell - \ell^{\text{ref}}$ ) then represents the optical delay between both arms. For a fixed stage position, tuning  $\lambda$  does not modify the speckle pattern if  $\delta\ell = 0$ . Therefore finding the stage position for which the speckle is not affected by a wavelength tuning enables to experimentally access the  $t = 0$  position with a good accuracy. This is the method I implemented and that I will further describe below.

To measure the stage position, the experiment performed is the following: for a set of stage positions the wavelength is tuned and the field is retrieved (with the phase-stepping technique presented in [Sec. 2.3.2.1](#)). For each stage position all fields obtained with different wavelengths are correlated to the central wavelength one and the correlation profiles are superposed as presented in [Fig. 2.6](#). The simulation results are obtained by exactly reproducing the experiment with the computer. Incoming fields are created as complex random Gaussian matrices of sizes  $50 \times 50$ . Their propagation is modeled by applying on one of the fields a phase delay  $\delta\phi = 2\pi\delta\ell/\lambda$ . A spectral decorrelation can be accounted by making the incoming fields  $\lambda$ -dependent<sup>9</sup>. Both of the individual arms fields are then summed to obtain the interferometer output field to correlate for different  $\delta\ell$  and  $\lambda$  values.

One can see that, in the experiment [Fig. 2.6\(c\)](#) as in the model [Fig. 2.6\(a,b\)](#), there is a stage position for which the correlation remains over a wide wavelength tuning range. To better extract this position the Fourier transform of each correlation line (i.e. for a fixed stage position) is calculated and plotted [Fig. 2.6\(d\)](#). From it it is possible to extract the stage position that fixes the time origin. Subtleties on this technique are detailed in [Appendix A.3](#).

### 2.3.4 Measurement of TMs

As briefly presented in [Sec. 1.3.2](#) the measurement of a TM requires to extract the field for a set of different input wavefronts. Theoretically, apart from the orthogonality requirement, the chosen basis does not matter. However it does experimentally. I will discuss in [Sec. 2.3.4.1](#) the choice of the basis. To extract the field (and more specifically recover the missing information on the phase) from an intensity measurement different techniques exist. The one used requires an interference between the field of interest and a reference field. I will discuss its implications in [Sec. 2.3.4.2](#) and the field extraction itself in [Sec. 2.3.2](#).

#### 2.3.4.1 Canonical vs. Hadamard basis

The canonical basis is an easy and straightforward illustration to explain TM measurements, or optimization techniques. However it suffers a major drawback: the amount of modulation on the

<sup>9</sup>For instance no spectral decorrelation is present the model in [Fig. 2.6\(a\)](#) but one is in [Fig. 2.6\(b\)](#).

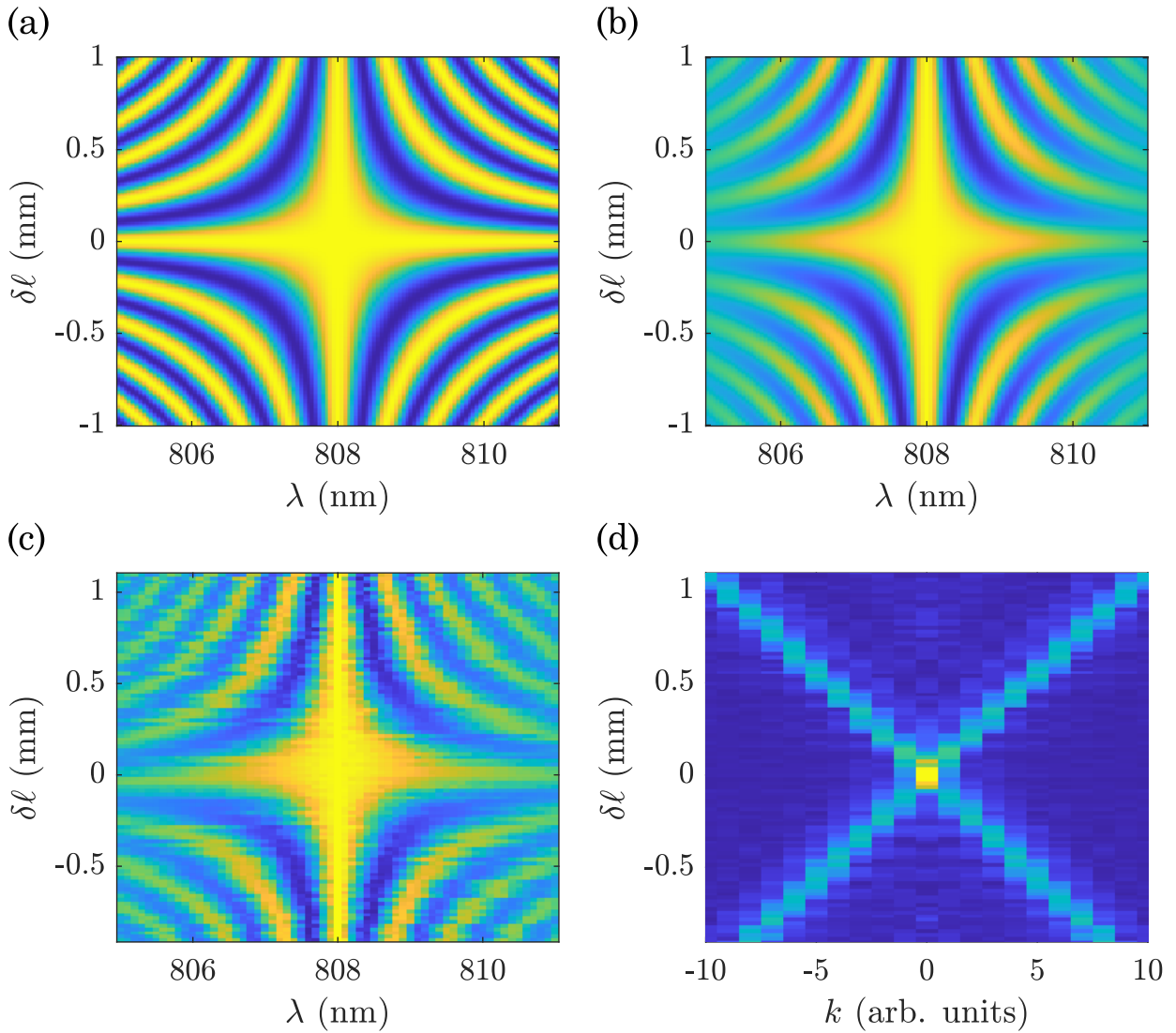


Figure 2.6: **Optical path equalization.** (a) Simple simulated model. (b) Model inserting the spectral decorrelation of the medium. (c) Experiment performed with a  $\text{TiO}_2$  sample with a transmittance of 0.3. (d) Fourier transform of the lines of (c) to better extract the position equalizing both optical paths.

field due to the change from one basis vector to another is very limited (it scales as  $1/N_{\text{SLM}}$ )<sup>10</sup>. This is the reason why the canonical basis is not practically used to measure TMs. The Hadamard basis is preferred. In an Hadamard basis indeed half of the pixels change from one vector to the other.

The Hadamard matrix is a matrix for which all coefficients are  $-1$  or  $1$  and whose lines/columns are all orthogonal. To construct them, Sylvester [Sylvester 1867] uses a recursive method such that they should be of size  $N_{\text{SLM}} \times N_{\text{SLM}}$  where  $N_{\text{SLM}}$  is a power of two, see Fig. 2.7(a). However alternative techniques enable to construct Hadamard matrices with other dimensions [Pratt et al. 1969].

Experimentally the basis vectors used are the Hadamard matrix lines reshaped on a square to

<sup>10</sup>The limited modulation when phase-stepping is vector to recover the phase information (see Sec. 2.3.2.1) is also detrimental.

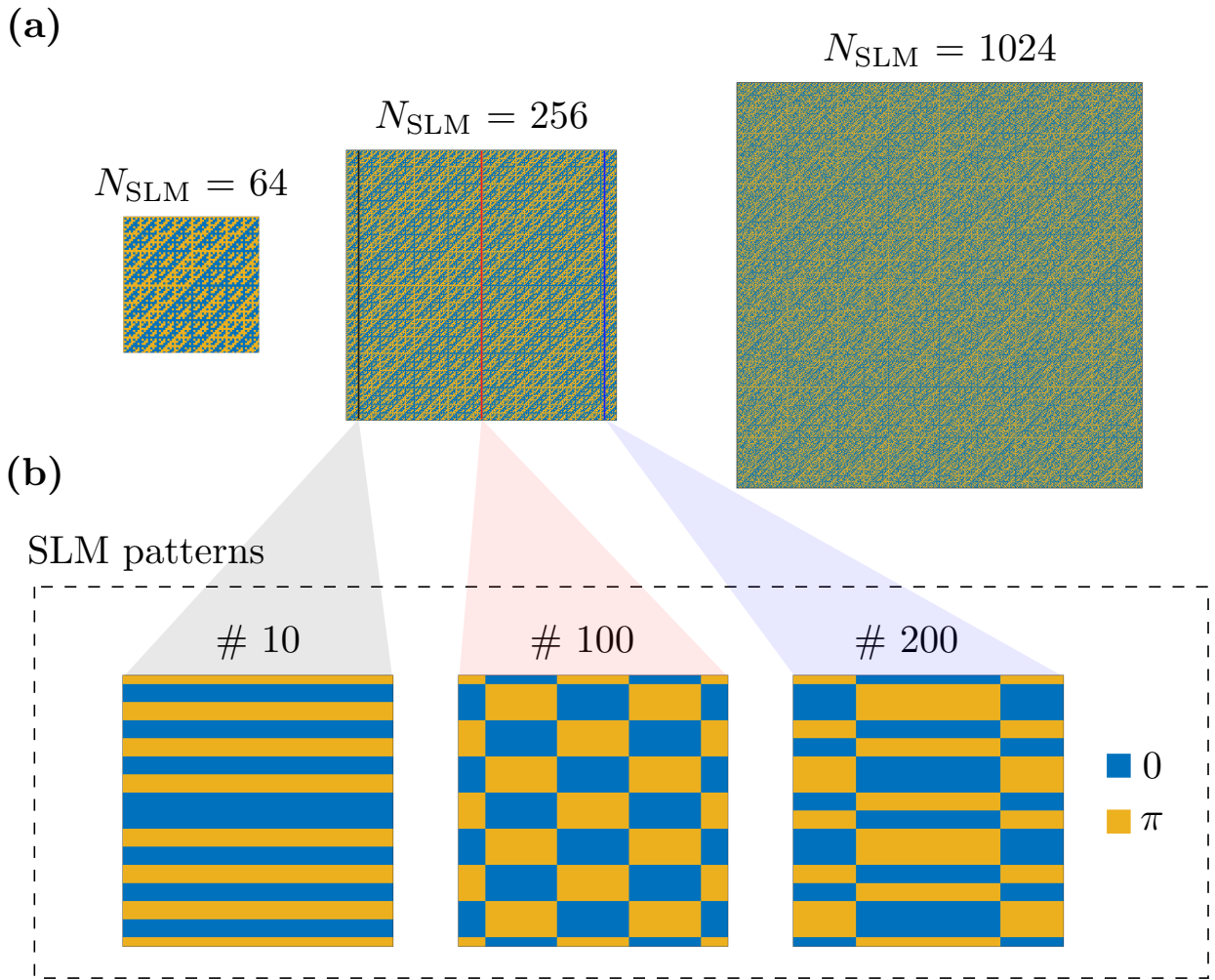


Figure 2.7: **Hadamard basis.** (a) Some examples of Hadamard matrices (sizes  $64 \times 64$ ,  $256 \times 256$  and  $1024 \times 1024$ ). (b) For the middle Hadamard matrix vectors are extracted and reshaped to be displayed on the SLM. Pixels correspond to phase values of 0 and  $\pi$ .

display on the SLM and where the values  $-1$  and  $1$  respectively correspond to phase delays of 0 and  $\pi$ , see Fig. 2.7(b). In all experiments performed  $N_{\text{SLM}} = 256, 1024$  or  $4096$ , depending on the level of control required and the ROI on the CCD. For practical reasons and to perform the modulation on the SLM, it is easier to display the TM in the canonical basis (for instance to visualize the TM itself or the SLM mask), a mere base transformation may then be performed.

#### 2.3.4.2 Internal vs. external reference

The question of the reference is crucial for measuring a TM. To extract the field from intensity measurements an interference is indeed required (it nonetheless has been achieved with a phase retrieval technique in [Drémeau et al. 2015]). Two reference options are possible to exploit: external and internal references.

- An external reference: not propagating through the scattering sample this reference can be a well characterized plane wave. It is convenient as it enables to extract the field on all CCD pixels but may not be very stable in time. This is the case presented in Fig. 2.1, where all the

active region of the SLM is hence modulated.

- An internal reference (or co-propagative reference): it propagates through the scattering sample. It is however a light that is not modulated by the SLM and that can interfere with the signal when phase-stepping is performed. Hence in this case a part of the active SLM region is attributed to the reference and is not modulated. One of its drawback is that, due to the scattering, the reference is not a plane wave but a speckle making it harder to recover information on some spatial CCD pixels where the reference speckle grain is dark and does not give access to the relative phase between different spatial positions. This technique is used in [Popoff et al. 2010], where the TM is normalized to correct for the reference speckle impact.

Both references only slightly differ in the monochromatic regime but are fundamentally different in the pulse regime. An internal reference will enable to access global information on the pulse and BBTM [Sec. 1.3.3.3](#) [Mounaix et al. 2017] as an external reference will enable time-gated measurement and hence TGT [Sec. 1.3.3.2](#) [Mounaix et al. 2016a]. If the question on the internal or external reference raises for the measurement of the transmission matrix, an external reference is mandatory to realize time-gated measurements and extract the temporal evolution of the field. In this thesis, when not explicitly specified, all TM measurements (and more generally field extractions) are realized with an external reference.

### 2.3.4.3 TM measurement

As explained in [Sec. 1.3.2](#) the TM measurement of a scattering sample requires to measure the field at its output for a basis of input vectors. Here only the notations will be set and the general method detailed. Different examples of TM measurements (and their properties) will be presented along the present work (see [Sec. 4.1](#)) The basis chosen for all TM measurements is, in this thesis, the Hadamard one with a number of input vectors denoted  $N_{\text{SLM}}$ . The number of pixels on the CCD where the field is measured is denoted  $N_{\text{CCD}}$ . The number of phase steps used to recover the field from intensity images (see [Sec. 2.3.2](#)) is denoted  $N^\phi$  and usually taken from 4 to 10. For each input vector of the Hadamard basis the field on the camera is recovered using the phase-stepping technique. From these measurements the TM is built.

## 2.3.5 TM characterization and level of control

Once the TM is measured it is important to characterize it, for instance by the degree of control  $\gamma$ , see [Eq. 1.27](#). The latter, based on the aspect ratio for a perfect random matrix needs to be more carefully calculated for an experimental measured TM, as presented in the following.

### 2.3.5.1 Speckle grain size and binning of the camera pixels

For a perfect random matrix each CCD values are independent. However the field is continuous and thus with no particular attention neighboring CCD pixels can be correlated. To consider them non correlated each pixel should bears information on only one speckle grain. However the speckle grain size depends on the imaging system, see [Sec. 1.1.3.1](#). The grain size is experimentally measured by extracting the FWHM of the speckle autocorrelation as discussed in [Sec. 3.1.1](#). This measurement is possible because a single speckle grain covers several camera pixels. Speckle grains are hence well resolved but give access to redundant information: when measuring a TM with  $N_{\text{CCD}}$  pixels the amount of non-redundant information is not given by  $N_{\text{CCD}}$  but by  $N_{\text{speckle}}$ , the number of independent speckle grains. To measure TMs faster and reduce the redundant information the camera pixels are often ‘‘binned’’. This binning procedure consists in averaging the values of  $N_{\text{bin}}$

neighboring pixels to form only one. To some degree this just consists in using the camera with a reduced spatial resolution and an improved sensibility. Adjusting the binning enables to measure TMs either suppressing any redundant information or resolving the speckle grains to take advantage of the spatial Fourier information. The reduced binning giving access to over-sampled TMs will be extensively discussed in [Sec. 3.2](#).

### 2.3.5.2 Different SLM modes addressing

Thanks to the binning it is possible to control the output modes of the TM (CCD pixels). To well characterize the level of control one also needs to ensure that the number of input modes (SLM modes) modulating the field is known. This number, given in first approximation by  $N_{\text{SLM}}$ , can be corrected from the bias induced by the setup. The removal of some SLM modes by the back aperture of the illumination objective has been mentioned in [Comm. 2.2.1](#). To better estimate the number of SLM controlled modes I use the information contained on the TM. The level of information gathered with each mode is contained in a vector  $P$ . For a better visualization  $P$ , expressed in the canonical basis, is reshaped and displayed with a colormap such that each pixel corresponds to a SLM spatial position. Each coefficient  $P_j$  is computed by taking the square root of the sum over the CCD dimension of the Hadamard product of the TM with its conjugate:

$$P_j = \sqrt{\sum_i (T \cdot T^*)_{i,j}} = \sqrt{\sum_i T_{i,j} \times T_{i,j}^*}, \quad (2.6)$$

with  $(A \cdot B)$  the Hadamard product of two matrices  $A$  and  $B$  of equal dimension. The SLM modes weights are visualized in [Fig. 2.8\(a\)](#). Applying a threshold and summing the number of modes above this threshold enables to obtain an estimate of the effective value of  $N_{\text{SLM}}$ , see [Fig. 2.8\(b\)](#).

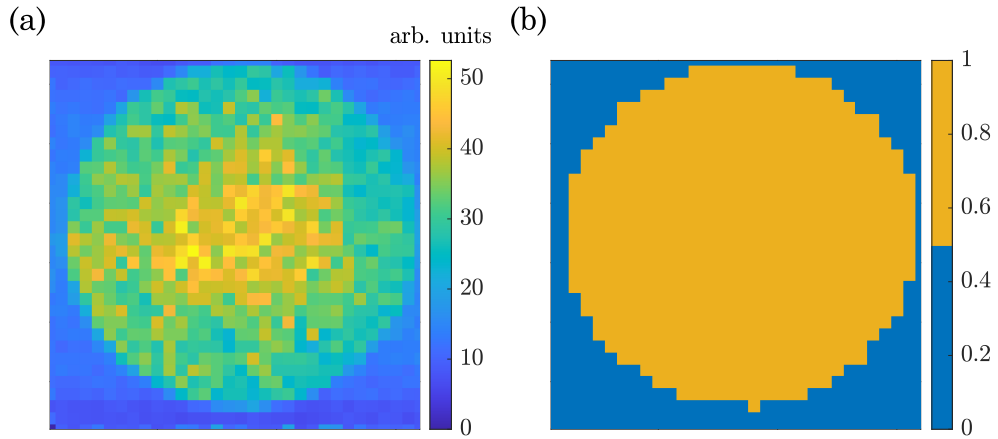


Figure 2.8: **Contribution of the different SLM modes to the wavefront shaping.** (a) Visualization of the importance of the different modes in the canonical basis using the measured TM and [Eq. 2.6](#). (b) Applying a threshold to count the number of effective SLM modes. In this specific experiment the number of effective modes is  $N_{\text{SLM}}^{\text{eff}} \simeq 660$  (out of 1024).

### 2.3.5.3 Level of control

From the knowledge of both the number of controlled modes and the number of independent speckle grains on the camera one can define the level of control. It is denoted  $\gamma$  and defined (and

approximated) by:

$$\gamma = \frac{N_{\text{CCD}}}{N_{\text{SLM}}} \left( \rightarrow \frac{N_{\text{speckle}}}{N_{\text{SLM}}^{\text{eff}}} \right). \quad (2.7)$$

In most experiments performed in this thesis,  $\gamma$  belongs to the interval  $[0.1, 0.3]$ .

#### 2.3.5.4 Illumination scheme

The positions of the illumination and the collection microscope objectives discussed here vary from experiments. The settings of [Chap. 5](#) are more standard: the illumination microscope objective illuminates the input side of the sample and the collection microscope objective images on the CCD camera the sample output face. These microscope objectives positions correspond to the ones that lead to the smallest speckle blob and the smallest speckle grain size. Hence with this configuration it is easier to collect as much as possible of the transmitted light.

The experimental configuration adopted in [Chap. 3](#) and [Chap. 4](#) is slightly different. The illumination microscope objective is moved away from the sample so that the illumination spot size increases<sup>11</sup>. This configuration is solely meant to increase the speckle blob size in order to perform averaging on the disorder configurations without moving the sample.

The collection microscope objective can also be moved away from the sample. It is the case for [Sec. 3.2.3](#) and [Chap. 4](#). The reason for this position is discussed in [Sec. 3.2.3](#). A scheme of the experimental configuration is presented in [Fig. 2.9](#).

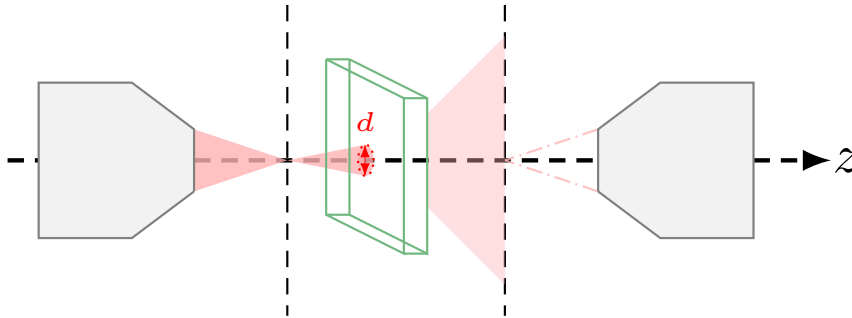


Figure 2.9: **Experimental configuration of both microscope objectives.** The illumination microscope objective can be moved away from the sample so that light covers a wide illumination area on the sample. The collection microscope objective can also be moved away from the sample or image its output surface.

## 2.4 Take home message

The experimental setup presented enables to measure the field beyond a scattering sample both in monochromatic settings and pulsed ones. The temporal aspects can be resolved with time-gated measurements enabled by a delay-line and a temporal probe. These two main properties make possible to experimentally measure TMs in general and TGTMs more specifically. The control over the input wavefront is limited to phase-only which we have seen not to be too dramatic.

<sup>11</sup>This corresponds to the out-of-focus configuration described in [Sec. 3.1.2.1](#) but a different purpose. Here no mesoscopic effects are involved.

# 3 | Monochromatic speckle and its manipulation with the transmission matrix

---

3.1	Speckle statistics . . . . .	111
3.1.1	Fully developed speckle and Rayleigh statistics . . . . .	111
3.1.2	Non-Rayleigh statistics . . . . .	114
3.1.2.1	Natural non-Rayleigh speckles . . . . .	114
3.1.2.2	Artificial non-Rayleigh speckles . . . . .	117
3.2	The transmission matrix beyond the transmission control . . . . .	123
3.2.1	Fourier filtering for correlation engineering . . . . .	124
3.2.2	An axial extend of the correlation control . . . . .	126
3.2.3	Simple control over the speckle grain size . . . . .	128
3.2.3.1	Illumination and collection microscope objectives positions . . . . .	128
3.2.3.2	Speckle grain size control . . . . .	129
3.3	Take home message . . . . .	131

---

This chapter aims at presenting natural speckle statistics and correlations, and also means to control both of them. We start by describing of the speckle pattern itself through its statistical properties in [Sec. 3.1](#): for a fully developed speckle the field statistics follow a Rayleigh distribution ([Sec. 3.1.1](#)) as already mentioned in [Sec. 1.1.3.1](#). Then, we discuss, in [Sec. 3.1.2](#), the emergence of non-Rayleigh field statistics. These non-Rayleigh distributions can be obtained naturally ([Sec. 3.1.2.1](#)) or artificially ([Sec. 3.1.2.2](#)). We review some WFS-based techniques which can alter the speckle statistics. We note that most of the techniques to modify the speckle statistics also alter the correlations among speckle grains (and reciprocally). We finally present in [Sec. 3.2](#) a TM approach that chiefly controls, through the use of the singular value decomposition, the speckle pattern correlations leaving the statistics unchanged.

## 3.1 Speckle statistics

### 3.1.1 Fully developed speckle and Rayleigh statistics

As presented in [Sec. 1.1.3](#) a speckle pattern has some remarkable properties [[Goodman 2007](#); [Goodman 1976](#); [Dainty 1980](#)]. When the light is sufficiently scrambled so that the field in one point results from the interference of many independent phasors, the speckle is said to be fully developed. Usually a

fully developed speckle intensity distribution follows an exponential decay with a probability density function (PDF) given by Eq. 3.1 and plotted in Fig. 3.1(a)

$$p(I) = \begin{cases} e^{-I/\langle I \rangle} / \langle I \rangle, & I \geq 0 \\ 0, & \text{otherwise} \end{cases} \quad (3.1)$$

This intensity statistics explains the visually well contrasted granular image of the speckle. This visual impression can be quantified through the contrast, defined by  $C = \sigma_I / \langle I \rangle$ , where  $\sigma_I = \sqrt{\langle I^2 \rangle - \langle I \rangle^2}$  is the standard deviation. The contrast value is 1 given the distribution of Eq. 3.1 (see Comm. 3.1.1), which means that the intensity variations are significant.

#### Comment 3.1.1.

Let us consider the intensity distribution given by Eq. 3.1 and compute its two first moments. We obtain  $\langle I \rangle = \int I P(I) dI$  and  $\langle I^2 \rangle = \int I^2 P(I) dI = 2\langle I \rangle^2$ . The speckle contrast is hence obtained by  $C = \frac{\sigma_I}{\langle I \rangle} = \sqrt{\frac{\langle I^2 \rangle}{\langle I \rangle^2} - 1} = 1$ . More generally the  $n^{\text{th}}$  moment of the distribution is given by the formula  $\langle I^n \rangle = n! \langle I \rangle^n$ .

This intensity distribution, is associated with a field statistics. Any usual fully developed speckle follows the so-called **Rayleigh statistics** which consists of a Rayleigh statistics for the field amplitude and an uniform statistics for the phase, both PDFs are given by Eq. 3.2 and illustrated in Fig. 3.1(b,c)

$$\begin{cases} p(x; \sigma^2) = \frac{x}{\sigma^2} \exp\left(\frac{-x^2}{2\sigma^2}\right), & x \in [0, \infty[ \text{ (for the amplitude)} \\ p(\theta) = \frac{1}{2\pi}, & \theta \in [-\pi, \pi] \text{ (for the phase)} \end{cases} \quad (3.2)$$

It is important to notice that the square of a Rayleigh distribution is an exponential distribution. Commonly, speckles following a Rayleigh statistics are referred to as ‘‘Rayleigh speckles’’.

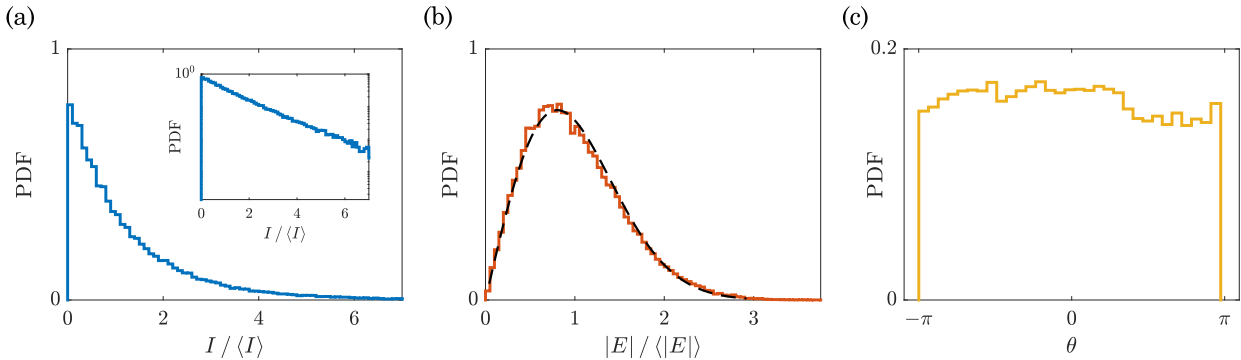


Figure 3.1: **Statistics of a speckle obtained from propagation in a thick  $\text{TiO}_2$  sample.** (a) Intensity statistics following an exponential decay. The inset represents the same plot with a logarithmic vertical scale. (b) Field amplitude following a Rayleigh statistics. The Rayleigh fit is represented with a black dashed line. (c) Flat field phase.

However, even when working with strongly scattering media the contrast measured can be reduced. This is for instance the case when the speckle observed is the result of the incoherent sum of two speckled fields. Let us take the example of a coherent non-polarized light propagating through a scattering medium. The field can be projected on two orthogonal linear polarizations. Each polarization will interfere separately to give a fully-developed well contrasted speckle pattern.

However the observed intensity image is the incoherent sum of both speckle patterns leading to a speckle pattern whose contrast is reduced by a factor of  $\sqrt{2}$ . This reasoning can be applied to the sum of more than two speckles: for  $M$  fields the contrast is reduced by  $\sqrt{M}$  [Goodman 1976]. This contrast diminution is well visible when observing the speckle resulting from the scattering through a given sample illuminated with monochromatic light or with a pulse (10 nm bandwidth in the experimental setup corresponding to several independent spectral channels,  $N_\lambda > 1$ ).

Another feature of the speckle pattern is the speckle grain size. The latter is fixed by the experimental configuration and parameters (the speckle size is diffraction-limited) and can be measured experimentally. For instance the speckle grain size is determined by the numerical aperture (NA) of the system. Its transversal dimension is given by  $b_\perp \approx \lambda/\text{NA}$ , see Eq. 1.6. The grain size corresponds to the short-range spatial correlations. In all experiments the speckle grain size is measured using the speckle autocorrelation. From a speckle image, the autocorrelation is computed and fitted with Gaussians along two perpendicular directions. The full width at half maximum (FWHM) is extracted and taken as the speckle grain size value. Most of the time the grain size is defined through the speckle intensity autocorrelation (the intensity is the accessible parameter). It is however possible to decide defining the speckle grain size from the field itself (or its amplitude). It is noteworthy that numerically the measured grain size from the field amplitude and the intensity give the same results but that the grain size obtained from the full field is larger by a factor of  $\sqrt{2}$ , as expected in case of a Gaussian autocorrelation shape. In the following, all grain sizes given are obtained from the field amplitude that the experimental setup enables to extract. A technique to extract the grain size from the TM is presented in Appendix A.5.

### 3.1.2 Non-Rayleigh statistics

In the previous section we discussed the manifestations of a Rayleigh speckle without considering its origin. How comes it that this distribution is so universal among speckles? This is due to the limited requirements for its emergence: a sum of numerous independent phasors. Since this statistics is so widely spread how to get non-Rayleigh speckles? The following section details how it is possible to observe them naturally in some specific conditions and how to actively favor them.

#### 3.1.2.1 Natural non-Rayleigh speckles

Non-Rayleigh speckle naturally emerge when considering non fully-developed speckles. The latter are obtained as a result of insufficient scattering. Their phase is not fully randomized by the scattering events therefore the statistics does not cover the entire  $[0-2\pi]$  range (or is not uniform).

Now in case of fully-developed speckles, to predict non-Rayleigh statistics it is useful to return to the assumptions under which it appears. It is derived assuming the field is a sum of a large number of statistically independent phasors. The central limit theorem leads to the circular complex Gaussian joint probability density function discussed above [Goodman 2007]. If some of these hypotheses are no longer fulfilled (e.g. not enough phasors such that the central limit theorem does not apply or non statistically independent phasors) non-Rayleigh behaviors may emerge. For instance, it was shown that near-field speckles intensity is dictated by the scattering surface statistical properties [Greffet et al. 1995]. More generally in the far field, prediction of the statistics has been studied in [Shnerb et al. 1991], where the higher moments of the intensity distribution are shown to be enhanced, confirmed by [Nieuwenhuizen et al. 1995; Kogan et al. 1993], see Eq. 3.3 taking into account the leading correction when by expanding in  $1/g$ ,

$$p\left(\frac{I}{\langle I \rangle}\right) = e^{-I/\langle I \rangle} \left\{ 1 + \frac{1}{3g} \left[ \left(\frac{I}{\langle I \rangle}\right)^2 - 4\left(\frac{I}{\langle I \rangle}\right) + 2 \right] \right\}, \quad I \geq 0. \quad (3.3)$$

This modified statistics is observed when the assumption that the conductance  $g \gg 1$  does not hold, i.e. when mesoscopic effect can be observed (see Sec. 1.4.3). Observed in 1D or 2D materials [Hömann et al. 2010; Garcia et al. 1989], this regime is complex to reach in 3D diffusive media at optical frequencies. Some recent and pioneering observations however have been made in dense colloidal suspensions [Scheffold et al. 1998], nano wires [Strudley et al. 2013], or ZnO [Strudley et al. 2014] as presented in Fig. 3.2. In [Strudley et al. 2014] two experimental configurations are studied: in-focus and out-of-focus. The in-focus configuration corresponds to the illumination microscope objective focusing the light on the sample while in the out-of-focus configuration the illumination microscope objective is moved away to increase the illumination spot on the sample. One observes deviations from the Rayleigh statistics for the in-focus configuration (red data points), where mesoscopic effects are the most present.

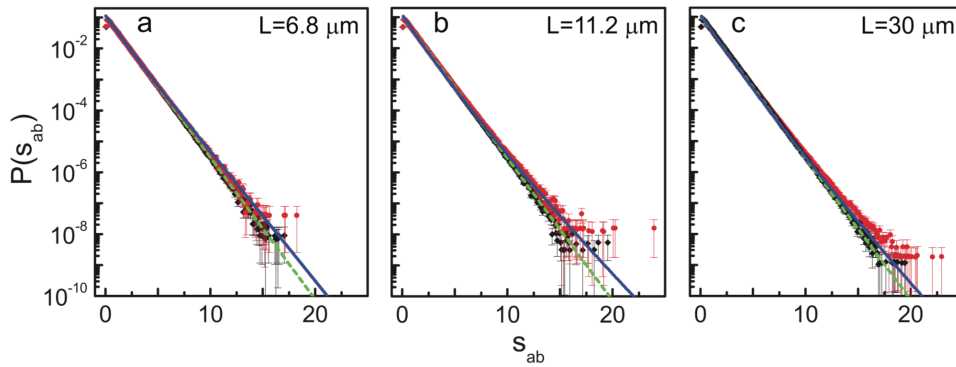


Figure 3.2: **Deviation from Rayleigh statistics due to mesoscopic effects.** Intensity distributions ( $P(s_{ab})$ , where  $s_{ab}$  is the normalized intensity) for different ZnO samples with thicknesses (a)  $L = 6 \mu\text{m}$ , (b)  $L = 11 \mu\text{m}$ , (c)  $L = 30 \mu\text{m}$ . Red and black points represent experimental data for in-focus and out-of-focus configurations. The dashed green line represents the intensity statistics of Eq. 3.1. The solid blue curve represents the fit from Eq. 3.3, with  $g = 40$ . Figure from [Strudley et al. 2014].

Taking advantage of the understanding of the non-Rayleigh emergence enables to artificially favor it as we will see in the next section.

### 3.1.2.2 Artificial non-Rayleigh speckles

#### Small deviations from the Rayleigh statistics

In [Bromberg et al. 2014], the authors introduced amplitude correlations to an existing speckle. The speckle is first generated by a random phase mask on a SLM, and correlations are then added to the phase mask. From these correlations the authors could generate speckles whose intensity statistics is an exponential decaying faster or slower than that of a Rayleigh speckle. In this way they redistribute the intensity among the speckle grains making for instance some grains brighter than the others. This intensity redistribution affects the contrast making it an indicator of the speckle type. In case of a Rayleigh speckle the contrast is  $C = 1$  (see Comm. 3.1.1), a speckle the contrast of which is  $C < 1$  is called **sub-Rayleigh** and a speckle for which, on the contrary,  $C > 1$  is said to be **super-Rayleigh**, see Fig. 3.3. However these modified intensity statistics are limited to the axial plane where the initial speckle was measured. Moving away from this plane the speckle slowly returns to Rayleigh statistics. It is due to the mechanism relying on interference.

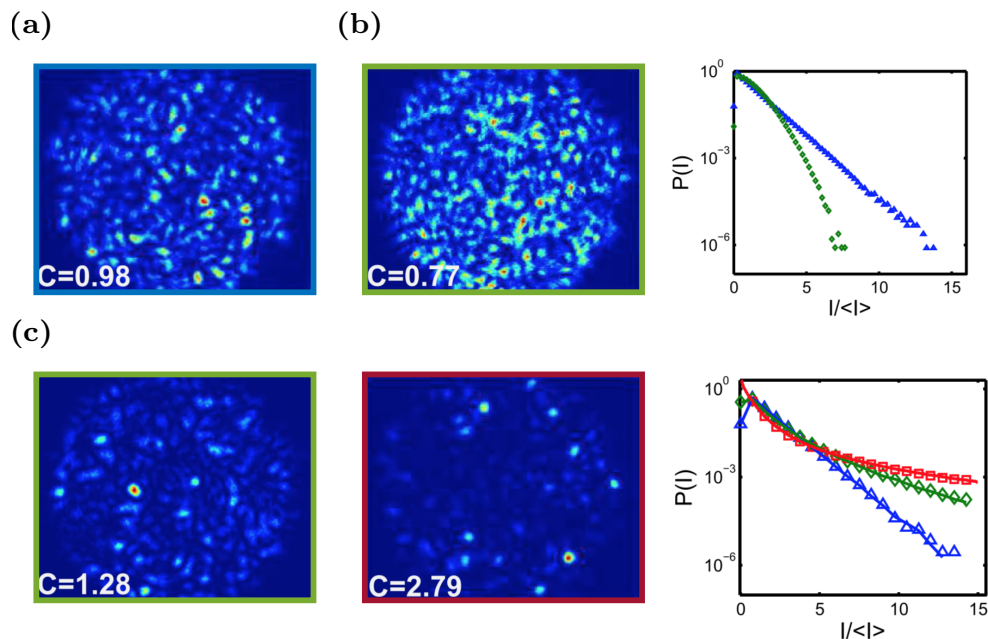


Figure 3.3: **Variations from Rayleigh statistics.** (a) Rayleigh speckle. (b) Sub-Rayleigh speckle in the left part and its intensity statistics (green) compared to the one of the Rayleigh speckle of (a) presented in blue on the right part. (c) Super-Rayleigh speckles and their statistics in the right part (green and red curves) compared to the Rayleigh statistics of (a). Figure adapted from [Bromberg et al. 2014].

Up to now we have reviewed speckles presenting small deviations from the Rayleigh statistics. An interesting question is whether it is possible to reach statistics that deviate much more and even design them arbitrarily.

### Manipulation of the speckle statistics: from tailored intensity statistics to non-local correlations

Before discussing some results, it is important to recall that modifying the speckle statistics, despite the inherent and fundamental interest it presents, would find plethora of applications. Speckle patterns are already widely used in imaging techniques [Lim et al. 2008; Mudry et al. 2012; Gateau et al. 2013]. Hence being able to control the speckle intensity statistics would enable to improve these techniques and broaden speckle patterns use. For instance super-Rayleigh speckle patterns have successfully replaced two photons for sparse illumination for blind-SIM (Structured Illumination Microscopy) in [Labouesse et al. 2017]. The use of a tailored spatial intensity statistics is also promising for optical tomography [Rosen et al. 2000]. But the use of speckle patterns is not limited to imaging only. They are used as optical tweezers to study particle diffusion [Douglass et al. 2012] or Brownian motion [Volpe et al. 2014]. They create random potentials for cold atoms [Lye et al. 2005; Billy et al. 2008].

As mentioned in Sec. 3.1.2.2, deviations from Rayleigh statistics were achieved in related works. To go even further and customize at will the intensity statistics, a technique has been developed in [Bender et al. 2018], (see Fig. 3.4 for some examples of the obtained intensity statistics). This result, similarly to [Bromberg et al. 2014], is only valid for a given imaging axial position. However as a difference the intensity statistics obtained can be arbitrary, and result from a non-linear optimization.

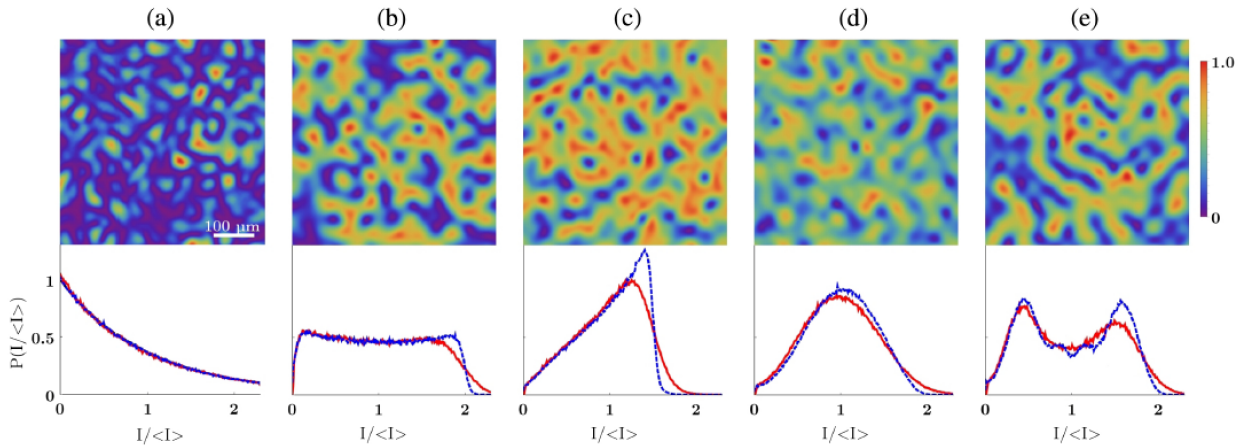


Figure 3.4: **Arbitrary intensity statistics.** (a) Rayleigh speckle pattern (top) and its exponential intensity statistics (bottom) (b-e) Customized intensity statistics and the corresponding speckle patterns. On all graphs the red solid line corresponds to the experimental data and the blue dashed one to numerical simulations. Figure from [Bender et al. 2018].

A similar technique is employed in [Li et al. 2021c] to create negative spatial correlation to reach super-resolution. Another variation presented in [Bender et al. 2019a] enables to customize the intensity statistics and insert non-local correlations<sup>1</sup> by encoding high order correlations into the phase front using the Gerber-Saxton algorithm and a non-linear optimization on the intensity PDF. Long-range correlations were also obtained in [Bender et al. 2019b]. These achievements are promising due to the importance of non-local correlations for applications such as smart target illumination [Akhlaghi et al. 2017].

### Monochromatic transmission matrix for global-focusing

We have discussed in Sec. 1.2.4 the achievements obtained with optimization and the TM in terms of spatial focusing. But with these techniques attention concentrates on spatial focusing on only one speckle grain. Conversely the SVD was used to globally enhance the delivered energy on one ROI. A legitimate question would be to consider focusing spatially on all the ROI, called **global-focus**. A way of doing so is to compute the input vector to display on the SLM with a targeted output vector all elements of which are ones. What would be the result? And what difference with the use of the SVD? We will discuss the impact of performing a global focus in terms of the field statistics. A further comparison in terms of enhancement is developed in Sec. 4.3.2.

As presented in Sec. 1.2.4, to focus on one speckle grain the incoming wavefront should be distorted such that all the phases of the different modes are aligned at the targeted point. When trying to focus simultaneously on all points of the ROI to form a global focus, the wavefront is distorted in such a way that the fields tends to partially acquire a common phase. The statistics hence no longer can be assumed to be a sum of random phasors. However it can be calculated considering a sum of random phasors plus a global phase, as presented in the complex plane in Fig. 3.5. The associated field statistics calculated and predicted by [Goodman 2007] is called **Ricin statistics**. It results in a near-homogeneous intensity on the camera where speckle grains are hard to identify. It is an extreme case of sub-Rayleigh speckles with an almost zero contrast, see Sec. 3.1.2.2. This

<sup>1</sup>In [Bender et al. 2018] spatial correlations were conserved.

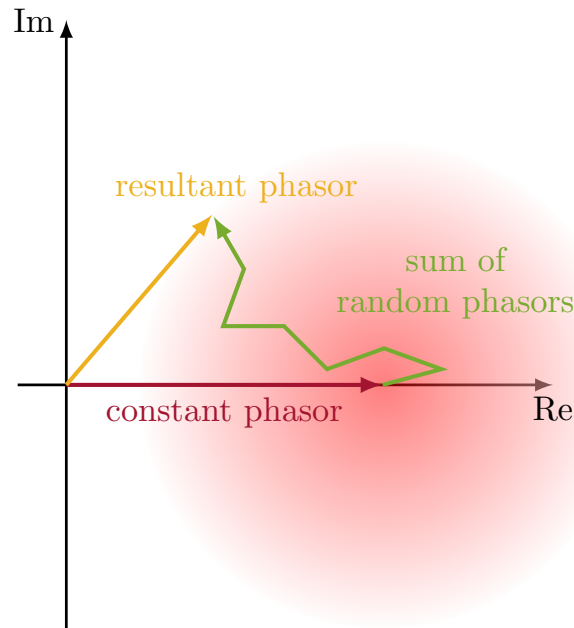


Figure 3.5: **Origin of the Rician statistics.** The Rician statistics emerges when one faces a sum of random phasors (green) plus a constant phasor (red) while the Rayleigh statistics results from the sum of only random phasors. Figure inspired from [Goodman 2007].

significant difference with a Rayleigh speckle is important to consider for potential application where a homogeneous illumination could be preferred rather than a speckled one. An experimental illustration of a Rician speckle statistic is presented and discussed in Fig. 4.4(b). A deeper study of the global-focusing is presented in Sec. 4.3.2 with an enhancement comparison with the SVD method (see also Appendix B.3). A straightforward difference between the global focusing and the SVD is the ability with the SVD method to tune the enhancement by selecting different singular vectors [Kim et al. 2012]. Moreover for phase and amplitude control linear algebra implies that the optimal enhancement should be obtained for the first singular vector.

We will discuss in the next sections other approaches that enable speckle correlation engineering without (or with very limited) modification of the speckle statistics. This method is based on the TM which is expected to contain all the information on the light propagation through the medium of interest.

### 3.2 The transmission matrix beyond the transmission control: speckle grain engineering

To control the speckle correlations or the speckle grain shape one can recall that a good analogy for speckle formation is the diffraction by a set of randomly positioned apertures, see Sec. 1.1.3.1.

The well known Abbe experiment of spatial filtering shows that a diffraction pattern can be altered by physically filtering in the Fourier plane some spatial frequencies. For instance removing the high spatial frequencies blurs the details and sharp edges of the initial image. Thus a filtering of the speckle spatial frequencies would, in principle, allow a control of the grain size and more generally the correlations of the speckle pattern. A physical spatial filtering already was introduced to generate thinner speckle grains [Di Battista et al. 2015; Di Battista et al. 2016]. This filtering

step also can be solely numeric when the TM of the system is measured. This method is introduced in [Boniface et al. 2017] where they use Fourier filtering of TMs to engineer the point spread function of a focus.

Hence, we present a method to engineer arbitrary spatial correlations on the speckle (see Sec. 3.2.1) with the singular value decomposition of the TM. We discuss the axial extension of this correlation control (see Sec. 3.2.2) with the generation of Bessel-like speckles. We conclude by a deeper understanding of the mechanism of the SVD spatial frequency selection with a modification of the illumination scheme (see Sec. 3.2.3) and a control of the speckle grain size, where we verify that the SVD does not alter the speckle statistics. For more information one can refer to [Devaud et al. 2021b].

### 3.2.1 Fourier filtering for correlation engineering

The speckle spatial frequencies filtering, inspired from [Boniface et al. 2017], is introduced on an example and illustrated in Fig. 3.6. First a TM is measured, and since the imaged plane corresponds

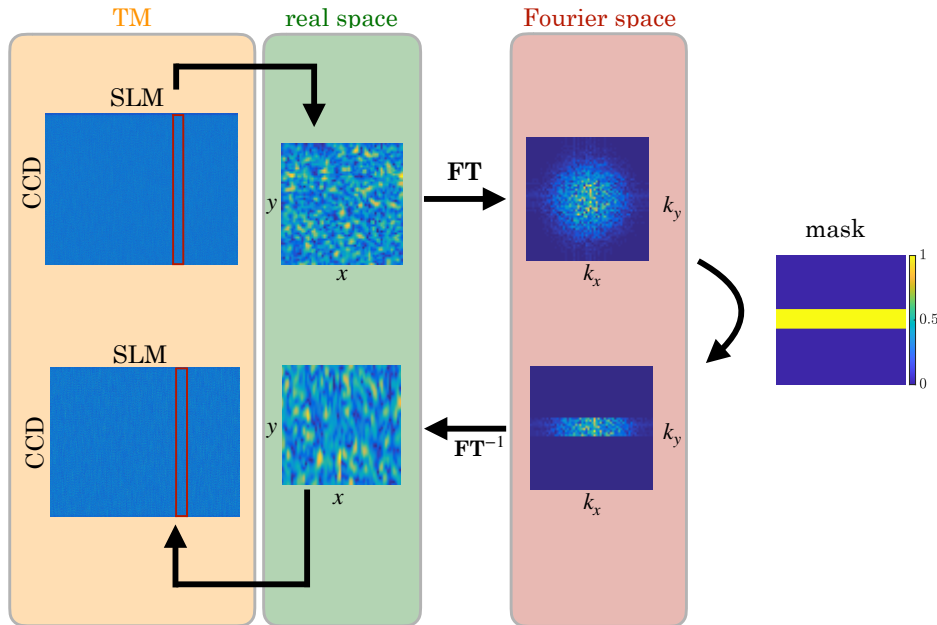


Figure 3.6: **Scheme of the different steps of the computational filtering of a TM.** From a measured TM each CCD speckle imaged is Fourier transformed (FT) and filtered with a mask (here a horizontal line). The filtered Fourier transform is Fourier back transformed  $FT^{-1}$  to the real space and used to form the filtered TM. Figure from [Devaud et al. 2021b].

to the output face of the complex medium, the initial  $k$ -space is flat and limited by a circle delimiting the maximal  $k$  values and defined by the numerical aperture. From this TM a filtered one is computed. The numerical filtering step consists in a Fourier filtering of the output space corresponding to the camera pixels. From the initial  $k$ -space, a filter is applied to select  $k$  components on the TM. Once the filtered TM containing only the targeted spectral frequencies is calculated, we perform the SVD of this filtered TM to obtain a set of singular vectors. These vectors hence contain the information

on the remaining  $k$ -components. The singular vectors are used (more precisely here the first singular vector  $v_1$ ) to modulate the input wavefront on the medium. The field measured after propagation in the scattering medium<sup>2</sup> is observed to be altered and to essentially be modified, following the filtering imposed on the TM. The resulting speckles measured experimentally are presented in Fig. 3.7. For comparison the speckle observed sending an incoming plane wave is presented in Fig. 3.7(a) together with its Fourier plane (uniform as mentioned before) and the autocorrelation along the  $x$  and  $y$  axes. The autocorrelation is computed with

$$C(\delta x) = |\langle E^*(x)E(x + \delta x) \rangle / \langle |E(x)|^2 \rangle|. \quad (3.4)$$

The axes are rescaled with the FWHM of the autocorrelation of the plane wave reference field. Two

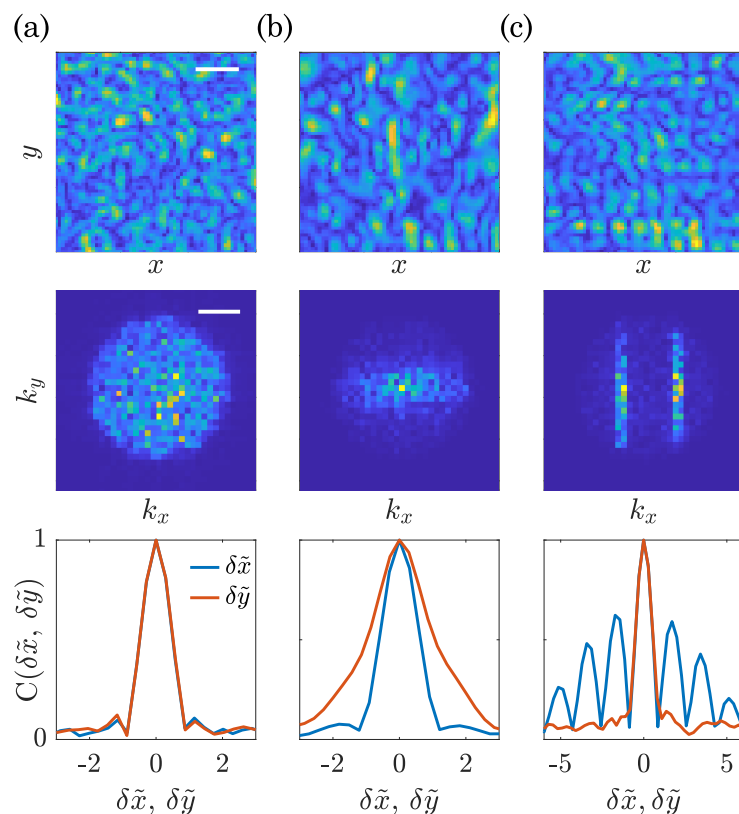


Figure 3.7: **Examples of filtering masks and obtained speckle correlations.** (a) From top to bottom: measured speckle pattern amplitude of a plane wave (reference), associated  $k$ -space and speckle autocorrelation along the  $x$  and  $y$  axes (see Eq. 3.4 for the autocorrelation formula). The tilde symbol stands for rescaled axis: the FWHM of the reference autocorrelation  $w_{\text{ref}}$  is used so that  $\delta\tilde{x} = \delta x/w_{\text{ref}}$ . (b) Same representations when using a filtering mask cutting high  $k_y$  components, resulting in elongated speckles in the  $x$  direction. (c) Wavy speckle with long-range correlations due to a two-slit filtering mask selecting some specific  $|k_x|$ -ranges. For all images the white scale bars are respectively,  $5 \mu\text{m}$  and  $2 \mu\text{m}^{-1}$  and the initial grain size is  $1.4 \mu\text{m}$ . The autocorrelation and the Fourier spaces are averaged over 4 disorder realizations. Figure from [Devaud et al. 2021b].

filtering mask as presented as example of the technique. In Fig. 3.7(b) we present the filter used to explain the filtering technique in Fig. 3.6 (filtering high  $k_y$  components): the speckles are no

<sup>2</sup>The medium is unchanged and thus only the input states bear the information on the filtering.

longer isotropic but elongated in the  $y$  direction. Another filtering mask is presented in Fig. 3.7(c), which this time selects some specific  $|k_x|$ -ranges, here two symmetric vertical stripes in  $k$ -space. This results in a wavy speckle presenting correlations beyond the grain size. With this technique the speckle correlations can be modified using any Fourier mask: short-range for the speckle grain and longer-range with an emerging pattern.

### 3.2.2 An axial extend of the correlation control

In [Boniface et al. 2017] the point spread function engineering was used to create Bessel beams. For that purpose the filtering mask used was a ring [McGloin et al. 2005]. Bessel beams are interesting as they propagate with less lateral spreading than gaussian beams [Durnin 1987; Durnin et al. 1988]. They already have been generated after scattering media [Di Battista et al. 2015; Di Battista et al. 2016; Boniface et al. 2017]. However Bessel-like speckle remains little studied, despite its introduction by [Turunen et al. 1991] and some more recent work [Cottrell et al. 2007; Dudley et al. 2012; Reddy et al. 2016; Liu et al. 2021]. Bessel-like speckle with their non-diffractive property would be promising to generate them [Phillips et al. 2016]. To do so we performed the same filtered TM experiment, but applying a ring mask in Fourier. To verify the axial properties of the speckles, we measure them along different transverse planes by translating axially the collection microscope objective. In Fig. 3.8(a), we present an image of an axial cut of the obtained tridimensional speckle. One can indeed see that Bessel speckle are thinner and longer than the reference speckle. To have a more quantitative idea of the Bessel characteristics of the speckle, the autocorrelation is plotted in Fig. 3.8(b) and compared to the autocorrelation of the reference speckle (black semi-dotted line). The autocorrelation along the  $y$  (blue solid line) is slightly thinner than the reference and one can see hints of the well-known Bessel oscillations. Along the  $z$  direction the autocorrelation is broadened confirming the elongated speckles. The ability of realizing Bessel-like speckle reveals a very important aspect of the SVD method to control correlations: the effect is not limited to the single  $z$  position where the TM has been measured (denoted  $z_0$ ). This is in stark contrast with [Bender et al. 2019b] where the effect relies on interferences. To illustrate this point the transverse grain size is measured for different  $z$  planes for different singular vectors ( $v_1$  and  $v_{80}$ ). The  $z$  axis is centered around  $z_0$ , axial position where the TM is measured, and expressed in terms of number of speckle grains (axial length measured at  $z_0$ ). In Fig. 3.9(a) the raw transverse grain size is plotted. Hence the diffraction is responsible for the speckle grain size increase along  $z$ . This global increase with  $z$  is suppressed in Fig. 3.9(b), normalizing the transverse grain size by the value obtained with a plane wave. Hence Fig. 3.9(b) gives the relative speckle grain evolution along  $z$ .

In the next sections we present some complementary information on the illumination scheme. We use a modified illumination scheme to induce, without any active filtering of the TM, a selectivity of the speckle pattern spatial frequencies by the SVD. This understanding leads to a very simple method to control the speckle grain size.

### 3.2.3 Simple control over the speckle grain size

#### 3.2.3.1 Illumination and collection microscope objectives positions

The positions of the illumination and of the collection microscope objectives have already been discussed in Sec. 2.3.5.4. So far the collection microscope objective images a plane located at the output surface of the sample. This plane is now (for this section and for Chap. 4) moved away from the sample. The reason for this position is to control the inhomogeneities of the speckle Fourier components. If the imaged plane is the medium output face, the Fourier components are only limited by the collection microscope numerical aperture (NA), and the Fourier transform of the speckle

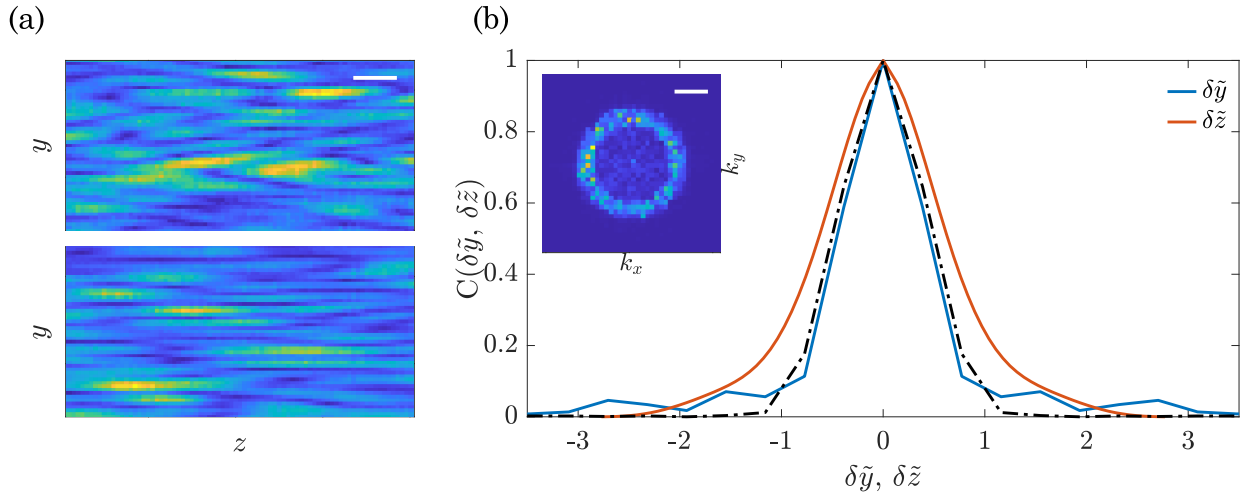


Figure 3.8: **Bessel-like speckles.** (a) Volumetric speckle cut on one  $x$  plane. The top image represents the speckle of reference when a plane wave is sent into the medium. The bottom image represents the speckle obtained when displaying on the SLM the first singular vector of a TM filtered with a ring. The speckle grains are elongated in  $z$  and thinner for their transverse directions. The white scale bar represents  $5 \mu\text{m}$ . (b) Plot of the autocorrelation  $C$  both along  $y$  (blue curve) and along  $z$  (red curve) for the same data as in (a). As in Fig. 3.7, the horizontal axis is rescaled by the FWHM of the reference autocorrelation. The dash-dotted black line indicates the reference autocorrelation (equivalent for both  $y$  and  $z$  directions due to the rescaling). For the autocorrelation, the data are averaged over all  $x$  positions. The inset shows the corresponding Fourier space distributions in the  $(x,y)$  plane at the TM position. The white scale bar measures  $2 \mu\text{m}^{-1}$ . Figure adapted from [Devaud et al. 2021b].

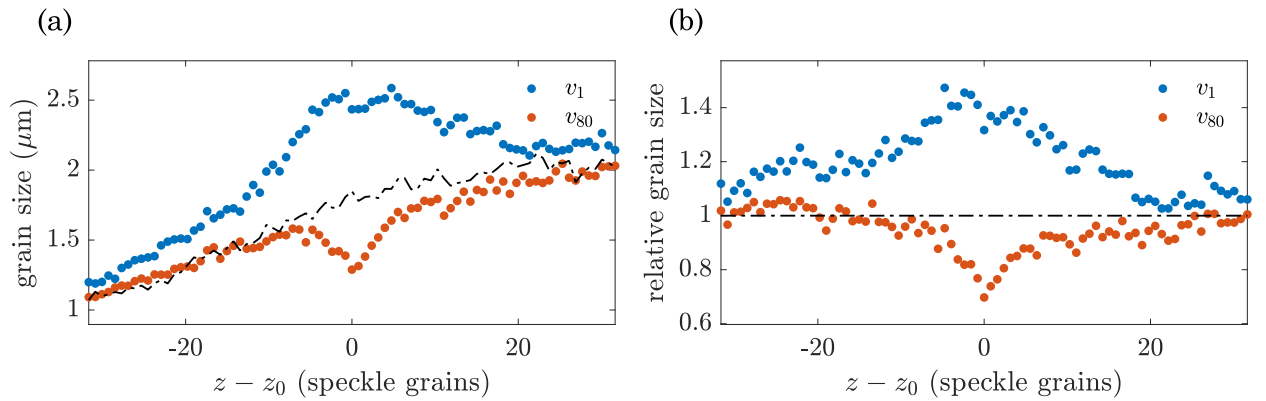


Figure 3.9: **Axial extent of the correlation control.** (a) Transverse speckle grain size (in  $\mu\text{m}$ ) along the axial dimension  $z$ . The first singular vector ( $v_1$ , blue) and an intermediate one ( $v_{80}$ , orange) are presented. The  $z$ -axis is rescaled by the axial extension of the reference speckle at  $z_0$  (position where the TM was measured). The global speckle grain size increase is due to diffraction. (b) Same data as for (a) but this time the relative speckle grain size is presented: all sizes are rescaled with the local reference grain size. Figure adapted from [Devaud et al. 2021b].

pattern is therefore a homogeneous disk. As we move away the collection microscope objective from the sample surface, the grain size increases, which corresponds to a decrease in the spatial

frequencies. It is no longer the NA that sets the bounds on the transmitted spatial frequencies but an effective filtering applies. A limiting case is worth mentioning: for a collection microscope positioned very far from the medium, only the Fourier component with  $k \simeq 0$  are collected, leading to a few big speckles grain. For intermediate positions low spatial frequencies are better transmitted than higher ones. The absence of sharp threshold leads to a non-uniform  $k$ -space distribution. The coupling between transmission properties and spatial frequencies is interesting: controlling one (for instance the transmission with the selection of singular vectors) leads to the simultaneous control of the other (the spatial frequencies). This is the purpose of the next section. A scheme of the experimental configuration is presented in Fig. 3.10.

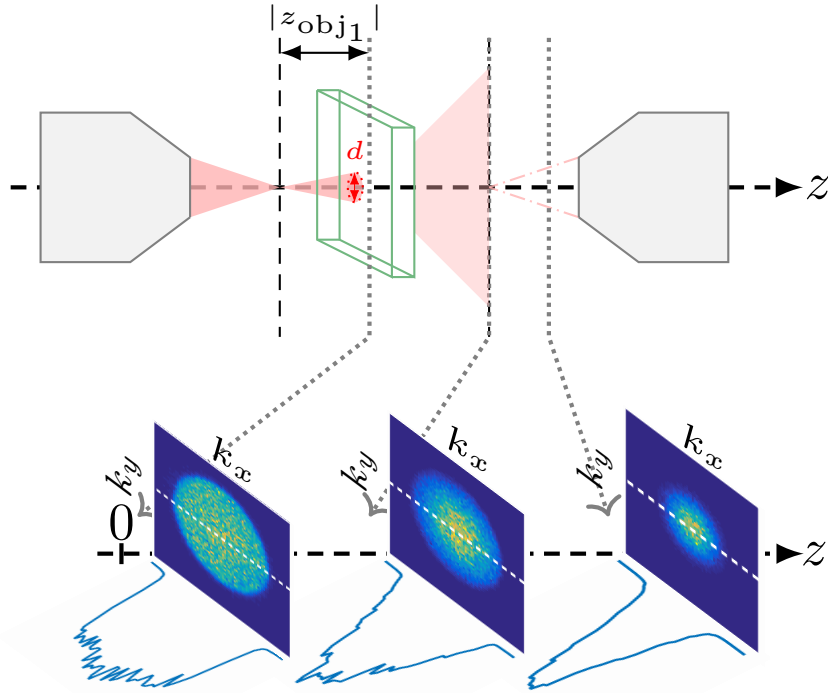


Figure 3.10: **Influence of the position of the collection microscope objective on the Fourier spectrum.** The illumination microscope objective is moved away from the sample so that light covers a wide illumination area on the sample. The collection microscope objective is also moved away from the sample in order for the weight of the Fourier components not to be homogeneous on the speckle. Imaging a plane close to the sample output face (denoted as  $z = 0$ ) leads to a speckle limited by the NA of the system and planes imaged with  $z > 0$  lead to non-flat Fourier spectra of the speckles. Figure adapted from [Devaud et al. 2021b].

### 3.2.3.2 Speckle grain size control

So far the experimental configuration is the one described in Fig. 3.10 (bottom left panel), where the collection microscope objective images the output surface of the medium. In the following, it is defocused in such a way that the speckle  $k$ -space is not NA-limited but presents a smooth radial decay of the mean energy. These variations are visible in Fig. 3.10 (bottom) and in the second and third rows of the first column of Fig. 3.11(a). Since it is present on all individual speckle patterns, the TM also contains this information in the Fourier domain. Moreover the TM is purposely over-sampled

on the CCD plane so that the spatial frequencies are well resolved.

When computing the SVD of the TM, a basis of singular vectors is obtained. They are sorted by transmission, whose relative values are accessible through the singular values. In case of a homogeneous  $k$ -space distribution all  $k$  values inside the NA are equally addressed and sending different singular vectors only affects the global transmission. For an inhomogeneous  $k$ -space another parameter comes into play: some  $k$ -components are associated with a higher transmission than others. To obtain the best transmission, exciting preferably these  $k$ -components is more efficient. Hence the transmission sorting induced by the SVD goes together with a selection of the  $k$  vectors. It is noteworthy that the same reasoning holds in [Sec. 3.2.1](#) and [Sec. 3.2.2](#), where the  $k$ -space inhomogeneity is brought by the filtering step. This  $k$  vectors sorting is well visible in [Fig. 3.11\(a\)](#)'s second and third rows: to obtain the best enhancement ( $v_1$ ) the selected  $k$  are concentrated close to the center of the Fourier plane, where energy is maximum. In contrast, for intermediate enhancements ( $v_{81}$ ), the  $k$  vectors selected are on the edge (forming a ring). For even smaller transmissions ( $v_{225}$ ) the uncontrolled light is no longer negligible<sup>3</sup> and acts as noise. As a result no clear  $k$  values are selected for the singular vectors associated with the smallest transmissions. This  $k$ -selectivity is not

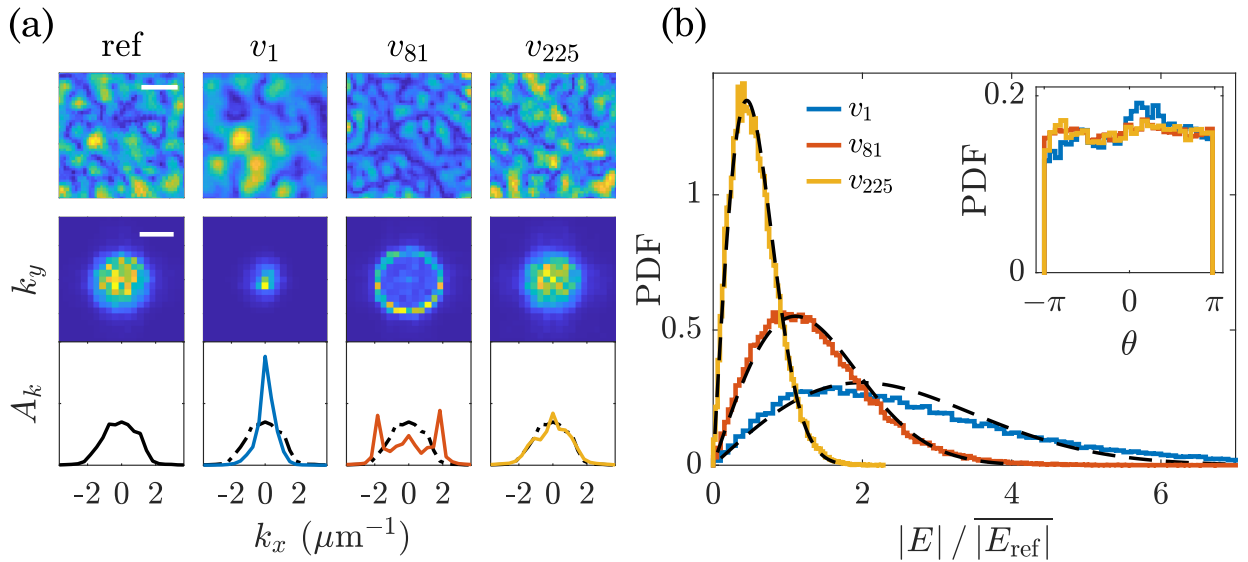


Figure 3.11: **Evolution of the speckle  $k$ -space with the singular vector # and speckle statistics.** (a) Speckle patterns and their Fourier transform. First row: speckle obtained for different inputs such as a plane wave for a reference and three different singular vectors ( $v_1$ ,  $v_{81}$  and  $v_{225}$  out of 225). Second row: amplitude of the spatial Fourier transform of the speckle patterns. Third row: cuts along the horizontal direction of the speckle  $k$ -spaces averaged over 3 pixel rows. The reference black curve is kept in dashed line for all singular vectors to allow comparison. The white scale bars are  $5 \mu\text{m}$  and  $2 \mu\text{m}^{-1}$  respectively. All data are individually normalized for a better observation and hence do not show the transmission variations. Fourier spaces and the associated cuts are averaged over 36 realizations of the disorder. (b) Speckle statistics for the same three singular vectors. The field amplitude follow a Rayleigh statistics which fits are presented with the dashed black lines. The inset displays the phase PDF. Figure adapted from [[Devaud et al. 2021b](#)].

only visible on the spatial Fourier transform of the speckle but also in the speckle itself. Indeed the  $k$  distribution is associated with the speckle grain size as visible on the first row of [Fig. 3.11\(a\)](#). For all

<sup>3</sup>The uncontrolled light amount is constant, thus for high transmissions it is negligible but for reduced transmission its impact is more important.

the singular vectors shown in Fig. 3.11(a) the amplitude and phase PDF are plotted in Fig. 3.11(b). The statistics remains Rayleigh which is an advantage for some applications where the speckle illumination is interesting, among others, for speckle-field digital holography microscopy [Park et al. 2009] and also blind structured illumination microscopy [Mudry et al. 2012].

To better quantify the variation in speckle grain size for each singular vector, the speckle grain size is measured and its relative value (speckle grain size divided by the speckle grain size obtained when illuminating the medium with a plane wave) is plotted in Fig. 3.12(a). The inset represents the associated measured field enhancements. An important observation is the possible smooth control of the speckle grain with the choice of singular vectors. To complement this experimental observation some simulation results are presented in Fig. 3.12(b). The TM is simulated using a random matrix

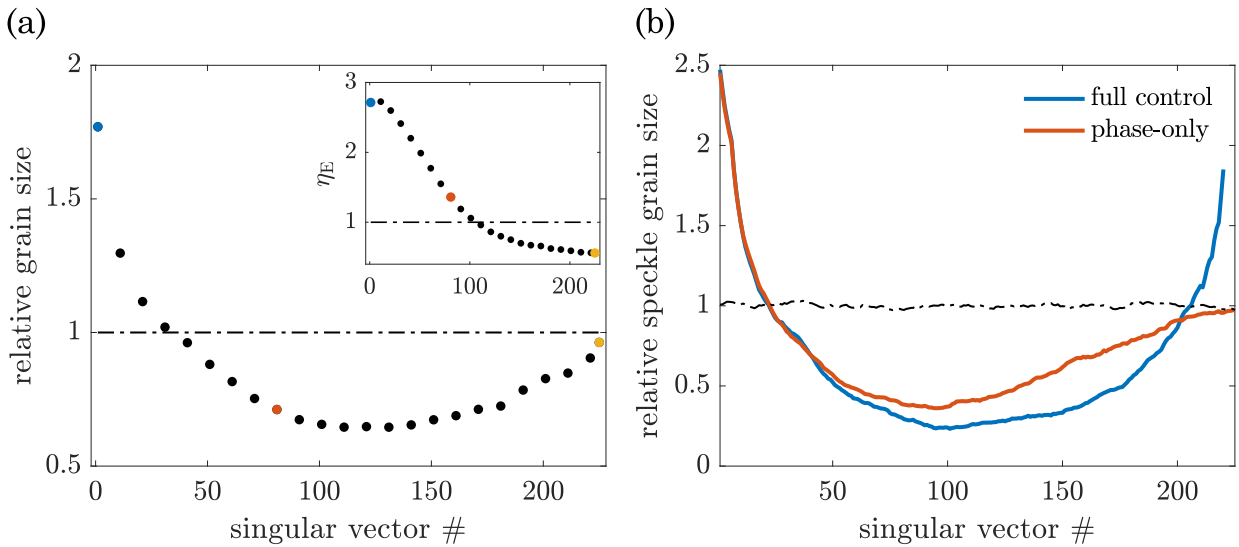


Figure 3.12: **Evolution of the grain size with the singular vector #.** (a) Grain size measured experimentally using the same data as for Fig. 3.11. The colored dots refer to the data displayed in Fig. 3.11. The grain size is bigger than the reference one for the first singular vectors and monotonically decreases to a value lower than the reference one for the middle singular vectors. For the last singular vectors the grain size smoothly recovers the reference value. The inset represents the measure field enhancements  $\eta_E$ . (b) Simulation of the speckle grain size using the RM model. The initial speckle grain size and the effective number of SLM modes are extracted from the data of (a) to better mimic the TM characteristics. The same behavior as for the experimental data is observed for phase-only control. For phase and amplitude control the grain size increases again for the last singular vectors. The data are averaged over 50 realizations and smoothed with a moving mean of 10 points. Figure adapted from [Devaud et al. 2021b].

which roughly includes some of the TM properties, such as the remaining grain size after the binning process (the experimental TM was purposely over-sampled) and the effective number of modes. The phase-only control shows results that are similar to the experimental data, for a better match with the enhancement values a fine tuning on the TM characteristics would be necessary. The phase and amplitude control brings new information on the grain size behavior: it is similar to the phase-only control for the first singular vectors but differs for the last singular vectors where a new increase of grain size should be expected.

A related technique to create anisotropic speckle grains in the same illumination configuration is described in Appendix B.2.

### 3.3 Take home message

In this chapter we discussed speckle statistics, correlations, and we propose ways to modify them. The knowledge of the transmission matrix of a system enables to obtain a very low contrasted speckle when performing a global-focusing with a Ricin statistics. However, the propagation of singular modes through the medium preserves the Rayleigh statistics of a general speckle. We experimentally verify that the SVD of the TM can be a tool for engineering the speckle correlations (both the grain size and longer-range correlations). The axial extension of the control exceeds several speckle grains enabling to generate Bessel-like speckles.



# 4 | From monochromatic to temporal aspects

---

4.1	Measurement of time-gated transmission matrices . . . . .	141
4.1.1	Measurement techniques . . . . .	141
4.1.1.1	Indirect measurement via the multi-spectral transmission matrix . . . . .	141
4.1.1.2	Direct measurement . . . . .	142
4.1.2	How to use a time-gated transmission matrix? . . . . .	143
4.2	Spatio-temporal focusing . . . . .	143
4.2.1	Focusing on one speckle grain . . . . .	144
4.2.2	Multi-time and multi-speckle focusing . . . . .	145
4.2.3	Extension to a temporal global-focus . . . . .	147
4.3	Singular value decomposition to control the energy delivery . . . . .	149
4.3.1	Singular value decomposition and pulse shape . . . . .	149
4.3.2	Comparison to the global-focusing . . . . .	152
4.3.3	Enhancement for different delays with a single phase mask . . . . .	154
4.3.4	Evolution of the control over the pulse . . . . .	155
4.3.5	Shift of the enhanced delay . . . . .	158
4.4	Temporal speckle grain size control . . . . .	160
4.5	Time gated transmission matrix on a waveguide . . . . .	161
4.5.1	Simulated geometry and protocol . . . . .	162
4.5.1.1	Geometry . . . . .	162
4.5.1.2	From spectral to temporal information . . . . .	162
4.5.1.3	Definition of $\tau = 0$ . . . . .	163
4.5.1.4	Calculation of the output field . . . . .	163
4.5.2	Results . . . . .	164
4.6	Take home message . . . . .	165

---

So far, we performed studies in the monochromatic regime and focused mainly on spatial effects. In this chapter we will consider temporal aspects by setting the laser in pulse mode. We will exploit the setup ability of performing time-gated measurements to directly work in the temporal regime. Spectral aspects (and the link with temporal ones) are discussed in [Chap. 1](#). We will briefly comment on TGTMs measurement in [Sec. 4.1](#). Then, in [Sec. 4.2](#), we will review the results already obtained with a TGTm to control light fields. In [Sec. 4.3](#), are presented in more details the possibilities of energy delivery using the SVD of the TGTm and discuss the similarities between a TGTm and a regular monochromatic TM in [Sec. 4.4](#). This chapter concludes by the presentation in [Sec. 4.5](#) of the

simulation scheme and results obtained by our collaborators when investigating pulse propagation in a disordered waveguide.

## 4.1 Measurement of time-gated transmission matrices

### 4.1.1 Measurement techniques

As mentioned in [Sec. 1.3.3.2](#) the MSTM and the TRTM should contain the same information. Hence when seeking informations on a specific delay, two approaches are possible: a direct measurement of the TGTM associated to this delay or an indirect measurement through the MSTM.

#### 4.1.1.1 Indirect measurement via the multi-spectral transmission matrix

The indirect measurement technique is based on the Fourier transform relation between frequency and time. Given the spectral scattering information, it is possible to compute the temporal one. This is for instance employed with MMFs in [[Carpenter et al. 2016](#); [Xiong et al. 2019](#); [Mounaix et al. 2019](#)].

This technique is very powerful as it grants access to temporal aspects of light propagation using only monochromatic light. In [Sec. 4.5](#), the same approach is used to simulate a pulse propagation in a waveguide. However this remains an indirect measurement and requires the (time demanding) measurement of several monochromatic TMs. In an experimental work such as the one presented here, a direct measurement is preferred.

#### 4.1.1.2 Direct measurement

The direct measurement does not differ much from the measurement of a monochromatic TM, presented generally in [Sec. 2.3.4](#) and more concretely in [Sec. 3.1.2.2](#). When considering TGTM's new precautions must be taken with regard to the exact positioning of the delay-line. The measurement is indeed performed for a given delay  $\tau_0$  in the pulse. To only gather information at this specific delay, the delay-line length is adjusted such that the probe pulse interferes with the scattered light at a delay  $\tau_0$ .

Also under monochromatic settings, it is relatively easy to balance the illumination between the scattered light and the probe to maximize the interference contrast, and hence optimize the field extraction. This is no longer the case for the pulsed mode, because the camera collects scattered light with various delays, where the light proportion for a given delay scales according to the pulse shape. Hence, for a targeted delay  $\tau_0$  close to the scattered pulse peak, interfering light represents a majority leading to well contrasted interferences. However, for a targeted delay  $\tau_0$  situated in the pulse tail, the amount of interfering light is drastically reduced and leads to smaller contrasts. The signal to noise ratio decreases, preventing an optimal field extraction (and hence TM measurement). The consequences of the TM measurement quality as a function of  $\tau_0$ , as well as its monitoring, are discussed over an example in [Sec. 4.3.4](#).

### 4.1.2 How to use a time-gated transmission matrix?

Once the TGTM is measured, using it is not different from a monochromatic TM. The input phase mask is determined and displayed on the SLM. Then the output field is measured, either at a specific delay or for all delays using the field extraction techniques presented in [Sec. 2.3.2](#).

In the next sections we will give examples of what the TGTM enables to do, i.e. spatio-temporal focusing ([Sec. 4.2](#)) and energy delivery control ([Sec. 4.3](#)).

## 4.2 Spatio-temporal focusing

Spatio-temporal focusing behind a scattering medium was achieved before the introduction of the TGTM object. Indeed it is interesting to note that, as for the monochromatic scheme where focusing behind a scattering sample was first realized with optimization techniques [Vellekoop et al. 2007; Vellekoop et al. 2008b], spatio-temporal focusing also was achieved first through optimization [Aulbach et al. 2011]. In the latter paper a spatial focus was observed behind a thick  $\text{TiO}_2$  layer for different delays, also selected with a delay-line, using a field amplitude feedback control. Foci obtained for optimization with different delay-line lengths are presented in Fig. 4.1.

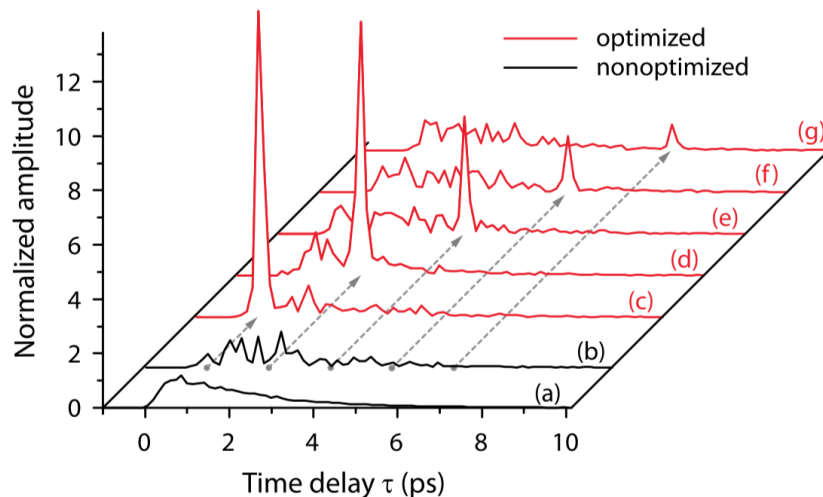


Figure 4.1: **Spatio-temporal focusing with optimization.** (a) Temporal profile averaged over 50 realizations for the non-optimized pulse. (b) Example of one single speckle amplitude temporal profile. (c-g) Temporal profiles for when optimizing the amplitude for different delays (dashed arrows) using 300 SLM modes. The position of  $\tau = 0$  is set as the maximum amplitude with no sample. Figure from [Aulbach et al. 2011].

In the following we will solely consider spatio-temporal focusing with a TGTM. When compared to the optimization approach, TMs not only enable us to focus on a single speckle grain, but also make it possible to engineer more complex foci. Similarly to the monochromatic case, scattering informations contained on the TM make it a powerful tool for reconfigurable focusing. Provided that the medium has not decorrelated, only one TM measurement is needed for several focusing experiments.

### 4.2.1 Focusing on one speckle grain

The procedure to obtain a spatio-temporal focus with a TGTM is the same as for a monochromatic TM: the input phase mask is computed using phase conjugation and displayed on the SLM. This focusing mask, only valid for the delay  $\tau_0$  where the TM has been measured, hence combines spatial focusing with temporal aspects. This spatio-temporal focusing with a TGTM already has been achieved and is presented in [Mounaix et al. 2016a]. Their experimental setup is similar to the one described in this thesis, with a sample made of a thick  $\text{ZnO}$  layer. Examples of spatio-temporal focusing experiments are presented in Fig. 4.2. In Fig. 4.2(a) the focusing on one speckle grain with a monochromatic TM (blue curve), measured for the pulse central frequency, is compared to the focusing with a TGTM (red curve) and to the reference pulse (black curve). For all three curves

the intensity is measured on the focusing position only. The monochromatic TM enables spatial focusing while the TGTm enables spatio-temporal focusing. Once the TM is measured the focusing

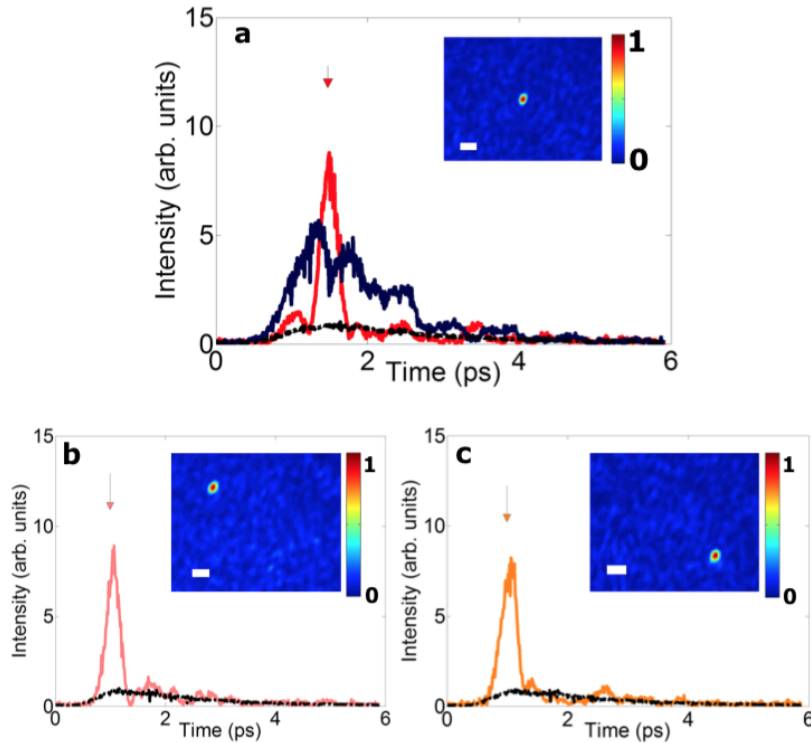


Figure 4.2: **Spatio-temporal focusing with a TGTm.** (a) Intensity measured at the focusing target position for the monochromatic focusing (blue) and the time-gated focusing (red). The black curve represents the averaged over 100 speckle grains of the pulse temporal profile. (b,c) Spatio-temporal foci for two different spatial positions for the same TGTm as in (a). The white scale bars in the insets represent 2  $\mu\text{m}$ . Figure from [Mounaix et al. 2016a].

can be reconfigured to different spatial target positions as visible in Fig. 4.2(b,c).

#### 4.2.2 Multi-time and multi-speckle focusing

Can we engineer more complex focusing? Yes due to the linearity allowing us to combine input vectors. It is then possible to measure for instance two TGTms (for  $\tau_1$  and  $\tau_2$ ), compute the focusing vectors for a given spatial targeted position and sum them. Taking the phase approximation of this resulting vector leads to the phase mask to display on the SLM to focus light on one position for two distinct delays. Focusing on the same spatial position for delays  $\tau_1$  and  $\tau_2$  is presented in Fig. 4.3(a). The comparison with focusing individually at these two delays is presented Fig. 4.3(b). A small enhancement decrease is observed for the multi-focusing.

An extension of Fig. 4.2(b,c), i.e. focusing on two spatial positions simultaneously for the same delay, also works. Hence it just requires to define the output target vector for two foci before taking its phase conjugation. A next step is its extension to the global-focusing presented in Sec. 3.1.2.2.

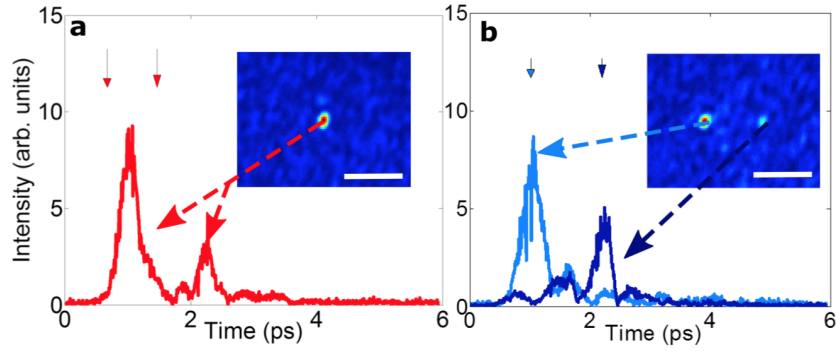


Figure 4.3: **Multi-delays focusing with a TGTm.** (a) Spatio-temporal focusing on the same spatial position for two different delays. (b) Individual spatio-temporal foci for two different spatial positions for the same TGTMs as in (a). The white scale bars in the insets corresponds to 5 μm. Figure from [Mounaix et al. 2016a].

### 4.2.3 Extension to a temporal global-focus

In this experiment a TGTm is measured for a delay  $\tau_0 = 1$  ps. The input phase mask is computed to target a global-focus at the output. The mask is displayed on the SLM and the field is measured along the pulse by scanning the delay-line. The averaged amplitude obtained is displayed in Fig. 4.4(a) (green curve) and compared to the plane wave input (gray curve). The energy delivery increases at  $\tau_0$ . As expected from the TM measurement and the extraction, relying on the interference with the unperturbed pulse, the width of the peak corresponds to the probe pulse width. This behavior is also observed with the focusing on a single speckle grain. Also observed in the spatio-temporal focusing experiments, the scattering information contained in the TGTm is limited to specific delays: the focusing is only effective around  $\tau_0$ .

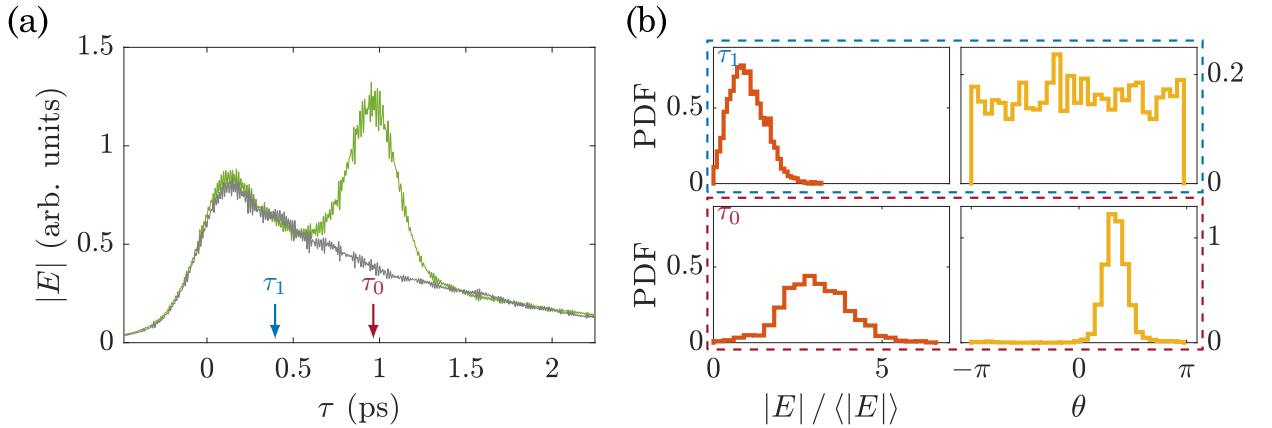


Figure 4.4: **Temporal global-focus.** (a) Averaged amplitude pulse profile for a plane wave input (gray) and the global-focusing input (green) calculated with a TGTm measured at  $\tau_0$ . (b) Field statistics for  $\tau_1$  (top) and  $\tau_0$  (bottom). The amplitude PDF is plotted on the left and the phase PDF on the right. The statistic is Rayleigh for delays different than  $\tau_0$  (i.e. for  $\tau_1$ ) while it is Rician around  $\tau_0$ . For these experiment  $\gamma \sim 0.1$ .

Moreover the statistical properties of the speckle pattern also becomes time dependent as visible in Fig. 4.4(b). Speckle statistics are compared for two different delays: the delay  $\tau_0$  for which the

TGTM has been measured and an arbitrary delay  $\tau_1$  different enough from  $\tau_0$ . For  $\tau_1$  the field follows a Rayleigh statistic characterized by a Rayleigh amplitude PDF and an homogeneous phase (see [Sec. 3.1.1](#)), both are presented in the top part of [Fig. 4.4\(b\)](#). Conversely the field statistic at  $\tau_0$  is Ricin, due to the preferred phase set, as already mentioned for the monochromatic global-focusing (see [Sec. 3.1.2.2](#)). The Ricin statistics corresponds to a Gaussian phase peaked around one value [Fig. 4.4\(b, bottom right\)](#) while the field amplitude is more symmetric than a Rayleigh distribution [Fig. 4.4\(b, bottom left\)](#).

Even though the global-focusing is impressive and allows to enhance the energy delivery at targeted delays in the pulse, the enhancement value is not tunable and the output field is necessarily Ricin. Both aspects are restricting potential applications. Imaging techniques would rather benefit from speckle patterns [[Park et al. 2009](#); [Mudry et al. 2012](#)]. Thus extending the control with the SVD of the TM achieved in monochromatic [[Kim et al. 2012](#)] would be promising.

## 4.3 Singular value decomposition to control the energy delivery

### 4.3.1 Singular value decomposition and pulse shape

As for focusing, the TGTM study with the SVD is no different than for the monochromatic regime. Here a TGTM is measured for a delay  $\tau_0 = 1.1$  ps with a degree of control  $\gamma \sim 0.3$ , for 225 singular vectors. For each singular vector, its phase is displayed on the SLM and the field is measured along the pulse by scanning the delay-line. The obtained pulse shapes (amplitude averaged over all CCD pixels) for the two extreme singular vectors ( $v_1$  and  $v_{225}$ ) are presented in [Fig. 4.5\(a\)](#). The first singular vector (blue curve) leads to an amplitude increase at  $\tau_0$  while the last singular vector (orange curve) leads to a decrease. The plane wave input is presented in gray for comparison. The green dots displayed in top mark the peak positions for the intermediate singular vectors. A smooth control of the energy delivered is possible. It is important to note that again a temporally localized enhancement is observed. It is in stark contrast with the extended one reached in MMFs when spatio-temporal correlations comes into plays [[Xiong et al. 2019](#)].

Even if the singular vectors are ordered by transmission, predicting the enhancement value is convenient for practical applications. In theory the amplitude enhancement should be given by the singular value itself, see [Appendix B.3](#). In [Fig. 4.5\(b\)](#), we plot the amplitude enhancements  $\eta_E$  for the data of [Fig. 4.5\(a\)](#). In monochromatic the amplitude (resp. intensity) enhancement was defined by the total amplitude (resp. intensity) over the ROI for the targeted vector divided by the the total amplitude (resp. intensity) over the ROI for the reference vector (usually an input plane wave). The definition for the pulse is the same. The amplitude (resp. intensity) is measured at  $\tau_0$ . For the reference it is possible, for improving the stability, to fit the exponential decay of the pulse and extract the amplitude (resp. intensity) value at  $\tau_0$  from it. When the averaging is sufficient (big ROIs or averaging over enough disorder realizations), which is the case in the experiments performed, the method employed to extract the reference amplitude (resp. intensity) does not matter.

In [Fig. 4.5\(b\)](#) the enhancements measured experimentally are plotted together with the normalized singular values  $\tilde{s}$ . Despite discrepancies that can be mainly attributed to phase-only control (see [Appendix B.4](#)) the data match theoretical predictions.

It can be visually observes, comparing [Fig. 4.4\(a\)](#) and [Fig. 4.5\(a\)](#), that the SVD enhancement does not look higher than the global-focus one, despite theoretical predictions. However these two experiments are not directly comparable due to their different degrees of control. In the next section we will compare the enhancements obtained for both the SVD and the global focusing.

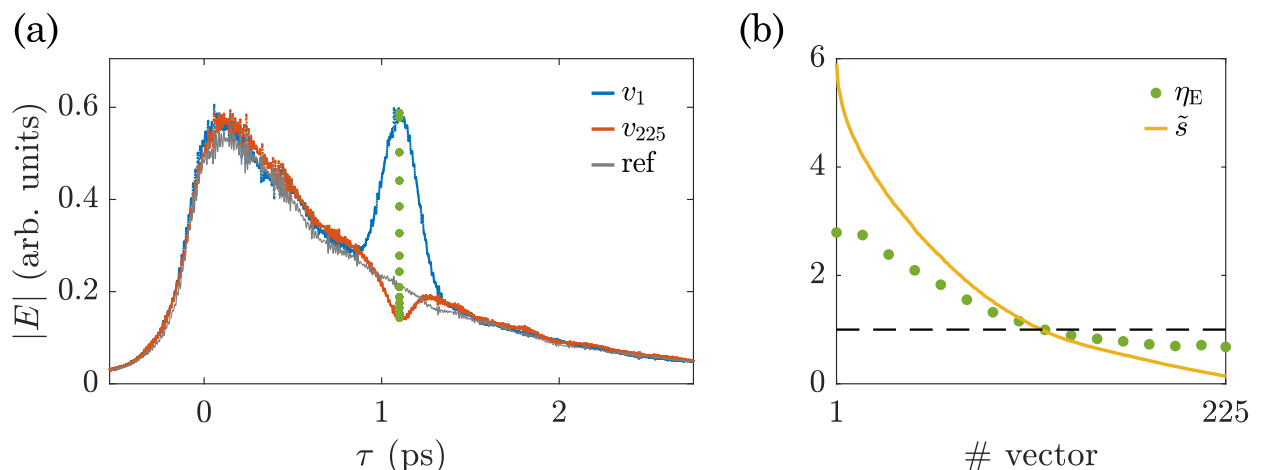


Figure 4.5: **Temporal control of the energy delivery with the SVD.** (a) Pulse averaged amplitude profile for the first singular (vector  $v_1$ , blue) and the last singular vector ( $v_{225}$ , orange) of a TGTm measured at  $\tau_0 = 1.1$  ps. The pulse obtained for a plane wave input (ref) is shown in gray. The green dots represent the peak values for some other singular vectors. (b) The field amplitude enhancement ( $\eta_E$ ) for all the singular vectors is plotted with green dots. The expected enhancement for phase and amplitude control (normalized singular values) is represented with the yellow curve. For this experiment  $\gamma \sim 0.3$ .

### 4.3.2 Comparison to the global-focusing

In this section I present a comparison of enhancement between the global-focusing and the first singular vector. The number of SLM modes is kept fixed ( $N_{\text{SLM}} = 256$  with  $N_{\text{SLM}}^{\text{eff}} \simeq 120$ ) and  $N_{\text{CCD}}$  varies. A TGTm is measured in the middle of the pulse ( $\tau_0 \sim 1.1$  ps) and both the first singular vector and the global-focusing vector are computed from it. The SLM is successively modulated by their phases while scanning the delay-line to extract the fields temporal evolution. The amplitude enhancements are measured at  $\tau_0$ , taking as a reference field the plane wave input and are plotted in Fig. 4.6(a). As theoretically expected (see Appendix B.3) the first singular vector performs a better enhancement than the global-focus. However due to several experimental limitations: the phase-only control, the measured TM not following the MP distribution because of remaining correlations; the laws predicted in Appendix B.3 does not match exactly the experimental data. Nevertheless the scalings in  $1/\sqrt{\gamma}$  still holds. A possible explanation requiring a deeper investigation could be the the existence of correlations, because the singular value variance differs from the Marchenko-Pastur one due to the relatively large illumination spot [Popoff et al. 2014; Hsu et al. 2017]. Another observable feature is the fact that the more asymmetric the TM is (large  $1/\sqrt{\gamma}$ ), the closer the first singular vector and the global-focusing enhancements are. In the limiting case where the output reduces to one single CCD pixel both are expected to be the same. A way to evaluate how similar are the global focusing and the different singular vectors is to compute their correlations. The field correlation between two vectors  $V_1$  and  $V_2$  is given by

$$C(V_1, V_2) = \frac{V_1^\dagger V_2}{\sqrt{V_1^\dagger V_1 V_2^\dagger V_2}} = \frac{V_1^\dagger V_2}{\|V_1\|_2 \|V_2\|_2}, \quad (4.1)$$

where  $\dagger$  represents the transpose conjugate. In Fig. 4.6(b) the correlations for vectors associated to the two colored arrows of Fig. 4.6(a) are presented. The strong correlation between the global-focus vector and the first singular vector explain the close enhancement values observed.

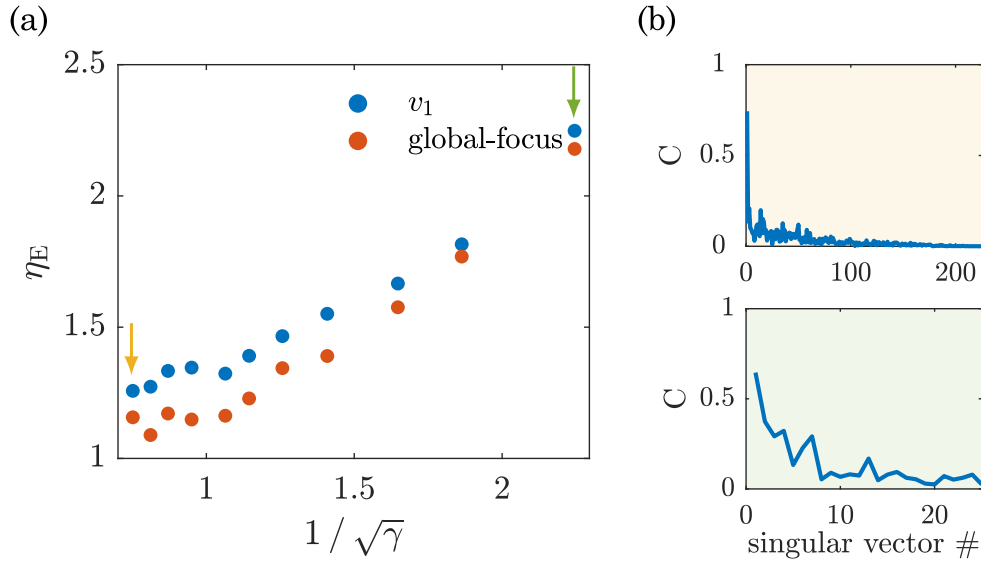


Figure 4.6: **Amplitude enhancement comparison between the first singular vector and the global-focus for a TGTM.** (a) Field amplitude enhancement  $\eta_E$  for the first singular vector ( $v_1$ , blue dots) and the global-focus (orange dots) for different values of  $\gamma$ . (b) Absolute value of the correlation between the singular vectors and the global-focus for two extreme degrees of control marked by the colored arrows.

### 4.3.3 Enhancement for different delays with a single phase mask

It was already mentioned in [Sec. 4.2.2](#) that summing the focusing masks to focus on several spatial temporal times was possible. In this section we show that it can also be achieved with the SVD. Consider a TRTM presented in [Fig. 4.7\(a\)](#). From it, three TGTMs, measured for  $\tau_1$ ,  $\tau_2$  and  $\tau_3$ , are selected. The individual SVDs of the TGTMs are performed, leading to three sets of singular vectors. We select the first singular vectors of each set ( $v_1^{(\tau_1)}$ ,  $v_1^{(\tau_2)}$  and  $v_1^{(\tau_3)}$ ) and sum them together to obtain another vector  $v_1^{(\tau_1, \tau_2, \tau_3)}$  [Fig. 4.7\(b, top\)](#). The first singular vector of the middle delay TGTM is also selected for comparison [Fig. 4.7\(b, bottom\)](#). The two vectors ( $v_1^{(\tau_1, \tau_2, \tau_3)}$  and  $v_1^{(\tau_2)}$ ) are then successively displayed on the SLM and the temporal fields are measured by scanning the delay-line. The profiles obtained are plotted in [Fig. 4.7\(c\)](#) together with a plane wave input as reference. One can see that the mask summing technique works to enhance the energy at different delays in the pulse. It is also noticeable that the demultiplication of the controlled delays comes with the cost of a reduced enhancement for the individual times. This is well visible when comparing the enhancement obtained at  $\tau_2$  when only controlling this delay (blue curve) or when controlling this delay among others (orange curve).

It is very important to keep in mind that for the experiment presented, the SVD was performed on the individual TGTMs and that the sum of the vectors was performed afterward, leading to the input vector  $v_1^{(\tau_1, \tau_2, \tau_3)}$ . Another workaround would have been to first sum the TGTMs and then compute the SVD of the resulting matrix, the obtained vector would have been  $v_1^{(\tau_1 + \tau_2 + \tau_3)}$ . The second approach, and all its implications, will be the subject of the [Chap. 5](#). To follow with this chapter, we will focus now on the differences between TGTMs measured for different delays.

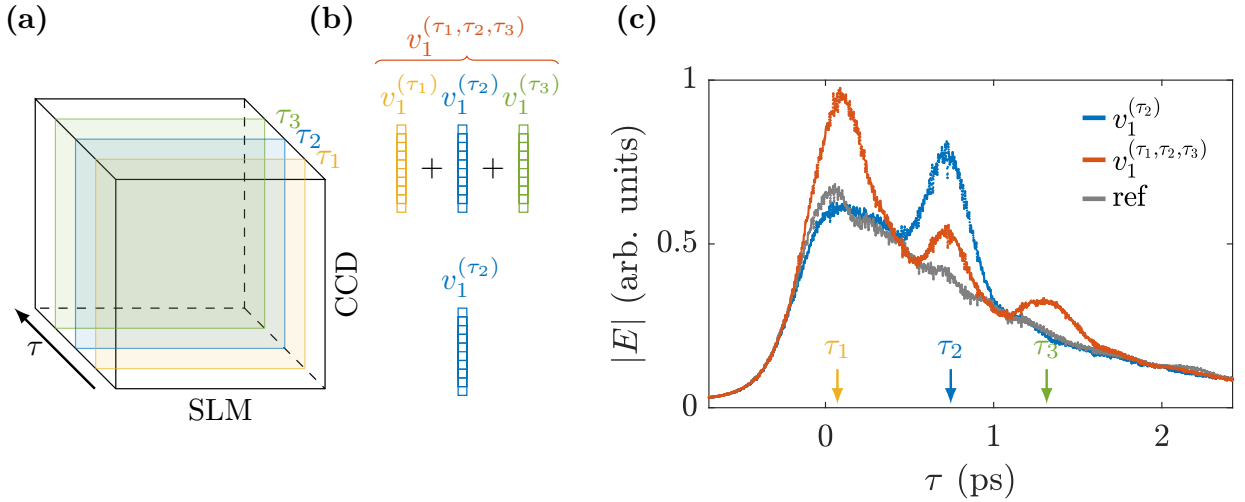


Figure 4.7: **Controlling several delays with one phase mask.** (a) Three TGTMs of the full TRTM are measured for delays  $\tau_1$ ,  $\tau_2$  and  $\tau_3$ . (b) The phase mask to display on the SLM for enhancing the energy delivery at  $\tau_1$ ,  $\tau_2$  and  $\tau_3$  is the phase of  $v_1^{(\tau_1, \tau_2, \tau_3)}$  obtained by summing the first singular vectors of the TGTMs measured for these specific delays. (c) Field amplitude measured for  $v_1^{(\tau_2)}$  (blue),  $v_1^{(\tau_1, \tau_2, \tau_3)}$  (orange) and an input plane wave (gray).

#### 4.3.4 Evolution of the control over the pulse

So far, in every experiment presented, (except for [Sec. 4.3.3](#)), the TGTMs were measured in the middle of the pulse. This choice was made in order to present clear results (peaks with good enhancements and well separated from the initial peak of the pulse). However all effects presented can be theoretically performed whatever the targeted delay  $\tau_0$  is. To illustrate this point, a set of TGTMs (with  $\gamma \sim 0.4$ ) is measured for a range of delays, their SVDs are performed and the field is measured when sending the first ( $v_1$ ) and the last ( $v_{225}$ ) singular vectors. The measured enhancements<sup>1</sup> are reported in [Fig. 4.8\(a\)](#): blue dots for the first singular vector ( $v_1$ ) and orange dots for the last one ( $v_{225}$ ). The (unscaled) gray pulse is present to visually help associate delays with the pulse shape. It is noteworthy that the enhancement is relatively flat until delays of 2.5 ps, where smooth evolution towards 1 is observable (a decrease for the first singular vector and an increase for the last singular vector). At long delays enhancements are no longer observed. Such a behavior was already observed for spatio-temporal focusing either with the TM or with optimization [[Aulbach et al. 2011](#); [Mounaix et al. 2016a](#)]. This lack of efficiency in the control for late times was attributed to noise. On the tail of the pulse light from non-controlled delays indeed predominates, restraining an accurate measurement of the TM or accurate setting of the optimized phase. Our experiments confirm these findings. Moreover we present in [Fig. 4.8\(b\)](#) and [Appendix A.4](#) a simple method to help knowing, from a TM, if the measurement was good or subjected to noise. The idea is as follows: when a field extraction is not subjected to noise the phase histogram of the TM should be uniform. However in case of noise one can observe oscillations for the TM in the canonical basis. This is well visible in [Fig. 4.8\(b\)](#) around  $-0.5$  ps: before the pulse the noise leads to a measured TM with peaked phase histograms while when signal is present the TM phase histogram is flatter. Increasing the number of phase steps used to extract the field and measure the TM helps reaching better extractions. This is the reason why, even though 4 phases are usually enough in the middle of the pulse to measure a TM I present here TMs measured with 10 phases. This allows the comparison

<sup>1</sup>Corrected from TM/peak positions mismatch, see [Sec. 4.3.5](#).

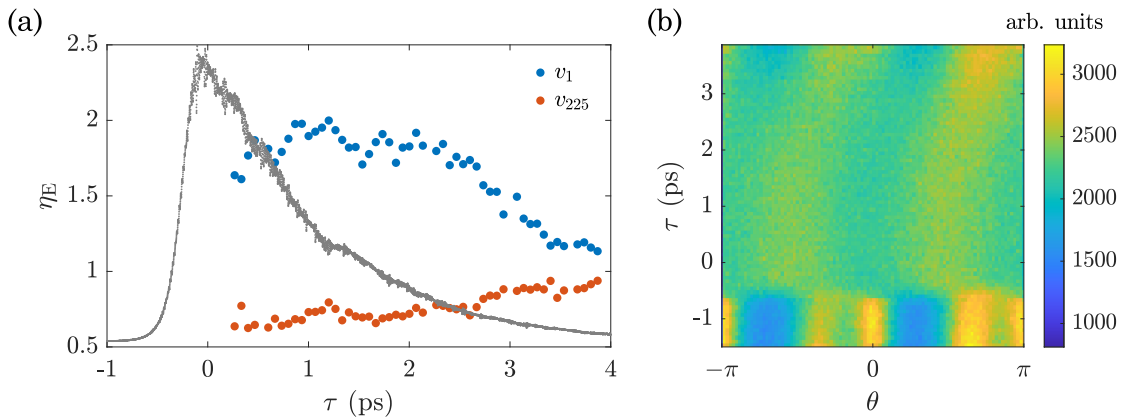


Figure 4.8: **Evolution of the enhancement along the pulse.** (a) Evolution of the enhancements of the first singular vector ( $v_1$ , blue dots) and the last singular vector ( $v_{225}$ , orange dots) for different delay times. For this experiment  $\gamma \sim 0.4$ . As a visual aid the plane wave output pulse is also displayed (arbitrary units, gray). Individual TGTMs have been measured with 10 phase steps per mode (instead of the usually 4 used) to reduce measurement noise in the pulse tail. (b) Image of the phase histograms of the different TGTMs. When noise predominates the phases are no longer uniform in the  $0-2\pi$  range but peaked.

of enhancements in a longer range of delays.

A method that could be employed to avoid signal issues in the pulse tail could be to tilt one of the beams (either the probe pulse or the scattered beam) to perform off-axis holography [Cuche et al. 2000]. Due to the introduced angle, the interference pattern changes to form fringes. The information on the first order can be extracted from the interference images with Fourier transform. However this technique comes with a loss of resolution, due to the need to resolve the fringes inside one speckle grain.

Apart from the noise issue mentioned above, no drastic enhancement difference were observable between TGTMs measured at different delays in the pulse. I will however discuss in the next section an enhancement behavior that is only detectable when studying TGTMs at early and late times.

### 4.3.5 Shift of the enhanced delay

For the data presented in Fig. 4.8(a), we measure the enhancement at the peak position. In most cases this extraction coincides with measuring the enhancement at the delay where the TGTm is measured. However some discrepancy are observable. It is well visible when plotting the pulse shapes obtained when sending the first singular vector and comparing to the TGTm position  $\tau_0$  represented by vertical dashed lines in Fig. 4.9(a). For early times the amplitude rise induced by the first SVD input is positioned at a delay  $\tau_0^+$  slightly larger than  $\tau_0$  (blue curve). For middle times no such a behavior is observable and the amplitude peak is situated at  $\tau_0$  (green curve). For late times, the peak position is not observed at  $\tau_0$  but for a shorter delay  $\tau_0^-$  (orange curve). The trend observed for three delays in Fig. 4.9(a) is systematic. In Fig. 4.9(b) the absolute value of the peak shift is presented as a function of the TGTm position  $\tau_0$ . A possible interpretation of this shift comes from the TM measurement. Because the measurement is realized using a non-Dirac temporal gate the information gathered on the TGTm does not include the single delay  $\tau_0$  but also neighboring delays (the peak width also being a consequence). Thus one could imagine a small temporal freedom for enhancing the field amplitude. In the middle of the pulse  $\tau_0^+$  and  $\tau_0^-$  are equivalent, no deviation is

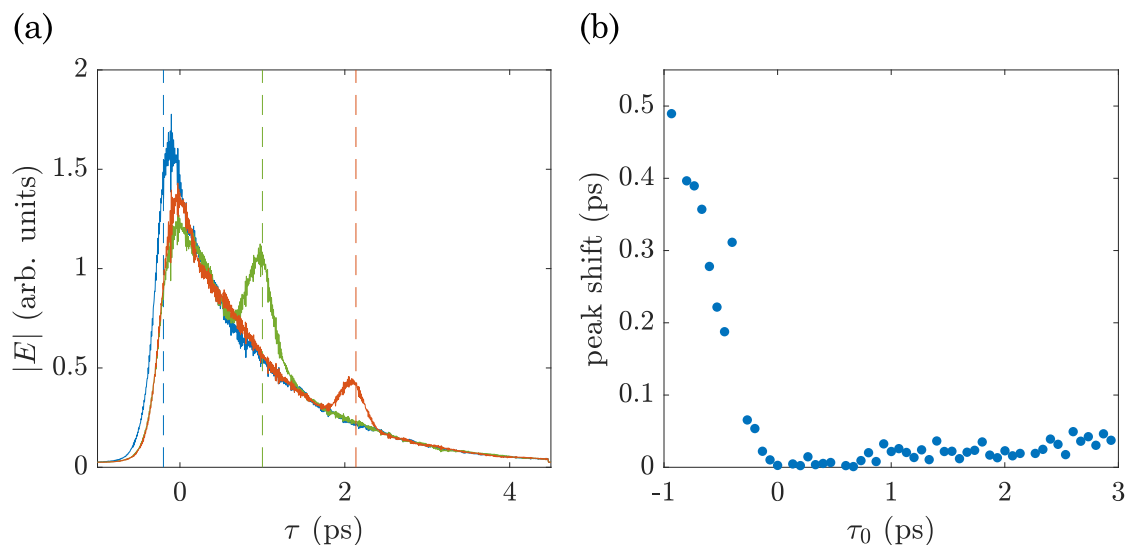


Figure 4.9: **Shift of the enhanced delay.** (a) Pulse shape for first singular vectors for three different delays: an early time (in the pulse peak rise, blue), an intermediate time (middle of the pulse, green) and a late time (pulse tail, orange). The delay for which the TGTm was measured is marked with the colored dashed lines. The enhanced peaks do not always coincide. At early times the increase is shifted to the later times hence at late times the peak is shifted to the earlier times. In both cases this corresponds to a shift in direction of the center of the pulse. In middle times no clear shift is visible. (b) Plot of the peak shift absolute value along the pulse.

observed. This is no longer the case at early or late times where energy enhancing is stronger where energy is naturally high.

#### 4.4 Temporal speckle grain size control

Because most of phenomena observed translate from the monochromatic regime to the pulse regime, one could wonder if this is also valid for the speckle grain size engineering presented in Sec. 3.2. To investigate this point the experimental conditions are set as in Sec. 3.2 (i.e. collection microscope objective moved away from the sample output plane) with non-uniform speckle patterns  $k$ -spaces. An induced SVD wavevector selectivity is therefore expected. An oversampled TGTm of size  $225 \times 1024$  is measured at  $\tau_0 = 1.1$  ps and its SVD is performed. The phase approximation of two different ( $v_1$  and  $v_{121}$ ) singular vectors is displayed successively on the SLM and the associated fields are extracted all along the pulse. The speckle grain size is then measured and plotted as a function, of the delay in Fig. 4.10.

One observes an enhanced grain size around 1.1 ps for the singular vector  $v_1$  (blue dots) while a decrease for the singular vector  $v_{121}$  (orange dots). Both plotted grain sizes are relative to the reference grain size: for each delay  $\tau$  the speckle grain size is divided by the one obtained for a plane wave input pulse.

All the results presented are realized under very partial control. Even though the degree of control  $\gamma$  is lower than 1, the TM is well approximated by a random matrix. It would be interesting to investigate the temporal effects of a more controlled system. Simple simulations, by adding unitarity constraint to the generated random TM, lack the temporal information, which shows that a more elaborated scheme is required. Simulation results with a waveguide geometry are presented

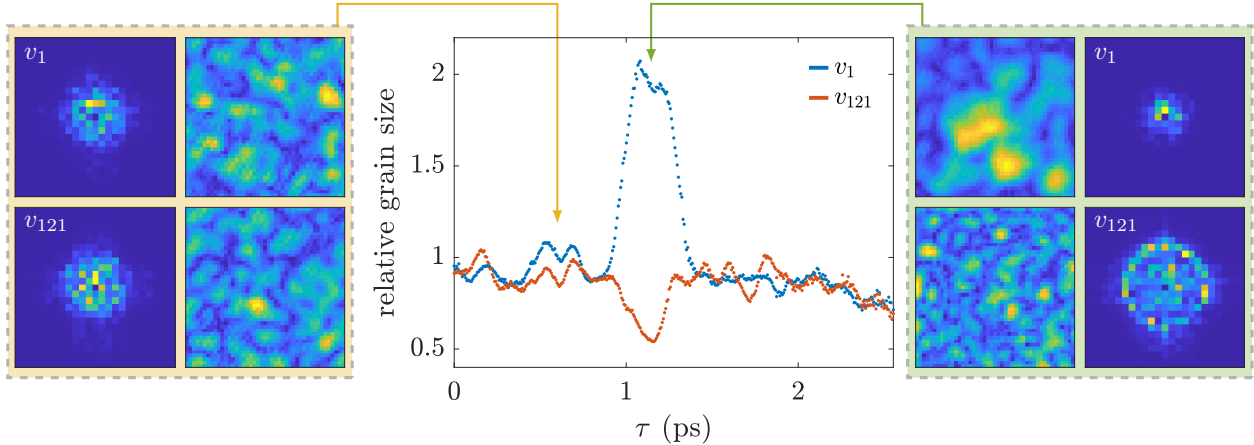


Figure 4.10: **temporal control of the grain size.** Temporal evolution of the speckle grain size along the pulse when displaying on the SLM the phase of two singular vectors:  $v_1$  (blue) and  $v_{121}$  (orange). The experimental configuration is such that the measured speckle have non-uniform  $k$ -space. For each delay  $\tau$  the measured grain size is normalized using the plane wave input pulse.

in the next section.

## 4.5 Time gated transmission matrix on a waveguide

To complement experimental results presented above I will discuss in this section some simulation results obtained in a waveguide geometry. These results were obtained by Jakob Melchard, Matthias Kühmayer and Stefan Rotter from the Institute for Theoretical Physics at Vienna University of Technology. I will first present the simulation itself in [Sec. 4.5.1](#) and the results in [Sec. 4.5.2](#).

### 4.5.1 Simulated geometry and protocol

#### 4.5.1.1 Geometry

For the simulations one seeks at a simple but realistic geometry. Differences from the experimental paint slab are worthwhile to test the robustness of experimental observations. For these reasons a 2D waveguide system is well suited. Such technique has already been used to complement experimental results [[Davy et al. 2021](#)]. The waveguide, whose dimensions ( $L = W/10$ , where  $L$  is the length and  $W$  the width) enable the propagation of 50 to 100 modes for the incoming frequencies of the pulse, is filled with obstacles (sphere with radi of  $W/100$ , filling fraction of 0.4) materialized by local refractive index mismatches ( $n_{\text{scatt}} = 3.5$ ), see [Fig. 4.11\(a\)](#).

#### 4.5.1.2 From spectral to temporal information

The stationary Helmholtz equation is solved for the set of targeted input wavelengths<sup>2</sup>. For each wavelength a monochromatic TM is calculated (one hence obtains a MSTM). It is noteworthy that the number of propagating modes (and hence the size of the different monochromatic TMs) depends on the input frequency due to the waveguide's dispersion relation. However only the modes that can propagate for all frequencies are kept for calculations (50 lowest ones in the result presented). This is done in order to only address modes that propagates for all input frequencies and avoid

<sup>2</sup>A similar approach is employed in [[Durand 2020](#)].

transmission artifacts due to the presence of non-propagating modes. A Fourier transform of the MSTM then enables to obtain the time resolved information<sup>3</sup> as in [Carpenter et al. 2016; Xiong et al. 2019; Mounaix et al. 2019] and illustrated Fig. 4.11(b).

#### 4.5.1.3 Definition of $\tau = 0$

To match the experimental zero-delay position, the temporal scale in the simulation is shifted such that  $\tau = 0$  corresponds to the time when the input pulse exits the scattering medium. The time when the pulse enters the scattering medium is well defined. To obtain  $\tau = 0$  we add to the entrance time the propagation delay. The latter is evaluated through the waveguide dimensions, effective refractive index and mean group velocity.

#### 4.5.1.4 Calculation of the output field

From the temporal information gathered one can extract the matrix corresponding with single delay (here we selected  $\tau_0$  around 1.1 ps), perform its SVD and compute the propagation in the waveguide for specific inputs. The temporal output field is computed based on the knowledge of the waveguide monochromatic response and the input modes. In the experiments, the field amplitude evolution averaged over all output positions is plotted as a function of the delay. We will discuss these temporal evolutions, presented in Fig. 4.11(c) in the following section.

### 4.5.2 Results

From the output field calculated one can extract the average amplitude temporal profile. The latter is presented Fig. 4.11(c). The solid gray line represents the reference profile (obtained when injecting a set of random inputs), the blue curve represents the output associated to the first singular vector ( $v_1$ ) and the orange curve represents the output of the last singular vector ( $v_{50}$ ). Both solid lines are associated to the phase and amplitude control, while dotted lines represent phase-only outputs.

To interpret Fig. 4.11(c) and allow a comparison with experimental results, it is important to stress the similarities and differences to the experiment. In the experiments the medium's number of modes is around five order of magnitude higher than the number of modes controlled, while in the simulations we can approach full control. From the waveguide TM we only keep the 50 lowest modes, corresponding to the ones existing for all injected frequencies, thus reaching above 50% of control. Also the aspect ratio of the TGTM gives  $\gamma = 1$ : unlike for experiments, to observe a significant effect, compensating the lack of control by drastically reducing  $\gamma$  (leading to non-square TMs) is not necessary. The pulse shapes obtained show a similar behavior as experiments, with a good agreement in the case of phase-only control. Not surprisingly the phase and amplitude control gives better enhancements results at  $\tau_0$ .

Two main observations are worth discussing. Firstly, it is instructive to note that the difference between phase-only and phase and amplitude is relatively small for the first singular vector, advocating for the interest of phase-only experimental use (also visible in random matrix simulations). The second observation relates to the transmission cancellation at  $\tau_0$  for the last singular vector with phase and amplitude control: a sufficient amount of control yields what could be reminiscent of a closed channel in time. This finding is consistent with the results of [Mounaix et al. 2019] where a close cancellation of the field was observed in multimode fibers. Also a major difference with the experiments is energy conservation. It is not valid in experiments due to the open geometry, but it

---

<sup>3</sup>The opposite approach i.e. measuring a temporal response to reach spectral aspects is also used [Sprik et al. 2008; Gérardin et al. 2014] but in acoustic not optics.

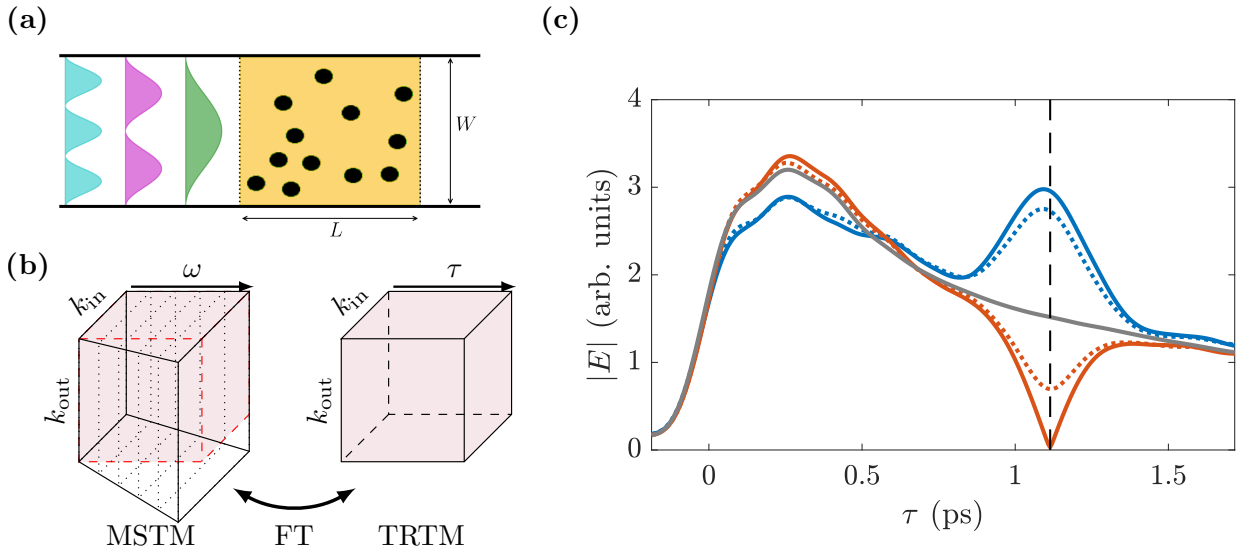


Figure 4.11: **Pulse propagation control on a waveguide.** (a) Schematic of the waveguide geometry. In this specific simulation the dimensions are  $W = 1$ ,  $L = W/10$ . The radius of a scatterer is  $W/100$ , its refractive index  $n_{scatt} = 3.5$  and the filling ratio 0.4. (b) The MSTM is measured for a set of input frequencies and only the modes propagating for all frequencies are kept. A Fourier transform (FT) is performed to get the TRTM. (c) Averaged amplitude evolution for random inputs (gray), for the first singular vector (blue) and for the last ( $v_{50}$ , orange) of the TGTM at 1.1 ps (indicated by the vertical dashed line). Solid lines represent phase and amplitude control while dotted lines represent phase-only control. The results are averaged over 10 realizations of disorder.

holds in the waveguide. This fact is not clearly visible in Fig. 4.11(c) as only the transmitted part is presented, omitting the reflection.

With Fig. 4.11(c), it is interesting to see that experimental results can be qualitatively reproduced with a waveguide simulation. The control over limitations introduced (e.g. reduced amount of control, phase-only constraint) could help better distinguish intrinsic effects from measurements limitations.

## 4.6 Take home message

In this chapter I presented some of the temporal aspects observable with the setup. A time-gated measurement enables to directly and easily measure TGTM for specific delays in the pulse. Most of the results obtained in monochromatic remain valid and acquire a temporal dimension. It is thus possible to realize spatio-temporal foci (even a global-focus), to have a temporal control of the energy delivery with the singular vectors of the TGTM, and even to extend the speckle grain size control. A linear combination of vectors allows to extend the control to multi-times. All effects are temporally localized where the TM is measured and their efficiency strongly depends on the quality of the TM measurement (thus harder to perform in the pulse tail). The simulation of a waveguide system enables to reach degrees of control that are unreachable experimentally. The results obtained support the experimental observation. The addition of the phase and amplitude control allows to reach states cancelling transmission for a given delay.

# 5 | Singular value decomposition as a correlation generator tool

---

5.1	Speckle correlations, a valuable tool . . . . .	171
5.1.1	Importance of the correlations . . . . .	171
5.1.2	TM-based operators to engineer field correlations . . . . .	172
5.1.3	An idea along the same lines . . . . .	173
5.2	SVD-based correlations and temporal illustration . . . . .	175
5.2.1	Modifications to the experimental geometry . . . . .	175
5.2.2	Observation of the effect . . . . .	176
5.2.3	Playing with the effect . . . . .	178
5.2.3.1	Controlling correlations for varied spaced matrices . . . . .	178
5.2.3.2	Extension to more than two matrices . . . . .	179
5.2.4	Importance of the transmission matrices coupling . . . . .	179
5.2.5	Correlation variation with the singular vectors . . . . .	181
5.3	A general concept not restricted to temporal aspects . . . . .	184
5.3.1	Multi-wavelength correlation . . . . .	184
5.3.2	Spatial correlation . . . . .	185
5.3.3	Comparison of some TM-based operators . . . . .	186
5.4	Cross-effects . . . . .	187
5.4.1	Time and frequency two conjugated variables . . . . .	188
5.4.2	Global phase between the two transmission matrices . . . . .	189
5.4.3	Mixing transmission matrices measured in different regimes . . . . .	190
5.5	Take home message . . . . .	191

---

This chapter is dedicated to the creation and control of speckle correlations. We present in [Sec. 5.1](#) a method similar to TM-based operators relying on the SVD of the sum of several TMs. The generality of the concept enables to correlate speckles for different delays in the pulse ([Sec. 5.2](#)) but also for different wavelengths or for different spatial areas ([Sec. 5.3](#)). Finally we present hybrid effects taking advantage of the time to frequency Fourier relation ([Sec. 5.4](#)).

## 5.1 Speckle correlations, a valuable tool

In this section we discuss the importance of speckle correlations and we present some operators based on the TM allowing their control. We conclude by introducing the method which is extensively studied in this chapter.

### 5.1.1 Importance of the correlations

The content of [Chap. 3](#) and the various work reported, illustrate the long-term efforts dedicated to control correlations and statistics of speckles. Because scattering appears as a major threat for imaging, one may want to exploit speckle correlations to improve imaging techniques. Thus, understanding light propagation and harnessing all possible types of MEs becomes essential. For instance the SIM (structured illumination microscopy) technique [[Gustafsson 2000](#); [Mudry et al. 2012](#)] can achieve twice the optical resolution of a conventional technique at the cost of knowing the illumination patterns. Knowledge on the illumination pattern can be reached thanks to ME which is extensively exploited for optical imaging [[Osnabrugge et al. 2017](#); [Bertolotti et al. 2012](#); [Yilmaz et al. 2015](#)]. However ME applies with a limited range. Techniques have been developed to increase the ME range [[Kadobianskyi et al. 2018](#); [Chen et al. 2019](#); [Jang et al. 2018](#)] each time by regulating propagation possibilities, without external control. To overcome this limitation, reconfigurable metamaterials are used [[Arruda et al. 2018](#)] to externally control the ME. But engineering at will the ME for every material remains a promising yet challenging prospect. One possible approach is to accept not having a broad range ME, but a rather selective one. This has been achieved by adequately using scattering informations contained in the TM.

### 5.1.2 TM-based operators to engineer field correlations

The TM information already has been extracted, for instance, through the construction of the WS operator. The latter, discussed in [Sec. 1.5](#), grants access to dispersion free states [[Fan et al. 2005](#)] and thus gives, after a scattering medium, speckle patterns that are resilient to small frequency variations. This was clearly observed in MMFs [[Xiong et al. 2016](#)]. The WS operator can be generalized to any set of two conjugated variables: time and frequency for the original version of the WS or position and momentum in [[Ambichl et al. 2017a](#)]. Also generalized to a discretized version, WS operator can even extend correlations to two arbitrarily spaced frequencies [[Ambichl et al. 2017b](#)] illustrating the increased correlation possibilities when setting aside the broad range control. This last prospect is a key-point used to customize the ME to obtain correlations with any arbitrary input and output tilt angles and directions [[Yilmaz et al. 2021](#)], see [Fig. 5.1\(a\)](#). The authors introduce an angular memory operator,

$$Q(\theta_i, \theta_0) = (T^\dagger T)^{-1} T^\dagger R^\dagger(\theta_0) T R(\theta_i), \quad (5.1)$$

where  $R$  is a rotation operators and  $\theta_{i,o}$  the input and output angles.

The creation of this operator answers a specific problem (here angular correlations). Another example of construction of TM-based operator is presented in [[Pai et al. 2021](#)]. The authors try to access “scattering invariant modes” which have the particularity of appearing to propagate through any medium like through air, see [Fig. 5.1\(b\)](#). Computing those modes requires knowing TMs, as they are defined by the eigenvalue problem

$$T_{\text{air}}^\dagger T_s X_n = \alpha_n X_n, \quad (5.2)$$

where  $T_{\text{air}}$  and  $T_s$  are TMs of respectively the air and the medium and where  $X_n$  is an eigenvector associated to the eigenvalue  $\alpha_n$ . Similarly to [[Yilmaz et al. 2021](#)], finding the modes of interest corresponds to calculating the eigen-modes of a TM-based operator.

All previous operators discussed have in common that the TMs depend on one varying parameter (e.g. the frequency, the spatial position, the angle). Informations are gathered for two fixed values of this parameter and the TMs are coupled by the operator.

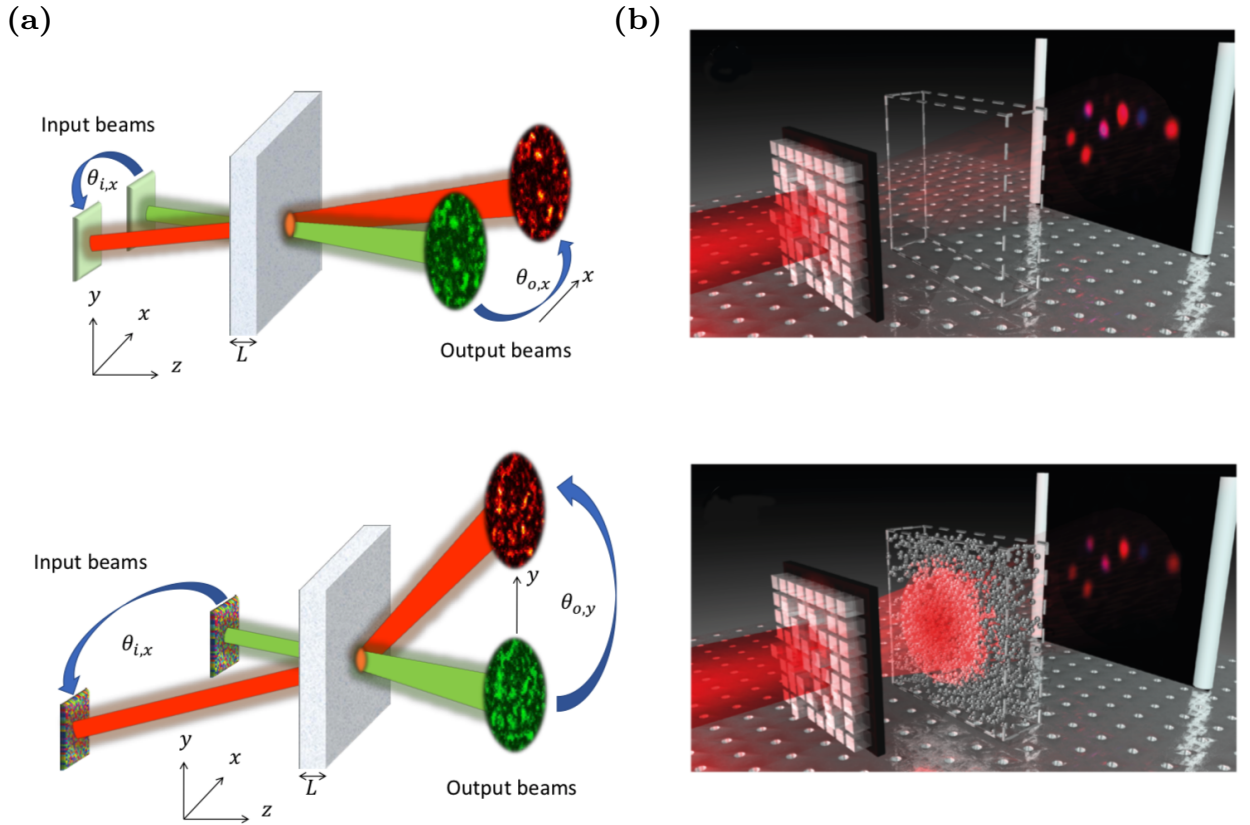


Figure 5.1: **Some TM-based operators.** (a) Illustration of the customized ME: conventional angular memory effect (top) and customized angular memory effect (bottom). Figure from [Yilmaz et al. 2021]. (b) Scattering invariant modes: light propagation through air (top) and same propagation but through a scattering medium (bottom). Figure from [Pai et al. 2021].

### 5.1.3 An idea along the same lines

Following the direction of enquiry presented in Sec. 5.1.2 we will start addressing the following question: is there an input vector  $X$ , that one could for instance send on a SLM, such that the output fields obtained from propagation, varying one given parameter, are the same, *i.e.*  $T_1 X = T_2 X$ ?

One way of determining  $X$  is to study<sup>1</sup>  $(T_1 - T_2)X = \mu X$ . Because matrices are not necessarily square, one need to study the SVD of<sup>2</sup>  $T_1 - T_2$ . In a more general frame we will study the problem  $(T_1 + e^{i\alpha} T_2)X = \mu X$ , where the relative global phase between the TMs could be varied (retrieving the initial combination for  $\alpha = \pi$ ).

## 5.2 SVD-based correlations and temporal illustration

In this section I present an illustration of the idea of SVD-based correlations. The temporal delay is chosen to be the TM parameter of interest. Hence the laser is set to pulse mode and we measure TGTMs. I first illustrate in Sec. 5.2.2 the principle described above (Sec. 5.1.3). Then, in Sec. 5.2.5,

<sup>1</sup>It is noteworthy that the case  $T_2^{-1} T_1 X = \mu X$  corresponds to [Pai et al. 2021].

<sup>2</sup>Reminiscent of the discrimination operator introduced in [Bouchet et al. 2021b].

I present a model to obtain analytical predictions of the correlations. This model is confronted to experiments and simulations.

### 5.2.1 Modifications to the experimental geometry

Before describing the experiments themselves, I will briefly mention the experimental differences with [Chap. 3](#) and [Chap. 4](#). First the sample used is thicker due to the need of having a longer temporal tail. It is still a TiO<sub>2</sub> layer suspended on a cover slip, but the transmittance is now of  $T \sim 0.16$  for approximatively the same scattering mean free path ( $\simeq 10 \mu\text{m}$ ). The illumination microscope objective is now focused on the scattering medium and the collection microscope objective is not moved away from the medium leading to a smaller speckle blob size. Thus, the averaging on the disorder realizations is now performed by manually moving the sample to illuminate another area. These modifications are associated to a change in the optics imaging the SLM on the back aperture of the illumination microscope objective. These modifications aims at optimizing the control over the different SLM modes. However it comes with the cost of a system NA reduction, responsible for a slightly lower transmission for random inputs than for plane waves, mainly visible in [Fig. 5.11](#). Also, we bin all images that are acquired (similarly to the binning for TM measurements) in order to limit equally all Fourier spaces (i.e. not having in the correlated images a better resolution than in the TM).

### 5.2.2 Observation of the effect

To illustrate the approach, we measure two TGTMs  $T_1$  and  $T_2$  with  $N_{\text{CCD}} = 529$  and  $\gamma \sim 1$  for respective delays  $\tau_1 = 0.9 \text{ ps}$  and  $\tau_2 = 1.7 \text{ ps}$ . We normalize them<sup>3</sup> and compute their difference. We calculate the SVD of  $T_1 - T_2$  which gives access to a set of singular vectors  $v_i^{(\tau_1 - \tau_2)}$ , see [Fig. 5.2\(a\)](#). To best meet the  $\mu = 0$  condition and reach  $T_1 X = T_2 X$ , the last singular vector  $v_{225}^{(\tau_1 - \tau_2)}$  (associated to the smallest singular value which is of about 2 here) is displayed, or rather its phase-only approximation, on the SLM and modulates the input phase. We measure the field at the output for  $v_{225}^{(\tau_1 - \tau_2)}$  and for a plane wave input by scanning the delay-line. The averaged amplitudes are presented in [Fig. 5.2\(b\)](#) with a solid green curve for  $v_{225}^{(\tau_1 - \tau_2)}$  and a solid gray curve for the plane wave input. No clear amplitude variation is visible. Binned fields amplitude at  $\tau_1$  and  $\tau_2$  with  $v_{225}^{(\tau_1 - \tau_2)}$  for input are represented in insets. No obvious similarity is observable. To highlight correlations a calculation is required. We thus correlate the output fields using the field correlation formula [Eq. 4.1](#), recalled below:

$$C(V_1, V_2) = \frac{V_1^\dagger V_2}{\sqrt{V_1^\dagger V_1 V_2^\dagger V_2}} = \frac{V_1^\dagger V_2}{\|V_1\|_2 \|V_2\|_2}, \quad (5.3)$$

where  $V_1$  and  $V_2$  are two complex vectors and  $\dagger$  represents the transpose conjugate. For the experiment the fields for all delays are correlated with the field measured at  $\tau_1$  (resp.  $\tau_2$ ). For the singular vector input it leads to the yellow curve (resp. red curve) in [Fig. 5.2\(c\)](#) top part and denoted  $C_{\tau_1}$  (resp.  $C_{\tau_2}$ ). Only the correlations with  $\tau_1$  are plotted for the plane wave input ( $C_{\tau_1}^{\text{ref}}$ ), for the figure clarity's sake.

Let us describe the plot for  $C_{\tau_1}$ , as the same observations hold for  $C_{\tau_2}$ . The reference field is naturally correlated with itself at  $\tau_1$ , however no correlations are visible for other non-neighboring times. At  $\tau_1$  the same correlation is visible for the singular vector while another correlation increase emerges at  $\tau_2$ . Therefore, to only see non expected correlations, we normalize  $C_{\tau_1}$  by  $C_{\tau_1}^{\text{ref}}$ : we plot

<sup>3</sup>The TMs are normalized by their total intensity to ensure both having the same weight in the sum. For TGTMs measured at two different delays the delay-dependent transmission indeed leads to TMs with different norms.

in Fig. 5.2(c) bottom part the difference of their absolute values. It is then well visible that the fields at  $\tau_1$  and  $\tau_2$  are correlated. In order to display the full non-redundant correlation information (the correlation information  $C_{\tau_1}(\tau_2)$  and  $C_{\tau_2}(\tau_1)$  is indeed the same) a 2D-correlation plot is proposed in Fig. 5.2(d). We display the absolute value of the correlation between two delays  $\tau$  and  $\tau'$  with a color map while the position along the axes is given by  $\tau_0 = (\tau + \tau')/2$  and  $\delta\tau = |\tau - \tau'|$ . On that plot one sees a correlation increase at  $((\tau_1 + \tau_2)/2 = 1.3 \text{ ps}, \tau_2 - \tau_1 = 0.8 \text{ ps})$ .

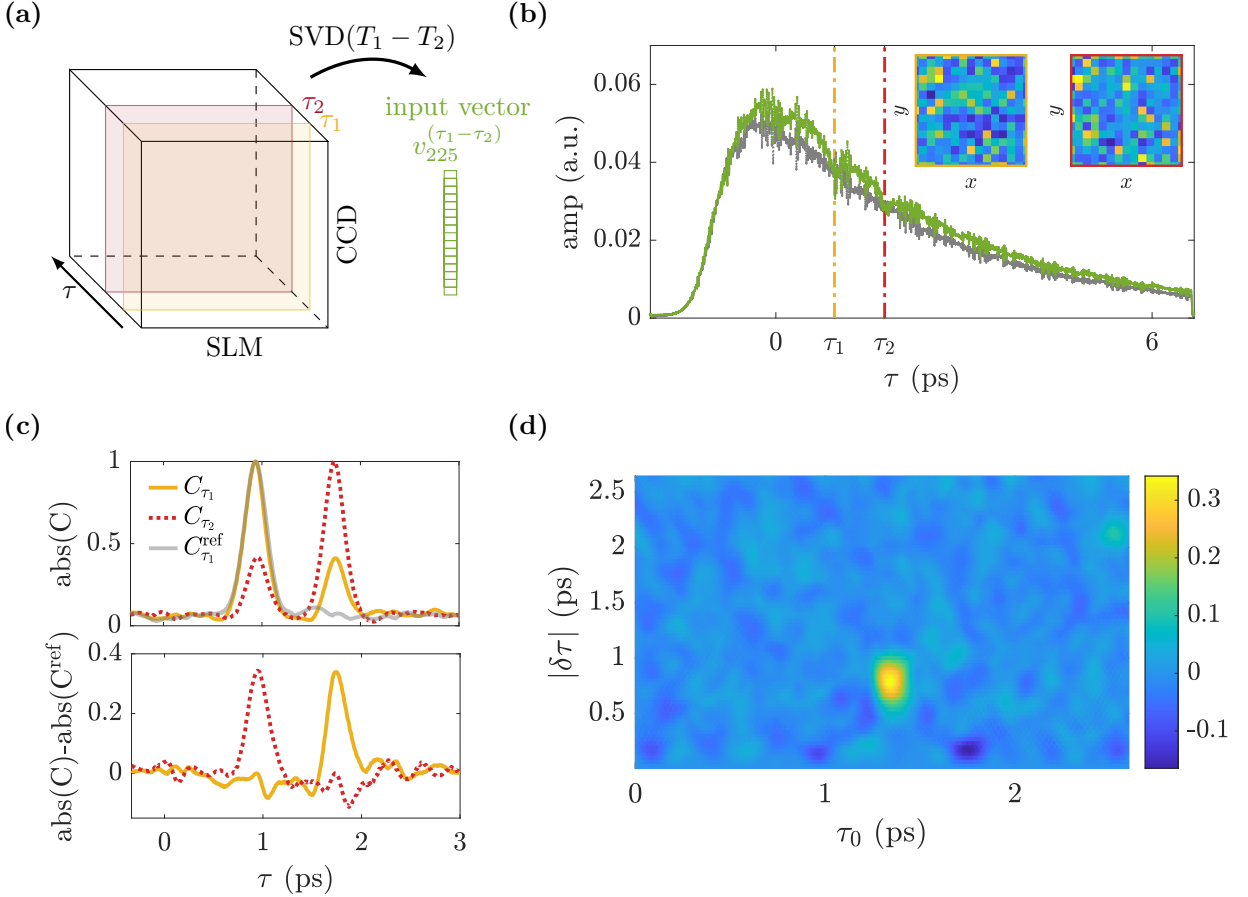


Figure 5.2: **Procedure and observation of the field correlation between two delays.** (a) We measure two TGTMs  $T_1$  and  $T_2$  for two delays  $\tau_1$  and  $\tau_2$ . We subtract subtracted them, calculate their SVD and extract the last singular vector  $v_{225}^{(\tau_1 - \tau_2)}$ . (b) Averaged pulse when sending  $v_{225}^{(\tau_1 - \tau_2)}$  (green curve) and for a plane wave input (gray). The insets represent the binned fields amplitude for  $\tau_1$  and  $\tau_2$  identifiable by the colored surrounding. (c) Absolute value of the field correlation. Top: Correlations measured with  $\tau_1$  when sending  $v_{225}^{(\tau_1 - \tau_2)}$  (yellow solid line) and with  $\tau_2$  for the same input (red dotted line). The gray solid line represents the correlation with  $\tau_1$  for the plane wave input. Bottom: Normalized correlations. For each delay, the absolute value of the correlation for the plane wave input is subtracted to the one corresponding to the  $v_{225}^{(\tau_1 - \tau_2)}$  input. (d) 2D-correlation plot, containing the full non redundant information. The correlation value is associated to a colormap and the axes are such that  $\tau_0 = (\tau + \tau')/2$  and  $|\delta\tau| = |\tau - \tau'|$ . The data are averaged over 4 disorder realizations.

From this experiment, a natural question is whether one could have simply obtained the field correlation by summing the individual singular vectors as done in Sec. 4.3.3. Also does only the correlation emerge for the singular vector associated with the singular values close to zero? Does

the field correlation happens at the expense of the amplitude control? To verify these points we performed additional experiments, that we now detail.

### 5.2.3 Playing with the effect

To test the robustness of the correlation effect we monitor some modifications: the impact of taking other singular vectors, the impact of the value of  $\alpha$  (global phase between the two TGTMs), the impact of the delays spacing between the TGTMs and the impact of summing more than two TGTMs. For the sake of brevity here we present only two examples containing more than one variation.

#### 5.2.3.1 Controlling correlations for varied spaced matrices

Here we measure a set TGTMs ( $N_{\text{CCD}} = 225$  and  $\gamma \sim 0.35$ ) for different delays and sum two by two the matrices. The obtained correlations are presented in Fig. 5.3, where the delay spacing between the two summed TGTMs is varied ( $\delta\tau = 0.4, 0.8, 1.6$  and  $3.2$  ps) keeping the central position fixed ( $\tau_0 = 2.7$  ps). As expected the correlation increase moves along the  $\delta\tau$  axis for a fixed  $\tau_0$ .

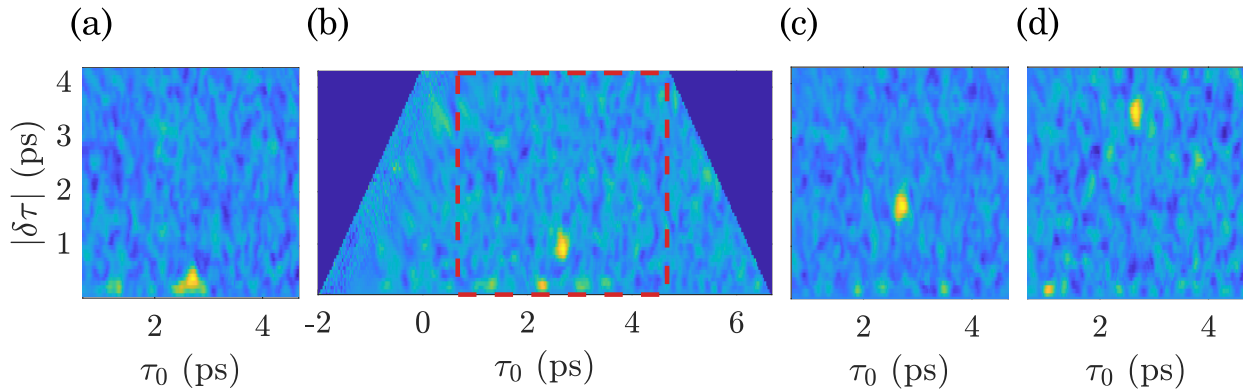


Figure 5.3: **Correlation displacement when varying the delays between the two TGTMs**. For all graphs the central delay is kept constant with a fixed  $\tau_0 = 2.7$  ps. The TGTMs spacing is varied with (a)  $\delta\tau = 0.4$  ps, (b)  $\delta\tau = 0.8$  ps. The red dashed rectangle represents the area displayed in all other graphs, (c)  $\delta\tau = 1.6$  ps and (d)  $\delta\tau = 3.2$  ps.

In addition to the correlation displacement, it is noteworthy that the effect remains when using the first singular vector of the sum of TGTMs (see Sec. 5.2.5 for the detailed explanation).

#### 5.2.3.2 Extension to more than two matrices

To test this technique even further, we now measure more than two (here three) TGTMs ( $N_{\text{CCD}} = 225$  and  $\gamma \sim 0.4$ ) for different delays and sum them. The first singular vector  $v_1^{(\tau_1+\tau_2+\tau_3)}$  is displayed on the SLM and we measure the field correlation. On the correlation plot of Fig. 5.4 (left part) one no longer observes a single but three correlation increases. The number and positions of these increases correspond to the combinations of two matrices among three. One hence gets three peaks at  $((\tau_1 + \tau_2)/2, \tau_2 - \tau_1)$ ,  $((\tau_3 + \tau_2)/2, \tau_3 - \tau_2)$  and  $(\tau_2, \tau_3 - \tau_2)$ , schematically represented in the right part of Fig. 5.4.

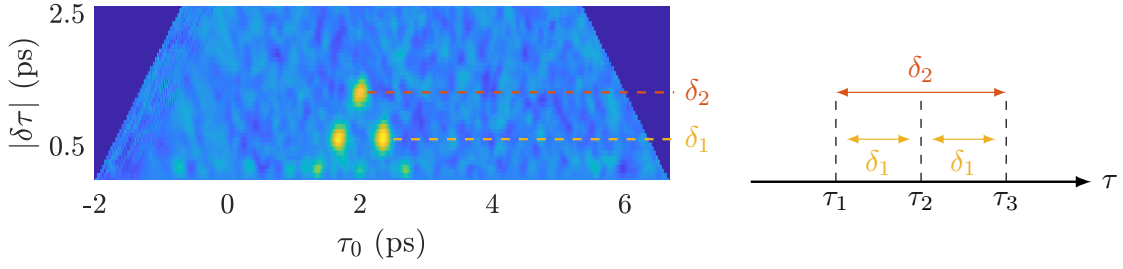


Figure 5.4: **Correlations when summing three TGTMs.** Left: Correlation plot presenting three enhancements. The enhancements are situated from left to right at  $(\tau_0 = 1.7$  ps,  $\delta\tau = 0.7$  ps),  $(\tau_0 = 2$  ps,  $\delta\tau = 1.3$  ps) and  $(\tau_0 = 2.3$  ps,  $\delta\tau = 0.7$  ps). Right: Schematic of the TGTMs respective delays ( $\tau_1 = 1.3$  ps,  $\tau_2 = 2$  ps and  $\tau_3 = 2.7$  ps) and the corresponding two by two couplings. The data are averaged over 4 disorder realizations.

It is important to note that with this experiment a first advantage of the SVD-based correlation emerges: its convenience enables a direct extension with more than two output fields. This adaptation is not that straightforward for the other operators described in Sec. 5.1.2.

#### 5.2.4 Importance of the transmission matrices coupling

The importance of the coupling between the TMs measured for different parameters was mentioned in Sec. 5.1.2. It will be illustrated here by comparing TMs summing with singular vectors summing used in Sec. 4.2.2 and Sec. 4.3.3. In Fig. 5.5, two TGTMs ( $N_{\text{CCD}} = 225$  and  $\gamma = 0.4$ ) are measured for  $\tau_1 = 0.9$  ps and  $\tau_2 = 1.7$  ps. They are either summed before taking the SVD and the first singular vector  $v_1^{(\tau_1+\tau_2)}$  is displayed on the SLM Fig. 5.5(a), or the individual SVD are performed and the two first singular vectors are summed obtaining  $v_1^{(\tau_1, \tau_2)}$  which is also displayed on the SLM Fig. 5.5(b). On the average pulse amplitude (top part of Fig. 5.5) no important difference is observed: both SLM masks lead to an increase of the amplitude at  $\tau_1$  and  $\tau_2$ . The increase is slightly less important for  $v_1^{(\tau_1+\tau_2)}$  but in absence of further study no conclusion can be made. The difference however arises when looking at the correlation plot (bottom part of Fig. 5.5). Correlations between  $\tau_1$  and  $\tau_2$  are expected to be observed at  $(\tau_0 = 1.3$  ps,  $\delta\tau = 0.8$  ps). It is the case for  $v_1^{(\tau_1+\tau_2)}$  but no correlations are visible for  $v_1^{(\tau_1, \tau_2)}$ . These results indicate that correlations emerge due to the coupling between the two TGTMs.

This coupling can be understood going back to the definition of the SVD, which consists in the eigen-decomposition of the transpose conjugate of the matrix times itself<sup>4</sup>. More precisely, the SVD of  $T_1 + T_2$  corresponds to the eigen-decomposition

$$(T_1 + T_2)^\dagger (T_1 + T_2) = \underbrace{T_1^\dagger T_1 + T_2^\dagger T_2}_{\text{individual terms}} + \underbrace{(T_1^\dagger T_2 + T_2^\dagger T_1)}_{\text{cross terms}}. \quad (5.4)$$

The two individual terms are responsible for amplitude increases at delays  $\tau_1$  and  $\tau_2$ , whereas the cross terms lead to the fields coupling.

One may notice correlation increases for small  $\delta\tau$  ( $\sim 0.2$  ps) at  $\tau_1$  and  $\tau_2$ . They are artifacts due to the enhanced intensity, see Comm. 5.2.1.

<sup>4</sup>This new matrix is square allowing an eigen-decomposition and hermitian leading to only has real positive eigenvalues.

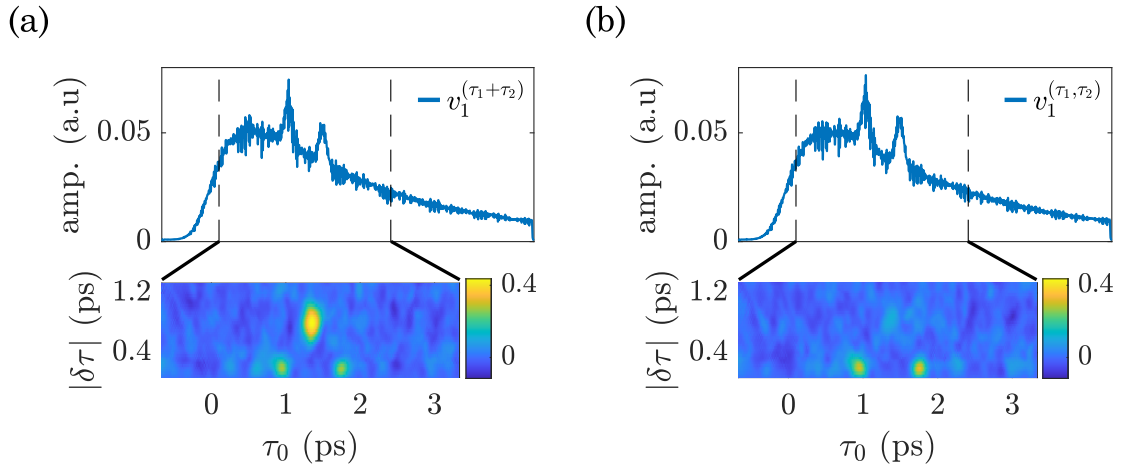


Figure 5.5: **SVD of the sum vs sum of the SVDs.** Two TGTMs measured for delays  $\tau_1$  and  $\tau_2$  and are either summed before taking the SVD (a) or the singular vectors are summed after (b). For both plots the top part represent the averaged amplitude temporal profile while the bottom part displays the correlation plot.

#### Comment 5.2.1.

Intensity induced correlations are surprising as the correlation formula Eq. 5.3 is normalized and should be intensity independent. However they appear here due to the measurement technique: the probe pulse has a width (its not the ideal Dirac) coupling in all measurements neighboring times. Hence when the intensity rises for a certain delay this rise reverberates on the neighboring delays as well, artificially introducing a correlation. For that reason all variations appearing in the correlations plot for  $|\delta\tau| \leq 0.2$  ps are disregarded.

In the next section a model is developed to predict the correlation values, so far not investigated.

### 5.2.5 Correlation variation with the singular vectors

We measure TGTMs ( $N_{\text{CCD}} = 225$  and  $\gamma \sim 0.3$ ). To monitor the correlation value change, several singular vectors  $v_i^{(\tau_1+\tau_2)}$  are displayed on the SLM. We measure the field correlations between them by correlating the fields at  $\tau_1$  and  $\tau_2$  for each input vector (which hence corresponds to the value of the correlation at  $(\tau_0, \delta\tau)$  in the 2D correlation plot). The absolute value of the experimental correlation is plotted in Fig. 5.6(a) with blue dots as a function of the normalized singular values  $\tilde{\mu}$  (normalized with a minimal dimension). Correlations are expected both for the first and the last singular vector according to the previous results. However the correlation value smoothly changes with  $\tilde{\mu}$  and a cancelation is even observed (for  $\tilde{\mu} \simeq 0.5$  here). To complement the experiment we perform a simulation using random matrices. We generate initial matrices using experimental parameters:  $N_{\text{CCD}} = 225$ ,  $N_{\text{SLM}}^{\text{eff}} = 680$  ( $\gamma \sim 0.3$ ) and insert a speckle grain size of 1.15 px in the simulation to take into account the remaining grain size after image binning. The results for phase and amplitude control, averaged over 10 matrices realizations, are presented on top of the experimental results with an orange solid line. The trend is well reproduced. A discrepancy is visible for the smallest values of  $\tilde{\mu}$  where a lower correlation is observed for the experiment, which can be attributed to the experimental TMs not exactly following MP law.

To go further and reach an analytical expression Eq. 5.4 is used to express the correlation. The

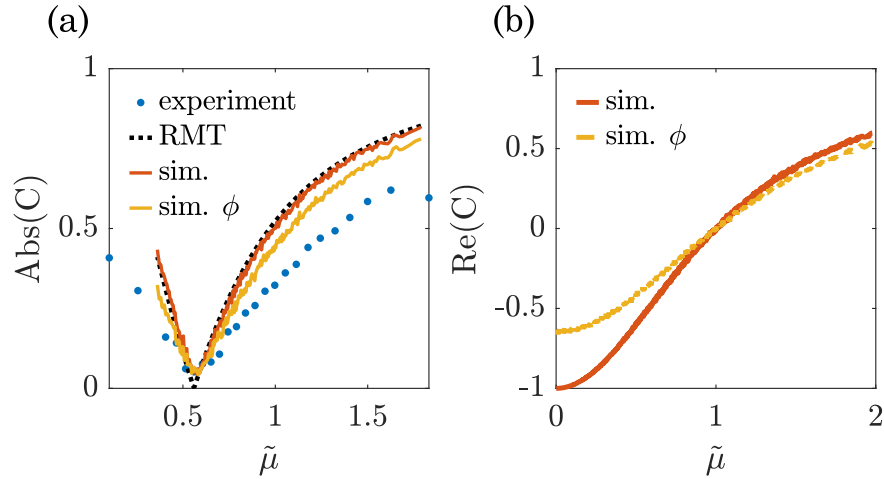


Figure 5.6: **Expected field correlations as a function of the normalized singular values.**

(a) Absolute value of the correlation as a function of the normalized singular values  $\tilde{\mu}$  for an experiment (blue dots) and the analytical prediction (black dotted line). A simulation inserting experimental parameters is plotted on top for phase and amplitude control (orange line) or phase only control (yellow line). Experimental data are averaged over 4 disorder realizations and simulated ones over 10 matrices realizations. (b) Simulation of the correlation variations with the normalized singular values  $\tilde{\mu}$ . The TMs are random matrices of sizes  $1024 \times 1024$ . The phase and amplitude correlation is plotted in orange while the phase-only is in yellow. The analytical prediction of Eq. 5.6 is presented with a black dotted line. Simulated data are averaged over 4 matrices realizations.

correlation of the two output fields for an input  $X$  vector is indeed given by

$$C \equiv C(T_1 X, T_2 X) = \frac{X^\dagger T_1^\dagger T_2 X}{\sqrt{X^\dagger T_2^\dagger T_2 X X^\dagger T_1^\dagger T_1 X}} = \frac{X^\dagger T_1^\dagger T_2 X}{\|T_2 X\|_2 \|T_1 X\|_2}. \quad (5.5)$$

If  $X$  is not a random vector but a singular vector of Eq. 5.4, then the correlation can be expressed solely in terms of the singular values and matrices dimensions by

$$C(T_1 X, T_2 X) \approx \frac{\mu^2/2 - N_{\text{CCD}}}{\mu^2/2 + N_{\text{CCD}}}, \left( \text{or } e^{-i\alpha} \frac{\mu^2/2 - N_{\text{CCD}}}{\mu^2/2 + N_{\text{CCD}}} \text{ for } T_1 + e^{i\alpha} T_2 \right) \quad (5.6)$$

The complete derivation of Eq. 5.6 can be found in Appendix B.5. The theoretical prediction for the correlation is also plotted in Fig. 5.6(a) together with the experimental results and the simulations, where we can observe a very good match with the simulations for phase and amplitude control.

In addition we perform another simulation to observe the effect of a square TM. The results show that with the SVD one can control the correlation degree between the fields for two distinct delays for both the absolute value and the real part<sup>5</sup>. For initially square TGTMs with phase and amplitude control the correlation can rise to 1 (in absolute value) as visible in Fig. 5.6(b), see III. 5.2.2 for a handwavy explanation. It is also visible that the phase-only constraints impacts more the correlation for the input vectors associated to small singular values as already observed for the speckle grain size control, see Fig. 3.12.

<sup>5</sup>We plot the real part instead of the absolute value in Fig. 5.6(b) to keep the information on the sign.

**Illustration 5.2.2.**

The smallest singular value is  $\tilde{\mu} = 0$ , thus one gets  $T_1\tilde{X} + T_2\tilde{X} = 0$  ( $\tilde{X}$  are the normalized singular vectors), and both vectors are expected to be the same but pointing in opposite directions as illustrated in Fig. 5.7(a). For the biggest singular value  $\tilde{\mu} = 2$ , vectors would be aligned if  $\|T_1\tilde{X}\|_2 = \|T_2\tilde{X}\|_2 = 1$ ; this is not the case thus the vectors are not completely aligned and the correlation does not reach 1, see Fig. 5.7(c). Intermediate values of  $\tilde{\mu}$  lead to intermediate correlations.

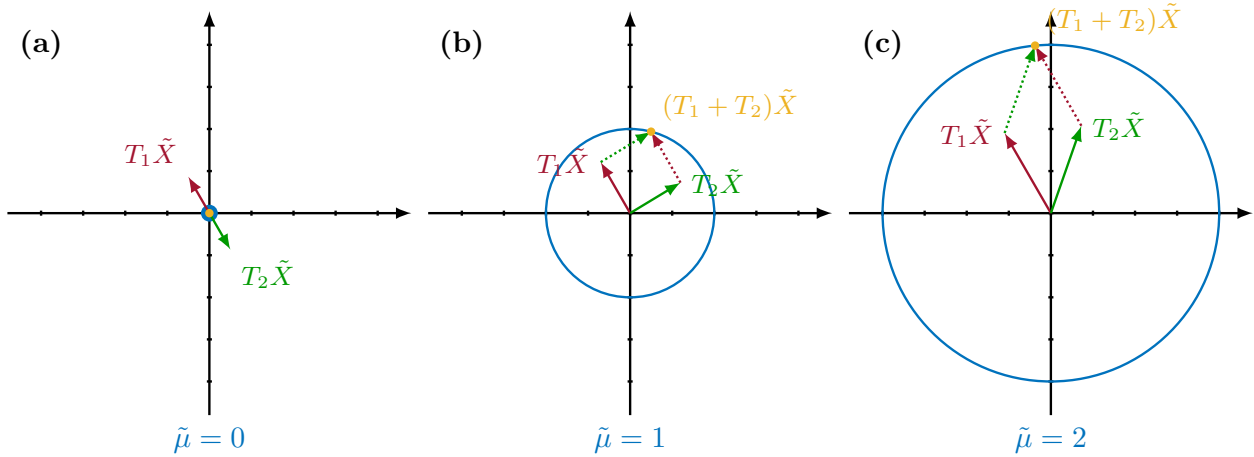


Figure 5.7: **Handwavy explanation of the correlation values.** Illustration of the two output behavior in a two dimensional vectorial space for (a)  $\tilde{\mu} = 0$ , (b)  $\tilde{\mu} = 1$  and (c)  $\tilde{\mu} = 2$ .

It is very interesting that Eq. 5.6 indicates that the correlation coefficient is real. An extension is discussed below.

### 5.3 A general concept not restricted to temporal aspects

So far, all experiments were realized in the temporal domain, however because the concept is very general it can also be applied to generate correlations in frequency (see Sec. 5.3.1) or for different spatial positions (see Sec. 5.3.2). We will illustrate the correlation phase control predicted by the model using the spectral correlation illustration. In all this section the laser is mode-locked to operate in the monochromatic regime with a tunable frequency.

#### 5.3.1 Multi-wavelength correlation

In simulations the impact of the global phase  $\alpha$  between the two TMs is illustrated in Fig. 5.8(a) using the same TMs dimensions and phase and amplitude control as for Fig. 5.6(b). For  $\alpha = 0$  one recovers the plot of Fig. 5.6(b). For  $\alpha = \pi$  the correlation value is symetrized with respect to 0. For intermediate values of  $\alpha$  the real part of the correlation is modulated between the latter two envelops. These variations are consistent with Eq. 5.6 and explain why taking the sum or the difference between the TMs ( $\alpha = 0$  or  $\alpha = \pi$ ) had no impact on the absolute value of the correlations.

Theses predictions can be verified experimentally. The parameter is now the illumination wavelength, and we measure two monochromatic TMs ( $N_{\text{CCD}} = 225$ ,  $\gamma \sim 0.35$ ) for  $\lambda_1 = 806$  nm and  $\lambda_2 = 810$  nm. We create the operator  $T_1 + e^{i\alpha}T_2$  and perform its SVD. The first singular vector is displayed on the SLM and we measure the output field while tuning the laser wavelength.

In Fig. 5.8(b) the output fields for all input wavelengths are correlated with the one measured at  $\lambda_1$ . The real part of the correlation is plotted in blue for  $\alpha = 0$  and the expected anti-correlation is observed. For  $\alpha = \pi$  (brown curve) one the real parts are correlated. The dotted black line represents the correlation with  $\lambda_1$  of the plane wave input showing no correlation at  $\lambda_2$ . We plot in Fig. 5.8(c) the imaginary part of the correlations as a function of the real part for the set of  $\alpha$  values. The central black dot corresponds to the plane wave input reference. It is noteworthy that Fig. 5.8(c) is expected from Eq. 5.6. However one can observe that for  $\alpha = 0$  the corresponding measurement does not lie on the real axis as expected but belong to the top right quarter of the complex plane indicating an experimental inherent global phase between the two TMs.

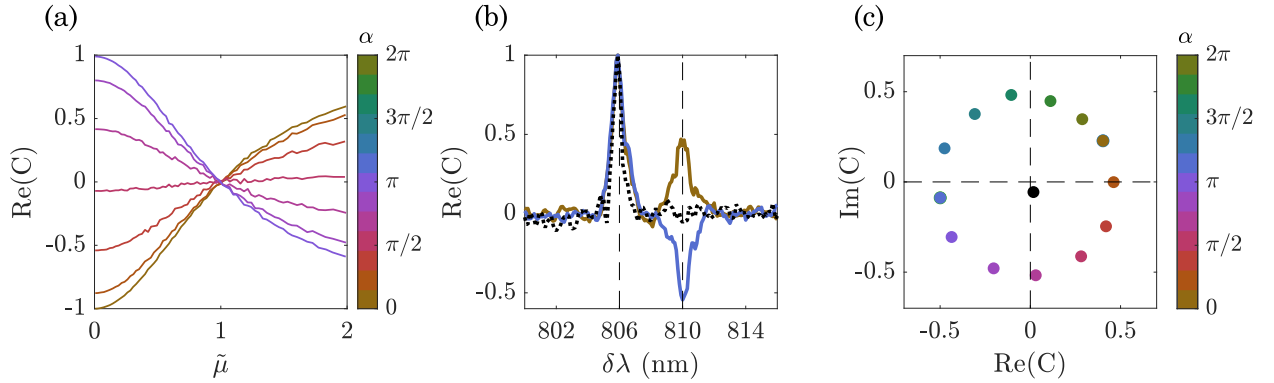


Figure 5.8: **Two-wavelength correlation.** (a) Real part of the correlation as a function of the normalized singular values  $\tilde{\mu}$  for different global phases  $\alpha$  between the TMs. (b) Plot of the correlation real part for  $\alpha = 0$  (brown curve) and  $\alpha = \pi$  (blue curve), the correlation for a plane wave input is presented with the dotted black line. The vertical dashed lines represent the wavelengths for which the TMs are measured. (c) Correlations presented in the complex plane for the a set of values  $\alpha$ . The black dot represents the plane wave input. The presented data are averaged over 4 disorder realizations.

These observations show a direct smooth control over the correlation phase. The latter is due to the intrinsic sorting of the singular values (which are real). In the methods presented in Sec. 5.1.2, the eigenvalues are complex and thus have no immediate sorting and thus no direct smooth phase control. An important point is that with the SVD-based correlation, an independent control over the phase and the amplitude of the correlations is reachable: the singular value sets the amplitude, and the global phase  $\alpha$  sets the correlation phase.

### 5.3.2 Spatial correlation

After observing the effect with the temporal delay and the wavelength as the TMs parameters it is possible to focus on the propagation for two different spatial positions. This approach is very related to [Pai et al. 2021], the main difference are the operator used and the fact that here both fields propagate through a scattering medium.

To perform the experiment, we measure two monochromatic TMs ( $N_{\text{CCD}} = 225$ ,  $\gamma \sim 0.35$ ) for  $\lambda = 808$  nm on two distinct spatial positions (marked by the colored dashed rectangles in Fig. 5.9(a,b)). We sum the TMs and calculate their SVD. The first singular vector is displayed on the SLM and we measure the field on a broad ROI. We compute the correlations with the spatial region ( $R_1$ ) where one of the TM was measured thanks to a moving spatial window. One observes a correlation increase when the moving window reaches the position where the other TM was measured ( $R_2$ ), see Fig. 5.9(c). The correlations values obtained for the binned and non-binned images are similar.

In case of the non binned images, the correlation value is slightly smaller: this behavior is expected as the image contains information on the high  $k$ -vectors that are not contained in the TM itself. Because this last experiment is similar to the one using the scattering invariant modes [Pai et al.

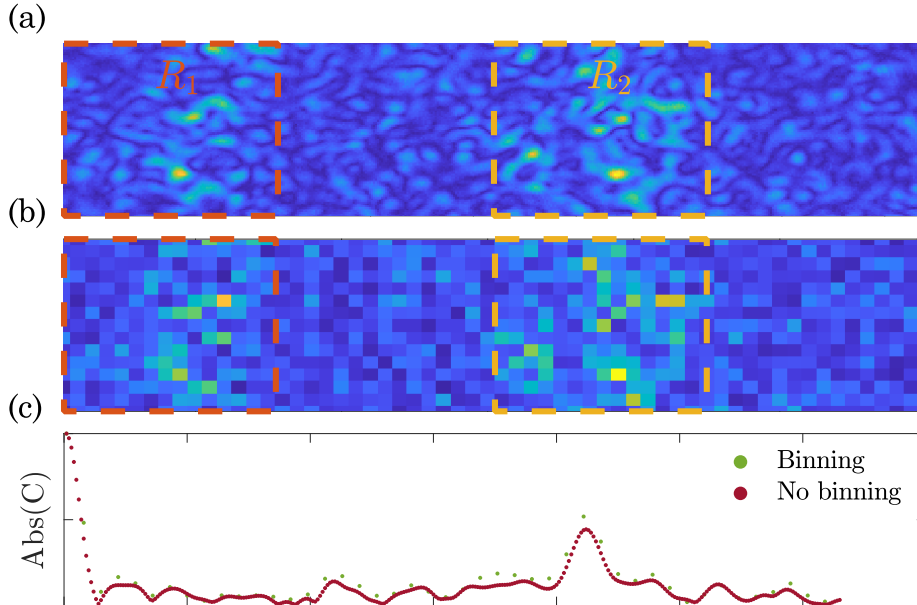


Figure 5.9: **Two ROIs correlations.** (a) Non binned speckle images. The two TMs are measured on the dashed colored areas. (b) Binned images. (c) Speckle correlations between the left zone (surrounded by the red dashed lines) and a moving window. The correlations values for the binned (green dots) and non binned (red dots) are presented along the window position. The data are averaged over 4 disorder realizations.

2021], it is interesting to compare them in more details.

### 5.3.3 Comparison of some TM-based operators

The different approaches that we will compare are the following: SVD of  $T_1 + T_2$ , eigen-decomposition of  $T_1^\dagger T_2$  and  $T_1^\dagger T_2 + T_2^\dagger T_1$  (to symmetrize the previous expression) as well as the discretized Wigner-Smith  $T_1^\dagger(T_1 - T_2)$ . For all of them the first part of the previous theoretical approach holds (with individual adaptations). The simulation results for TMs<sup>6</sup> of size  $1024 \times 1024$  and phase and amplitude control are represented in Fig. 5.10(a), with the absolute value of the correlations as a function of the input vectors (not manually ordered). In general all TM-based operators give similar results (correlation modulation from 0 to  $\simeq 0.8 - 1$  with individual characteristics that we will detail below. The SVD is the only operator undeniably spanning the full range of correlations (from 0 to 1) whereas for other operators either the maximal correlation is limited or the fast oscillations (due to the vectors ordering) do not allow to visually predict a zero-correlation. The SVD also leads to balanced intensities between the outputs. It is noteworthy (but natural) that a symmetrized form of the operator allows to balance the output intensity. This is verified for all four operators studied, see Fig. 5.10(b): the two symmetric ones lead to balanced intensities whereas the two asymmetric ones lead to un-balanced intensities. It is noteworthy that [Pai et al. 2021] due to the propagation through air, one of the TMs was unitary, modifying the expected results. The impact of having a

<sup>6</sup>And are valid whatever the experimental parameter used: time, frequency etc...

unitary TM is discussed through simulations in [Sec. 6.3](#).

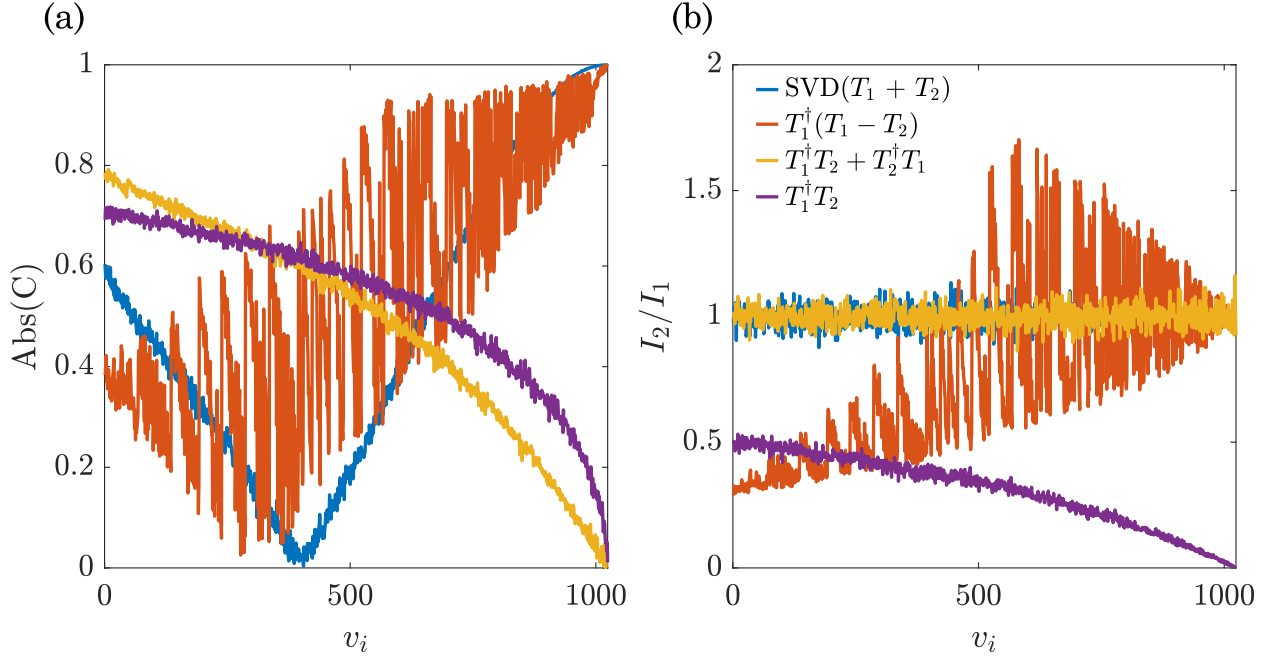


Figure 5.10: **Correlations for some TM-based operators.** Simulated TMs have size  $1024 \times 1024$ . Different operators are computed:  $T_1 + T_2$  with SVD (blue),  $T_1^\dagger(T_1 - T_2)$  (orange),  $T_1^\dagger T_2 + T_2^\dagger T_1$  (yellow) and  $T_1^\dagger T_2$  (purple). (a) Absolute value of the correlation as a function of the singular vectors. (b) Ratio of the output intensities for both field. Data are averaged over 4 TMs realizations.

## 5.4 Cross-effects

So far we restricted ourselves to one varying parameter for each experiment. TMs were measured for two (or more) parameters values, and the correlations were measured while varying this parameter by shaping the wavefront using the computed singular vector. However all accessible parameters are not independent. For instance the time (pulse delay in the experiment) and the frequency (wavelength in the experiment) are conjugated variables linked by a Fourier transform. Having information on the time also leads to frequency information. This property is actually already exploited when using the MSTM information to obtain the TRTM, see [Sec. 1.3.3.2](#). In this section we will see how spectral (resp. temporal) information can enable to generate temporal (resp. spectral) correlations, that we will refer as “cross-effects”.

### 5.4.1 Time and frequency two conjugated variables

I will present here two “mirror” experiments: (a) measurement of two monochromatic TMs for  $\lambda_1$  and  $\lambda_2$  and observation of the temporal correlations when sending a pulse and (b) measurement of two TGTMs for  $\tau_1$  and  $\tau_2$  and observation of frequency correlations. These two experiments are realized under very similar conditions<sup>7</sup> and thus I will present the details of (a) but only the results of (b).

<sup>7</sup>See [Appendix A.3](#) for the detail of an operation difference.

We measure two monochromatic TMs with  $N_{\text{CCD}} = 225$ ,  $\gamma \sim 0.1$  for  $\lambda_1 = 805.5$  nm and  $\lambda_2 = 810.5$  nm. We compute the SVD of the sum. The first singular vector  $v_1^{(\lambda_1+\lambda_2)}$  is expected to be associated to a correlation of the fields for these two wavelengths in the monochromatic setting. But here the laser is unlocked and the field along the pulse is measured by scanning the delay-line when displaying on the SLM the phase of  $v_1^{(\lambda_1+\lambda_2)}$ . The field correlation plot is computed and presented in Fig. 5.11(a, top). A checkerboard of correlation is visible and its spacing corresponds to  $\delta\tau = \lambda_0^2/(c\delta\lambda) \simeq 0.4$  ps. The spectral field coupling turns into a temporal coupling via the Fourier transform relation. It is also noteworthy that the the average pulse amplitude (Fig. 5.11(a, bottom)) is modulated along the pulse, with  $\delta\tau \simeq 0.4$  ps.

Equivalent results hold for the mirror experiment. The two TGTMs are measured for  $\tau_1 \simeq 0.9$  ps and  $\tau_2 \simeq 1.7$  ps. With the monochromatic tuning, a correlation checkerboard is also visible (Fig. 5.11(b, top)) with a spacing of  $\delta\lambda = \lambda_0^2/(c\delta\tau) = 2.7$  nm, and the amplitude is also modulated. On these experiments, the higher transmission for the plane wave input (reference) discussed in Sec. 5.2.1 is visible.

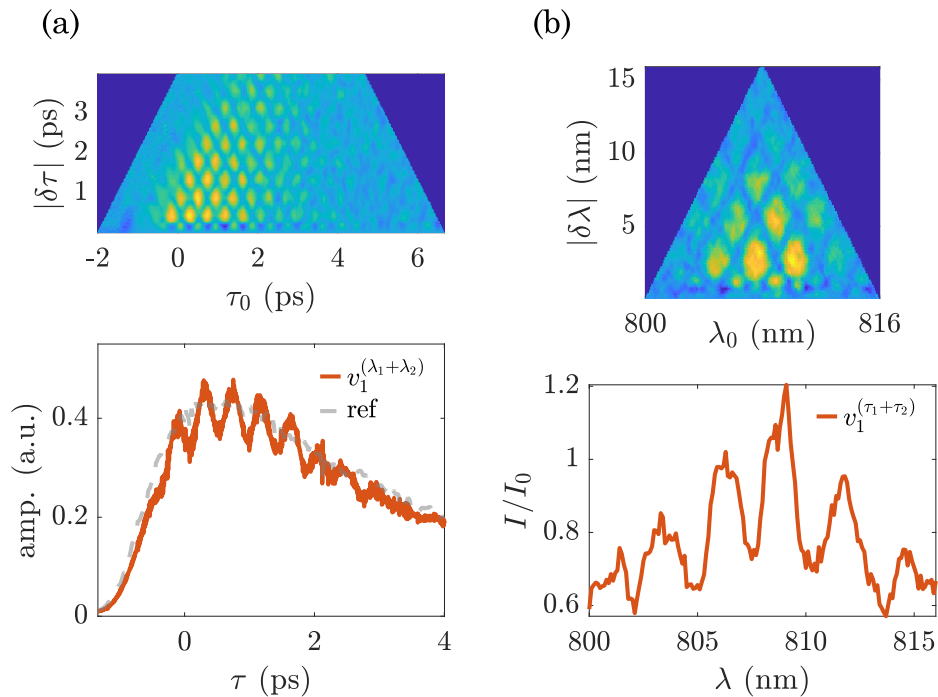


Figure 5.11: **Temporal and spectral cross effects.** TMs with  $N_{\text{CCD}} = 225$ ,  $\gamma \sim 0.1$  are measured (a) in monochromatic for two wavelengths ( $\lambda_1 = 805.5$  nm and  $\lambda_2 = 810.5$  nm) and (b) in the pulse for two delays ( $\tau_1 \simeq 0.9$  ps and  $\tau_2 \simeq 1.7$  ps). Top graphs represent the correlation plots while bottom graphs show the averaged amplitude profiles. All data are averaged over 4 disorder realizations.

Such correlation and amplitude modulations are very handy and could act as combs for probing or illuminating media. The simplicity of their obtention as well as their regularity would make them valuable tools for engineered probing or illumination.

On previous experiments the simple summing of the TMs was used, it is noteworthy that the previous variations (global phase for instance) still hold. I will present on the next section the impact of a global phase  $\alpha$  between the two TMs on the example (a).

### 5.4.2 Global phase between the two transmission matrices

The experiment is the same as in Fig. 5.11(a). The global phase  $\alpha$  between the two summed monochromatic TMs ( $T_1 + e^{i\alpha}T_2$ ) is varied in the range  $[0, 2\pi]$ . Both on the correlation plot and the averaged pulse amplitude the phase induces a translation of the correlation (resp. amplitude) maxima. From 0 to  $2\pi$  one maximum spans the full interstice between two successive maxima. The same phenomenon can be observed for the second cross effect (TGTMs with a frequency scan).

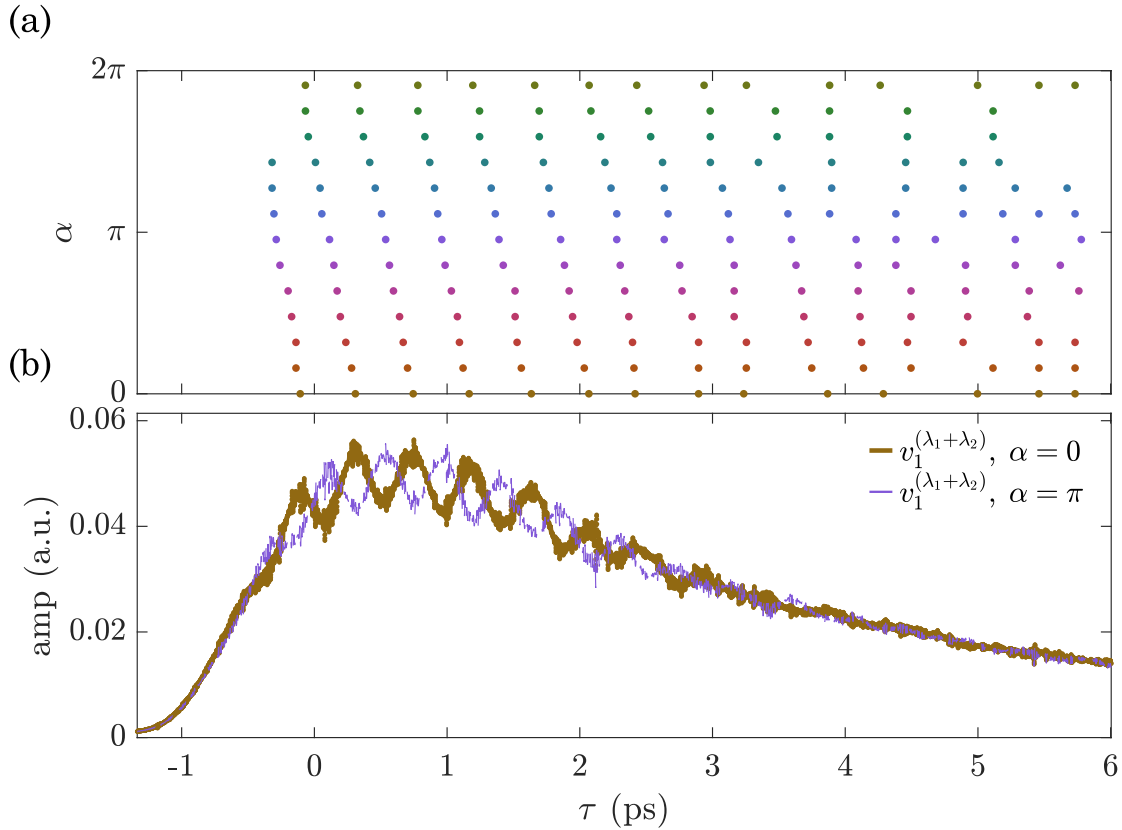


Figure 5.12: **Global phase between TMs and comb shift.** Same experiment as in Fig. 5.11(a): two monochromatic TMs are measured and summed but here a global phase difference  $\alpha$  is set between the TMs. (a) Track of the amplitude peaks position along the pulse for  $\alpha$  in the range 0 to  $2\pi$ . (b) Averaged pulse amplitude for  $\alpha = 0$  (brown curve) and  $\alpha = \pi$  (purple curve). One can visually see shifted peaks maxima.

### 5.4.3 Mixing transmission matrices measured in different regimes

Because the technique to induce correlations is so simple one can even consider summing TMs which have been measured for different parameters.

In this experiment two matrices are measured with  $N_{\text{CCD}} = 225$  and  $\gamma \sim 0.1$ . One monochromatic TM at  $\lambda_1 = 808$  nm and one TGTM at  $\tau_1 \simeq 1.3$  ps. We calculate the SVD of their sum and display on the SLM the phase of the first singular vector  $v_1^{(\tau_1 + \lambda_1)}$ . Fields are measured for both a pulse scan for the broadband mode Fig. 5.13(a) and a wavelength scan in monochromatic mode Fig. 5.13(b). The same correlation pattern is observed in both cases: a V shape starting at  $\tau_0$  (resp.  $\lambda_0$ ) for  $\delta\tau = 0$  (resp.  $\delta\lambda = 0$ ). Let us present and give an interpretation for the case (a), a similar one holding for

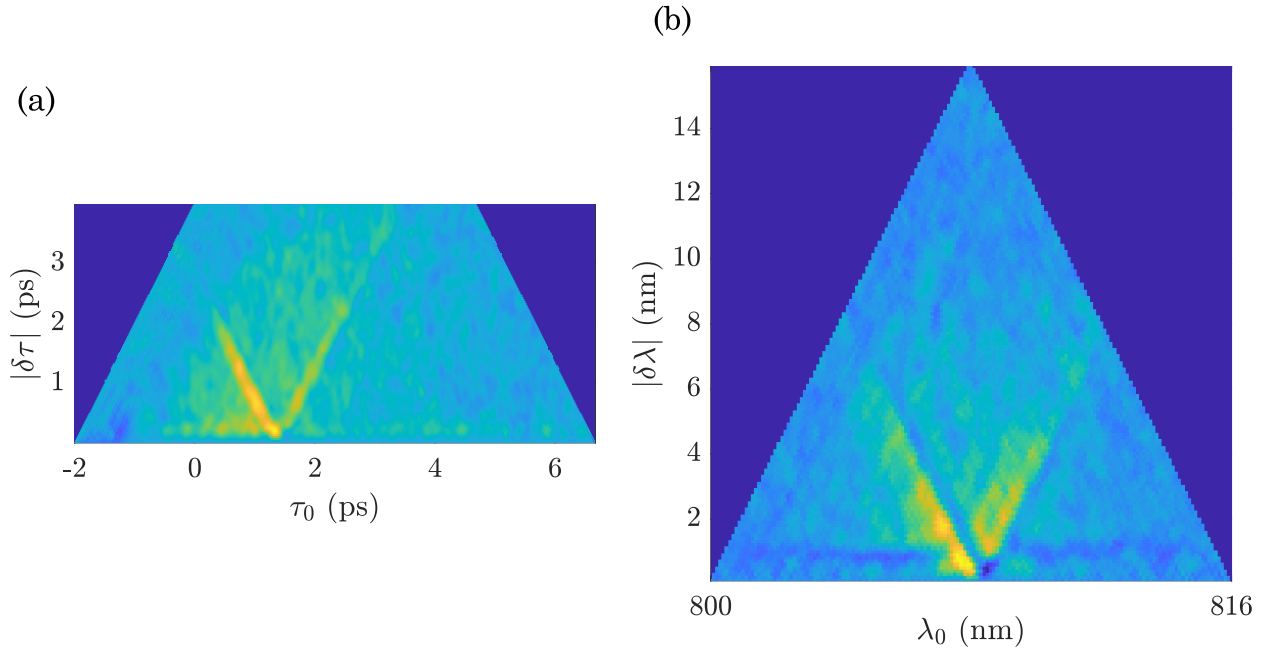


Figure 5.13: **Correlation when mixing transmission matrices.** Two TMs are measured ( $N_{\text{CCD}} = 225$  and  $\gamma \sim 0.1$ ), one monochromatic TM at  $\lambda_1 = 808$  nm and one TGTM at  $\tau_1 \simeq 1.3$  ps. The first singular vector of their sum  $v_1^{(\tau_1+\lambda_1)}$  is displayed on the SLM. Temporal correlations (a) and spectral correlations (b) are measured. The data are averaged over 8 media realizations.

(b). First, the V shape correlation indicates that fields from all delays are partially correlated with the field at  $\tau_0$  but not between them. An interpretation is as follows: when summing  $T_{\tau_1}$  and  $T_{\lambda_1}$  the temporal information at  $\tau_1$  is coupled to the spectral information at  $\lambda_1$ . This coupling results in a correlation, for all delays, of the spectral component  $\lambda_1$  of the light with this same spectral component contributing to the speckle at  $\tau_1$ . Further experiment would be required to validate this interpretation. This would however mean that a spectrally selective correlation is achievable within the pulse.

## 5.5 Take home message

In this chapter we reviewed some TM-based operators allowing a control of the speckle correlations. We presented a new method based on the SVD of two (or more) TMs. The concept being very general we could correlate the fields for specific delays in a pulse, for specific propagating wavelengths etc. More elaborated correlations (temporal long-range or spectral long-range correlations) also were achieved using the Fourier relation between time and frequency. An analytical model, based on random matrices properties, allows to predict the correlations. A key-point of this chapter is that the SVD of a TM not only allows access to input states with energy selectivity and wavenumber selectivity but also holds a multi-parameter correlation selectivity. In the next chapter we consider an extension to non fully-random matrices.

# 6 | What about optical fibres?

---

6.1	Multimode optical fibers, a versatile tool . . . . .	205
6.1.1	An overview of optical fibers . . . . .	205
6.1.2	A mixing tool . . . . .	207
6.1.3	Complete measurement of the TM of a MMF . . . . .	210
6.2	$\chi$ -axial memory effect in SI-MMF . . . . .	212
6.2.1	An overview of memory effect and its application for MMF . . . . .	212
6.2.2	Observation of $\chi$ -axial memory effect in forward scattering complex media . .	213
6.2.3	$\chi$ -axial memory effect in SI-MMF . . . . .	215
6.2.3.1	Observation of the effect . . . . .	215
6.2.3.2	Correlation widths . . . . .	219
6.2.3.3	Correlation slope . . . . .	220
6.2.3.4	Spectral and axial widths . . . . .	223
6.2.3.5	Some applications . . . . .	225
6.3	SVD induced correlations in multimode fibers . . . . .	225
6.3.1	MMF mode solver and fiber TM . . . . .	226
6.3.2	Correlation . . . . .	226
6.3.2.1	Abrupt correlation variations . . . . .	228
6.3.2.2	Full correlation control . . . . .	231
6.4	Take home message . . . . .	234

---

In this chapter I will focus on multimode fibers (MMFs). After presenting them (Sec. 6.1.1) I will discuss their properties and focus on their commonly considered drawback: the mixing (Sec. 6.1.2). Similarly to complex media with their inherent scattering, this apparent weakness of MMFs may be used as an asset. The same tools described in the other chapters (TM, WFS, etc...) will be harnessed to take advantage of the mixing. The differences with complex media (e.g. possibility of measuring complete TMs, Sec. 6.1.3) will be discussed as well as their similarities (e.g. remaining of the chromato-axial ( $\chi$ -axial) ME, Sec. 6.2).

Hence two main results will be presented in this chapter: experimental results on the  $\chi$ -axial ME in MMFs Sec. 6.2 and simulations of the extension of the field correlation with the SVD to MMFs Sec. 6.3.

## 6.1 Multimode optical fibers, a versatile tool

### 6.1.1 An overview of optical fibers

Optical fibers are widely present nowadays in almost all science and technological fields. Even though their use, as we know it, is recent, they have a long history. Already the Greeks, who developed glass manufacturing (creating lenses [Sines et al. 1987]) and optics [Lloyd 1973], realized the guidance potentiality of glass cylinders [Smith 1999]. But the discovery of total internal reflexion by J.-D. Colladon [Colladon 1842] and J. Tyndall [Tyndall 1870] marked the beginning of optical fibers in the mid-19th Century. They observed that light propagating in a medium could, under specific angular conditions, be totally refracted at the interface with a lower refractive index medium, making it possible to engineer light-guidance devices. The optical fibers first uses were, one century later in 1950, essentially concentrated on medical purposes and bundles of fibers were used as endoscopes [Hopkins et al. 1954]. In 1966, thanks to the recent laser discovery, C. Kao and G. A. Hockham associated fibers and lasers to initiate optical fibers communication [Kao et al. 1966], achievement awarded by the Nobel Prize in 2009.

As mentioned optical fibers rely on the total internal reflexion phenomena. A core of refractive index  $n_1$  is surrounded by a cladding of refractive index  $n_2 < n_1$ . When a light ray propagates on the core with an angle  $i$  (relative to the symmetry axis) lower than  $i_c$  (given by  $\sin(i_c) = n_2/n_1$ ), then the light ray experiences total internal reflexion when reaching the cladding and hence only propagates in the fiber core. This guidance condition defines the numerical aperture of the fiber, i.e. the range of acceptance angles, which only depends on the refractive index mismatch ( $\text{NA} = \sqrt{n_1^2 - n_2^2}$ ). If index  $n_1$  is homogeneous the fibers are the so-called step-index (SI) fibers. It is also possible to create a fiber which refractive index radially varies (i.e. with the distance to the center), they are then graded-index (GI) fibers. This engineered refractive index profile is typically introduced in order to reduce modal dispersion. To understand this property (see III. 6.1.1), and more generally to describe light propagation through MMFs, the ray optic scheme is convenient. A ray optics approach is a good approximation as long as the MMF radius is large compared to the wavelength that propagates through it [Jackson 1999] such that the light does not “feel” the boundaries and the interface may be locally considered plane. Equivalently this condition corresponds to a fiber having a lots of modes. The number of transverse spatial modes  $N_{\text{modes}}$  that can propagate through the fiber is indeed determined by the radius of the fiber core  $r_c$  together with its numerical aperture and the illumination wavelength<sup>1</sup>. It is given by  $N_{\text{modes}} = V^2/2$ , where  $V = 2\pi r_c \text{NA}/\lambda$  with  $r_c$  the core radius is the normalized frequency [Senior et al. 2009]. The term MMF concerns fibers for which  $N_{\text{modes}} \gg 1$ , on the contrary fibers with only one propagation mode are called **single modes fibers** and fibers allowing the propagation of only a few modes are called **few modes fibers**. Rays optics hence can be solely used for MMF where the radius is large compared to the wavelength. For instance a fiber of 50  $\mu\text{m}$  diameter fulfils this condition when illuminated by a 800 nm source (there are approximatively 60 wavelengths in the diameter) but it is no longer well verified when the same source illuminates a fiber of 10  $\mu\text{m}$  diameter (only 10 wavelengths per diameter). A modal approach is then required to describe light propagation. For SI-MMF under the weak guidance approximation (small NA), the propagation eigenmodes are given by the Linearly polarized (LP) modes [Snyder et al. 2012].

Nowadays optical fibers are increasingly considered for telecommunications [Richardson et al. 2013], still for medical purposes as minimally invasive endoscopes [Choi et al. 2012; Papadopoulos et al. 2013], but also for fiber-optic sensors [Zhao et al. 2004; Xiong et al. 2020] or even illumination

<sup>1</sup>For instance not considering the factor two on the number of modes coming from the polarization.

(optic-fiber lamps). They are very promising for laser fibers [Wright et al. 2017] or as reconfigurable linear operators in quantum photonics [Leedumrongwatthanakun et al. 2020; Matthès et al. 2019]. However in the latter papers often single mode fibers or few modes fibers most of them graded-index are used due to the inherent difficulty of spatial multiplexing. MMF, which would fill a gap and provide multiplexing possibility, are thus intensively studied.

### 6.1.2 A mixing tool

On many of the potential applications listed above (especially for telecommunications or endoscopy) a major limitation comes from the complicated field obtain after the fiber which results in a speckle intensity pattern. The origin of this field scrambling is particularly due to the dispersion and mode mixing. An illustration of the modal<sup>2</sup> dispersion is presented III. 6.1.1.

#### Illustration 6.1.1.

Let us consider two MMFs fibers, one SI and one GI, of length  $L$  and consider the two extremal rays propagating through them: the ray traveling straight along the axis of the fiber and the ray entering the fiber with the maximal angle, see Fig. 6.1. In case of the SI-MMF, the rays follow straight lines and the delay-time between the two paths is easily calculable from geometry: the physical increase of distance divided by the speed of light in the medium of index  $n_1$  (see Fig. 6.1(a)). For the GI-MMF, on the contrary, the light propagation does not follow a straight line but a path depending on the index profile (for instance a sinusoidal path for parabolic GI-fibers, see Fig. 6.1(b)). The time-delay between the two paths is not as direct to compute, indeed because the refractive index depends on the radial position so does the light speed. But the idea is that the light propagating on the longest geometrical path will propagate faster than the one propagating straight due to the smaller refractive index encountered and hence reduce the time-delay between both paths.

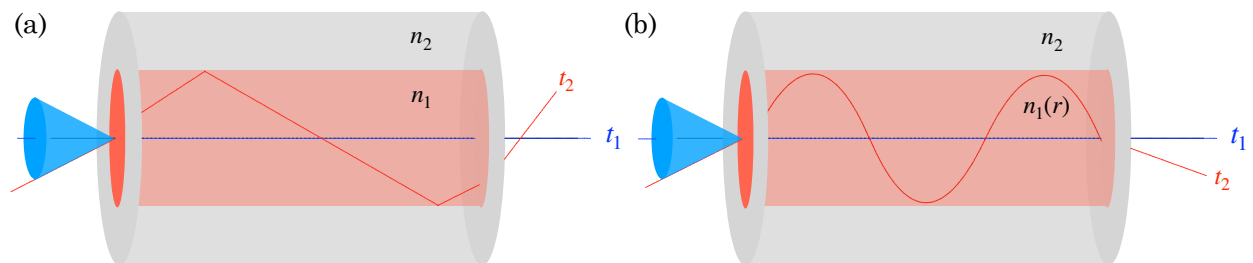


Figure 6.1: **Illustration of modal dispersion in a MMF in the ray optics picture.** Two extremal rays, one with the lower incidence (blue) and one with the highest acceptable incidence (red) are presented, they experience different propagation delays (respectively  $t_1$  and  $t_2$ ). The numerical aperture of the fiber is represented with the blue cone. (a) SI-MMF: the rays propagation is straight in the fiber core (refractive index  $n_1 > n_2$ ). (b) GI-MMF: the propagation follows a curve dictated by the refraction index profile. For a parabolic GI-fiber the path is sinusoidal.

Of course, to avoid this modal dispersion the use of single mode fibers (or limited using GI-MMFs) is natural, but multiplexing remains the goal [Berdagué et al. 1982; Richardson et al. 2013; Pauwels et al. 2019]. As a result of the modal dispersion, the intensity pattern at the output of a MMF when coherently illuminated, is a speckle pattern (modes with different accumulated phases interfering). This speckle pattern is the usual signature of disorder. However in MMFs one only refers to disorder

<sup>2</sup>The dispersion can also be chromatic.

when propagation modes are coupled [Matthès et al. 2021]. Otherwise the light propagation is determined by the fibers modes (that can be approximated or simulated). The coupling in itself is very complex and depends on many parameters as refractive index inhomogeneities, diameter fluctuations, presence of impurities, fiber bending, etc... [Ho et al. 2013] and its effects grows with the fiber length [Xiong et al. 2018; Chiarawongse et al. 2018]. Similarly to complex media, several techniques based on WFS have been developed to control the output field: optimization [Caravaca-Aguirre et al. 2013], digital phase conjugation [Papadopoulos et al. 2012], TM measurement [Carpenter et al. 2014; Choi et al. 2012]. For short straight fibers, the use of the TM and of an accurate theoretical model to evaluate the fiber parameters even enables finding the fiber appropriate basis and couple the field to the so-called propagation invariant modes (PIMs) resulting of invariant propagation up to hundreds of millimeters [Plöschner et al. 2015].

Moreover if a wealth of efforts are made to limit the mode coupling, taking advantage of it is also possible. The mixing associated to the ability of controlling it (e.g. by bending the fiber [Xiong et al. 2017; Xiong et al. 2019]), is a key element to turn MMFs into interesting platforms [Matthès et al. 2019]. Similarly to the observation of two-photon interference in scattering media [Defienne et al. 2014], the same was achieved after a MMF or with optical fiber multiports [Defienne et al. 2016; Weihs et al. 1996]. In this regard, MMF can be used to create reconfigurable and scalable quantum circuits [Leedumrongwatthanakun et al. 2020] whose fully programable aspect is an advantage already targeted when engineering interferometers [Carolan et al. 2015].

### 6.1.3 Complete measurement of the TM of a MMF

Up to now the parallel of light propagation in MMF and through scattering media has been highlighted. The differences also need to be discussed. In complex media, due to the very high number of propagating modes, the reflected light, the light scattered on the sides and the finite numerical aperture of the collection microscope objective, the TM measurements are always partial. TMs hence are well approximated by random matrices [Popoff et al. 2010] with all the advantages it brings (possibility to perform simple simulations and obtain theoretical expressions from RMT, see Sec. 5.2.5) but also the drawbacks (difficulty of reaching mesoscopic effects and access open and close channels, see Sec. 1.4.2). In contrast, MMFs with their fixed (and controllable) number of propagating modes together with their finite numerical aperture and forward propagation, do not suffer the same limitations so that the TM of an MMF is unitary [Li et al. 2021b]<sup>3</sup>. When considering the transmission matrix of a fiber a parallel with the scattering matrix can be drawn (they both are unitary). To keep on with this comparison both polarizations in the fiber can be interpreted as the transmission and reflection matrices in a scattering experiment. Hence the sub-transmission matrix for one polarization follows the DMPK model and its singular values are distributed with the bimodal law [Xiong et al. 2018; Chiarawongse et al. 2018] (Eq. 1.24) enabling to reach the equivalent for polarization of the open and closed channels. The “open channel” consisting to maintained polarization whereas the “closed channel” consisting in a completely converted polarization, as experimentally observed in [Xiong et al. 2018]. The full control of the modes, in addition to the ability of programming unitary transformations, enables to manipulate weak localization effects (control of coherent backscattering of light [Bromberg et al. 2016]). This full control also enables to observe MMF’s principal modes (eigenmodes of the Wigner-Smith operator, see Sec. 1.5) [Carpenter et al. 2015; Ambichl et al. 2017b; Xiong et al. 2017; Xiong et al. 2016], so far not accessed in complex media. As for complex media, the Wigner-Smith operator can be generalized to other external parameters, see Sec. 1.5. Applied with respect to the fiber deformations its eigenvectors prove to be

<sup>3</sup>This unitarity is no longer valid for MMFs when working with short pulses of light and considering specific output delays as in [Xiong et al. 2019].

optical channels resilient to strong deformations [Matthès et al. 2021].

It is nevertheless important to note that the non-unitarity of the TM of a complex medium is not always detrimental and a characteristic that one would want to avoid [Nardi et al. 2021]. The ability of independently controlling all modes is, on the contrary, a major asset. In absence of unitarity, output modes can be controlled independently. When optimizing the incoming wavefront to increase the energy on one output mode a unitary transformation automatically induces an energy decrease in the other modes, preventing an individual mode control [García-Martín et al. 2002; Xiong et al. 2019]. This constraint is realised for non-unitary transformations. However, in case of energy conservation, the more modes there are, the less impact this negative correlation has.

I will present in Sec. 6.2 the observation of a natural spectral correlation occurring in MMFs and follow in Sec. 6.3 by the extension to MMFs of the induced correlations presented in Chap. 5.

## 6.2 $\chi$ -axial memory effect in SI-MMF

### 6.2.1 An overview of memory effect and its application for MMF

As briefly presented in Sec. 1.1.4.1 the optical ME and its variations have been widely studied. Pioneer work on this direction includes its theoretical [Feng et al. 1988b] and experimental [Freund et al. 1988] highlights. The effect is the following: a tilt on the incoming wavefront illuminating a scattering material results in the tilt of the resulting speckle pattern. This observation is effective in various media such as isotropic thin scattering screens [Li et al. 1994] or thick forward scattering tissues [Schott et al. 2015]. A similar effect linking a shift on the illumination wavefront and the speckle pattern was also reported for anisotropic media [Judkewitz et al. 2015]. Recently these two effects were shown to be two special cases of a more general tilt/shift memory effect [Osnabrugge et al. 2017], illustrated in Fig. 6.2. Even more recently a study showed that the knowledge of the TM of a medium, and more specifically the basis in which the TM is diagonal (or quasi-diagonal), brings information on the field modification along propagation on this medium [Li et al. 2021b]. This approach enables to predict the ME for any arbitrary geometry. Applying it to MMFs, the authors retrieved the rotational ME [Amitonova et al. 2015; Li et al. 2021b] and the quasi-radial ME [Li et al. 2021b].

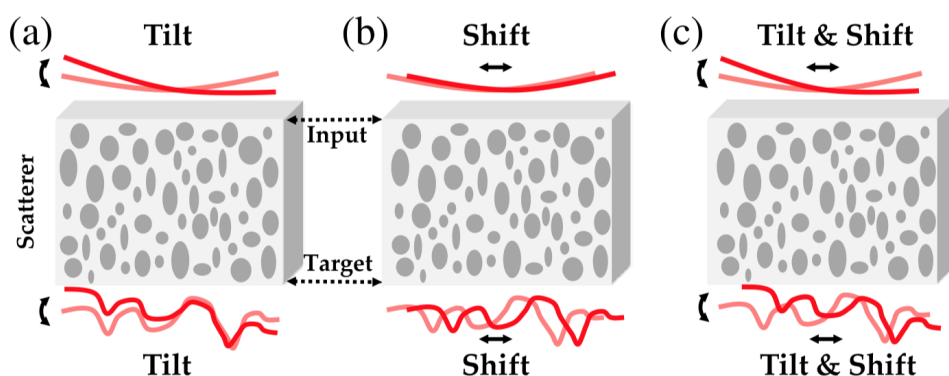


Figure 6.2: **Three different types of spatial ME.** (a) A tilt in the incoming wavefront results in a tilt in the output field. (b) A shift in the incoming wavefront results in a shift on the output field. (c) Generalized ME combining tilts and shifts. Figure from [Osnabrugge et al. 2017].

These ME, very important for imaging purposes [Bertolotti et al. 2012; Katz et al. 2012; Katz

et al. 2014; Yang et al. 2014], can also be used as priors in compressive sensing for the rapid characterization of TMs [Li et al. 2021a].

It is important to note that the different ME do not restrict to spatial aspects as we will see briefly in Sec. 6.2.2 and in more details in Sec. 6.2.3.

### 6.2.2 Observation of $\chi$ -axial memory effect in forward scattering complex media

Extending the purely spatial correlation studies, a ME linking spatial and spectral degrees of freedom has been recently observed on thin (1 mm brain tissue) scattering samples [Zhu et al. 2020]. In the article they report the observation of an axial translation of a focusing spot when tuning the input wavelength highlighting a coupling between spectral ( $\lambda$ ) and axial ( $z$ ) variables. The origin of such a link comes from the Fresnel equation:

$$E(x, y, z) = -\frac{i}{\lambda} \frac{e^{ikz}}{z} \iint E(x', y', 0) e^{\frac{ik}{2z} [(x-x')^2 + (y-y')^2]} dx' dy', \quad (6.1)$$

where the field observation point is at the position  $(x, y, z)$  and  $\lambda$  is the field wavelength. In Eq. 6.1 the field evolution depends on the product  $\lambda z$ , making the field unchanged (up to a global phase) if this product remains constant through propagation [Vesga et al. 2019]. Such a ME is very promising for imaging and has been shown to enable ultrashort laser focusing and scanning inside a thin scattering medium [Arjmand et al. 2021].

### 6.2.3 $\chi$ -axial memory effect in SI-MMF

Due to the origin of the  $\chi$ -axial ME in scattering media, i.e. the  $\lambda z$  conservation, there is hope to observe such an effect in SI-MMF that intrinsically holds the same property [Čižmár et al. 2012].

Advantages of the observation of a  $\chi$ -axial ME in MMFs are numerous. Indeed MMFs are widely used and even essential tools for imaging purposes. A good characterization of a  $\chi$ -axial ME would enable a volumetric control of the field at a distal facet of the fibre and to make existing imaging techniques non invasive. It would also, as all already observed MEs, facilitate image reconstruction and accelerate TM measurements thanks to the prior information it brings. A simple example that illustrates possible applications is the speed up and non invasiveness of the “spot scanning” imaging technique of [Papadopoulos et al. 2012].

The presentation that follows is based on the work presented in [Devaud et al. 2021a]. Some of the mains results are explained without going into all details.

#### 6.2.3.1 Observation of the effect

To observe the  $\chi$ -axial ME a setup, relying on the elements of the main experimental setup presented in Fig. 2.1, is used. A simplified scheme of its main elements is presented in Fig. 6.3. The laser is used in monochromatic mode and its wavelength is tuned to probe the spectral response of the system. Compared to Chap. 3, Chap. 4, and Chap. 5, the scattering sample is replaced by a short MMF: its length and its core radius vary from one experiment to the other and its NA is 0.22. The illumination microscope objective’s NA is taken slightly larger than the fiber’s to well address all the propagating modes. The collection microscope objective together with a tube lens images on a camera (Basler ace: acA1300-30uc) a plane at an axial position  $z$  ( $z = 0$  being set for the output facet of the fiber). This imaged position is adjustable by moving the collection microscope objective.

As a first test the monochromatic TM of the fiber is measured at  $z = 0$  and  $\lambda_0 = 800$  nm and a focus performed (see Fig. 6.4(a) central panel). When tuning the incoming wavelength (for instance increasing it by  $\delta\lambda > 0$ ) the focus vanishes. It is however possible to restore the focus by moving

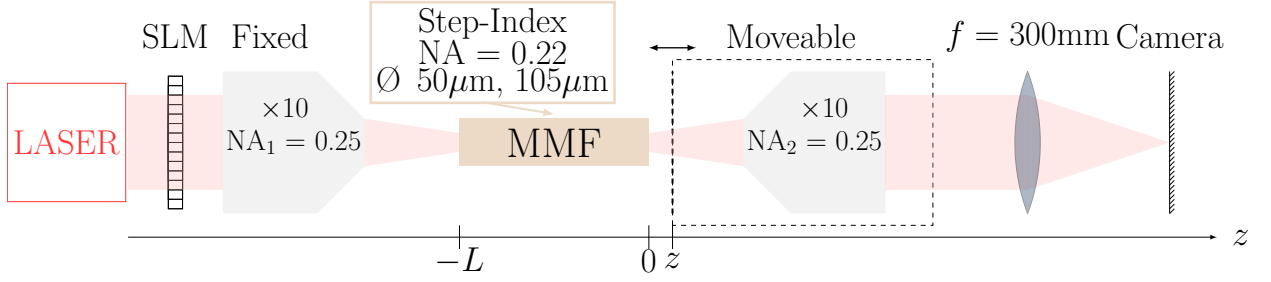


Figure 6.3: **Scheme of the experimental setup.** The laser illuminates the MMF with tunable monochromatic light and the output field at different axial positions  $z$  is imaged on a CCD camera. Wavefront shaping is performed with the SLM (represented here in transmission for schematic convenience).

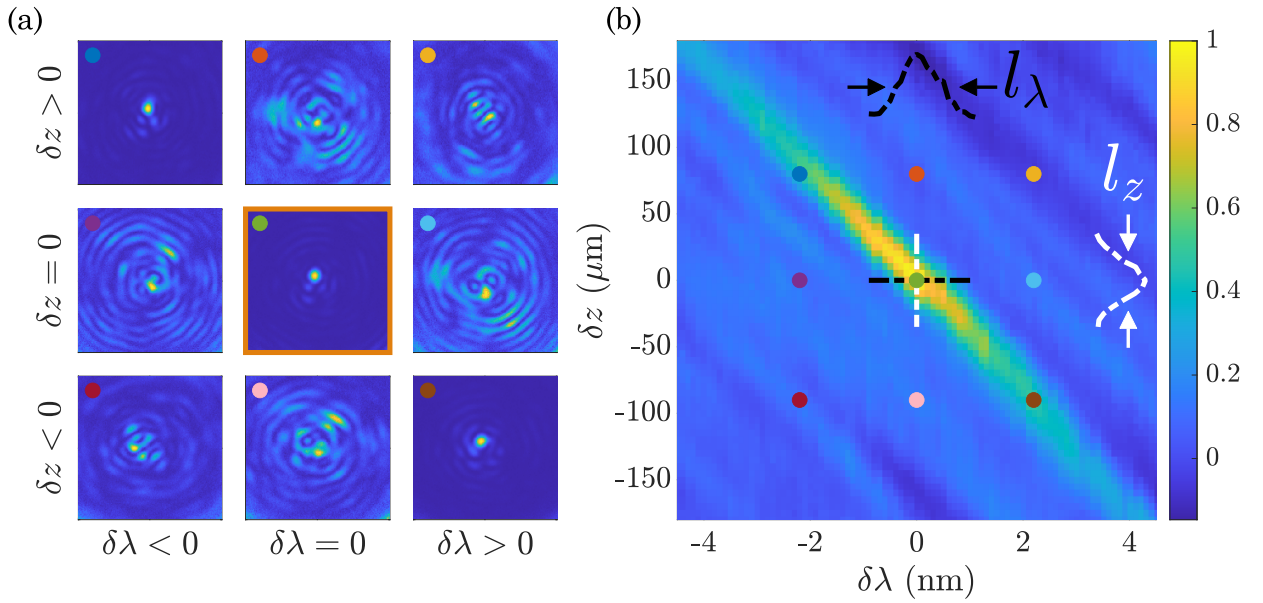


Figure 6.4: **Observation of the  $\chi$ -axial effect.** (a) A focussed spot engineered for  $\delta\lambda = 0$  and  $\delta z = 0$  vanishes when varying  $\lambda$  or  $z$  independently. However a conjoint shift of  $\lambda$  and  $z$  enables to maintain the focus. (b) Correlation plot in the  $(\delta\lambda, \delta z)$  plane for an initial speckle pattern. An anti-diagonal of high correlation appears supporting the observation made with the focussed spot. The color dots link images of (a) and (b). The spectral (resp. axial) width  $l_\lambda$  (resp.  $l_z$ ) of the correlation for a fixed  $z$  (resp.  $\lambda$ ) are plotted on the edge.

the imaged plane with  $\delta z < 0$ . Valid for a focus, this  $\chi$ -axial translation, is also expected to be valid when entering the MMF with a random phase front (generated with the SLM). However the output images are no longer foci, easily identifiable from a speckle, but speckle themselves. Hence the effect would no longer be directly visible and a quantification is needed: the speckle correlation. It is noteworthy that even though the effect then needs analysis to be uncovered, the very sharp intensity variations of a speckle pattern is an asset to evaluate the correlations.

Experiments are performed as follows: for each wavelength (on the range  $(800 \pm 5)$  nm) a set of intensity images are captured by the camera while performing an axial scan of the collection microscope objective. All intensity images are then correlated to the reference one defined as the image taken for the central wavelength (800 nm) and the output facet of the fiber ( $z = 0$ ) according

to the formula<sup>4</sup>

$$C(\delta\lambda, \delta z) = \frac{\langle \tilde{I}(\delta\lambda, \delta z) \tilde{I}_0 \rangle}{\sqrt{\langle \tilde{I}^2(\delta\lambda, \delta z) \rangle \langle \tilde{I}_0^2 \rangle}}, \quad (6.2)$$

with  $\tilde{I} = I - \langle I \rangle$ , and where  $\langle \rangle$  stands for spatial averaging over all speckle grains. The 0 index represents the reference speckle image. The correlations are plotted on the  $(\delta\lambda, \delta z)$  plane in Fig. 6.4(b). A high correlation line, in accordance with the focus experiment, is observed. Some experimental precautions and post-processings are performed and briefly discussed in Comm. 6.2.1.

### Comment 6.2.1.

Importantly, before computing the correlation product of experimental images we numerically corrected potential transverse drifts due to slight axial misalignment. Since the light energy is centered on the fiber core, long-range spatial transverse variations of intensity were also compensated to get a zero correlation value when speckles are uncorrelated. Finally, we underline that the speckle transverse dilatation (speckle broadening) after the fiber is not of critical importance to characterize spectro-axial correlations because  $\lambda z$  is a perfect invariant of free space propagation in the Fresnel approximation (see Fig. 6.5).

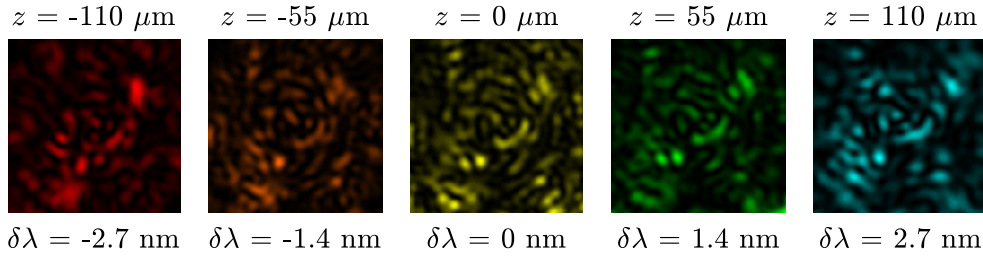


Figure 6.5: **Invariant speckle.** Speckle images along the high correlation line. The transverse dilatation of the speckle with the axial position is compensated by the wavelength tuning.

In the following we are going to discuss the characteristics of the correlation plot (Fig. 6.4): the short-range correlation variations are discussed Sec. 6.2.3.2, the slope of the high correlation line in Sec. 6.2.3.3 and the long-range evolution in Sec. 6.2.3.4. The models used will be briefly mentioned but no details on the derivation will be presented, they can be found in [Devaud et al. 2021a].

### 6.2.3.2 Correlation widths

The short-range dimensions correspond to the widths of the line profiles along  $\lambda$  (resp.  $z$ ) for fixed  $z$  (resp.  $\lambda$ ) values. The width of the line profile  $l_z$  along the  $z$  axis corresponds to the speckle longitudinal width and hence qualitatively equals the Rayleigh length  $z_R$ :  $z_R = \frac{2\lambda}{\text{NA}^2}$  [Halford et al. 1987a]. Experimentally we obtain  $l_z \simeq 31 \mu\text{m}$  full width half maximum (FWHM), in agreement with the Rayleigh length expression ( $l_z = 33 \mu\text{m}$  for a 0.22-NA fiber at  $\lambda = 800 \text{ nm}$ ). Correspondingly, the spectral width along the  $\lambda$  axis, for a fixed  $z$ -coordinate, is equal to the spectral grain size  $l_\lambda = \frac{2n_1\lambda^2}{L\text{NA}^2}$  [Rawson et al. 1980]. Here, we measured spectral widths (FWHM) equal to 0.8 nm for  $L = 58 \text{ mm}$ , in agreement with the analytical expression of  $l_\lambda$ . It is important to point out that  $l_\lambda$  is often referred to as the spectral bandwidth of the fiber (the same comment holds for  $l_z$ ). It indeed gives the spectral detuning for which the speckle is preserved. The existence of the  $\chi$ -axial ME, and the long-range dimension of the correlation graph, enables to obtain correlation bandwidths much larger than the usually considered  $l_z$  and  $l_\lambda$ .

<sup>4</sup>This is the Pearson correlation already introduced in Chap. 4 and Chap. 5 but for intensity.

### 6.2.3.3 Correlation slope

Before considering the long-range dimensions of the correlation plot a legitimate question needs to be addressed: could the high correlation line visible in Fig. 6.4(b) just be a consequence of the experimental setup chromatic dependence? The answer is no and two indications support this point.

- The evaluation of the chromaticity of the experimental setup optical components is a first indication. The microscope objectives used are treated against chromaticity in the visible range. At 800 nm it remains  $\frac{\delta z}{\delta \lambda} \approx 0.4 \mu\text{m nm}^{-1}$ . The lens used is plane-convex, made of N.BK7 glass. The chromaticity evaluated at 800 nm gives  $\frac{\delta z}{\delta \lambda} \approx 0.1 \mu\text{m nm}^{-1}$ . These values are far different from the effect observed both in order of magnitude and in sign.
- Another verification is to observe the effect when changing the optical fiber. The experiment was thus performed for different fiber lengths ( $L = 29, 58$  and  $120$  mm) with the same numerical aperture (0.22) and core diameter ( $\varnothing = 50 \mu\text{m}$ ). The effect held in all case but the slope  $\delta z/\delta \lambda$  of the high correlation line varied illustrating an effect of the fiber itself.

To understand the origin and the value of this slope ray optics simplicity is convenient. The ray optics approximation model holds due to the fiber diameter ( $50 \mu\text{m}$ ) being large enough in comparison with the working wavelength ( $\lambda_0 = 800$  nm) see [Jackson 1999] and Sec. 6.1.1. In the ray optics model propagation along a SI-MMF is similar to free-space propagation in the Fresnel approximation. The modulus of the transverse component of the wavevector is conserved and the optical path length scales quadratically with the incident illumination angle [Li et al. 2021b]. The same conclusions as for [Zhu et al. 2020] hence hold (see Sec. 6.2.2). The differential of the equation  $\lambda z = \text{const.}$  results in:

$$\frac{\delta z}{\delta \lambda} = -\frac{L}{n_1 \lambda_0}, \quad (6.3)$$

where  $L$  is the fiber length, and where  $n_1$ , the refractive index contrast of the core with the output medium, is due to Snell-Descartes's law applying at the output facet of the MMF. Experimental results are confronted to Eq. 6.3 predictions in Fig. 6.6 with good agreement. Changing the fiber radius from  $50 \mu\text{m}$  to  $105 \mu\text{m}$  does not significantly modify the measured slopes, also in agreement with the ray optics model. Another model based on the fiber's eigenmodes gives similar results. Under

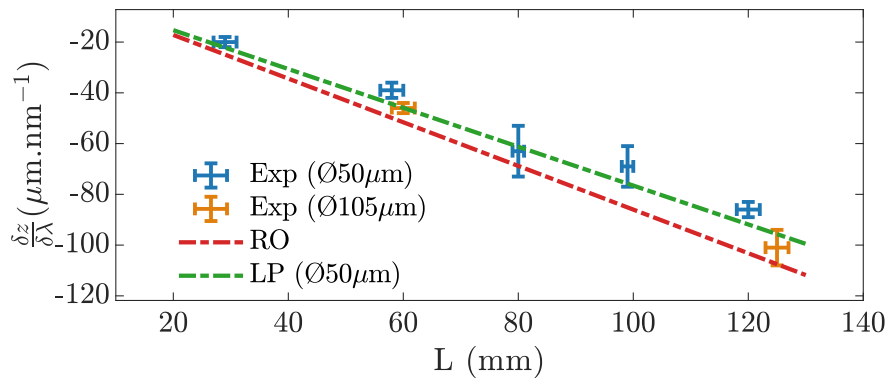


Figure 6.6: **Models predictions for the slope of the  $\chi$ -axial effect and experimental results.** Experimental slopes measured for different fiber lengths and two core diameters ( $\varnothing = 50 \mu\text{m}$ , blue dots, and  $\varnothing = 105 \mu\text{m}$ , orange dots). The expected slope obtained from ray optics (RO) calculations is represented with the red dashed line. The green dashed line represents the slope obtained from the calculation with the LP modes (for  $\varnothing = 50 \mu\text{m}$  and  $\epsilon = 0.11$ , see Eq. 6.4).

the weak-guidance approximation the eigenmodes of SI-MMFs are the LP modes (Sec. 6.1.1). The correlation expression (Eq. 6.2) can be analytically expressed with the LP modes. It not surprisingly depends on the fiber length as well as the illuminating wavelength  $\lambda$  and very importantly provides information on the intrinsic fiber effect. Finding the coupling between  $\lambda$  and  $z$  that maximizes the correlation gives the expected slope of the ME:

$$\frac{\delta z}{\delta \lambda} = -(1 - \epsilon) \frac{L}{n_1 \lambda_0}, \quad (6.4)$$

where  $\epsilon$  is a positive constant depending essentially on the fiber parameters, estimated to 0.11 and the refractive index  $n_1$  is again added to take into account the Snell-Descartes law. This model is plotted together with the ray optics predictions and the experimental results in Fig. 6.6, confirming the good agreement of the observations with this simple model.

#### 6.2.3.4 Spectral and axial widths

When observing the experimental results one observes a long-range decay of the correlation: this would be the spectral equivalent of the ME-range. To extract it, the correlation landscape is projected on the  $z$  and  $\lambda$  axes as presented in Fig. 6.7(a). This projection corresponds to keeping for each  $z$  (resp.  $\lambda$ ) the maximal value of the correlation reached when varying  $\lambda$  (resp.  $z$ ). This value is naturally obtained along the high correlation line. Experimentally we observe a spectral

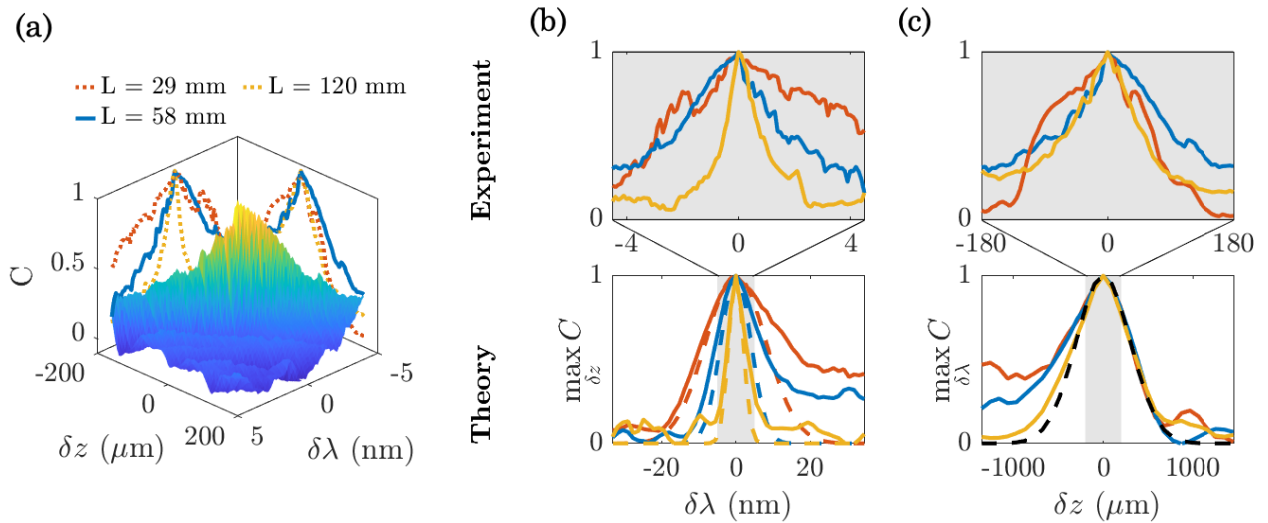


Figure 6.7: **ME range: spectral and axial bandwidths.** (a) Surface plot of the correlation measured for a fiber of diameter  $\varnothing=50\mu\text{m}$  and length  $L=28$  mm length. The spectral (resp. axial) width corresponds to the projection on the  $\lambda$  (resp.  $z$ ) axis, and is presented with a solid blue line. The spectral and axial widths of the  $L = 29$  mm fiber are represented on top (dotted red line) as well as those of the  $L = 120$  mm fiber (dotted yellow line). (b-c) Top: Recall of the experimental projections of (a). Bottom: Simulations of the fiber intrinsic spectral and axial widths (solid lines) and comparison with the theoretical values obtained from the LP model (dashed lines) for the same three fiber lengths. The grey domains indicate where the top corresponding experimental data are measured. (b) Spectral width: both values obtained from the analytical LP model (and the simulation) and experiments show a dependence with the fiber length. (c) Axial width: because it does not depend on the fiber length only one plot (black dashed line) is presented for the analytical model.

correlation width ( $\Delta\lambda$ ) varying with the fiber length and a constant axial correlation width ( $\Delta z$ ). These bandwidths cannot be explained with the ray optics model. Hence to extract them, the LP model is required. From it we obtain:

$$\begin{cases} \max_{\delta z} C = \exp \left[ - \left( \frac{\delta\lambda}{\Delta\lambda} \right)^2 \right], & \text{with } \Delta\lambda = \alpha \frac{2n_1\lambda_0 r_c}{\text{NAL}} \\ \max_{\delta\omega} C = \exp \left[ - \left( \frac{\delta z}{\Delta z} \right)^2 \right], & \text{with } \Delta z = \alpha(1 - \epsilon) \frac{2n_1 r_c}{\text{NA}} \end{cases}, \quad (6.5)$$

where  $r_c$  is the fiber radius and  $\alpha$  is a fiber-dependent prefactor close to unity. At first glance the qualitative agreement is good:  $\Delta\lambda$  depends on the fiber length but  $\Delta z$  does not. However experimentally measured bandwidths are smaller (not surprisingly due to experimental imperfect measurements) than theoretical ones by a factor  $\sim 3$  to  $5$ , the order of magnitude remaining correct.

### 6.2.3.5 Some applications

An important point is to stress for further applications of the  $\chi$ -axial ME: if the LP model is needed to retrieve all characteristics (including the spectral and axial bandwidths) of the ME it is not needed to solely determine the ME slope when ray optics models applies. The simplicity of the slope dependence makes it easy to implement in various situations. Possible applications are numerous. Some of them are related to the general existence of a ME (prior information for instance). Some, imaging related, take advantage more specifically on the spectral information. The  $\chi$ -axial ME opens the possibility to tune the wavelength while imaging [Pikálek et al. 2019], to perform wavefront corrections for non-linear microscopy [Morales-Delgado et al. 2015; Hofer et al. 2020] or also to gather information on objects subjected to inelastic scattering or broadband fluorescence (by extending the confocal microscopy technique of [Loterie et al. 2015]).

## 6.3 SVD induced correlations in multimode fibers

To illustrate the impact of the TM unitarity and full control discussed above (Sec. 6.1.3), the speckle correlation control with the SVD, presented in Chap. 5, is now also investigated in the case of MMFs. The study is solely numerical but confronts the results of the recurrently-used simple model which is based on the simulation of random matrices to the results obtained with a MMF mode solver [Popoff 2020].

### 6.3.1 MMF mode solver and fiber TM

The code used from [Popoff 2020], solving the transverse scalar propagation equation, enables to calculate the modes for fibers of arbitrary index-profiles and their TMs. On this sections the calculations are made for SI-MMFs whose parameters (NA, radius, length...) as well as the illumination wavelength can be varied Fig. 6.8(a). The modes obtained are represented in Fig. 6.8(b) for a fiber with a NA of 0.22, a radius of 25  $\mu\text{m}$ , a length of 10 cm, illuminated by a 800 nm monochromatic source. The TM ( $T_1$ ) in the mode basis is then calculated using the modes and their propagation constants<sup>5</sup>. For perfect straight fibers, as simulated here, the TM is diagonal on the mode basis Fig. 6.8(c). The projection of each mode on the pixel basis enables to also obtain the TM in this basis Fig. 6.8(d).

<sup>5</sup>For a waveguide (e.g. an optical fiber), the propagation constant of a mode determines how the amplitude and the phase of the light (for a given frequency) vary along the propagation direction.

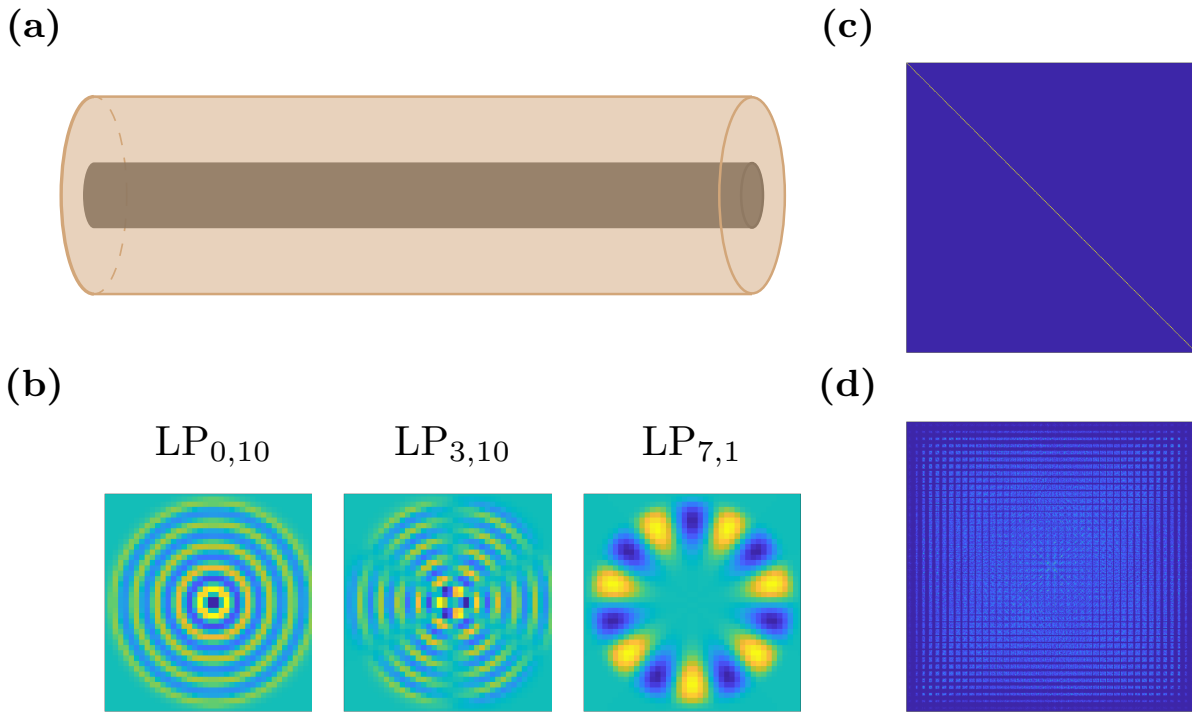


Figure 6.8: **Simulated modes of SI-MMF and its TM.** (a) Scheme of the simulated MMF with length  $L = 10$  cm, diameter  $\varnothing = 50 \mu\text{m}$ ,  $NA = 0.22$ , illuminated with a  $800 \text{ nm}$  monochromatic light. (b) Radial profile for three out of 470 (polarization excluded) modes:  $LP_{0,10}$ ,  $LP_{3,10}$ ,  $LP_{7,1}$ . (c) TM on the mode basis (size  $470 \times 470$ ). (d) TM on the pixel basis (size  $42^2 \times 42^2$ ). The size is arbitrary and depends on the resolution set for the calculations.

### 6.3.2 Correlation

Once the TM of the fiber is known, so is the output field. By choosing another set of parameters for a second fiber the field-correlation technique employed in [Chap. 5](#) can be tested. Here we study the same fiber illuminated with a different wavelength which is  $\lambda = 700 \text{ nm}$ <sup>6</sup> and its TM ( $T_2$ ) is computed. Both TMs in the pixel basis are summed and their SVD is performed. It is important to note that even though the two fibers do not have the same number of modes, they have the same size in the pixel basis (with however a different rank,  $\text{rank}(T_1) < \text{rank}(T_2)$ , whose impact will be discussed later). The obtained singular vectors (phase and amplitude) are then propagated in the two fibers and the output fields are correlated. The real<sup>7</sup> part of the correlation is presented in [Fig. 6.9\(a\)](#) as a function of the singular values<sup>8</sup> ( $\mu$ ). Two main observations are worth discussing:

- The evolution is not smooth as in the previous results with correlations abruptly going to 0 for some values of  $\mu$ .
- Correlations real part span the  $[-1, 1]$  range whereas the absolute part is fixed at 1.

The two following parts harness them individually.

<sup>6</sup>Any of the parameters of the fiber, or even several, could also have been modified.

<sup>7</sup>The real part instead of the absolute value is chosen here, this choice is explained in [Sec. 6.3.2.2](#) and [Sec. B.5.2](#).

<sup>8</sup>Due to the rank of the sum of the TMs not being analytically predictable the normalization of the singular values (see [Comm. 1.4.3](#)) is not performed here.

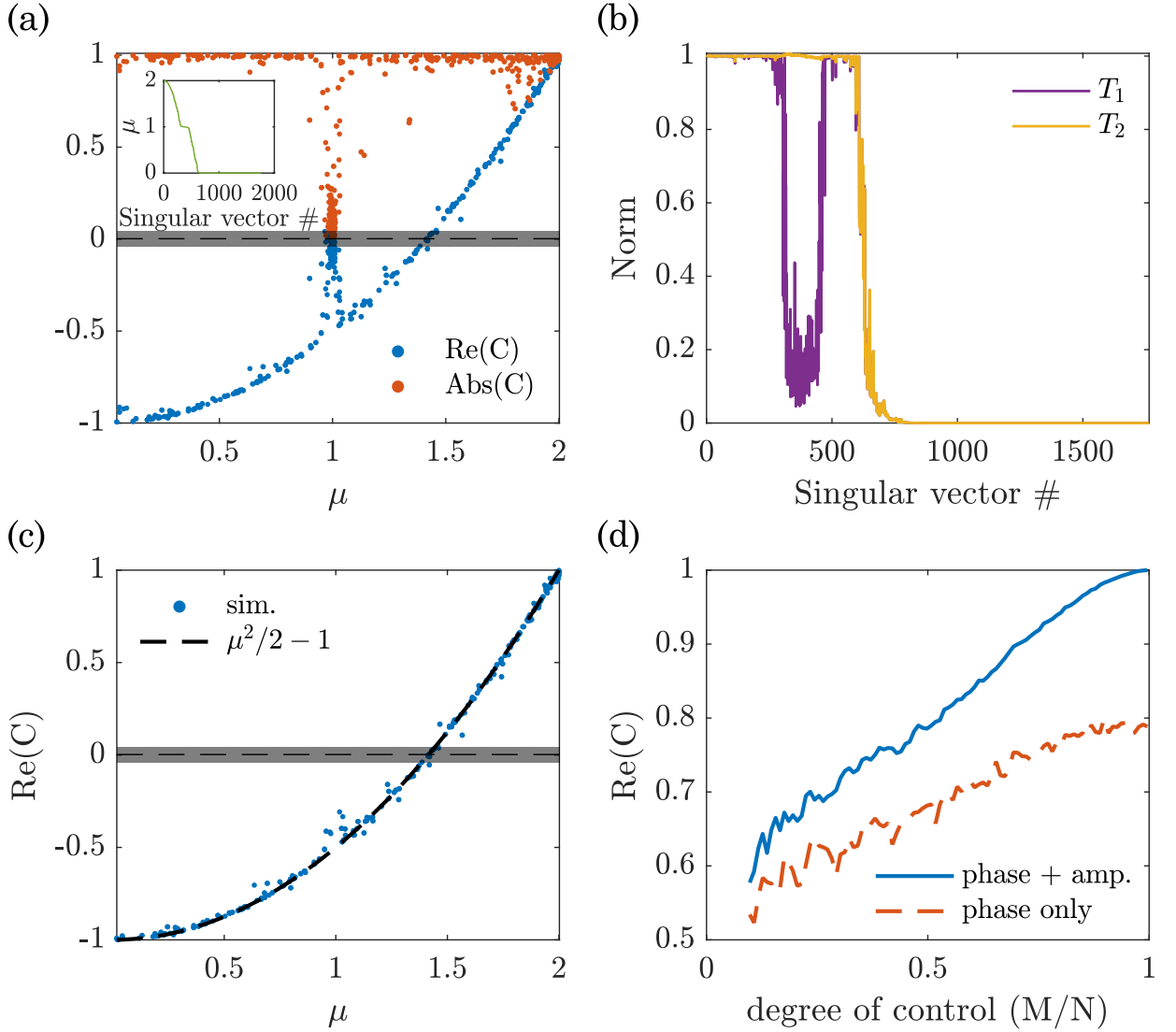


Figure 6.9: **SVD-based correlations of the output field of MMFs.** Simulation of two fibers TMs ( $T_1$  and  $T_2$ ) and SVD of their sum enables to control the output field correlation. (a) Real part (blue) and absolute value (orange) of the correlation as a function of the singular values  $\mu$ . The inset represents the singular values as a function of the singular vector number  $\#$ . The dashed black line represents the mean correlation for a random input vector and the grey shaded area its standard deviation. (b) Norm of the output vectors as a function of the singular vector  $\#$ . A norm drop is observed for the lower-rank TM ( $T_1$ ). The number of non-zero singular values gives access to the matrices ranks. (c) Real part of the correlation as a function of the singular values  $\mu$  after reordering of the singular vectors with respect to the output field norm of the lower-rank TM. It is noteworthy that the number of singular vectors used in (a) and (c) is different due to the exclusion of some vectors after the sorting. The prediction value for the real part is plotted in top with a dashed black line. (d) Simulation of the correlation evolution for the higher singular value for different degrees of unitarity of the TMs with the unitary random matrix model.  $M/N = 1$  corresponds to a random unitary matrix whereas  $M/N \ll 1$  corresponds to a fully random matrix. The simulations are made both for phase and amplitude (solid blue line) and phase only (orange dashed line) control.

### 6.3.2.1 Abrupt correlation variations

It is well visible in Fig. 6.9(a) that except for a couple of singular vectors that lead to zero correlation (as if they were random input vectors), the overall correlation trend is smooth. This observed singularity for some vectors also appears in the singular value distribution presented in the inset of the Fig. 6.9(a). The singular values are plotted as a function of the singular vector # which leads to a continuous decrease as the SVD algorithm sorts the vectors by decreasing singular values. Contrarily to what was previously observed (see Fig. 5.6) experimentally or in simulations, the values do not decrease monotonically but encounter a plateau at 1. Looking more carefully (and varying the two fibers parameters) one can observe that the length of this plateau corresponds to the two fibers number-of-modes difference, and hence the TMs rank's difference mentioned in Sec. 6.3.2. A qualitative explanation is the following: even though the modes of the two fibers are different they remain similar enough such that the TMs almost commute (one can almost find a basis in which both TMs are diagonal). The lower-rank TM ( $T_1$ ) hence can be considered as a sub-part of the higher-rank one ( $T_2$ ). There is hence a set of singular vectors (the set size corresponds to the rank difference) that contain information for the higher-rank matrix but are unphysical for the lower-rank one. Due to the quasi unitarity of the TMs (perfect fibers with no losses and forward propagation) the singular values of the individual TMs are (almost all) 1 and the singular values associated to this set of singular vectors is hence 1. Because the SVD sorts the vectors by decreasing singular values it results on the observed plateau. Thus the singular vectors associated with the plateau contain information on the propagation through one fiber only (the one associated to the higher-rank TM). The transmission is still possible for one fiber (with the singular value of the associated TM, i.e. 1) but no significant correlation is present. This is well visible in Fig. 6.9(b) where the norms of the output vectors (after propagation through the different fibers) are computed. Due to the close to loss-free propagation the norm is conserved: an input unit-norm vector should exit with a unit-norm. This is the case of all singular vectors of non-zero singular values for the higher-mode fiber. However it is visible that the norm drops for some singular vectors in case of the lower-mode fiber. To reach the promising smooth control one hence needs to withdraw troublesome vectors. Taking advantage of the norm information enables to do so: the singular vectors can be sorted by decreasing norm using the lower-rank TM. The result of the correlations obtained with this ordering are presented in Fig. 6.9(c). The abrupt peak to zero correlation is no longer visible.

The results obtained with the simulated TMs of MMFs are interesting to compare with the random matrix model.

### 6.3.2.2 Full correlation control

When working with two unitary matrices expanding the norm  $\|T_1 X + T_2 X\|_2^2$  as a scalar product<sup>9</sup> gives  $\text{Re}(C) = \mu^2/2 - 1$ . Thus, as seen in Fig. 6.9(c) the real part of the correlation values spans the full range of  $[-1, 1]$ , leading to a possible complete control by choosing the accurate singular vector. However the control on the absolute value is lost (all input vectors leading to an absolute value of the correlation of one, see Appendix B.5.). This is different from the experiment results obtained with layers of paint and the random matrix simulations, where the correlations could at maximum only span the range  $[-0.6, 1]$  or  $[0.6, -1]$  depending on the TMs relative phase and where the absolute value of the correlation could be controlled. This better performance for the singular vectors associated with high singular values is easy to understand by following on the qualitative explanation of the limited range in III. 5.2.2. The correlation limitation for leading singular vectors was due to the two output vectors norms not being 1. It was hence possible to obtain the final vector (whose norm is given by the leading singular value) with two non necessarily collinear vectors.

<sup>9</sup>Which corresponds to al-Kashi theorem in two dimensions.

In case of unitary matrices the norm constraints make this limitation vanish: to obtain a vector of norm two (expected leading singular value) with two unit-norm vectors the only solution is that they are collinear and hence, in our measurement terms, correlated.

This possibility of reaching high correlations with leading singular vectors is very promising as they are the most resistant to noise and the experimental phase-only constraint (see [Sec. 2.2.2.3](#), [Sec. 3.2.3](#) and [Sec. 5.2.5](#)). But these results also illustrate the importance of non-unitary transformations realising constraints.

The correlation control results are also consistent with RM-based simulations. In the previous chapters (mainly in [Sec. 3.2.3](#) and [Sec. 5.2.5](#)) simulations have been performed by imitating a TM using a random matrix, with very accurate results. It is possible to go further adding to the random matrix more features to mimic different experimental constraints or prior information. One addition that can be done is making the TM unitary to estimate the impact of full control. Unitary random matrices (some of their properties are discussed in [Appendix B.6](#)) can be built using the QR decomposition as presented in [Comm. 6.3.1](#).

#### Comment 6.3.1.

The simulation of a unitary random matrix is performed with the following steps, see [[Ozols 2009](#); [Mezzadri 2006](#)]:

1. Create a random Gaussian i.i.d. matrix  $S$ .
2. Perform the QR decomposition of the matrix:  $S = QR$ .
3. Create a diagonal matrix  $D$  from the diagonal coefficients of  $R$ , renormalized to have modulus 1.
4. Create the target matrix:  $M = QD$ .

Due to the unitarity of  $M$ , all its eigenvalues are  $\mu = 1$ .

Once created the degree of unitarity is adjustable by extracting only a subpart (size  $M \times M$ ) of the unitary matrix (size  $N \times N$ ) leading to a sub-unitary matrix. For more details on sub-unitary matrices see [[Zyczkowski et al. 2000](#)] and [Appendix B.6](#). In most experimental systems, access is often limited to only a subpart of the full TM due to the incomplete control, where the unitary effects do not remain. Optical fibers are a specific case where the absence of reflected light allows to consider TMs unitary.

In [Fig. 6.9\(d\)](#) the degree of unitarity ( $M/N$ ) of two TMs is varied (extraction of subparts of unitary random matrices) and the corresponding correlation value for the leading singular vector plotted. For phase and amplitude control correlations vary from 1 (for  $M/N = 1$  corresponding to unitary matrices), as expected and seen with fiber TMs, to 0.6 for mere random matrices (as already observed and predicted, see [Sec. 5.2.5](#)). Not surprisingly for phase-only control the correlations are lower. They still reach 0.8 in case of unitarity.

If, as shown in this section, it is possible to correlate the speckles after propagation in a MMF for two different incoming wavelengths, this technique requires a WSF device. I will present in [Sec. 6.2](#) the observation of a natural spectral correlation occurring in MMFs.

## 6.4 Take home message

In this chapter we discussed the implications of the high control reachable with MMFs. I present experimental results of the  $\chi$ -axial ME observed in MMF and analyze its main characteristics. I

also extend the experimental results of [Chap. 5](#) to MMFs. Using a code that solves fibers modes it is possible to reconstruct the TM of a MMF and compare the results with the simple RM model (adding to it the unitarity constraint).

# Conclusion

Light scattering is a complex process that can be described at different levels. In strongly scattering media, the random walk followed by photons leads to a diffusion equation for the intensity. However, coherent aspects remain and one can observe complex interferences behind scattering media. This complex interference pattern can be controlled by means of wavefront shaping techniques, using devices such as spacial light modulators. In this thesis we exploit the transmission matrix that links input and output fields. Performing the singular value decomposition of the latter matrix grants access to the medium modes, and is a powerful tool to control light propagation.

In [Chap. 3](#) we compared the Rayleigh statistics of speckles obtained from singular modes with the Ricin statistics of speckles induced by global focusing techniques. Singular modes of an over-sampled transmission matrix are used to control the speckle grain size and more generally the speckle correlations. This control can be performed by numerical filtering of the spatial Fourier components of the transmission matrix. Because the singular value decomposition sorts modes by transmission, associating specific  $k$ -components to transmission values allows a control of Fourier components of the output field. Modifying the experimental configuration to obtain inhomogeneous speckle Fourier transforms allows a direct (without the matrix filtering step) control of the speckle grain size.

These monochromatic results are extended to the broadband regime in [Chap. 4](#) and are further supported by simulations in a waveguide geometry. Taking advantage of the time-gated aspect of the setup, we measured time-gated transmission matrices. Coupling the input light to specific singular modes of a time-gated transmission matrix measured for a delay  $\tau_0$  allows a controlled power delivery at this delay. An optimal enhancement is even expected for the first singular vector (associated to the highest singular value) while keeping a Rayleigh distributed speckle pattern.

In [Chap. 5](#) we exploited the singular value decomposition to couple light propagation between different scattering “landscapes”. These landscapes can either be relatively similar when illuminating one scattering medium with different wavelengths, or completely different when light propagates through two different media. The technique we developed uses the singular value decomposition of a sum of transmission matrices, and allows for a smooth and adaptable control of speckle correlations, both in phase and amplitude. We predict the correlation with an analytical derivation based on random matrices. Finally, exploiting conjugated quantities improves the engineering of correlations, and can for instance be used to generate temporal and spectral correlation combs.

In [Chap. 6](#) using numerical simulations, we showed that this correlation control extends to multimode fibers, for which we explore the impact the unitarity of the transmission matrix. This last chapter also highlights the observation and description of a new memory effect in fibers, reminiscent of the chromato-axial memory effect observed in forward scattering media, that couples axial translations of the imaging plane with spectral detuning.

Even though this work mainly represents an exercise of light manipulation, some applications could benefit from it. Indeed all results obtained can help improving existing imaging techniques such as structured illumination microscopy. The information and control obtained could also benefit the development of non-invasive imaging and light control in biological media. From a fundamental point

of view, further research on the light-matter interaction using tools developed here is in the logical continuity of this work, especially in the temporal domain. For instance, this work considers equally most delays in the pulse, and a selective study or control of the photons experiencing small or strong scattering (hence quickly exiting the medium or in the contrary remaining longer in the medium) would be very instructive. Moreover adding to the time-gated transmission matrix measurement a time-gated reflexion matrix measurement would provide a deeper understanding and control of temporal light propagation. Such simultaneous measurements might be difficult to achieve, but could be conceived when considering the stability of the medium and the experimental setup. Another interesting direction for that work would be to study, on the contrary, dynamic media and look for propagating states robust against scatterers movements. So far continuous optimization techniques are used for that purpose mostly in biological samples [Blochet et al. 2017]. Eventually, even if in this thesis I presented results and techniques, as far as I am concerned I feel that my work has opened the way toward more research rather than has closed the questioning. One question leading to an answer opening itself the path to two more questions, and so on, similarly to a fight against the Hydra of Lerna Fig. 6.10. On a final note, remember that in each of the works presented in this thesis, scattering is never perceived as a limitation, but rather as a framework allowing the emergence of effects and of their predictions using random matrix theory.



Figure 6.10: **Heracles fighting the Lernaean Hydra, Greek vase-painting.** One of the twelve Labors of Heracles was to kill the Hydra of Lerna. The Hydra possessed many heads with a poisonous breath. To kill it, Heracles started by cutting off heads, but for every head chopped off, the Hydra would regrow two other heads.

# A | Experimental complements

## A.1 Laser jitter

As explained in [Sec. 2.2.1](#), the laser used is a mode-locked Ti:sapphire pulsed laser. It can be manually prevented from mode-locking and used as a monochromatic source. This operation is however not optimized and the laser is unstable in monochromatic mode. The frequency is prone to a jitter. Our commercial spectrometer has a limited resolution of  $\approx 0.1$  nm, precluding any jitter quantification. For a convenient access to the emitting wavelength fluctuations  $\delta\lambda$ , we use the medium itself. A similar idea was already used with scattering media [[Kohlgraf-Owens et al. 2010](#); [Redding et al. 2013b](#)] or in long MMF to construct high resolution spectrometers [[Redding et al. 2014](#); [Redding et al. 2013a](#)]. A small fluctuation in the incoming wavelength results in the modification of the speckle pattern. Hence measuring the speckle decorrelation for different wavelengths ([Fig. A.1\(a\)](#)) enables to calibrate this home made spectrometer ([Fig. A.1\(b\)](#)). The measured frequency fluctuations for monochromatic mode are presented in [Fig. A.1\(c\)](#). The relative wavelength fluctuations (measured fluctuations divided by the input light bandwidth) can be estimated to 0.2.

This small jitter of the monochromatic source (even smaller for the pulse) generally does not affect experiments. However it can preclude frequency resolved measurements below 0.1–0.2 nm.

## A.2 Impact of phase-only control

This appendix aims at completing the discussion on the phase only constraint of [Sec. 2.2.2.3](#).

To complement [Fig. 2.2](#) and [III. 2.2.2](#), that illustrate the importance of the phase information over the amplitude to modulate the wavefront, we present here a simulation of a phase conjugation experiment. A TM of size  $1024 \times 1024$  is simulated with a random matrix and a targeted output vector is computed. This vector aims at focusing light in the center of the output plane using phase conjugation, the targeted 2D image (amplitude value of the reshaped vector) is presented in [Fig. A.2\(a\)](#). The output obtained is displayed in [Fig. A.2\(b\)](#) with a measured signal to noise ratio SNR of 35. Equivalent results are presented in [Fig. A.2\(c,d\)](#) for partial modulations. In [Fig. A.2\(c\)](#) we use only the phase information of the input vector, which leads to  $\text{SNR}^\varphi \approx 31$ . Conversely, in [Fig. A.2\(d\)](#) we only use the amplitude information of the input vector. As expected, no focused light appears with  $\text{SNR}^{\text{amp.}} \approx 0.6$ .

We present below a method to control both phase and amplitude with a phase only SLM, that only requires work on the data acquisition and analysis (no experimental alignment). As mentioned in [Sec. 2.2.2.3](#), this technique exploits the zero<sup>th</sup> diffraction order [[Van Putten et al. 2008](#); [Guillon et al. 2017](#)] instead of the usual 1<sup>st</sup> order. It thus allows flexibility and easy alignment but at the cost of keeping the unmodulated light. Because this technique only requires coding and experimentally cutting non-zero diffraction orders, it is easy to implement. A schematic of its different steps is presented [Fig. A.3](#).

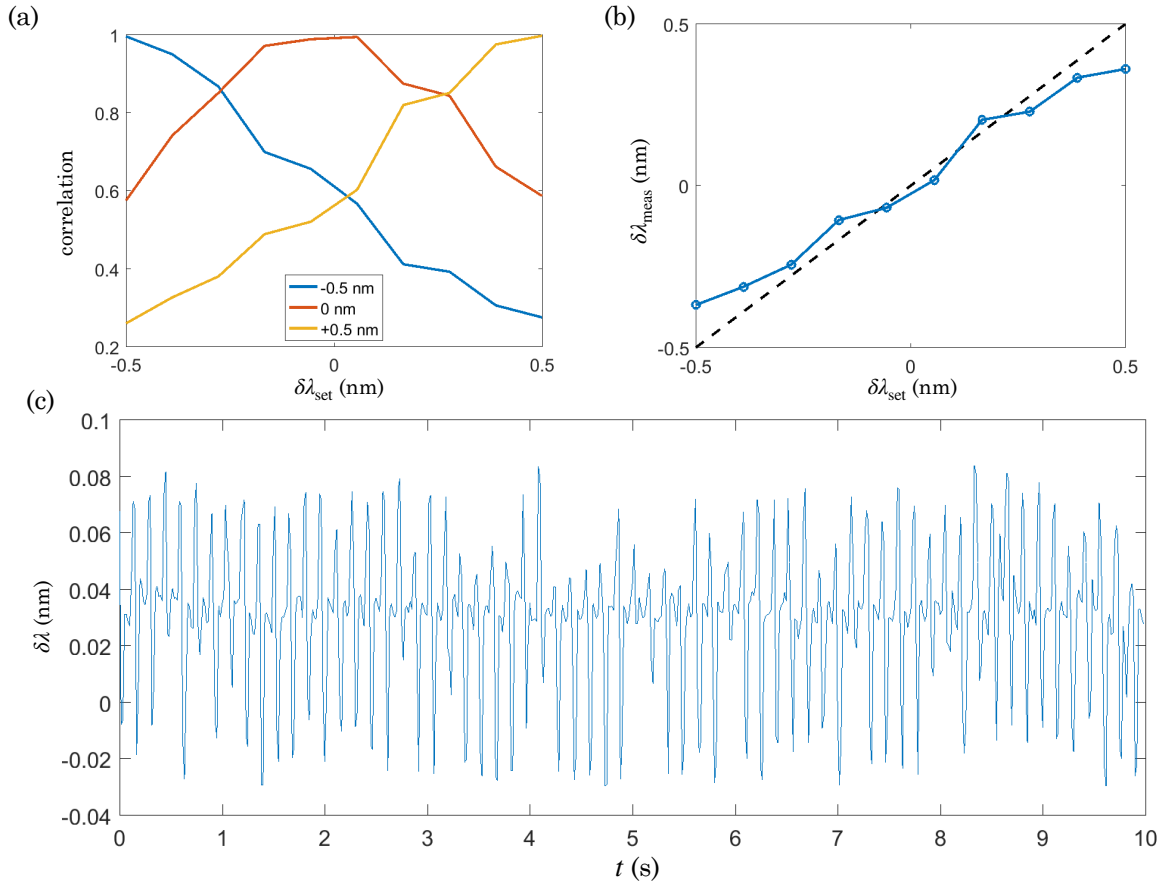


Figure A.1: **Laser fluctuations.** (a) Speckle correlation when varying the wavelength of the incoming light. The three colored lines represent the correlation with the speckle obtained from three different reference wavelengths. (b) Result of the calibration of (a): the variation of the correlation value enables to retrieve the wavelength initially set. (c) Observation of the laser jitter in time for the laser monochromatic mode.

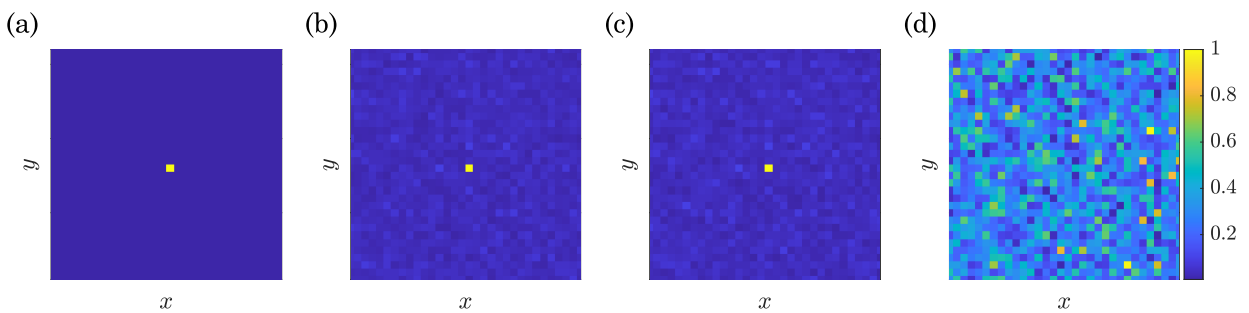


Figure A.2: **Impact of partial information to modulate the incoming wavefront for phase conjugation.** TM of size  $1024 \times 1024$  is simulated using random matrices. (a) Targeted output field amplitude. Field amplitude obtained for phase and amplitude control of the input vector (b), phase only control (c) and amplitude only control (d). In each plot all values are normalized by the higher amplitude such that the color scale is between 0 and 1 to all plots.

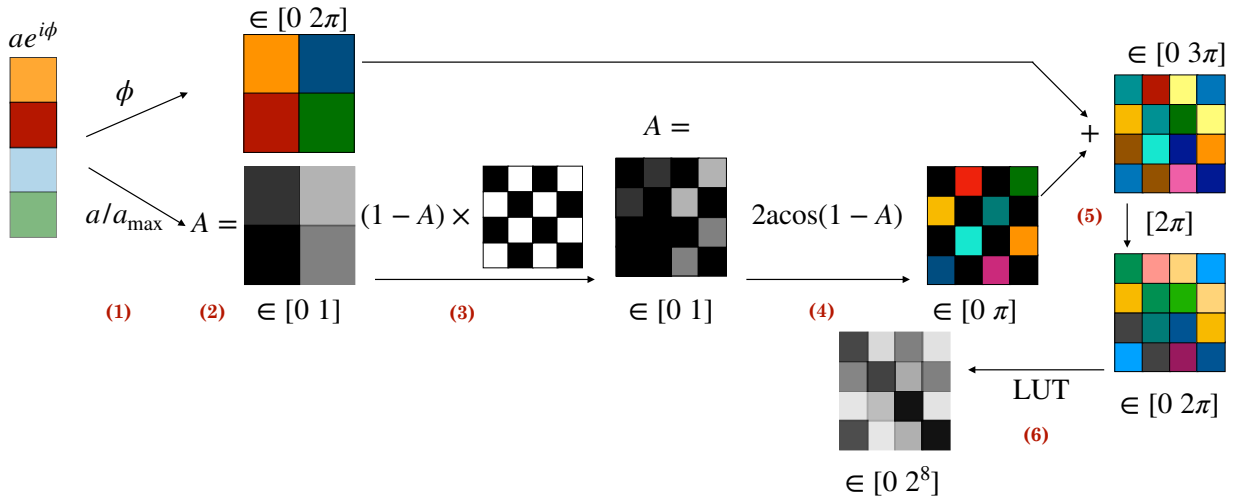


Figure A.3: **Schematic of the phase and amplitude control on the diffraction zero-order with a phase-only SLM.** (1) Separate phase (colors) and amplitude (grey level) of the vector and reshape them for the SLM. (2) Normalize amplitude  $A$  between 0 and 1. (3) Multiply  $1-A$  by the checkerboard. (4) Transform the amplitude modulation in a phase value. The factor of 2 makes the phases belong to  $[0 \pi]$ . (5) Sum the two phases (from phase itself and from amplitude) and keep its value modulo  $2\pi$ . (6) Transform the phase to grey level with the SLM LUT.

Implementing the phase and amplitude control with the zero order technique can be done following the steps illustrated in Fig. A.3.

Even if the enhancement (focus intensity over background intensity) we experimentally obtained when focusing light with a phase and amplitude vector is higher compared to the one of a phase-only input, it is noteworthy that the absolute intensity in the focus is higher for phase-only control than for phase and amplitude. Indeed in the latter case a non-negligible part of the light is not transmitted. In a more general way, highly uneven amplitudes in the input vector leads to a drop of transmission<sup>1</sup>. For this reason, in this thesis, we solely use phase-only control.

### A.3 Zero-delay stage position

This appendix aims at pointing out a subtlety about the zero-delay definition presented in Sec. 2.3.3. This feature, only visible for very thick and scattering media, was not observable with the medium used in Chap. 3 and Chap. 4, but is with the one used in Chap. 5.

#### A.3.1 Zero-delay position for very scattering media

For the detailed explanation of the zero-delay definition, see Sec. 2.3.3. Here is a brief recall: the laser is set in monochromatic mode, and for each wavelength in a set, we vary the delay-line length while acquiring the field for a plane wave input. For each delay-line length, we correlate the different fields with the central wavelength one (808 nm). We present the real parts of the correlations in the first column of Fig. A.4. We calculate and display their Fourier transform in the second column

<sup>1</sup>This issue has been noticed and discussed in [Guillon et al. 2017], where some adjustments to the amplitude normalization were hence performed.

of Fig. A.4. A fit enables to define the delay-line length associated to  $\tau = 0$ . The orange dashed line represents the cut (for  $k = 0$ ) plotted in the third column.

For scattering media not elongating too much an input pulse, the correlations are well defined and not excessively blurred by the spectral decorrelation, see Fig. 2.6(b), and the temporal origin is well marked. In Fig. A.4(a) the results are different while the same plane wave input is displayed on the SLM. The average pulse profile is even visible in Fig. A.4(a) third column. However the extraction of  $\tau = 0$  can still be performed.

An interesting effect shows up when measuring a TM ( $N_{\text{CCD}} = 225$ ,  $\gamma \sim 0.3$  and for a delay in the pulse  $\tau_1 \simeq 1$  ps) and performing the same extraction with the first singular vector displayed on the SLM. A shift of the temporal origin is observed. The value of this shift seems related to  $\tau_1$  (represented by the vertical green dashed line). This phenomenon is attributed to the light phase alignment induced by the SVD mask at  $\tau_1$ .

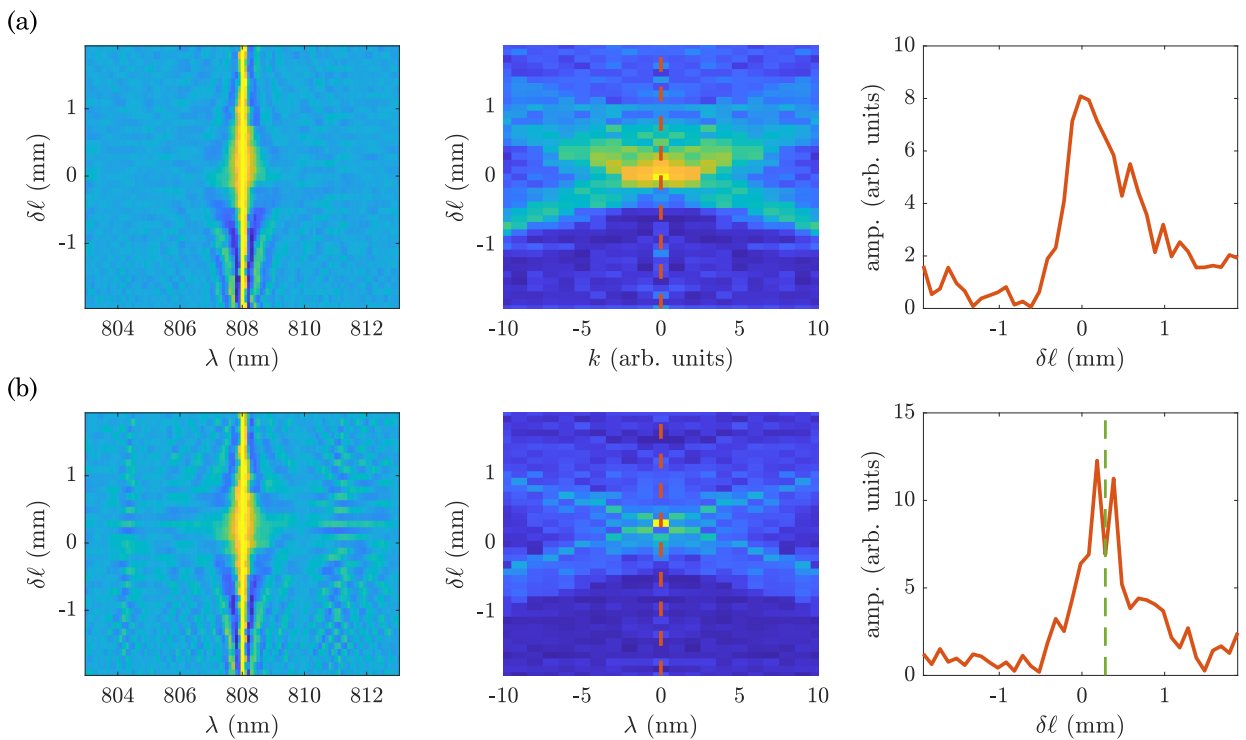


Figure A.4: **Zero-delay of a thick scattering medium.** The medium used is a thick layer of  $\text{TiO}_2$  suspended on a glass cover of transmission  $T \sim 0.16$ . First column represent the correlation real part, second column the absolute value of the Fourier transform and third column is a plot of the  $k = 0$  cut of the second column. (a) Plane wave input. (b) First singular vector of a TGTM measured at  $\tau_1 \simeq 1$  ps ( $\tau = 0$  being defined with (a)) with  $N_{\text{CCD}} = 225$  and  $\gamma \sim 0.3$ . The vertical green dashed line represents the position equivalent to  $\tau_1$ .

With no major implication in most of the experiments this feature needs to be taken into account when performing cross-effect experiments as in Sec. 5.4.

### A.3.2 Implication for the time to frequency cross effect

When performing the cross effect from time to frequency (i.e. two TGTM's measured for different delays  $\tau_1$  and  $\tau_2$  in the pulse, the first singular vector of their sum  $v_1^{(\tau_1+\tau_2)}$ ) is displayed on the SLM

while realizing a frequency scan to extract the field), the position of the delay-line matters. If it is set to the position  $\tau = 0$ , three delays are involved ( $\tau_1$ ,  $\tau_2$  and  $\tau_2 - \tau_1$ ) instead of one ( $\tau_2 - \tau_1$ ). Hence a correlation pattern involving both the checkerboard discussed in [Sec. 5.4](#) and fringes is visible. To prevent this, the stage position is set to  $\tau_1$  when performing this specific experiment.

## A.4 Evaluating the measurement quality of a transmission matrix

As presented in [Chap. 4](#) the quality of the TM measurement can be evaluated using its phase histogram. The idea is as follows: for a fully developed speckle the statistic is Rayleigh (inter alia, uniform phase repartition over  $[0, 2\pi]$ ). The TM corresponds to the reshaping of many speckle fields, obtained for a set of SLM inputs. Thus, under the Rayleigh speckle assumption, the phase histogram of the TM should be uniform. If this is generally well followed one can observe the apparition of a wavy behavior when measuring for instance TGTMs on the pulse tail (see [Fig. 4.8](#)). Where is this modulation coming from? How to interpret it? And ultimately, how to get rid of it (or at least limit it)? I present here a very minimalistic understanding of the effect.

Let us first recall the TM measurement. It is based on the field extraction for all the elements of the basis (Hadamard basis in this work). When the reference beam and scattered beam are balanced the contrast of their interference is maximal. Fitting the intensity variations gives access to the missing phase information. However if the beams are very unbalanced, or if a significant amount of non interfering light is also present on the acquired images, the intensity modulation induced by the phase-stepping becomes very small. Hence the extraction of the phase information is subject to errors. For instance when the intensity of a CCD pixel does not vary while performing phase-stepping, the resultant calculated field is null. Its amplitude is zero while its phase is not defined and arbitrarily fixed by the software. Thus when measuring a field (and thus a TM) in bad experimental conditions preferential phases are obtained<sup>2</sup>. When displaying the phase histogram, it is no longer flat as expected for a Rayleigh speckle but peaked around one phase value.

After measuring a TM in the Hadamard basis I usually perform a change of basis to the canonical basis. This step requires to multiply the initial matrix by the Hadamard matrix (change-of-basis matrix). Because all Hadamard elements are +1 or -1, the previous single preferential phase is split into two  $\pi$  apart. This explains the phase histogram observed experimentally.

It is very practical to note from this effect that the quality of the TM measurement can thus be evaluated simply by looking at its phase histogram. The larger the amplitude of the fluctuations the worse the measurement.

In order to improve the field extraction one solution consists of increasing the number of phase steps at the cost of also increasing the measurement time. For these reasons in this work I mainly extracted the field with 4 phases for monochromatic light or in early times in the pulse while using more (usually 10) when working in the pulse tail.

## A.5 Some information contained in the transmission matrix

There is a lot of information contained in the TM. In this appendix I will briefly summarize which information can be easily extracted from a TM.

---

<sup>2</sup>The amount of the over representation of that specific phase is obviously proportional to the number of zero field values in the TM.

### A.5.1 Speckle information

Due to the TM construction from the different fields measured for different SLM inputs, information on the speckle is inherently present. However one has to keep in mind that the CCD camera pixels binning (when measuring the TM) is to be taken into account when comparing some results with the direct measurement of the field. I will discuss here a method to access the speckle grain size from the TM itself. The speckle grain size extraction has been discussed in [Sec. 3.1.1](#). Because it relies on the speckle autocorrelation a minimal resolution is required. However in the TM usually the binning is such that the speckle grains are not well resolved. Nonetheless it is still possible to access this information. Indeed the binning is done to prevent any redundant information on the TM (it enables to have quicker and smaller measurements). Any redundant information would impact the rank of the TM. For a random matrix (independently from the random probability law) the rank corresponds to the participation number ( $N_{\text{part}}$ ) defined in [[Davy et al. 2012](#)] by

$$N_{\text{part}} = \frac{(\sum_n \tau_n)^2}{\sum_n \tau_n^2}, \quad (\text{A.1})$$

where  $\tau_n$  are the eigenvalues of  $T^\dagger T$ . In case of a perfectly binned TM the ratio of the participation number to the matrix smaller dimension, called normalized participation number and denoted  $\tilde{N}_{\text{part}}$ , is 1. Deviations from 1 brings information on the redundant information still present and hence to the remaining grain size. Taking the initial binning value  $N_{\text{bin}}$  into account, one gets the initial grain size by

$$\text{grain size} = \frac{N_{\text{bin}}}{\tilde{N}_{\text{part}}}. \quad (\text{A.2})$$

Even more information can be extracted from the TM. For instance the TM speckle  $k$ -space information enables anticipating the possibility of a speckle grain size control, discussed in details in [Sec. 3.2.3](#).

### A.5.2 SLM information

The information of the contribution of each SLM mode can be extracted from the TM and is discussed in [Sec. 2.3.5.2](#). From the modes' contribution information one can extract the effective number of controlled modes ( $N_{\text{SLM}}^{\text{eff}}$ ) which on some experimental configurations is different from  $N_{\text{SLM}}$ . The knowledge of  $N_{\text{SLM}}^{\text{eff}}$  is primordial to determine a more precise value of  $\gamma$ , the degree of control. It is important to compare the experimental results to simulations or analytical predictions.

# B | Theoretical complements and results

## B.1 Speckle grains dimensions

This appendix present a quick evaluation of the speckle grain dimensions, see [Gatti et al. 2008; Magatti et al. 2009] for more advanced models. Let us consider an illuminated area  $\Delta$  and a speckle observed at a position  $z_C$  (such that  $z_C \gg \Delta$ ) along the axial direction as illustrated in Fig. B.1. Considering two extremal points on the illumination area  $A$  and  $B$  we compute the optical path

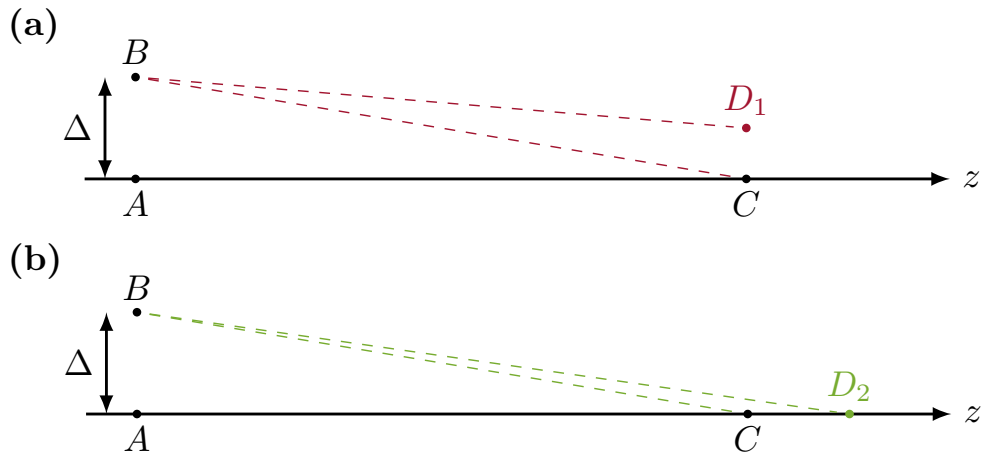


Figure B.1: **Three dimensional speckle.** Evaluation of the transverse speckle grain size (a) and longitudinal (b).

difference  $\delta$  to reach  $C$ :

$$\delta = BC - AC = \sqrt{z_C^2 + \Delta^2} - z_C \simeq z_C \left( 1 + \frac{\Delta^2}{2z_C^2} \right) - z_C = \frac{\Delta^2}{2z_C} + \mathcal{O}\left(\frac{1}{z_C^3}\right). \quad (\text{B.1})$$

Let us now consider the variations of  $\delta$  when moving away from  $C$  either radially, see Fig. B.1(a) or longitudinally, see Fig. B.1(b).

### Transverse speckle grain size

Similarly to Eq. B.1 the path  $\delta' = BD - AD$  can be calculated.

$$\begin{aligned}
\delta' &= BD_1 - AD_1 \\
&= \sqrt{z_C^2 + (D_1C - \Delta)^2} - \sqrt{z_C^2 + D_1C^2} \simeq z_C \left( 1 + \frac{(D_1C - \Delta)^2}{2z_C^2} \right) - z_C \left( 1 + \frac{D_1C^2}{2z_C^2} \right) \\
&= z_C \left( 1 + \frac{(D_1C - \Delta)^2}{2z_C^2} \right) - z_C \left( 1 + \frac{D_1C^2}{2z_C^2} \right) \\
&= -\frac{D_1C\Delta}{z_C} + \frac{\Delta^2}{2z_C} + \mathcal{O}\left(\frac{1}{z_C^3}\right).
\end{aligned} \tag{B.2}$$

The variation between  $\delta$  and  $\delta'$  is given by  $-\frac{D_1C\Delta}{z_C} + \mathcal{O}\left(\frac{1}{z_C^3}\right)$ . The speckle transverse width  $b_\perp$  can be defined as the distance  $D_1C$  such that  $|\delta - \delta'| \simeq \lambda/2$ . Thus one gets,

$$b_\perp \approx \frac{1}{2} \frac{\lambda z_C}{\Delta}. \tag{B.3}$$

### Longitudinal speckle grain size

Along the same lines for the longitudinal speckle dimension,

$$\delta - \delta' = \frac{\Delta^2}{2z_C} - \frac{\Delta^2}{2(z_C + CD_2)} = \frac{\Delta^2}{2z_C} \left( 1 - \frac{1}{1 + CD_2/z_C} \right) \simeq \frac{\Delta^2}{2z_C} \frac{CD_2}{z_C} \tag{B.4}$$

One obtains  $b_{//}$  for  $|\delta - \delta'| \simeq \lambda/2$

$$b_{//} \approx \frac{\lambda z_C^2}{\Delta^2}. \tag{B.5}$$

## B.2 Elongated speckle grains with unidimensional singular value decomposition

In this appendix I will present an alternative method for producing elongated speckles using the SVD without resorting to the Fourier filtering of Sec. 3.2.1. This technique will be limited to the creation of asymmetric speckle grains and requires to position the collection microscope objective in such a way that the  $k$ -space is inhomogeneous. The technique is less intuitive than the Fourier filtering method but due to the simplicity of its implementation and the robust results it gives it is worth mentioning.

The idea is to only perform the SVD along one dimension of the output region (for instance along  $y$ ). Doing so would enable to gather the Fourier information only along the chosen dimension and hence select the input vectors that would enlarge the speckle grain solely on this direction. However, written as it is, in a matrix form, all the CCD pixels contribute to the TM output dimension. It is then necessary to remember that the matrix form is a useful manner of dealing with the ‘‘TM’’ object. But this object can be seen as a four order tensor: each input and output being itself a second order tensor. Both for input and output the spatial dimensions have been merged for practical reasons. Here we can decide to separate the two output dimensions to display the TM as a cube, see Fig. B.2. The three axes being the SLM dimension (size  $N_{\text{SLM}}$ ), the  $x$  dimension of size  $\sqrt{N_{\text{CCD}}}$  and the  $y$  dimension of size  $\sqrt{N_{\text{CCD}}}$ <sup>1</sup>. For different positions  $x_0$  one can extract a sub-TM  $T_{x_0}$  which only bears

<sup>1</sup>We assume for simplicity that the ROI is square.

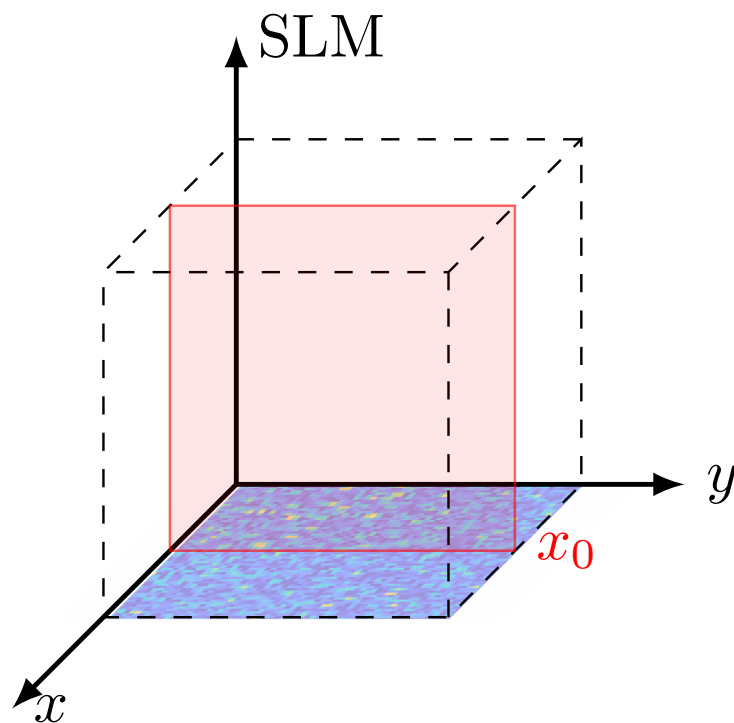


Figure B.2: **1D-SVD principle.** The TM is displayed as a cube by separating  $x$  and  $y$  dimension of the output. Each slice then represents the speckle observed when displaying on the SLM one element of the basis. For a fixed value of  $x$  ( $x_0$ ), the matrix  $T_{x_0}$  (light red area), is extracted.

information on one column of the ROI. Taking the SVD of  $T_{x_0}$  gives access to the corresponding singular vectors. Performing the same operation for all  $x_0$  in the ROI leads to a set of singular vectors. Summing together all the first singular vectors one obtains the so-called first 1D singular vector.

Experimentally obtained speckles from the first singular vector  $v_1$  of the regular SVD and the 1D SVD discussed above are shown in Fig. B.3. In the case of the regular SVD the grains are enlarged in both  $x$  and  $y$  directions whereas for the one-dimensional SVD the elongation only happens in one direction leading to elongated speckle grains.

## B.3 Intensity and field amplitude enhancements

This appendix presents some analytical results for the enhancements expected for the global focusing and the singular vectors. Both the intensity and the field amplitude enhancements are derived. The intensity enhancement scaling with  $\gamma$  is also discussed. The case of the field amplitude enhancement is more complicated: a derivation from the field amplitude is not straightforward. A link with the intensity statistic however exists in case of Rayleigh speckles.

### B.3.1 Intensity enhancement

Let us first focus on the derivation of the intensity enhancement. The latter is defined as the full intensity on the camera (summed over the whole ROI) of the input vector of interest divided by the

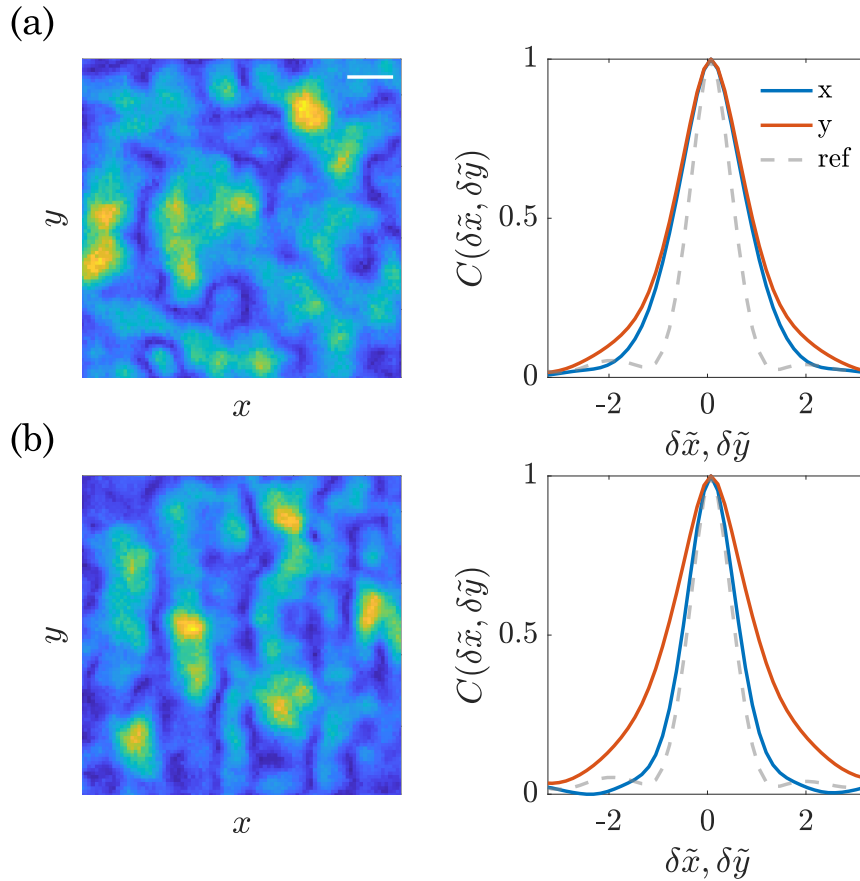


Figure B.3: **Anisotropic speckles with the 1D-SVD.** (a) Right panel: field amplitude for  $v_1$  (scale bar:  $5\ \mu\text{m}$ ) Left panel: associated autocorrelation plotted along the  $x$  (blue) and  $y$  (orange) directions compared to the reference speckle autocorrelation (grey dashed). The  $x$ -axes are rescaled by the FWHM of the reference speckle autocorrelation. (b) The same for the 1D SVD. The autocorrelation curves are averaged over 9 realizations. Figure adapted from [Devaud et al. 2021b].

full intensity for a random vector<sup>2</sup>. In this appendix we will focus on two different types of input vectors: the global-focus and the SVD. Given a TM  $T_{(n,m)}$  (size  $n \times m$  given in brackets on the bottom right of the matrix), the global-focus input  $G_{(m,1)}$  can be calculated. It is defined such that  $T_{(n,m)}G_{(m,1)} = I_{(n,1)}$  where the coefficients of  $I$  are all unity.

### B.3.1.1 Transmitted field

To express the transmitted field we decompose the vector onto the singular vectors of  $T$ . We have  $T_{(n,m)} = U_{(n,n)} \times S_{(m,m)} \times V_{(m,m)}^\dagger$ , giving

$$G_{(m,1)} = T_{(m,n)}^\dagger I_{(n,1)} = V_{(m,m)} S_{(m,n)}^\dagger U_{(n,n)}^\dagger I_{(n,1)} = \sum_i^m s_i \sum_j^n u_{j,i}^* V_i, \quad (\text{B.6})$$

<sup>2</sup>In simulations it is important to well normalize the input vectors.

where  $s_i$  are the singular values and  $u_{j,i}$  the elements of  $U$ . On the SLM normalized vectors are displayed so that we have a field at the output  $E_G$ :

$$\tilde{G} = \frac{G}{\|G\|_2} = \frac{\sum_i s_i \sum_j u_{j,i}^* V_i}{\sqrt{\sum_i |s_i \sum_j u_{j,i}^*|^2}} \rightarrow E_G = \frac{\sum_i s_i^2 \sum_j u_{j,i}^* U_i}{\sqrt{\sum_i |s_i \sum_j u_{j,i}^*|^2}}. \quad (\text{B.7})$$

Similarly, for a random input vector,  $R$  can be decomposed onto the singular vectors of  $T$  with projection coefficients  $\beta_i$  and normalized ( $\tilde{R}$ ) to get a field  $E_R$ :

$$\tilde{R} = \frac{R}{\|R\|_2} = \frac{\sum_i \beta_i V_i}{\sqrt{\sum_i |\beta_i|^2}} \rightarrow E_R = \frac{\sum_i s_i \beta_i U_i}{\sqrt{\sum_i |\beta_i|^2}}. \quad (\text{B.8})$$

And finally the  $i^{\text{th}}$  singular vector gives an field output:

$$V_i \rightarrow E_i = s_i U_i. \quad (\text{B.9})$$

### B.3.1.2 Intensity enhancement

From the fields the full intensity can be directly calculated by taking the transpose conjugate of the vector times itself. For the random input, the total output intensity is then

$$I_R = \frac{\sum_i s_i^2 |\beta_i|^2}{\sum_i |\beta_i|^2} \simeq \langle s^2 \rangle \text{ (weighted arithmetic mean)}. \quad (\text{B.10})$$

Caution here the mean is computed over  $m$  values, see [Comm. B.3.1](#).

#### Comment B.3.1.

Usually for the MP law singular values of a matrix of size  $m \times n$  are defined by

$$\tilde{s}_i^{\text{MP}} = \frac{s_i}{\sqrt{\frac{1}{\min(n,m)} \sum_{j=1}^{\min(n,m)} s_j^2}}, \quad (\text{B.11})$$

this regardless of the respective values of  $m$  and  $n$ , as mentioned in [Sec. 1.4.2.2](#). However for a TM,  $m$  and  $n$  have a physical meaning, that is the number of controlled modes ( $N_{\text{SLM}}$ ) and the degrees of freedom ( $N_{\text{CCD}}$ ). They are no longer interchangeable. That is the reason why two normalizations will be adopted: The MP law one (defined above) to strictly follow the quarter-circle law and the more physical one (defined below). When studying transmission related phenomena, the mean over the singular values is computed over all singular values (the one equal to 0 should be also included as they bring information on the transmission). The alternative normalization is then given by

$$\tilde{s}_i = \frac{s_i}{\sqrt{\frac{1}{N_{\text{SLM}}} \sum_{j=1}^{N_{\text{SLM}}} s_j^2}}. \quad (\text{B.12})$$

It is noteworthy that for  $N_{\text{SLM}} > N_{\text{CCD}}$  (our experimental case), one has  $\tilde{s}_i = \tilde{s}_i^{\text{MP}} / \sqrt{\gamma}$ .

The same holds for the global-focusing, involving this time the product of two weighted arithmetic mean, giving

$$I_G = \frac{\sum_i s_i^4 |\sum_j u_{j,i}^*|^2}{\sum_i s_i^2 |\sum_j u_{j,i}^*|^2} \approx \frac{\langle s^4 \rangle}{\langle s^2 \rangle}. \quad (\text{B.13})$$

However a difference with the random input vector is to note. The weight coefficients are not independent of the singular values. Hence Eq. B.13 is a rough approximation and will not be an exact fit to the data. It nonetheless enables to reach an approximate enhancement value and a scaling. For the singular vector one trivially has

$$I_i = s_i^2. \quad (\text{B.14})$$

The intensity enhancements  $\eta_I^R$ ,  $\eta_I^G$  and  $\eta_I^i$  can hence be expressed. They are compared in the extreme case of  $i = 1$  ( $v_1$ ),

$$\eta_I^R \simeq 1 \leq \eta_I^G \approx \frac{\langle s^4 \rangle}{\langle s^2 \rangle^2} \leq \eta_I^1 \simeq \frac{s_1^2}{\langle s^2 \rangle} = \tilde{s}_1^2. \quad (\text{B.15})$$

The first inequality comes from Jensen's theorem and the second from the mean value theorem.

### B.3.1.3 Scaling with $\gamma$

From the MP distribution  $\mu_\rho$  one can compute its moments and express a scaling of the intensity enhancements. The formula is

$$\int x^r d\mu_\rho(x) = \sum_{k=0}^{r-1} \frac{\rho^k}{k+1} \binom{r}{k} \binom{r-1}{k}, \quad r \geq 1, \quad (\text{B.16})$$

where  $\rho = 1/\gamma$  with our definitions ( $\gamma = N_{\text{CCD}}/N_{\text{SLM}}$ ). Because we use singular values and not eigenvalues we need to access the first and second moments of this distribution<sup>3</sup>. We obtain,

$$\langle s^4 \rangle = 1 + 1/\gamma \text{ and } \langle s^2 \rangle = 1, \quad (\text{B.17})$$

giving us a scaling for the global-focus. For the first singular vector the MP distribution needs to be used again to express the scaling of the first singular value  $s_1$ . It is given by  $1 + 1/\sqrt{\gamma}$ . In conclusion we should get for the scalings with  $\gamma$

$$\eta_I^G \approx 1 + \frac{1}{\gamma} \text{ and } \eta_I^1 \simeq \left(1 + \frac{1}{\sqrt{\gamma}}\right)^2. \quad (\text{B.18})$$

Note that because  $\gamma \geq 0$  we recover  $\eta_I^1 \geq \eta_I^G$ .

Despite the information gathered on the intensity enhancement, there is no direct way of computing the field amplitude enhancement. Because experimentally this is a quantity we can measure (and that I usually work with only to avoid confusions between intensity and field amplitude), it would be convenient to have an analytical formula. We are going to see in the next section that for Rayleigh speckles field amplitude and intensity enhancement are linked.

## B.3.2 Field amplitude enhancement

In a general frame there is no easy way of linking the intensity enhancement and the amplitude enhancement. It is noteworthy that this corresponds to the the comparison of  $\|\cdot\|_1$  and  $\|\cdot\|_2$  as  $\eta_I = \|\cdot\|_2^2$  and  $\eta_E = \|\cdot\|_1$ . One knows that in general there is  $\|\cdot\|_\infty \leq \|\cdot\|_2 \leq \|\cdot\|_1$ . Can we say something more?

Yes!

---

<sup>3</sup>Not the second and fourth moments.

When looking at the field statistics,  $\|\cdot\|_1$  approximates the first moment of the distribution (mean), and  $\|\cdot\|_2^2$  approximates the second moment (variance + mean squared). If the field statistics belongs to a family of distribution parametrized by a scale coefficient  $\sigma$ , then both  $\|\cdot\|_1$  and  $\|\cdot\|_2$  scale with  $\sigma$ , and thus their ratio is a constant independent of  $\sigma$ .

This is the case for the Rayleigh distribution for which we will explicitly derive the relation between  $\|\cdot\|_1$  and  $\|\cdot\|_2$ .

**Comment B.3.2.**

A Rayleigh statistic has a density probability function given by

$$f(x; \sigma^2) = \frac{x}{\sigma^2} \exp\left(\frac{-x^2}{2\sigma^2}\right), \quad (\text{B.19})$$

where  $x \in [0, \infty[$ . Hence  $\|\cdot\|_1$  and  $\|\cdot\|_2$  are respectively given by

$$\begin{cases} \|\cdot\|_2 \simeq \sqrt{\int_{\mathbb{R}_+} \frac{x^2}{\sigma^2} x e^{\frac{-x^2}{2\sigma^2}} = \sqrt{2}\sigma,} \\ \|\cdot\|_1 \simeq \int_{\mathbb{R}_+} \frac{x}{\sigma^2} x e^{\frac{-x^2}{2\sigma^2}} = \sqrt{\frac{\pi}{2}}\sigma. \end{cases} \quad (\text{B.20})$$

It results that for  $a$  and  $b$  two vectors following a Rayleigh statistic,

$$\frac{\|a\|_1}{\|b\|_1} = \frac{\|a\|_1}{\|a\|_2} \frac{\|b\|_2}{\|b\|_1} \frac{\|a\|_2}{\|b\|_2} \simeq \frac{\|a\|_2}{\|b\|_2}. \quad (\text{B.21})$$

It does not depend on the values of  $\sigma_a$  and  $\sigma_b$ !

Now because the amplitude enhancement  $\eta_E$  is the ratio of  $\|\cdot\|_1$ , and that the intensity enhancement  $\eta_I$  corresponds to the ratio of  $\|\cdot\|_2^2$ , one gets

$$\boxed{\eta_E \simeq \sqrt{\eta_I}} \quad (\text{B.22})$$

**Comment B.3.3.**

It works also for the exponential distribution.

In conclusion, when sending different singular vectors the amplitude enhancement may be simply expressed in terms of the normalized singular values. This is because both the fields obtained for the random input (or plane wave input) and the singular vector follow Rayleigh statistics. However this trick no longer holds when performing a global-focus as the field distribution is then Ricin.

### B.3.3 Enhancement simulations for the SVD and the global-focus

To illustrate the previous points: (i) singular vectors amplitude enhancement, (ii) intensity enhancements scalings and (iii) better enhancement for the first singular vector than the global focus; simulations are presented in Fig. B.4. They are realized using the simple RM model without including experimental limitations (as the speckle grain size). For Fig. B.4(a), we generate a TM with  $N_{\text{SLM}} = 400$  and  $N_{\text{CCD}} = 225$ . The field enhancement for phase and amplitude control is compared to the normalized<sup>4</sup> singular values, for which we obtain a very nice similarity. We also plot the phase-only enhancement to give an idea of the enhancement reduction. In Fig. B.4(b) we compare intensity

<sup>4</sup>Using the SLM dimension.

enhancements between the first singular vector (solid blue line) and the global focus (orange blue line). The phase-only limitations are represented with the same colors in dashed lines. The value of  $N_{\text{SLM}}$  is fixed to 256 and  $N_{\text{SLM}}$  varies to change the degree of control. Both intensity enhancements are plotted as functions of  $1/\gamma$  and their respective scalings, given in Eq. B.18, are presented with black dotted-dashed lines. One can see that as predicted the evolution of  $\eta_1^1$  follows well its scaling but that  $\eta_1^G$  deviates from it. The enhancement is larger indicating that more weight is given to high transmissive channels than to low ones.

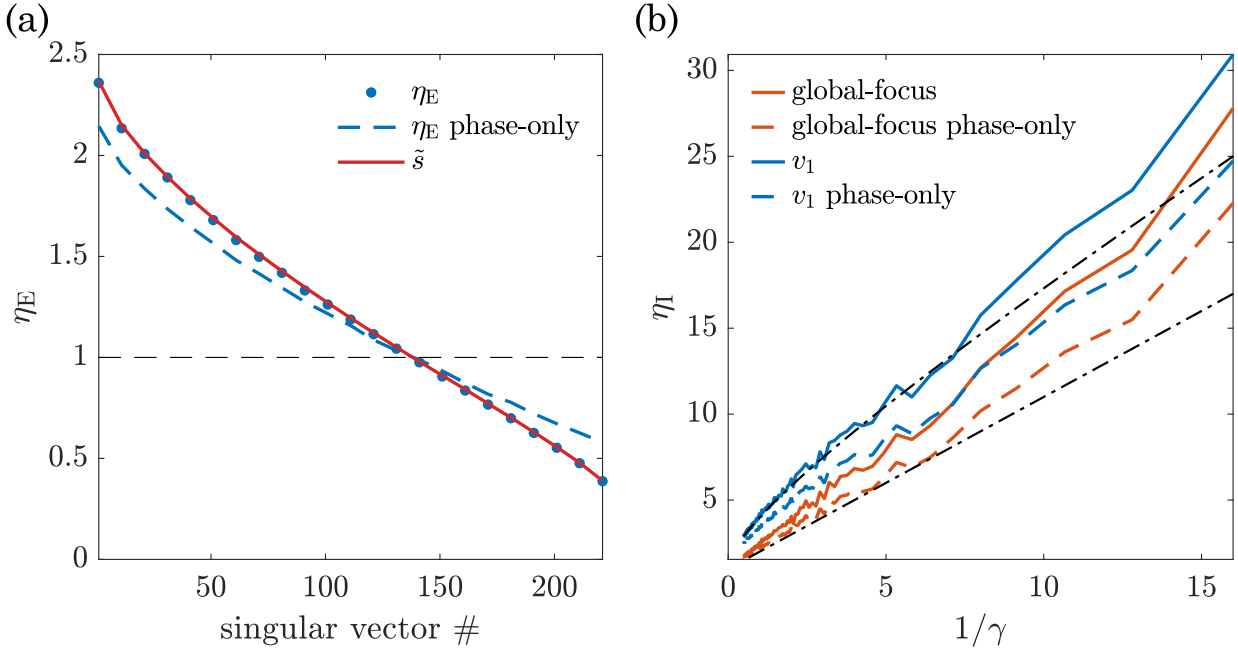


Figure B.4: **Amplitude enhancement prediction and intensity scalings.** (a) Field amplitude enhancement values obtained for different singular vectors in case of full control (blue dots) or phase-only control (blue dashed line) compared to the normalized singular values  $\tilde{s}$  (red line). The simulated TM is of size  $225 \times 400$  and the data are averaged over 10 realizations. (b) Comparison of intensity enhancement values and predicted scalings with the degree of control  $\gamma$ . In blue the enhancement for the  $v_1$  and in orange the enhancement for the global-focusing vector. For both the phase and amplitude control is plotted with solid lines whereas the phase-only is plotted with dashed lines. To vary  $\gamma$ , the number of  $N_{\text{SLM}}$  is kept fixed at 256 and  $N_{\text{CCD}}$  varies. The data are averaged over 10 realizations.

## B.4 Phase-only impact on the enhancement

This appendix aims at investigating the impact of phase-only control on the enhancement. In Fig. 4.5(b), recalled in Fig. B.5(a), one observes that the predicted amplitude enhancement is not perfectly matching the measured one. The question is: can we attribute this discrepancy to phase-only control? To find an answer enhancement simulations are performed using the measured TM. In Fig. B.5(b) the simulated enhancement obtained by propagating different singular vectors for phase and amplitude (red curve) or phase-only (blue curve) using the measured TM are presented. For both plots, the ratio between phase-only enhancements and phase and amplitude enhancements are presented in Fig. B.5(c). It is visible that the trend is similar so that the discrepancy between enhancement

predictions and experiments can chiefly be attributed to phase-only control.

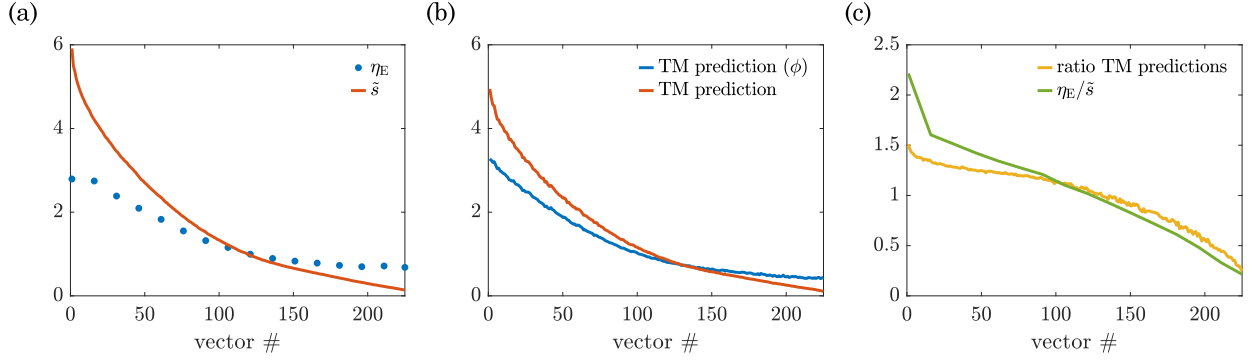


Figure B.5: **Phase-only impact on the amplitude enhancement.** (a) Reminder of the enhancement results presented in Fig. 4.5(b). The normalized singular values  $\tilde{s}$  are compared to the measured enhancements (blue dots). (b) Simulated enhancement obtained from the experimental TM for phase and amplitude control (red curve) and phase-only control (blue curve). (c) Ratio between phase-only and phase and amplitude enhancements for the TM-based predictions (yellow) and the experimental observation and theoretical expectation (green curve).

## B.5 SVD-based correlations: derivations and results

This appendix aims at developing some aspects of the SVD-based correlation technique. The calculations to reach Eq. 5.6 are derived in Sec. B.5.1 and an additional derivation for unitary random matrices is developed in Sec. B.5.2.

### B.5.1 For random matrices

Recall that  $T_1$  and  $T_2$  are two random matrices of size  $n \times m$ , where all coefficients are independent and have the same complex normal distribution  $\mathcal{N}_{\mathbb{C}}(0, \sigma^2)$ . Let us fix two parameters  $\alpha$  and  $\beta$ , and define:

$$M = \frac{e^{i\beta}T_1 + e^{i\alpha}T_2}{2} \quad \text{and} \quad \Delta = \frac{e^{i\beta}T_1 - e^{i\alpha}T_2}{2}$$

Using Comm. B.5.1,  $M$  and  $\Delta$  are independent, and all of their coefficients have the same complex normal distribution  $\mathcal{N}_{\mathbb{C}}(0, \sigma^2/2)$ . In particular, we draw  $M \in \mathcal{M}_{n,m}(\mathbb{C})$  which is now a fixed matrix, but  $\Delta$  is still random.

#### Comment B.5.1.

We denote  $\mathcal{N}(x, \sigma^2)$  the real normal distribution, of mean  $x \in \mathbb{R}$  and standard deviation  $\sigma \in \mathbb{R}_+^*$ ; and denote  $\mathcal{N}_{\mathbb{C}}(z, \sigma^2)$  the complex normal distribution, of mean  $z \in \mathbb{C}$  and standard deviation  $\sigma \in \mathbb{R}_+^*$ . Recall that we have

$$\forall z \in \mathbb{C}, \forall \sigma \in \mathbb{R}_+^*, \quad Z \sim \mathcal{N}_{\mathbb{C}}(z, \sigma^2) \Leftrightarrow \begin{cases} \Re(Z) \text{ and } \Im(Z) \text{ are independent} \\ \Re(Z) \sim \mathcal{N}(\Re(z), \sigma^2/2) \\ \Im(Z) \sim \mathcal{N}(\Im(z), \sigma^2/2) \end{cases}$$

Recall that the complex standard normal distribution has mean 0 and standard deviation 1. If  $Z \sim \mathcal{N}_{\mathbb{C}}(0, 1)$  and  $z \in \mathbb{C}$ , we have  $zZ \sim \mathcal{N}_{\mathbb{C}}(0, |z|^2)$ . In particular, a complex normal

distribution of mean 0 is invariant by multiplication with a complex of modulus 1.

Finally, given two independent random variables  $X$  and  $Y$  with the same (complex) normal distribution, the sum  $S = X + Y$  and the difference  $D = X - Y$  are independent. Indeed,  $S$  and  $D$  are jointly normally distributed, and are uncorrelated:

$$\mathbb{E}[SD] - \mathbb{E}[S] \cdot \mathbb{E}[D] = \underbrace{\mathbb{E}[X^2 - Y^2]}_{=0} - \mathbb{E}[X + Y] \cdot \underbrace{\mathbb{E}[X - Y]}_{=0} = 0$$

We write the singular value decomposition of the matrix  $2M = VSU^\dagger$ , where  $U \in \mathcal{M}_{m,m}(\mathbb{C})$  and  $V \in \mathcal{M}_{n,n}(\mathbb{C})$  are unitary matrices and  $S \in \mathcal{M}_{n,m}(\mathbb{R}_+)$  is diagonal. Let  $X$  and  $Y$  be the right and left singular vectors associated to a singular value  $\mu$ . More precisely,  $\mu$  is the  $i$ -th coefficient of  $S$  for some  $i$ , and  $X$  and  $Y$  are respectively the  $i$ -th column of  $U$  and  $V$ . We have

$$(2M)X = \mu Y \quad \text{and} \quad Y^\dagger(2M) = \mu X^\dagger$$

Define now the correlation  $C(T_1X, T_2X)$  between vectors  $T_1X$  and  $T_2X$ .

$$C(T_1X, T_2X) = \frac{X^\dagger T_1^\dagger T_2X}{\|T_1X\|_2 \cdot \|T_2X\|_2}$$

Rewriting  $T_1X$  and  $T_2X$  using  $M$  and  $\Delta$ , we obtain

$$\begin{aligned} e^{i\beta} T_1X &= (M + \Delta)X = \frac{\mu}{2}Y + \Delta X \\ e^{i\alpha} T_2X &= (M - \Delta)X = \frac{\mu}{2}Y - \Delta X \end{aligned}$$

We define the random variable  $Z = Y^\dagger \Delta X$ . Summing over coefficients of  $\Delta$ , we show that  $Z$  is normally distributed with mean 0 and variance  $\|X\|_2^2 \cdot \|Y\|_2^2 \cdot \sigma^2/2$ . Because  $X$  and  $Y$  are unit vectors,  $Z \sim \mathcal{N}_{\mathbb{C}}(0, \sigma^2/2)$ .

$$\begin{aligned} \|T_1X\|^2 &= X^\dagger T_1^\dagger T_1X = \left(\frac{\mu}{2}Y^\dagger + X^\dagger \Delta^\dagger\right) \left(\frac{\mu}{2}Y + \Delta X\right) = \frac{\mu^2}{4} + \|\Delta X\|_2^2 + \mu \Re(Z) \\ \|T_2X\|_2^2 &= X^\dagger T_2^\dagger T_2X = \left(\frac{\mu}{2}Y^\dagger - X^\dagger \Delta^\dagger\right) \left(\frac{\mu}{2}Y - \Delta X\right) = \frac{\mu^2}{4} + \|\Delta X\|_2^2 - \mu \Re(Z) \end{aligned}$$

We are finally ready to write the correlation between  $T_1X$  and  $T_2X$ .

$$\begin{aligned} C(T_1X, T_2X) &= \frac{e^{i(\beta-\alpha)} \left(\frac{\mu}{2}Y^\dagger + X^\dagger \Delta^\dagger\right) \left(\frac{\mu}{2}Y - \Delta X\right)}{\sqrt{\frac{\mu^2}{4} + \|\Delta X\|_2^2 + \mu \Re(Z)} \sqrt{\frac{\mu^2}{4} + \|\Delta X\|_2^2 - \mu \Re(Z)}} \\ &= e^{i(\beta-\alpha)} \cdot \frac{\frac{\mu^2}{4} - \|\Delta X\|_2^2 - i\Im(Z)}{\sqrt{\left(\frac{\mu^2}{4} + \|\Delta X\|_2^2\right)^2 - \mu^2 \Re(Z)^2}} \end{aligned}$$

To reach an analytical formula, one now needs to be able to express  $\|\Delta X\|_2^2$ . In [Comm. B.5.2](#), we use the fact that  $\Delta$  is a random matrix, with coefficients having a complex normal distribution  $\mathcal{N}_{\mathbb{C}}(0, \sigma^2/2)$ , and we show that  $\|\Delta X\|_2^2 \approx n \cdot \sigma^2/2$ .

**Comment B.5.2.**

Let's consider  $R \in \mathcal{M}_{n,m}(\mathbb{C})$ , elements of which are random variables with a complex normal distribution  $\mathcal{N}_{\mathbb{C}}(0, \sigma^2)$ , and  $X \in \mathcal{M}_{m,1}(\mathbb{C})$  an arbitrary unit vector. One wants to compute  $\|RX\|_2^2$ .

A short calculation gives  $\|RX\|_2^2 = \sum_{i=1}^n (\sum_{j=1}^m m_{ij}x_j)^2$ . For each  $j$ ,  $x_j$  is a constant, hence  $m_{ij}x_j$  is normally distributed with standard deviation  $x_j \cdot \sigma$ . The sum of normally distributed random variables is also normally distributed, with a standard deviation equal to the square root of the sum of each standard deviation squared. Hence, for all  $i$ , the random variable  $\sum_{j=1}^m m_{ij}x_j$  is normally distributed, with a standard deviation equal to  $\|X\|_2 \cdot \sigma = \sigma$ .

Therefore,  $\|RX\|_2^2$  is the sum of  $n$  independent random variables, each of them equal to the square of a normal law of standard deviation  $\sigma$ . The expected value of the square of a random variable of mean 0 is equal to the square of the standard deviation. Thus, by linearity of expectation, the expected value of  $\|RX\|_2^2$  is equal to  $n \cdot \sigma^2$ . To prove that the value of  $\|RX\|_2^2$  is concentrated around its mean, one can notice that  $\|RX\|_2^2/\sigma^2$  follows a  $\chi_n^2$  distribution, for which tail inequalities are known (see Lemma 1 from [Laurent et al. 2000]).

$$\forall a > 0, \quad \mathbb{P}(2\sqrt{na} \leq \|RX\|_2^2/\sigma^2 - n \leq 2\sqrt{na} + 2a) \geq 1 - 2e^{-a}$$

When  $a = 4$ , this inequality shows that  $4\sqrt{n} \leq \|RX\|_2^2/\sigma^2 - n \leq 4\sqrt{n} + 2$  with probability at least 95%.

Thus, in the correlation formula, terms involving  $Z$  are negligible, and we write

$$C(T_1X, T_2X) \approx e^{i(\beta-\alpha)} \cdot \frac{\mu^2/2 - \sigma^2 \cdot n}{\mu^2/2 + \sigma^2 \cdot n} \quad (\text{B.23})$$

Recall that  $\mu$  is a singular value of  $2M$ , whose coefficients are independent and normally distributed with mean 0 and variance  $2\sigma^2$ . Using random matrix theory, Marchenko-Pastur law shows that  $\mu^2$  ranges from  $2\sigma^2(\sqrt{n} - \sqrt{m})^2$  and  $2\sigma^2(\sqrt{n} + \sqrt{m})^2$ . When  $n = m$ , absolute correlations range from  $-1$  to  $0.6$ .

**Comment B.5.3.**

It is noteworthy that the only matrix dimension remaining in the formula is  $n$ , corresponding to the output dimension ( $N_{\text{CCD}}$ ). This will be of interest when considering the correlation value evolution for non square matrices.

**B.5.2 For random unitary matrices**

Let us now consider two unitary random matrices  $T_1$  and  $T_2$ , drawn uniformly at random (which corresponds to the distribution induced by the Haar measure over the group of unitary matrices). See Appendix B.6 for an explanation on how to generate  $T_1$  and  $T_2$  using the QR decomposition of a random gaussian matrix.

As in the previous section, we compute the SVD decomposition of  $M = e^{i\beta}T_1 + e^{i\alpha}T_2 = VSU^\dagger$ , where  $\alpha$  and  $\beta$  are two parameters. Let  $X$  and  $Y$  be the right and left singular vectors associated to a singular value  $\mu$ . More precisely,  $\mu$  is the  $i$ -th coefficient of  $S$  for some  $i$ , and  $X$  and  $Y$  are respectively the  $i$ -th column of  $U$  and  $V$ . We are interested in the correlation between  $T_1X$  and  $T_2X$ , that is

$$C(T_1X, T_2X) = \frac{X^\dagger T_1^\dagger T_2 X}{\|T_1X\|_2 \cdot \|T_2X\|_2}$$

Because  $T_1, T_2, U$  and  $V$  are unitary matrices, we have  $\|T_1X\|_2 = \|T_2X\|_2 = 1$ . Thus, the correlation  $C(T_1X, T_2X)$  is equal to the  $i$ -th diagonal value of the matrix  $C = U^\dagger T_1^\dagger T_2 U$ . As a product of unitary matrix,  $C$  is unitary. Alternatively, one can write

$$CC^\dagger = (U^\dagger T_1^\dagger T_2 U)(U^\dagger T_1^\dagger T_2 U)^\dagger = U^\dagger T_1^\dagger T_2 U U^\dagger T_2^\dagger T_1 U = I.$$

We are now going to show that  $C$  is a diagonal matrix. Because it is also a unitary matrix, its diagonal coefficients will be complex numbers of modulus 1. Using both the definition of  $M$  and its singular value decomposition, one can write

$$\begin{aligned} M^\dagger M &= (e^{i\beta}T_1 + e^{i\alpha}T_2)^\dagger (e^{i\beta}T_1 + e^{i\alpha}T_2) = 2I + e^{i(\alpha-\beta)}T_1^\dagger T_2 + e^{i(\beta-\alpha)}T_2^\dagger T_1 \\ M^\dagger M &= (VSU^\dagger)^\dagger (VSU^\dagger) = US^2U^\dagger. \end{aligned}$$

Combining both equations gives  $e^{i(\alpha-\beta)}T_1^\dagger T_2 + e^{i(\beta-\alpha)}T_2^\dagger T_1 = US^2U^\dagger - 2I$ , which imply that

$$(e^{i(\alpha-\beta)}C) + (e^{i(\alpha-\beta)}C)^\dagger = U^\dagger (e^{i(\alpha-\beta)}T_1^\dagger T_2 + e^{i(\beta-\alpha)}T_2^\dagger T_1)U = S^2 - 2I.$$

This shows that the real part of  $e^{i(\alpha-\beta)}C$  is a diagonal matrix, equal to  $S^2/2 - I$ . We can conclude by using [Comm. B.5.4](#), arguing that because  $T_1$  and  $T_2$  are random unitary matrices, then all coefficients from  $S$  are distinct with probability 1.

#### Comment B.5.4.

Let  $Z$  be a unitary matrix. We are going to show that if either its real part  $\Re(Z)$  or its imaginary part  $\Im(Z)$  is diagonal with distinct coefficients, then  $Z$  is also diagonal, with complex diagonal coefficients of modulus 1.

First, observe that the matrices  $(Z + Z^\dagger)$  and  $(Z - Z^\dagger)$  commute:

$$(Z + Z^\dagger)(Z - Z^\dagger) = Z^2 - (Z^\dagger)^2 = (Z - Z^\dagger)(Z + Z^\dagger)$$

More precisely, this means that  $\Re(Z)$  and  $\Im(Z)$  commute, and that both matrices stabilize the eigen-spaces of the other matrix. If  $\Re(Z)$  is a diagonal matrix with distinct coefficient, then each of its eigen-space has dimension 1 and is spanned by one of the vectors of the canonical basis. Thus, each vector of the canonical basis is an eigen vector of  $\Im(Z)$ , which in turn is diagonal. Hence,  $Z$  is diagonal, and because it is also unitary then diagonal coefficients must be complex of modulus 1.

Observe that the hypothesis that diagonal coefficients are distinct is necessary, as illustrated by the following example of unitary matrix, whose real part is diagonal.

$$Z = \begin{pmatrix} 1 & i \\ -i & 1 \end{pmatrix} \quad \Re(Z) = \begin{pmatrix} 1 & 0 \\ 0 & 1 \end{pmatrix} \quad \Im(Z) = \begin{pmatrix} 0 & 1 \\ -1 & 0 \end{pmatrix}$$

Going back to our correlations, we showed that the correlation between  $T_1X$  and  $T_2X$  is a complex of modulus 1, such that  $\Re(e^{i(\alpha-\beta)}C(T_1X, T_2X)) = \mu^2/2 - 1$ . Thus, we have

$$C(T_1X, T_2X) = e^{i(\beta-\alpha)} \cdot (\mu^2/2 - 1 \pm i\mu\sqrt{1 - \mu^2/4})$$

## B.6 Unitary random transmission matrices: construction and some properties

This appendix aims to explore some properties of sub-unitary matrices (sub-matrix of a unitary matrix, see [\[Zyczkowski et al. 2000\]](#) for some work on the subject). Sub-unitary matrices are useful

in physics and a straightforward application lies in the domain of light propagation through complex media. As detailed in [Sec. 1.3.1](#) the medium can be characterised by its scattering matrix  $S$  (size  $N \times N$ ), which in case of energy conservation (non absorbing medium) is unitary. The latter matrix is often decomposed onto four sub-matrices:  $R$ ,  $T$ ,  $R'$ ,  $T'$ , which represent the transmissions and reflexions from both sides of the medium (all with sizes  $N/2 \times N/2$ ).

In most works only a subpart of the TM ( $T$ ) is accessible due to the incomplete experimental control. Thus this appendix will mainly focus on the properties of  $T$  and some part of it (matrices of sizes  $M \times M$ ) to predict what one can expect to observe experimentally. The case of optical fibers (with almost no reflection) is noteworthy as the TM of an optical fiber may be considered unitary. Hence matrices such that  $M > N/2$  will also be considered.

### B.6.1 Matrix generation

For this study the first step is to create the  $S$  matrix as a random unitary matrix. This is performed with the QR decomposition detailed in [Comm. 6.3.1](#). and in [[Ozols 2009](#); [Mezzadri 2006](#)]. However the recipe to construct the matrix as presented in [Comm. 6.3.1](#) puts aside some legitimate questions raised in [[Ozols 2009](#)], only a short summary is presented below.

- **Justifications of the steps of [Comm. 6.3.1](#)** In a QR decomposition of a matrix,  $Q$  is unitary and  $R$  is an upper diagonal matrix. There is no uniqueness of the decomposition. However if the diagonal elements of  $R$  are only positive reals, the decomposition is unique and we will refer to it as the “true” decomposition. Matrices obtained from the implemented algorithms are not necessarily giving the true QR decomposition. A manner of reaching it from any QR decomposition consists in manually obtaining a decomposition  $Q'R'$  with  $Q' = QD$  and  $R' = D^\dagger R$ , where  $D$  is computed in the third step of [Comm. 6.3.1](#). The unitary matrix  $Q'$  then corresponds to the unitary matrix of the true QR decomposition.
- **Ensemble of the “unitary random matrix”** Starting with a matrix with Gaussian i.i.d. elements, its true QR decomposition gives  $Q$  uniformly distributed on unitary random matrices [[Ozols 2009](#)] which is also referred as the unitary Haar ensemble.

### B.6.2 Impact of sub-unitary matrices size on the singular values

#### B.6.2.1 Singular values range and bimodal law

Now that the random unitary matrix  $S$  is constructed we will focus our attention on sub-matrices of size  $M \times M$ . The full TM is the case where  $M = N/2$ , and a partial control corresponds to  $M < N/2$ . Let us first investigate how the distribution of the squared singular values evolves with the size  $M$  of the sub-matrix (see [Comm. B.6.1](#)). Simulation results are presented [Fig. B.6](#).

#### Comment B.6.1.

In the following we will perform only singular value decompositions (SVD) to be able to extend the results to the experimental case where non square matrices may be encountered. This is not a problem in itself but some precautions need to be taken. When performing the SVD of a matrix  $M$  Matlab by convention returns the singular values as the square root of the eigenvalues of  $M^\dagger M$ . In theoretical papers the matrix whose modes are studied is more often  $M^\dagger M$  [[Goetschy et al. 2013](#)]. Hence when considering the singular value distribution and looking for open and closed channels we will square the singular values to be consistent with the common use.

For  $M = N$  all the singular values are 1 due to the matrix being unitary. When decreasing  $M$  the number of singular values equal to one decreases to one single when  $M = N/2$ . For  $M$  smaller

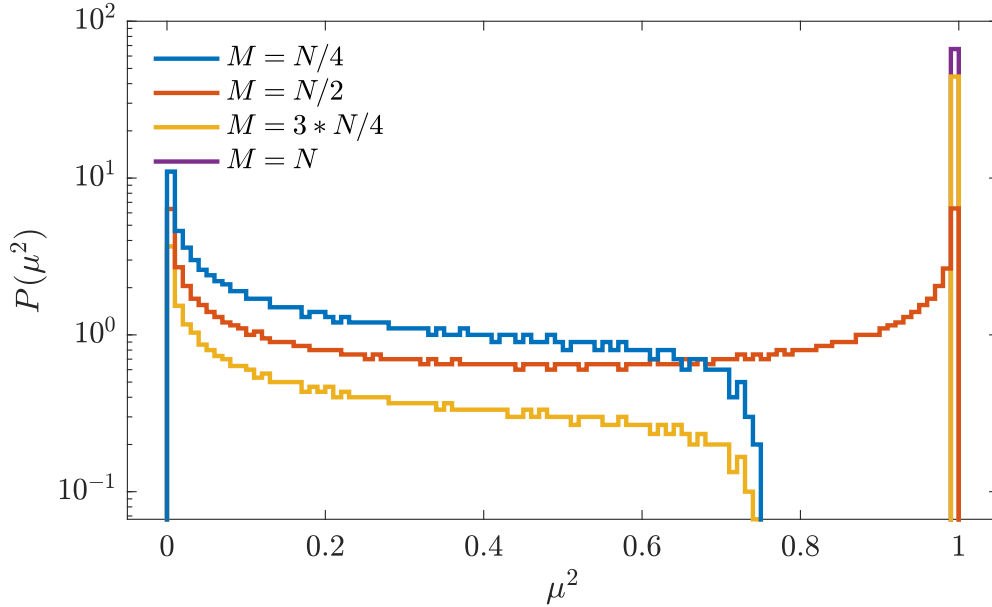


Figure B.6: Histograms of  $\mu^2$  for different  $N$  in logarithmic scale. For  $M = N$  (purple) all the singular values are 1. For  $N/2 < M < N$  (yellow) some values smaller than 1 emerge, all the other remain at 1. For  $M = N/2$  (red) all values span from 0 to 1. For  $M < N/2$  (blue) all singular values of 1 have disappeared. For this simulation  $N = 4000$  and data are averaged over 20 realizations.

than  $N/2$  none of them remains. This transition is understandable with symmetry arguments. To sum up we have:

- $M = N$ : all  $|\mu| = 1$
- $M > N/2$ :  $|\mu| = 1$  + some values such that  $|\mu| < 1$
- $M < N/2$ : all  $|\mu| < 1$

This graph is qualitatively consistent with the results of [Goetschy et al. 2013]. A short mathematical insight is presented in [Comm. B.6.2](#).

#### Comment B.6.2.

It is shown in [Ginibre 1965] that for a random matrix of size  $N$  with i.i.d. complex Gaussian coefficients of mean 0 and standard deviation  $\sigma = \sqrt{1/N}$  (called Ginibre ensemble), the distribution of eigenvalues converges towards the uniform distribution on the unit disk.

Furthermore, it is shown in [Petz et al. 2004] that the coefficients of a random unitary matrix of size  $N$  are identically distributed (but are not independent), that the distribution of coefficients converges towards a Gaussian of standard deviation  $1/\sqrt{N}$ , and that coefficient from a sub-matrix of size  $M$  are asymptotically independent.

Hence, a sub-matrix of size  $M$  of a random unitary matrix of size  $N \gg M$  asymptotically corresponds to a scaled version of the Ginibre ensemble. If we multiply each coefficient of the sub-matrix by  $\sqrt{N/M}$ , we obtain a random matrix with asymptotically i.i.d complex Gaussian coefficients of mean 0 and standard deviation  $\sigma = \sqrt{1/N}$ , which corresponds to the original Ginibre ensemble. Thus, the distribution of eigenvalues of the (unscaled) sub-matrix converges towards the uniform distribution on the disk of radius  $\sqrt{M/N}$ .

### B.6.2.2 Singular values distribution and Marchenko-Pastur

It is known that a sub-matrix of a Haar unitary matrix<sup>5</sup> converges to a Gaussian random matrix in distribution<sup>6</sup> [Petz et al. 2004]. Hence taking sub-matrices of the constructed unitary random matrix one expects to recover the random Gaussian i.i.d. matrices properties.

There is a hand-wavy explanation: the more elements of the initially unitary matrix are removed the more the obtained sub-matrix has “forgotten” about its unitarity and one gets closer to a mere random matrix. To evaluate this assumption the distributions of the sub-matrices are compared to the Marchenko-Pastur (MP) distribution in Fig. B.7.

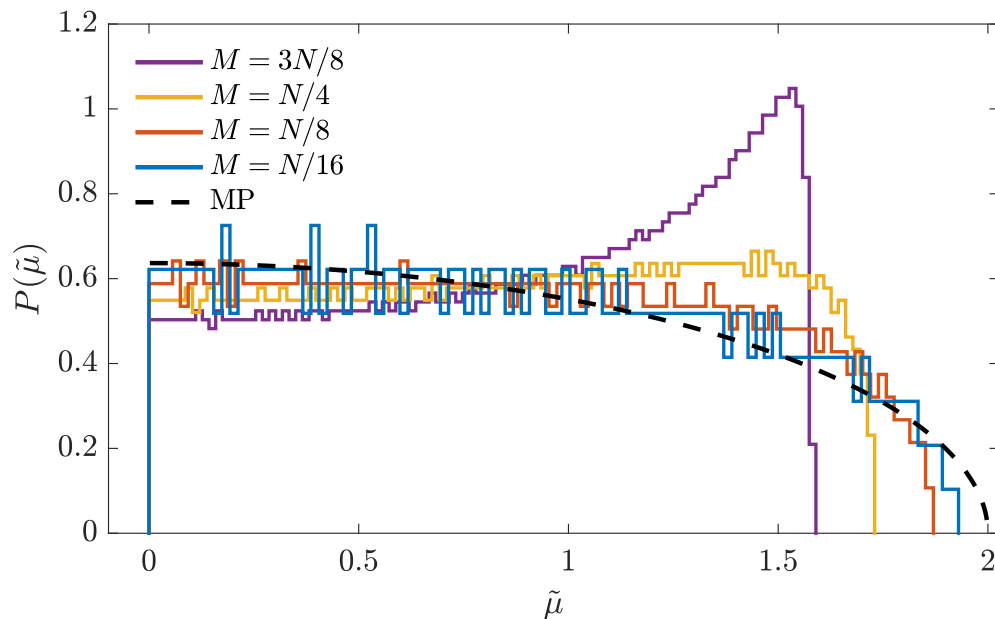


Figure B.7: Comparison of the normalised singular value ( $\tilde{\mu}$ ) distribution for different sizes of sub-unitary matrices. These distributions are compared to the expected MP distribution. The smaller the sub-matrix the better the agreement. For this simulation  $N = 8000$  and data are averaged over 10 realizations.

One observes that in case of partial control ( $M < N/2$ ) the random character of the matrix is well verified, explaining the validity of this approximation for experimentally measured TMs [Popoff et al. 2010]. Moreover we see that when  $M \geq N/4$  (50% control when measuring a TM) the distribution is different enough from MP to maybe expect being able to see mesoscopic effects.

<sup>5</sup>A Haar unitary matrix is a random matrix drawn from the Haar distribution on unitary matrices, which corresponds to the uniform distribution on unitary matrices.

<sup>6</sup>See [Tao 2012] for the definition of convergence in distribution.



# Bibliography

- [[Aguiar et al. 2016](#)] Aguiar, Hilton B de, Sylvain Gigan, and Sophie Brasselet (2016). “Enhanced nonlinear imaging through scattering media using transmission-matrix-based wave-front shaping”. In: *Physical Review A* 94.4, p. 043830 (cited on page [53](#)).
- [[Aguiar et al. 2017](#)] Aguiar, Hilton B de, Sylvain Gigan, and Sophie Brasselet (2017). “Polarization recovery through scattering media”. In: *Science advances* 3.9, e1600743 (cited on page [53](#)).
- [[Akbulut et al. 2011](#)] Akbulut, Duygu, Thomas J Huisman, Elbert G van Putten, Willem L Vos, and Allard P Mosk (2011). “Focusing light through random photonic media by binary amplitude modulation”. In: *Optics express* 19.5, pp. 4017–4029 (cited on page [77](#)).
- [[Akbulut et al. 2016](#)] Akbulut, Duygu, Tom Strudley, Jacopo Bertolotti, Erik PAM Bakkers, Ad Lagendijk, Otto L Muskens, Willem L Vos, and Allard P Mosk (2016). “Optical transmission matrix as a probe of the photonic strength”. In: *Physical Review A* 94.4, p. 043817 (cited on page [64](#)).
- [[Akhlaghi et al. 2017](#)] Akhlaghi, Milad I and Aristide Dogariu (2017). “Tracking hidden objects using stochastic probing”. In: *Optica* 4.4, pp. 447–453 (cited on page [120](#)).
- [[Akkermans et al. 2007](#)] Akkermans, Eric and Gilles Montambaux (2007). *Mesoscopic physics of electrons and photons*. Cambridge university press (cited on page [21](#)).
- [[Ambichl et al. 2017a](#)] Ambichl, Philipp, Andre Brandstötter, Julian Böhm, Matthias Kühmayer, Ulrich Kuhl, and Stefan Rotter (2017a). “Focusing inside disordered media with the generalized Wigner-Smith operator”. In: *Physical review letters* 119.3, p. 033903 (cited on pages [39](#), [66](#), [172](#)).
- [[Ambichl et al. 2017b](#)] Ambichl, Philipp, Wen Xiong, Yaron Bromberg, Brandon Redding, Hui Cao, and Stefan Rotter (2017b). “Super- and anti-principal-modes in multimode waveguides”. In: *Physical Review X* 7.4, p. 041053 (cited on pages [66](#), [172](#), [211](#)).
- [[Amitonova et al. 2015](#)] Amitonova, Lyubov V, Allard P Mosk, and Pepijn WH Pinkse (2015). “Rotational memory effect of a multimode fiber”. In: *Optics express* 23.16, pp. 20569–20575 (cited on page [213](#)).
- [[Anderson 1985](#)] Anderson, Philip W (1985). “The question of classical localization A theory of white paint?” In: *Philosophical Magazine B* 52.3, pp. 505–509 (cited on page [69](#)).
- [[Andreoli 2014](#)] Andreoli, Daria (2014). “Contrôle spatio-temporel multi-spectral de la lumière en milieux complexes”. PhD thesis. Université Pierre et Marie Curie-Paris VI (cited on page [82](#)).
- [[Andreoli et al. 2015](#)] Andreoli, Daria, Giorgio Volpe, Sébastien Popoff, Ori Katz, Samuel Grésillon, and Sylvain Gigan (2015). “Deterministic control of broadband light through a multiply scattering medium via the multispectral transmission matrix”. In: *Scientific reports* 5.1, pp. 1–8 (cited on pages [23](#), [24](#), [49](#)).
- [[Arjmand et al. 2021](#)] Arjmand, Payvand, Ori Katz, Sylvain Gigan, and Marc Guillon (2021). “Three-dimensional broadband light beam manipulation in forward scattering samples”. In: *Optics Express* 29.5, pp. 6563–6581 (cited on page [215](#)).

- [Arruda et al. 2018] Arruda, Tiago J, Alexandre S Martinez, and Felipe A Pinheiro (2018). “Controlling optical memory effects in disordered media with coated metamaterials”. In: *Physical Review A* 98.4, p. 043855 (cited on page 171).
- [Aubry et al. 2009] Aubry, Alexandre and Arnaud Derode (2009). “Random matrix theory applied to acoustic backscattering and imaging in complex media”. In: *Physical review letters* 102.8, p. 084301 (cited on page 58).
- [Aulbach et al. 2011] Aulbach, Jochen, Bergin Gjonaj, Patrick M Johnson, Allard P Mosk, and Ad Lagendijk (2011). “Control of light transmission through opaque scattering media in space and time”. In: *Physical review letters* 106.10, p. 103901 (cited on pages 41, 143, 144, 156).
- [Babcock 1953] Babcock, Horace W (1953). “The possibility of compensating astronomical seeing”. In: *Publications of the Astronomical Society of the Pacific* 65.386, pp. 229–236 (cited on page 31).
- [Bachelard et al. 2014] Bachelard, Nicolas, Sylvain Gigan, Xavier Noblin, and Patrick Sebbah (2014). “Adaptive pumping for spectral control of random lasers”. In: *Nature physics* 10.6, pp. 426–431 (cited on page 69).
- [Badon et al. 2020] Badon, Amaury, Victor Barolle, Kristina Irsch, A Claude Boccara, Mathias Fink, and Alexandre Aubry (2020). “Distortion matrix concept for deep optical imaging in scattering media”. In: *Science advances* 6.30, eaay7170 (cited on page 67).
- [Bagnoud et al. 2004] Bagnoud, Vincent and Jonathan D Zuegel (2004). “Independent phase and amplitude control of a laser beam by use of a single-phase-only spatial light modulator”. In: *Optics letters* 29.3, pp. 295–297 (cited on page 80).
- [Bao 2005] Bao, Minhang (2005). *Analysis and design principles of MEMS devices*. Elsevier (cited on page 33).
- [Beenakker 1997] Beenakker, Carlo WJ (1997). “Random-matrix theory of quantum transport”. In: *Reviews of modern physics* 69.3, p. 731 (cited on pages 41, 42, 55).
- [Bender et al. 2018] Bender, Nicholas, Hasan Yilmaz, Yaron Bromberg, and Hui Cao (2018). “Customizing speckle intensity statistics”. In: *Optica* 5.5, pp. 595–600 (cited on pages 119, 120).
- [Bender et al. 2019a] Bender, Nicholas, Hasan Yilmaz, Yaron Bromberg, and Hui Cao (2019a). “Creating and controlling complex light”. In: *APL Photonics* 4.11, p. 110806 (cited on page 120).
- [Bender et al. 2019b] Bender, Nicholas, Hasan Yilmaz, Yaron Bromberg, and Hui Cao (2019b). “Introducing non-local correlations into laser speckles”. In: *Optics express* 27.5, pp. 6057–6067 (cited on pages 120, 127).
- [Bender et al. 2021] Bender, Nicholas, Alexey Yamilov, Arthur Goetschy, Hasan Yilmaz, Chia Wei Hsu, and Hui Cao (2021). “Depth-Targeted Energy Deposition Deep Inside Scattering Media”. In: *arXiv preprint arXiv:2105.13417* (cited on page 67).
- [Berdagué et al. 1982] Berdagué, S and P Facq (1982). “Mode division multiplexing in optical fibers”. In: *Applied optics* 21.11, pp. 1950–1955 (cited on page 208).
- [Berkovits et al. 1994] Berkovits, Richard and Shechao Feng (1994). “Correlations in coherent multiple scattering”. In: *Physics Reports* 238.3, pp. 135–172 (cited on pages 20, 23, 43).
- [Berto et al. 2017] Berto, Pascal, Hervé Rigneault, and Marc Guillon (2017). “Wavefront sensing with a thin diffuser”. In: *Optics letters* 42.24, pp. 5117–5120 (cited on page 86).
- [Bertolotti et al. 2012] Bertolotti, Jacopo, Elbert G Van Putten, Christian Blum, Ad Lagendijk, Willem L Vos, and Allard P Mosk (2012). “Non-invasive imaging through opaque scattering layers”. In: *Nature* 491.7423, pp. 232–234 (cited on pages 171, 213).
- [Billy et al. 2008] Billy, Juliette, Vincent Josse, Zhanchun Zuo, Alain Bernard, Ben Hambrecht, Pierre Lukan, David Clément, Laurent Sanchez-Palencia, Philippe Bouyer, and Alain Aspect (2008). “Direct observation of Anderson localization of matter waves in a controlled disorder”. In: *Nature* 453.7197, pp. 891–894 (cited on page 119).

- [Blochet et al. 2017] Blochet, Baptiste, Laurent Bourdieu, and Sylvain Gigan (2017). “Focusing light through dynamical samples using fast continuous wavefront optimization”. In: *Optics letters* 42.23, pp. 4994–4997 (cited on page 237).
- [Böhm et al. 2018] Böhm, Julian, Andre Brandstötter, Philipp Ambichl, Stefan Rotter, and Ulrich Kuhl (2018). “In situ realization of particlelike scattering states in a microwave cavity”. In: *Physical Review A* 97.2, p. 021801 (cited on page 66).
- [Boniface et al. 2017] Boniface, Antoine, Mickael Mounaix, Baptiste Blochet, Rafael Piestun, and Sylvain Gigan (2017). “Transmission-matrix-based point-spread-function engineering through a complex medium”. In: *Optica* 4.1, pp. 54–59 (cited on pages 123, 124, 126).
- [Boniface et al. 2019a] Boniface, Antoine, Baptiste Blochet, Jonathan Dong, and Sylvain Gigan (2019a). “Noninvasive light focusing in scattering media using speckle variance optimization”. In: *Optica* 6.11, pp. 1381–1385 (cited on page 38).
- [Boniface et al. 2019b] Boniface, Antoine, Ivan Gusachenko, Kishan Dholakia, and Sylvain Gigan (2019b). “Rapid broadband characterization of scattering medium using hyperspectral imaging”. In: *Optica* 6.3, pp. 274–279 (cited on page 50).
- [Boniface et al. 2020] Boniface, Antoine, Jonathan Dong, and Sylvain Gigan (2020). “Non-invasive focusing and imaging in scattering media with a fluorescence-based transmission matrix”. In: *Nature communications* 11.1, pp. 1–7 (cited on page 45).
- [Booth 2014] Booth, Martin J (2014). “Adaptive optical microscopy: the ongoing quest for a perfect image”. In: *Light: Science & Applications* 3.4, e165–e165 (cited on page 32).
- [Bouchet et al. 2021a] Bouchet, Dorian, Stefan Rotter, and Allard P Mosk (2021a). “Maximum information states for coherent scattering measurements”. In: *Nature Physics* 17.5, pp. 564–568 (cited on page 67).
- [Bouchet et al. 2021b] Bouchet, Dorian, Lukas M Rachbauer, Stefan Rotter, Allard P Mosk, and Emmanuel Bossy (2021b). “Optimal control of coherent light scattering for binary decision problems”. In: *arXiv preprint arXiv:2108.03755* (cited on page 173).
- [Bromberg et al. 2016] Bromberg, Y, B Redding, SM Popoff, and H Cao (2016). “Control of coherent backscattering by breaking optical reciprocity”. In: *Physical Review A* 93.2, p. 023826 (cited on page 211).
- [Bromberg et al. 2014] Bromberg, Yaron and Hui Cao (2014). “Generating non-Rayleigh speckles with tailored intensity statistics”. In: *Physical Review Letters* 112.21, p. 213904 (cited on pages 117–119).
- [Bromberg et al. 2019] Bromberg, Yaron, Brandon Redding, Sebastien M Popoff, Ningbo Zhao, Guifang Li, and Hui Cao (2019). “Remote key establishment by random mode mixing in multimode fibers and optical reciprocity”. In: *Optical Engineering* 58.1, p. 016105 (cited on page 69).
- [Brouwer et al. 1997] Brouwer, PW, KM Frahm, and CWJ Beenakker (1997). “Quantum mechanical time-delay matrix in chaotic scattering”. In: *Physical review letters* 78.25, p. 4737 (cited on page 66).
- [Burresti et al. 2014] Burresti, Matteo, Lorenzo Cortese, Lorenzo Pattelli, Mathias Kolle, Peter Vukusic, Diederik S Wiersma, Ullrich Steiner, and Silvia Vignolini (2014). “Bright-white beetle scales optimise multiple scattering of light”. In: *Scientific reports* 4.1, pp. 1–8 (cited on page 8).
- [Cao et al. 1999] Cao, Hui, YG Zhao, ST Ho, EW Seelig, QH Wang, and RPH Chang (1999). “Random laser action in semiconductor powder”. In: *Physical Review Letters* 82.11, p. 2278 (cited on page 69).
- [Cao et al. 2003] Cao, Hui, Alexey Yamilov, Junying Xu, Eric Seelig, and Robert PH Chang (2003). “Lasing in disordered media”. In: *Novel In-Plane Semiconductor Lasers II* 4995, pp. 134–143 (cited on page 69).

- [Caravaca-Aguirre et al. 2013] Caravaca-Aguirre, Antonio M, Eyal Niv, Donald B Conkey, and Rafael Piestun (2013). “Real-time resilient focusing through a bending multimode fiber”. In: *Optics express* 21.10, pp. 12881–12887 (cited on page 209).
- [Carminati et al. 2000] Carminati, R, JJ Saenz, J-J Greffet, and M Nieto-Vesperinas (2000). “Reciprocity, unitarity, and time-reversal symmetry of the S matrix of fields containing evanescent components”. In: *Physical review A* 62.1, p. 012712 (cited on pages 41, 44).
- [Carminati et al. 2021] Carminati, Rémi and John C Schotland (2021). *Principles of Scattering and Transport of Light*. Cambridge University Press (cited on pages 12, 16, 20).
- [Carolan et al. 2015] Carolan, Jacques, Christopher Harrold, Chris Sparrow, Enrique Martín-López, Nicholas J Russell, Joshua W Silverstone, Peter J Shadbolt, Nobuyuki Matsuda, Manabu Oguma, Mikitaka Itoh, et al. (2015). “Universal linear optics”. In: *Science* 349.6249, pp. 711–716 (cited on page 210).
- [Carpenter et al. 2014] Carpenter, Joel, Benjamin J Eggleton, and Jochen Schröder (2014). “110x110 optical mode transfer matrix inversion”. In: *Optics express* 22.1, pp. 96–101 (cited on page 209).
- [Carpenter et al. 2015] Carpenter, Joel, Benjamin J Eggleton, and Jochen Schröder (2015). “Observation of Eisenbud–Wigner–Smith states as principal modes in multimode fibre”. In: *Nature Photonics* 9.11, pp. 751–757 (cited on pages 65, 211).
- [Carpenter et al. 2016] Carpenter, Joel, Benjamin J Eggleton, and Jochen Schröder (2016). “Complete spatiotemporal characterization and optical transfer matrix inversion of a 420 mode fiber”. In: *Optics letters* 41.23, pp. 5580–5583 (cited on pages 52, 141, 163).
- [Carr et al. 2018] Carr, Jessica A, Marianne Aellen, Daniel Franke, Peter TC So, Oliver T Bruns, and Mounji G Bawendi (2018). “Absorption by water increases fluorescence image contrast of biological tissue in the shortwave infrared”. In: *Proceedings of the National Academy of Sciences* 115.37, pp. 9080–9085 (cited on page 30).
- [Chaigne et al. 2014] Chaigne, Thomas, Ori Katz, A Claude Boccara, Mathias Fink, Emmanuel Bossy, and Sylvain Gigan (2014). “Controlling light in scattering media non-invasively using the photoacoustic transmission matrix”. In: *Nature Photonics* 8.1, pp. 58–64 (cited on pages 39, 45).
- [Chavali et al. 2007] Chavali, Sasidhar, Philip M Birch, Rupert Young, and Chris Chatwin (2007). “Synthesis and reconstruction of computer generated holograms by a double pass technique on a twisted nematic-based liquid crystal spatial light modulator”. In: *Optics and lasers in engineering* 45.3, pp. 413–418 (cited on page 80).
- [Chen et al. 2019] Chen, Meijun, Honglin Liu, Zhentao Liu, Puxiang Lai, and Shensheng Han (2019). “Expansion of the FOV in speckle autocorrelation imaging by spatial filtering”. In: *Optics Letters* 44.24, pp. 5997–6000 (cited on page 171).
- [Cheong et al. 1990] Cheong, Wai-Fung, Scott A Pahl, and Ashley J Welch (1990). “A review of the optical properties of biological tissues”. In: *IEEE journal of quantum electronics* 26.12, pp. 2166–2185 (cited on page 13).
- [Chiarawongse et al. 2018] Chiarawongse, Poom, Huanan Li, Wen Xiong, Chia Wei Hsu, Hui Cao, and Tsampikos Kottos (2018). “Statistical description of transport in multimode fibers with mode-dependent loss”. In: *New Journal of Physics* 20.11, p. 113028 (cited on pages 209, 211).
- [Choi et al. 2011] Choi, Wonjun, Allard P Mosk, Q-Han Park, and Wonshik Choi (2011). “Transmission eigenchannels in a disordered medium”. In: *Physical Review B* 83.13, p. 134207 (cited on pages 56, 57).
- [Choi et al. 2012] Choi, Youngwoon, Changhyeong Yoon, Moonseok Kim, Taeseok Daniel Yang, Christopher Fang-Yen, Ramachandra R Dasari, Kyoung Jin Lee, and Wonshik Choi (2012). “Scanner-free and wide-field endoscopic imaging by using a single multimode optical fiber”. In: *Physical review letters* 109.20, p. 203901 (cited on pages 207, 209).

- [Choi et al. 2013] Choi, Youngwoon, Timothy R Hillman, Wonjun Choi, Niyom Lue, Ramachandra R Dasari, Peter TC So, Wonshik Choi, and Zahid Yaqoob (2013). “Measurement of the time-resolved reflection matrix for enhancing light energy delivery into a scattering medium”. In: *Physical review letters* 111.24, p. 243901 (cited on page 51).
- [Čižmár et al. 2011] Čižmár, Tomáš and Kishan Dholakia (2011). “Shaping the light transmission through a multimode optical fibre: complex transformation analysis and applications in biophotonics”. In: *Optics express* 19.20, pp. 18871–18884 (cited on pages 79, 80).
- [Čižmár et al. 2012] Čižmár, Tomáš and Kishan Dholakia (2012). “Exploiting multimode waveguides for pure fibre-based imaging”. In: *Nature communications* 3.1, pp. 1–9 (cited on page 215).
- [Colladon 1842] Colladon, Daniel (1842). “Sur les réflexions d’un rayon de lumière à l’intérieur d’une veine liquide parabolique”. In: *Comptes rendus* 15.1800 (cited on page 205).
- [Conkey et al. 2012] Conkey, Donald B, Albert N Brown, Antonio M Caravaca-Aguirre, and Rafael Piestun (2012). “Genetic algorithm optimization for focusing through turbid media in noisy environments”. In: *Optics express* 20.5, pp. 4840–4849 (cited on page 38).
- [Cottrell et al. 2007] Cottrell, Don M, Julia M Craven, and Jeffrey A Davis (2007). “Nondiffracting random intensity patterns”. In: *Optics letters* 32.3, pp. 298–300 (cited on page 126).
- [Cuche et al. 2000] Cuche, Etienne, Pierre Marquet, and Christian Depeursing (2000). “Spatial filtering for zero-order and twin-image elimination in digital off-axis holography”. In: *Applied optics* 39.23, pp. 4070–4075 (cited on pages 87, 158).
- [Curry et al. 2011] Curry, Nathan, Pierre Bondareff, Mathieu Leclercq, Niek F Van Hulst, Riccardo Sapienza, Sylvain Gigan, and Samuel Grésillon (2011). “Direct determination of diffusion properties of random media from speckle contrast”. In: *Optics letters* 36.17, pp. 3332–3334 (cited on pages 25, 27, 83).
- [Dainty 1980] Dainty, John C (1980). “An introduction to Gaussian speckle”. In: *Proc. SPIE*. Vol. 243, pp. 2–8 (cited on page 111).
- [Davy et al. 2012] Davy, Matthieu, Zhou Shi, and Azriel Z Genack (2012). “Focusing through random media: Eigenchannel participation number and intensity correlation”. In: *Physical Review B* 85.3, p. 035105 (cited on page 249).
- [Davy et al. 2015a] Davy, Matthieu, Zhou Shi, Jing Wang, Xiaojun Cheng, and Azriel Z Genack (2015a). “Transmission eigenchannels and the densities of states of random media”. In: *Physical review letters* 114.3, p. 033901 (cited on page 64).
- [Davy et al. 2015b] Davy, Matthieu, Zhou Shi, Jongchul Park, Chushun Tian, and Azriel Z Genack (2015b). “Universal structure of transmission eigenchannels inside opaque media”. In: *Nature communications* 6.1, pp. 1–6 (cited on page 57).
- [Davy et al. 2021] Davy, Matthieu, Matthias Kühmayer, Sylvain Gigan, and Stefan Rotter (2021). “Mean path length invariance in wave-scattering beyond the diffusive regime”. In: *Communications Physics* 4.1, pp. 1–7 (cited on pages 43, 66, 162).
- [De Rosny et al. 2010] De Rosny, Julien, Geoffroy Lerosey, and Mathias Fink (2010). “Theory of electromagnetic time-reversal mirrors”. In: *IEEE Transactions on Antennas and Propagation* 58.10, pp. 3139–3149 (cited on page 35).
- [Defienne et al. 2014] Defienne, H, M Barbieri, Benoît Chalopin, Béatrice Chatel, IA Walmsley, BJ Smith, and S Gigan (2014). “Nonclassical light manipulation in a multiple-scattering medium”. In: *Optics letters* 39.21, pp. 6090–6093 (cited on page 210).
- [Defienne 2015] Defienne, Hugo (2015). “Quantum walks of photons in disordered media”. PhD thesis. Paris 6 (cited on page 45).
- [Defienne et al. 2016] Defienne, Hugo, Marco Barbieri, Ian A Walmsley, Brian J Smith, and Sylvain Gigan (2016). “Two-photon quantum walk in a multimode fiber”. In: *Science advances* 2.1, e1501054 (cited on page 210).

- [Derode et al. 2003] Derode, Arnaud, Arnaud Tourin, Julien de Rosny, Mickaël Tanter, Sylvain Yon, and Mathias Fink (2003). “Taking advantage of multiple scattering to communicate with time-reversal antennas”. In: *Physical Review Letters* 90.1, p. 014301 (cited on page 69).
- [Devaud et al. 2021a] Devaud, Louisiane, Marc Guillon, Ivan Gusachenko, and Sylvain Gigan (2021a). “Chromato-axial memory effect in step index multimode fibers”. In: *APL Photonics* (cited on pages 215, 219).
- [Devaud et al. 2021b] Devaud, Louisiane, Bernhard Rauer, Jakob Melchard, Matthias Kühmayer, Stefan Rotter, and Sylvain Gigan (2021b). “Speckle engineering through singular value decomposition of the transmission matrix”. In: *Physical Review Letters* 127.9, p. 093903 (cited on pages 124, 132–137, 256).
- [Di Battista et al. 2016] Di Battista, D, D Ancora, M Leonetti, and G Zacharakis (2016). “Tailoring non-diffractive beams from amorphous light speckles”. In: *Applied Physics Letters* 109.12, p. 121110 (cited on pages 123, 126).
- [Di Battista et al. 2015] Di Battista, Diego, Giannis Zacharakis, and Marco Leonetti (2015). “Enhanced adaptive focusing through semi-transparent media”. In: *Scientific reports* 5.1, pp. 1–8 (cited on pages 123, 126).
- [Dorokhov 1996] Dorokhov, ON (1996). “On the coexistence of localized and extended electronic states in the metallic phase”. In: *30 Years Of The Landau Institute—Selected Papers*. World Scientific, pp. 234–237 (cited on page 55).
- [Douglass et al. 2012] Douglass, Kyle M, Sergey Sukhov, and Aristide Dogariu (2012). “Superdiffusion in optically controlled active media”. In: *Nature photonics* 6.12, pp. 834–837 (cited on page 119).
- [Drémeau et al. 2015] Drémeau, Angélique, Antoine Liutkus, David Martina, Ori Katz, Christophe Schülke, Florent Krzakala, Sylvain Gigan, and Laurent Daudet (2015). “Reference-less measurement of the transmission matrix of a highly scattering material using a DMD and phase retrieval techniques”. In: *Optics express* 23.9, pp. 11898–11911 (cited on page 95).
- [Dudley et al. 2012] Dudley, Angela, Ruslan Vasilyeu, Vladimir Belyi, Nikolai Khilo, Piotr Ropot, and Andrew Forbes (2012). “Controlling the evolution of nondiffracting speckle by complex amplitude modulation on a phase-only spatial light modulator”. In: *Optics Communications* 285.1, pp. 5–12 (cited on page 126).
- [Durand et al. 2019] Durand, M, SM Popoff, R Carminati, and A Goetschy (2019). “Optimizing light storage in scattering media with the dwell-time operator”. In: *Physical review letters* 123.24, p. 243901 (cited on page 66).
- [Durand 2020] Durand, Mathieu (2020). “Optimisation de la propagation lumineuse en milieux désordonnés: temps de séjour, dispersion temporelle, et focalisation”. PhD thesis. Université Paris sciences et lettres (cited on pages 26, 66, 67, 162).
- [Durnin et al. 1988] Durnin, J, JJ Miceli, and Joseph H Eberly (1988). “Comparison of Bessel and Gaussian beams”. In: *Optics letters* 13.2, pp. 79–80 (cited on page 126).
- [Durnin 1987] Durnin, JJA (1987). “Exact solutions for nondiffracting beams. I. The scalar theory”. In: *JOSA A* 4.4, pp. 651–654 (cited on page 126).
- [Fan et al. 2005] Fan, Shanhui and Joseph M Kahn (2005). “Principal modes in multimode waveguides”. In: *Optics letters* 30.2, pp. 135–137 (cited on pages 65, 172).
- [Fayard et al. 2015] Fayard, N, A Cazé, R Pierrat, and Rémi Carminati (2015). “Intensity correlations between reflected and transmitted speckle patterns”. In: *Physical Review A* 92.3, p. 033827 (cited on page 65).
- [Feng et al. 1988a] Feng, Shechao, Charles Kane, Patrick A Lee, and A Douglas Stone (1988a). “Correlations and fluctuations of coherent wave transmission through disordered media”. In: *Physical review letters* 61.7, p. 834 (cited on pages 20, 21, 23, 43).

- [Feng et al. 1988b] Feng, Shechao, Charles Kane, Patrick A Lee, and A Douglas Stone (1988b). “Correlations and fluctuations of coherent wave transmission through disordered media”. In: *Physical review letters* 61.7, p. 834 (cited on page 212).
- [Feynman et al. 1963] Feynman, Richard P., Robert B Leighton, and Matthew Sands (1963). *The Feynman Lectures on Physics*. Vol. vol. 1. Mainly mechanics, radiation and heat. Addison-Wesley (cited on page 8).
- [Fienup 1982] Fienup, James R (1982). “Phase retrieval algorithms: a comparison”. In: *Applied optics* 21.15, pp. 2758–2769 (cited on page 87).
- [Fink 1993] Fink, Mathias (1993). “Time-reversal mirrors”. In: *Journal of Physics D: Applied Physics* 26.9, p. 1333 (cited on page 35).
- [Fink 1997] Fink, Mathias (1997). “Time reversed acoustics.” In: *Physics today* 50.3, pp. 34–40 (cited on page 34).
- [Fink et al. 2001] Fink, Mathias and Claire Prada (2001). “Acoustic time-reversal mirrors”. In: *Inverse problems* 17.1, R1 (cited on page 35).
- [Fisher et al. 1981] Fisher, Daniel S and Patrick A Lee (1981). “Relation between conductivity and transmission matrix”. In: *Physical Review B* 23.12, p. 6851 (cited on pages 21, 43).
- [Fisher 2012] Fisher, Robert A (2012). *Optical phase conjugation*. Academic press (cited on page 35).
- [Foucart et al. 2013] Foucart, Simon and Holger Rauhut (2013). “An invitation to compressive sensing”. In: *A mathematical introduction to compressive sensing*. Springer, pp. 1–39 (cited on page 70).
- [Françon 2012] Françon, Maurice (2012). *Laser speckle and applications in optics*. Elsevier (cited on page 17).
- [Freund 1990] Freund, Isaac (1990). “Looking through walls and around corners”. In: *Physica A: Statistical Mechanics and its Applications* 168.1, pp. 49–65 (cited on page 23).
- [Freund et al. 1988] Freund, Isaac, Michael Rosenbluh, and Shechao Feng (1988). “Memory effects in propagation of optical waves through disordered media”. In: *Physical review letters* 61.20, p. 2328 (cited on pages 23, 212).
- [Gabor 1949] Gabor, Dennis (1949). “Microscopy by reconstructed wave-fronts”. In: *Proceedings of the Royal Society of London. Series A. Mathematical and Physical Sciences* 197.1051, pp. 454–487 (cited on page 87).
- [Garcia et al. 1989] Garcia, N and AZ Genack (1989). “Crossover to strong intensity correlation for microwave radiation in random media”. In: *Physical review letters* 63.16, p. 1678 (cited on page 115).
- [Garcia et al. 1992] Garcia, N, AZ Genack, and AA Lisyansky (1992). “Measurement of the transport mean free path of diffusing photons”. In: *Physical Review B* 46.22, p. 14475 (cited on page 82).
- [García-Martín et al. 2002] García-Martín, A, F Scheffold, M Nieto-Vesperinas, and JJ Sáenz (2002). “Finite-size effects on intensity correlations in random media”. In: *Physical review letters* 88.14, p. 143901 (cited on page 212).
- [Gateau et al. 2013] Gateau, Jérôme, Thomas Chaigne, Ori Katz, Sylvain Gigan, and Emmanuel Bossy (2013). “Improving visibility in photoacoustic imaging using dynamic speckle illumination”. In: *Optics letters* 38.23, pp. 5188–5191 (cited on page 118).
- [Gatti et al. 2008] Gatti, A, D Magatti, and F Ferri (2008). “Three-dimensional coherence of light speckles: theory”. In: *Physical Review A* 78.6, p. 063806 (cited on pages 19, 251).
- [Genack et al. 1990] Genack, AZ and JM Drake (1990). “Relationship between optical intensity, fluctuations and pulse propagation in random media”. In: *EPL (Europhysics Letters)* 11.4, p. 331 (cited on page 28).
- [Genack 1987] Genack, Azriel Z (1987). “Optical transmission in disordered media”. In: *Physical review letters* 58.20, p. 2043 (cited on page 82).

- [Gérardin et al. 2014] Gérardin, Benoît, Jérôme Laurent, Arnaud Derode, Claire Prada, and Alexandre Aubry (2014). “Full transmission and reflection of waves propagating through a maze of disorder”. In: *Physical review letters* 113.17, p. 173901 (cited on pages 44, 56, 58, 163).
- [Gérardin et al. 2016] Gérardin, Benoît, Jérôme Laurent, Philipp Ambichl, Claire Prada, Stefan Rotter, and Alexandre Aubry (2016). “Particlelike wave packets in complex scattering systems”. In: *Physical Review B* 94.1, p. 014209 (cited on page 66).
- [Ginibre 1965] Ginibre, Jean (1965). “Statistical ensembles of complex, quaternion, and real matrices”. In: *Journal of Mathematical Physics* 6.3, pp. 440–449 (cited on page 277).
- [Goetschy et al. 2013] Goetschy, A and AD Stone (2013). “Filtering random matrices: the effect of incomplete channel control in multiple scattering”. In: *Physical review letters* 111.6, p. 063901 (cited on pages 56, 59, 64, 275, 276).
- [Goodman 1976] Goodman, Joseph W (1976). “Some fundamental properties of speckle”. In: *JOSA* 66.11, pp. 1145–1150 (cited on pages 111, 113).
- [Goodman 2007] Goodman, Joseph W (2007). *Speckle phenomena in optics: theory and applications*. Roberts and Company Publishers (cited on pages 17–19, 23, 37, 111, 115, 121, 122).
- [Goodman et al. 1967] Goodman, Joseph W and RW Lawrence (1967). “Digital image formation from electronically detected holograms”. In: *Applied physics letters* 11.3, pp. 77–79 (cited on page 87).
- [Goorden et al. 2014a] Goorden, Sebastianus A, Marcel Horstmann, Allard P Mosk, Boris Škorić, and Pepijn WH Pinkse (2014a). “Quantum-secure authentication of a physical unclonable key”. In: *Optica* 1.6, pp. 421–424 (cited on page 69).
- [Goorden et al. 2014b] Goorden, Sebastianus A, Jacopo Bertolotti, and Allard P Mosk (2014b). “Superpixel-based spatial amplitude and phase modulation using a digital micromirror device”. In: *Optics express* 22.15, pp. 17999–18009 (cited on page 81).
- [Greffet et al. 1995] Greffet, Jean-Jacques and Rémi Carminati (1995). “Relationship between the near-field speckle pattern and the statistical properties of a surface”. In: *Ultramicroscopy* 61.1-4, pp. 43–50 (cited on page 115).
- [Guan et al. 2012] Guan, Yefeng, Ori Katz, Eran Small, Jianying Zhou, and Yaron Silberberg (2012). “Polarization control of multiply scattered light through random media by wavefront shaping”. In: *Optics letters* 37.22, pp. 4663–4665 (cited on page 69).
- [Guillon et al. 2017] Guillon, Marc, Benoît C Forget, Amanda J Foust, Vincent De Sars, Monika Ritsch-Marte, and Valentina Emiliani (2017). “Vortex-free phase profiles for uniform patterning with computer-generated holography”. In: *Optics express* 25.11, pp. 12640–12652 (cited on pages 81, 241, 243).
- [Gustafsson 2000] Gustafsson, Mats GL (2000). “Surpassing the lateral resolution limit by a factor of two using structured illumination microscopy”. In: *Journal of microscopy* 198.2, pp. 82–87 (cited on page 171).
- [Halford et al. 1987a] Halford, C.E., W.L. Gamble, and N. George (1987a). “Experimental investigation of the longitudinal characteristics of laser speckle”. In: *Optical engineering* 26.12 (cited on page 219).
- [Halford et al. 1987b] Halford, CE, WL Gamble, and Nicholas George (1987b). “Experimental investigation of the longitudinal characteristics of laser speckle”. In: *Optical Engineering* 26.12, p. 261263 (cited on page 19).
- [Hardy 1998] Hardy, John W (1998). *Adaptive optics for astronomical telescopes*. Vol. 16. Oxford University Press on Demand (cited on pages 32, 35).
- [Hart et al. 1969] Hart, Robert W and Richard A Farrell (1969). “Light scattering in the cornea”. In: *JOSA* 59.6, pp. 766–774 (cited on page 9).

- [Ho et al. 2013] Ho, Keang-Po, Joseph M Kahn, IP Kaminow, T Li, and AE Willner (2013). “Mode coupling and its impact on spatially multiplexed systems”. In: *Optical Fiber Telecommunications VI* 17, pp. 1386–1392 (cited on page 209).
- [Hofer et al. 2020] Hofer, Matthias, Siddarth Shivkumar, Bilal El Waly, and Sophie Brasselet (2020). “Coherent anti-Stokes Raman scattering through thick biological tissues by single-wavefront shaping”. In: *Physical Review Applied* 14.2, p. 024019 (cited on page 225).
- [Höhmnn et al. 2010] Höhmnn, R, U Kuhl, H-J Stöckmann, L Kaplan, and EJ Heller (2010). “Freak waves in the linear regime: A microwave study”. In: *Physical review letters* 104.9, p. 093901 (cited on page 115).
- [Hong et al. 2014] Hong, Guosong, Shuo Diao, Junlei Chang, Alexander L Antaris, Changxin Chen, Bo Zhang, Su Zhao, Dmitriy N Atochin, Paul L Huang, Katrin I Andreasson, et al. (2014). “Through-skull fluorescence imaging of the brain in a new near-infrared window”. In: *Nature photonics* 8.9, pp. 723–730 (cited on page 30).
- [Hopkins et al. 1954] Hopkins, Harold H and N Singh Kapany (1954). “A flexible fibrescope, using static scanning”. In: *Nature* 173.4392, pp. 39–41 (cited on page 205).
- [Horstmeyer et al. 2015] Horstmeyer, Roarke, Haowen Ruan, and Changhuei Yang (2015). “Guidestar-assisted wavefront-shaping methods for focusing light into biological tissue”. In: *Nature photonics* 9.9, pp. 563–571 (cited on pages 32, 34, 39, 40).
- [Hougne et al. 2021] Hougne, Philipp del, Rémi Sobry, Olivier Legrand, Fabrice Mortessagne, Ulrich Kuhl, and Matthieu Davy (2021). “Experimental realization of optimal energy storage in resonators embedded in scattering media”. In: *Laser & Photonics Reviews* 15.3, p. 2000335 (cited on page 66).
- [Hsieh et al. 2010] Hsieh, Chia-Lung, Ye Pu, Rachel Grange, and Demetri Psaltis (2010). “Digital phase conjugation of second harmonic radiation emitted by nanoparticles in turbid media”. In: *Optics express* 18.12, pp. 12283–12290 (cited on page 39).
- [Hsu et al. 2015] Hsu, Chia Wei, Arthur Goetschy, Yaron Bromberg, A Douglas Stone, and Hui Cao (2015). “Broadband coherent enhancement of transmission and absorption in disordered media”. In: *Physical review letters* 115.22, p. 223901 (cited on pages 53, 65).
- [Hsu et al. 2017] Hsu, Chia Wei, Seng Fatt Liew, Arthur Goetschy, Hui Cao, and A Douglas Stone (2017). “Correlation-enhanced control of wave focusing in disordered media”. In: *Nature Physics* 13.5, pp. 497–502 (cited on pages 59, 65, 152).
- [Hulst et al. 1981] Hulst, Hendrik Christoffel and Hendrik C van de Hulst (1981). *Light scattering by small particles*. Courier Corporation (cited on page 10).
- [Imry 1986] Imry, Yoseph (1986). “Active transmission channels and universal conductance fluctuations”. In: *EPL (Europhysics Letters)* 1.5, p. 249 (cited on page 41).
- [Jackson 1999] Jackson, John David (1999). *Classical electrodynamics*. 3rd. John Wiley and Sons (cited on pages 206, 221).
- [Jacucci et al. 2021] Jacucci, Gianni, Lukas Schertel, Yating Zhang, Han Yang, and Silvia Vignolini (2021). “Light management with natural materials: From whiteness to transparency”. In: *Advanced materials* 33.28, p. 2001215 (cited on pages 8, 69).
- [Jang et al. 2014] Jang, Mooseok, Haowen Ruan, Haojiang Zhou, Benjamin Judkewitz, and Changhuei Yang (2014). “Method for auto-alignment of digital optical phase conjugation systems based on digital propagation”. In: *Optics express* 22.12, pp. 14054–14071 (cited on page 35).
- [Jang et al. 2015] Jang, Mooseok, Haowen Ruan, Ivo M Vellekoop, Benjamin Judkewitz, Euiheon Chung, and Changhuei Yang (2015). “Relation between speckle decorrelation and optical phase conjugation (OPC)-based turbidity suppression through dynamic scattering media: a study on in vivo mouse skin”. In: *Biomedical optics express* 6.1, pp. 72–85 (cited on page 36).

- [Jang et al. 2018] Jang, Mooseok, Yu Horie, Atsushi Shibukawa, Joshua Brake, Yan Liu, Seyedeh Mahsa Kamali, Amir Arbabi, Haowen Ruan, Andrei Faraon, and Changhuei Yang (2018). “Wavefront shaping with disorder-engineered metasurfaces”. In: *Nature photonics* 12.2, pp. 84–90 (cited on page 171).
- [John 1984] John, Sajeev (1984). “Electromagnetic absorption in a disordered medium near a photon mobility edge”. In: *Physical Review Letters* 53.22, p. 2169 (cited on page 69).
- [Johnson et al. 2003] Johnson, Patrick M, Arnout Imhof, Boris PJ Bret, Jaime Gómez Rivas, and Ad Lagendijk (2003). “Time-resolved pulse propagation in a strongly scattering material”. In: *Physical Review E* 68.1, p. 016604 (cited on page 83).
- [Judkewitz et al. 2015] Judkewitz, Benjamin, Roarke Horstmeyer, Ivo M Vellekoop, Ioannis N Papadopoulos, and Changhuei Yang (2015). “Translation correlations in anisotropically scattering media”. In: *Nature physics* 11.8, pp. 684–689 (cited on page 213).
- [Kadobianskyi et al. 2018] Kadobianskyi, Mykola, Ioannis N Papadopoulos, Thomas Chaigne, Roarke Horstmeyer, and Benjamin Judkewitz (2018). “Scattering correlations of time-gated light”. In: *Optica* 5.4, pp. 389–394 (cited on page 171).
- [Kafesaki et al. 2000] Kafesaki, M, RS Penciu, and EN Economou (2000). “Air bubbles in water: a strongly multiple scattering medium for acoustic waves”. In: *Physical review letters* 84.26, p. 6050 (cited on page 6).
- [Kao et al. 1966] Kao, K Charles and George A Hockham (1966). *Dielectric-fibre surface waveguides for optical frequencies*. Vol. 113. 7, pp. 1151–1158 (cited on page 205).
- [Katz et al. 2011] Katz, Ori, Eran Small, Yaron Bromberg, and Yaron Silberberg (2011). “Focusing and compression of ultrashort pulses through scattering media”. In: *Nature photonics* 5.6, pp. 372–377 (cited on page 41).
- [Katz et al. 2012] Katz, Ori, Eran Small, and Yaron Silberberg (2012). “Looking around corners and through thin turbid layers in real time with scattered incoherent light”. In: *Nature photonics* 6.8, pp. 549–553 (cited on page 213).
- [Katz et al. 2014] Katz, Ori, Pierre Heidmann, Mathias Fink, and Sylvain Gigan (2014). “Non-invasive single-shot imaging through scattering layers and around corners via speckle correlations”. In: *Nature photonics* 8.10, pp. 784–790 (cited on page 213).
- [Kelly 2018] Kelly, Damien P (2018). “Measuring the Phase of an Optical Field from Two Intensity Measurements: Analysis of a Simple Theoretical Model”. In: *International Journal of Optics* 2018 (cited on page 86).
- [Kim et al. 2012] Kim, Moonseok, Youngwoon Choi, Changhyeong Yoon, Wonjun Choi, Jaisoon Kim, Q-Han Park, and Wonshik Choi (2012). “Maximal energy transport through disordered media with the implementation of transmission eigenchannels”. In: *Nature photonics* 6.9, pp. 581–585 (cited on pages 47, 48, 122, 149).
- [Kogan et al. 1993] Kogan, Eugene, Moshe Kaveh, Rene Baumgartner, and Richard Berkovits (1993). “Statistics of waves propagating in a random medium”. In: *Physical Review B* 48.13, p. 9404 (cited on page 115).
- [Kohlgraf-Owens et al. 2010] Kohlgraf-Owens, Thomas W and Aristide Dogariu (2010). “Transmission matrices of random media: means for spectral polarimetric measurements”. In: *Optics letters* 35.13, pp. 2236–2238 (cited on page 239).
- [Labouesse et al. 2017] Labouesse, Simon, Awoke Negash, Jérôme Idier, Sebastien Bourguignon, Thomas Mangeat, Penghuan Liu, Anne Sentenac, and Marc Allain (2017). “Joint reconstruction strategy for structured illumination microscopy with unknown illuminations”. In: *IEEE Transactions on Image Processing* 26.5, pp. 2480–2493 (cited on page 119).
- [Lambert et al. 2020] Lambert, William, Laura A Cobus, Thomas Frappart, Mathias Fink, and Alexandre Aubry (2020). “Distortion matrix approach for ultrasound imaging of random scattering

- media”. In: *Proceedings of the National Academy of Sciences* 117.26, pp. 14645–14656 (cited on page 67).
- [Landauer et al. 1987] Landauer, R and M Buttiker (1987). “Diffusive traversal time: Effective area in magnetically induced interference”. In: *Physical Review B* 36.12, p. 6255 (cited on page 26).
- [Laurent et al. 2000] Laurent, Beatrice and Pascal Massart (2000). “Adaptive estimation of a quadratic functional by model selection”. In: *Annals of Statistics*, pp. 1302–1338 (cited on page 270).
- [Leach et al. 2005] Leach, Jonathan, Mark R Dennis, Johannes Courtial, and Miles J Padgett (2005). “Vortex knots in light”. In: *New Journal of Physics* 7.1, p. 55 (cited on page 80).
- [Ledesma-Carrillo et al. 2017] Ledesma-Carrillo, L, CM Gómez-Sarabia, M Torres-Cisneros, R Guzmán-Cabrera, C Guzmán-Cano, and J Ojeda-Castañeda (2017). “Hadamard circular masks: high focal depth with high throughput”. In: *Optics express* 25.15, pp. 17004–17020 (cited on page 77).
- [Leedumrongwatthanakun et al. 2020] Leedumrongwatthanakun, Saroch, Luca Innocenti, Hugo Defienne, Thomas Juffmann, Alessandro Ferraro, Mauro Paternostro, and Sylvain Gigan (2020). “Programmable linear quantum networks with a multimode fibre”. In: *Nature Photonics* 14.3, pp. 139–142 (cited on pages 207, 210).
- [Leith et al. 1966] Leith, Emmett N and Juris Upatnieks (1966). “Holographic imagery through diffusing media”. In: *JOSA* 56.4, pp. 523–523 (cited on page 35).
- [Lemoult et al. 2009] Lemoult, Fabrice, Geoffroy Lerosey, Julien de Rosny, and Mathias Fink (2009). “Manipulating spatiotemporal degrees of freedom of waves in random media”. In: *Physical review letters* 103.17, p. 173902 (cited on page 41).
- [Li et al. 1994] Li, JH and AZ Genack (1994). “Correlation in laser speckle”. In: *Physical Review E* 49.5, p. 4530 (cited on page 213).
- [Li et al. 2021a] Li, Shuhui, Charles Saunders, Daniel J Lum, John Murray-Bruce, Vivek K Goyal, Tomáš Čížmár, and David B Phillips (2021a). “Compressively sampling the optical transmission matrix of a multimode fibre”. In: *Light: Science & Applications* 10.1, pp. 1–15 (cited on page 213).
- [Li et al. 2021b] Li, Shuhui, Simon AR Horsley, Tomáš Tyc, Tomáš Čížmár, and David B Phillips (2021b). “Memory effect assisted imaging through multimode optical fibres”. In: *Nature Communications* 12.1, pp. 1–13 (cited on pages 211, 213, 221).
- [Li et al. 2021c] Li, Zheng, Xiaoyu Nie, Fan Yang, Xiangpei Liu, Dongyu Liu, Xiaolong Dong, Xingchen Zhao, Tao Peng, M Suhail Zubairy, and Marlan O Scully (2021c). “Superresolving second-order correlation imaging using synthesized colored noise speckles”. In: *arXiv preprint arXiv:2102.06079* (cited on page 120).
- [Lim et al. 2008] Lim, Daryl, Kengyeh K Chu, and Jerome Mertz (2008). “Wide-field fluorescence sectioning with hybrid speckle and uniform-illumination microscopy”. In: *Optics letters* 33.16, pp. 1819–1821 (cited on page 118).
- [Liu et al. 2021] Liu, Ruifeng, Bingcheng Qing, Shupeng Zhao, Pei Zhang, Hong Gao, Shouqian Chen, and Fuli Li (2021). “Generation of Non-Rayleigh Nondiffracting Speckles”. In: *Physical Review Letters* 127.18, p. 180601 (cited on page 126).
- [Liutkus et al. 2014] Liutkus, Antoine, David Martina, Sébastien Popoff, Gilles Chardon, Ori Katz, Geoffroy Lerosey, Sylvain Gigan, Laurent Daudet, and Igor Carron (2014). “Imaging with nature: Compressive imaging using a multiply scattering medium”. In: *Scientific reports* 4.1, pp. 1–7 (cited on page 70).
- [Lloyd 1973] Lloyd, Geoffrey Ernest Richard (1973). *Greek science after Aristotle*. Chatto & Windus (cited on page 205).

- [Loterie et al. 2015] Loterie, Damien, Sebastianus A Goorden, Demetri Psaltis, and Christophe Moser (2015). “Confocal microscopy through a multimode fiber using optical correlation”. In: *Optics letters* 40.24, pp. 5754–5757 (cited on page 225).
- [Lye et al. 2005] Lye, JE, L Fallani, Michele Modugno, DS Wiersma, C Fort, and Massimo Inguscio (2005). “Bose-Einstein condensate in a random potential”. In: *Physical review letters* 95.7, p. 070401 (cited on page 119).
- [Magatti et al. 2009] Magatti, D, A Gatti, and F Ferri (2009). “Three-dimensional coherence of light speckles: experiment”. In: *Physical Review A* 79.5, p. 053831 (cited on pages 19, 251).
- [Marčenko et al. 1967] Marčenko, Vladimir A and Leonid Andreevich Pastur (1967). “Distribution of eigenvalues for some sets of random matrices”. In: *Mathematics of the USSR-Sbornik* 1.4, p. 457 (cited on page 59).
- [Mastiani et al. 2021] Mastiani, Bahareh and Ivo M Vellekoop (2021). “Noise-tolerant wavefront shaping in a Hadamard basis”. In: *Optics Express* 29.11, pp. 17534–17541 (cited on page 77).
- [Matthès et al. 2019] Matthès, Maxime W, Philipp del Hougne, Julien de Rosny, Geoffroy Lerosey, and Sébastien M Popoff (2019). “Optical complex media as universal reconfigurable linear operators”. In: *Optica* 6.4, pp. 465–472 (cited on pages 207, 210).
- [Matthès et al. 2021] Matthès, Maxime W, Yaron Bromberg, Julien de Rosny, and Sébastien M Popoff (2021). “Learning and avoiding disorder in multimode fibers”. In: *Physical Review X* 11.2, p. 021060 (cited on pages 208, 212).
- [McCabe et al. 2011] McCabe, David J, Ayhan Tajalli, Dane R Austin, Pierre Bondareff, Ian A Walmsley, Sylvain Gigan, and Béatrice Chatel (2011). “Spatio-temporal focusing of an ultrafast pulse through a multiply scattering medium”. In: *Nature communications* 2.1, pp. 1–5 (cited on page 40).
- [McDowell et al. 2010] McDowell, Emily J, Meng Cui, Ivo M Vellekoop, Vahan A Senekerimyan, Zahid Yaqoob, and Changhuei Yang (2010). “Turbidity suppression from the ballistic to the diffusive regime in biological tissues using optical phase conjugation”. In: *Journal of biomedical optics* 15.2, p. 025004 (cited on pages 35, 68).
- [McGloin et al. 2005] McGloin, David and Kishan Dholakia (2005). “Bessel beams: diffraction in a new light”. In: *Contemporary Physics* 46.1, pp. 15–28 (cited on page 126).
- [McKinney et al. 2000] McKinney, JD, MA Webster, KJ Webb, and AM Weiner (2000). “Characterization and imaging in optically scattering media by use of laser speckle and a variable-coherence source”. In: *Optics Letters* 25.1, pp. 4–6 (cited on page 25).
- [Mello et al. 1988] Mello, PA, P Pereyra, and N Kumar (1988). “Macroscopic approach to multi-channel disordered conductors”. In: *Annals of Physics* 181.2, pp. 290–317 (cited on page 55).
- [Mezzadri 2006] Mezzadri, Francesco (2006). “How to generate random matrices from the classical compact groups”. In: *arXiv preprint math-ph/0609050* (cited on pages 232, 274).
- [Mie 1908] Mie, Gustav (1908). “Beiträge zur Optik trüber Medien, speziell kolloidaler Metallösungen”. In: *Annalen der physik* 330.3, pp. 377–445 (cited on page 11).
- [Mitalas et al. 1992] Mitalas, R and KR Sills (1992). “On the photon diffusion time scale for the sun”. In: *The Astrophysical Journal* 401, p. 759 (cited on pages xxi, xxii).
- [Morales-Delgado et al. 2015] Morales-Delgado, Edgar E, Demetri Psaltis, and Christophe Moser (2015). “Two-photon imaging through a multimode fiber”. In: *Optics express* 23.25, pp. 32158–32170 (cited on page 225).
- [Moser et al. 2019] Moser, Simon, Monika Ritsch-Marte, and Gregor Thalhammer (2019). “Model-based compensation of pixel crosstalk in liquid crystal spatial light modulators”. In: *Optics express* 27.18, pp. 25046–25063 (cited on page 78).

- [Mosk et al. 2012] Mosk, Allard P, Ad Lagendijk, Geoffroy Lerosey, and Mathias Fink (2012). “Controlling waves in space and time for imaging and focusing in complex media”. In: *Nature photonics* 6.5, pp. 283–292 (cited on pages 24, 46, 68).
- [Mounaix 2017] Mounaix, Mickaël (2017). “Matricial approaches for spatio-temporal control of light in multiple scattering media”. PhD thesis. Paris 6 (cited on pages 34, 50, 52, 82, 83, 89).
- [Mounaix et al. 2016a] Mounaix, Mickael, Hugo Defienne, and Sylvain Gigan (2016a). “Deterministic light focusing in space and time through multiple scattering media with a time-resolved transmission matrix approach”. In: *Physical Review A* 94.4, p. 041802 (cited on pages 53, 96, 145–147, 156).
- [Mounaix et al. 2016b] Mounaix, Mickael, Daria Andreoli, Hugo Defienne, Giorgio Volpe, Ori Katz, Samuel Grésillon, and Sylvain Gigan (2016b). “Spatiotemporal coherent control of light through a multiple scattering medium with the multispectral transmission matrix”. In: *Physical review letters* 116.25, p. 253901 (cited on page 50).
- [Mounaix et al. 2017] Mounaix, Mickael, Hilton B de Aguiar, and Sylvain Gigan (2017). “Temporal recompression through a scattering medium via a broadband transmission matrix”. In: *Optica* 4.10, pp. 1289–1292 (cited on pages 53, 96).
- [Mounaix et al. 2019] Mounaix, Mickael and Joel Carpenter (2019). “Control of the temporal and polarization response of a multimode fiber”. In: *Nature communications* 10.1, pp. 1–8 (cited on pages 52, 141, 163, 165).
- [Mudry et al. 2012] Mudry, Emeric, Kamal Belkebir, J Girard, Julien Savatier, Emmeran Le Moal, C Nicoletti, Marc Allain, and Anne Sentenac (2012). “Structured illumination microscopy using unknown speckle patterns”. In: *Nature Photonics* 6.5, pp. 312–315 (cited on pages 118, 130, 149, 171).
- [Nardi et al. 2021] Nardi, Alfonso, Felix Tebbenjohanns, Massimiliano Rossi, Shawn Divitt, Andreas Norrman, Sylvain Gigan, Martin Frimmer, and Lukas Novotny (2021). “Controlling spatial coherence with an optical complex medium”. In: *arXiv preprint arXiv:2109.04297* (cited on page 212).
- [NASA 2007] NASA (2007). *The 8-minute travel time to Earth by sunlight hides a thousand-year journey that actually began in the core*. Issue #50: Ancient sunlight. [https://sunearthday.nasa.gov/2007/locations/ttt\\_sunlight.php](https://sunearthday.nasa.gov/2007/locations/ttt_sunlight.php). Accessed: 2021-10-30 (cited on page xxi).
- [Nieuwenhuizen et al. 1995] Nieuwenhuizen, Th M and MCW Van Rossum (1995). “Intensity distributions of waves transmitted through a multiple scattering medium”. In: *Physical review letters* 74.14, p. 2674 (cited on page 115).
- [Ntziachristos 2010] Ntziachristos, Vasilis (2010). “Going deeper than microscopy: the optical imaging frontier in biology”. In: *Nature methods* 7.8, pp. 603–614 (cited on pages 13, 14).
- [Ojambati et al. 2016] Ojambati, Oluwafemi S, John T Hosmer-Quint, Klaas-Jan Gorter, Allard P Mosk, and Willem L Vos (2016). “Controlling the intensity of light in large areas at the interfaces of a scattering medium”. In: *Physical Review A* 94.4, p. 043834 (cited on pages 39, 65).
- [Osnabrugge et al. 2017] Osnabrugge, Gerwin, Roarke Horstmeyer, Ioannis N Papadopoulos, Benjamin Judkewitz, and Ivo M Vellekoop (2017). “Generalized optical memory effect”. In: *Optica* 4.8, pp. 886–892 (cited on pages 171, 213, 214).
- [Ozols 2009] Ozols, Maris (2009). “How to generate a random unitary matrix”. In: *unpublished essay on http://home.lu.lv/sd20008* (cited on pages 232, 274).
- [Pai et al. 2021] Pai, Pritam, Jeroen Bosch, Matthias Kühmayer, Stefan Rotter, and Allard P Mosk (2021). “Scattering invariant modes of light in complex media”. In: *Nature Photonics* 15.6, pp. 431–434 (cited on pages 67, 172–174, 186, 187).

- [Papadopoulos et al. 2012] Papadopoulos, Ioannis N, Salma Farahi, Christophe Moser, and Demetri Psaltis (2012). “Focusing and scanning light through a multimode optical fiber using digital phase conjugation”. In: *Optics express* 20.10, pp. 10583–10590 (cited on pages 209, 215).
- [Papadopoulos et al. 2013] Papadopoulos, Ioannis N, Salma Farahi, Christophe Moser, and Demetri Psaltis (2013). “High-resolution, lensless endoscope based on digital scanning through a multimode optical fiber”. In: *Biomedical optics express* 4.2, pp. 260–270 (cited on page 207).
- [Pappu et al. 2002] Pappu, Ravikanth, Ben Recht, Jason Taylor, and Neil Gershenfeld (2002). “Physical one-way functions”. In: *Science* 297.5589, pp. 2026–2030 (cited on page 69).
- [Park et al. 2012a] Park, Jung-Hoon, ChungHyun Park, Hyunseung Yu, Yong-Hoon Cho, and YongKeun Park (2012a). “Active spectral filtering through turbid media”. In: *Optics letters* 37.15, pp. 3261–3263 (cited on page 69).
- [Park et al. 2012b] Park, Jung-Hoon, Chunghyun Park, Hyunseung Yu, Yong-Hoon Cho, and YongKeun Park (2012b). “Dynamic active wave plate using random nanoparticles”. In: *Optics Express* 20.15, pp. 17010–17016 (cited on page 69).
- [Park et al. 2009] Park, YongKeun, Wonshik Choi, Zahid Yaqoob, Ramachandra Dasari, Kamran Badizadegan, and Michael S Feld (2009). “Speckle-field digital holographic microscopy”. In: *Optics express* 17.15, pp. 12285–12292 (cited on pages 130, 149).
- [Paudel et al. 2013] Paudel, Hari P, Chris Stockbridge, Jerome Mertz, and Thomas Bifano (2013). “Focusing polychromatic light through strongly scattering media”. In: *Optics express* 21.14, pp. 17299–17308 (cited on pages 40, 53).
- [Pauwels et al. 2019] Pauwels, Jaël, Guy Van der Sande, and Guy Verschaffelt (2019). “Space division multiplexing in standard multi-mode optical fibers based on speckle pattern classification”. In: *Scientific reports* 9.1, pp. 1–9 (cited on page 208).
- [Pendry et al. 1990] Pendry, JB, A MacKinnon, and AB Pretre (1990). “Maximal fluctuations—a new phenomenon in disordered systems”. In: *Physica A: Statistical Mechanics and its Applications* 168.1, pp. 400–407 (cited on page 55).
- [Petz et al. 2004] Petz, Dénes and Júlia Réffy (2004). “On asymptotics of large Haar distributed unitary matrices”. In: *Periodica Mathematica Hungarica* 49.1, pp. 103–117 (cited on pages 277, 278).
- [Phillips et al. 2016] Phillips, DB, Ruiqing He, Qian Chen, GM Gibson, and MJ Padgett (2016). “Non-diffractive computational ghost imaging”. In: *Optics express* 24.13, pp. 14172–14182 (cited on page 126).
- [Pierangeli et al. 2019] Pierangeli, D, G Marcucci, and C Conti (2019). “Large-scale photonic Ising machine by spatial light modulation”. In: *Physical review letters* 122.21, p. 213902 (cited on page 70).
- [Pierangeli et al. 2021] Pierangeli, Davide, Mushegh Rafayelyan, Claudio Conti, and Sylvain Gigan (2021). “Scalable spin-glass optical simulator”. In: *Physical Review Applied* 15.3, p. 034087 (cited on page 70).
- [Pikálek et al. 2019] Pikálek, Tomáš, Johanna Trägårdh, Stephen Simpson, and Tomáš Čižmár (2019). “Wavelength dependent characterization of a multimode fibre endoscope”. In: *Optics express* 27.20, pp. 28239–28253 (cited on page 225).
- [Plöschner et al. 2015] Plöschner, Martin, Tomáš Tyc, and Tomáš Čižmár (2015). “Seeing through chaos in multimode fibres”. In: *Nature Photonics* 9.8, pp. 529–535 (cited on page 210).
- [Poirier-Quinot 2019] Poirier-Quinot, Marie (2019). “Imagerie médicale, quand la Physique rencontre la médecine”. In: *La Revue 3IE* 97 (cited on page 29).
- [Popoff 2020] Popoff, Sébastien M. (2020). *pyMMF: a simple module in Python for numerically finding multimode fiber modes under the scalar approximation*. Version 0.4. DOI: [10.5281/zenodo.4075298](https://doi.org/10.5281/zenodo.4075298). URL: <https://doi.org/10.5281/zenodo.4075298> (cited on pages 225, 226).

- [Popoff et al. 2010] Popoff, Sébastien M, Geoffroy Lerosey, R Carminati, Mathias Fink, Albert Claude Boccara, and Sylvain Gigan (2010). “Measuring the transmission matrix in optics: an approach to the study and control of light propagation in disordered media”. In: *Physical review letters* 104.10, p. 100601 (cited on pages 44, 58, 63, 69, 77, 95, 210, 278).
- [Popoff et al. 2011] Popoff, Sébastien Michel, Alexandre Aubry, Geoffroy Lerosey, Mathias Fink, Albert-Claude Boccara, and Sylvain Gigan (2011). “Exploiting the time-reversal operator for adaptive optics, selective focusing, and scattering pattern analysis”. In: *Physical review letters* 107.26, p. 263901 (cited on page 47).
- [Popoff et al. 2014] Popoff, SM, A Goetschy, SF Liew, A Douglas Stone, and Hui Cao (2014). “Coherent control of total transmission of light through disordered media”. In: *Physical review letters* 112.13, p. 133903 (cited on pages 59, 152).
- [Prada et al. 1994] Prada, Claire and Mathias Fink (1994). “Eigenmodes of the time reversal operator: A solution to selective focusing in multiple-target media”. In: *Wave motion* 20.2, pp. 151–163 (cited on page 47).
- [Pratt et al. 1969] Pratt, William K, Julius Kane, and Harry C Andrews (1969). “Hadamard transform image coding”. In: *Proceedings of the IEEE* 57.1, pp. 58–68 (cited on page 94).
- [Putten 2011] Putten, Eibert Gerjan van (2011). “Disorder-enhanced imaging with spatially controlled light”. In: (cited on page 82).
- [Rawson et al. 1980] Rawson, Eric G, Joseph W Goodman, and Robert E Norton (1980). “Frequency dependence of modal noise in multimode optical fibers”. In: *JOSA* 70.8, pp. 968–976 (cited on page 220).
- [Redding et al. 2013a] Redding, Brandon, Sebastien M Popoff, and Hui Cao (2013a). “All-fiber spectrometer based on speckle pattern reconstruction”. In: *Optics express* 21.5, pp. 6584–6600 (cited on pages 69, 239).
- [Redding et al. 2013b] Redding, Brandon, Seng Fatt Liew, Raktim Sarma, and Hui Cao (2013b). “Compact spectrometer based on a disordered photonic chip”. In: *Nature Photonics* 7.9, pp. 746–751 (cited on page 239).
- [Redding et al. 2014] Redding, Brandon, Mansoor Alam, Martin Seifert, and Hui Cao (2014). “High-resolution and broadband all-fiber spectrometers”. In: *Optica* 1.3, pp. 175–180 (cited on pages 69, 239).
- [Reddy et al. 2016] Reddy, Salla Gangi, P Chithrabhanu, Pravin Vaity, A Aadhi, Shashi Prabhakar, and RP Singh (2016). “Non-diffracting speckles of a perfect vortex beam”. In: *Journal of Optics* 18.5, p. 055602 (cited on page 126).
- [Richardson et al. 2013] Richardson, David J, John M Fini, and Lynn E Nelson (2013). “Space-division multiplexing in optical fibres”. In: *Nature photonics* 7.5, pp. 354–362 (cited on pages 207, 208).
- [Roddier 1999] Roddier, François (1999). “Adaptive optics in astronomy”. In: (cited on page 32).
- [Rosen et al. 2000] Rosen, Joseph and Mitsuo Takeda (2000). “Longitudinal spatial coherence applied for surface profilometry”. In: *Applied optics* 39.23, pp. 4107–4111 (cited on page 119).
- [Rossum et al. 1999] Rossum, MCW van van and Th M Nieuwenhuizen (1999). “Multiple scattering of classical waves: microscopy, mesoscopy, and diffusion”. In: *Reviews of Modern Physics* 71.1, p. 313 (cited on pages 12, 13, 82).
- [Rotter et al. 2011] Rotter, Stefan, Philipp Ambichl, and Florian Libisch (2011). “Generating particlelike scattering states in wave transport”. In: *Physical review letters* 106.12, p. 120602 (cited on page 66).
- [Rotter et al. 2017] Rotter, Stefan and Sylvain Gigan (2017). “Light fields in complex media: Mesoscopic scattering meets wave control”. In: *Reviews of Modern Physics* 89.1, p. 015005 (cited on pages 21, 25, 42, 44, 55, 64, 83).

- [Salameh et al. 2020] Salameh, Chrystelle, Flore Salviat, Elora Bessot, Miléna Lama, Jean-Marie Chassot, Elodie Mouloungui, Yan Wang, Marc Robin, Arnaud Bardouil, Mohamed Selmane, et al. (2020). “Origin of transparency in scattering biomimetic collagen materials”. In: *Proceedings of the National Academy of Sciences* 117.22, pp. 11947–11953 (cited on page 9).
- [Sapienza et al. 2010] Sapienza, Luca, Henri Thyrrestrup, Søren Stobbe, Pedro David Garcia, Stephan Smolka, and Peter Lodahl (2010). “Cavity quantum electrodynamics with Anderson-localized modes”. In: *Science* 327.5971, pp. 1352–1355 (cited on page 69).
- [Sapienza et al. 2007] Sapienza, Riccardo, Pedro D García, J Bertolotti, MD Martin, A Blanco, L Vina, C López, and DS Wiersma (2007). “Observation of resonant behavior in the energy velocity of diffused light”. In: *Physical review letters* 99.23, p. 233902 (cited on page 82).
- [Sarma et al. 2016] Sarma, Raktim, Alexey G Yamilov, Sasha Petrenko, Yaron Bromberg, and Hui Cao (2016). “Control of energy density inside a disordered medium by coupling to open or closed channels”. In: *Physical review letters* 117.8, p. 086803 (cited on page 57).
- [Savo et al. 2020] Savo, Romolo, Andrea Morandi, Jolanda S Müller, Fabian Kaufmann, Flavia Timpu, Marc Reig Escalé, Michele Zanini, Lucio Isa, and Rachel Grange (2020). “Broadband Mie driven random quasi-phase-matching”. In: *Nature Photonics* 14.12, pp. 740–747 (cited on page 69).
- [Saxon 1955] Saxon, David S (1955). “Tensor scattering matrix for the electromagnetic field”. In: *Physical Review* 100.6, p. 1771 (cited on page 41).
- [Scheffold et al. 1998] Scheffold, Frank and Georg Maret (1998). “Universal conductance fluctuations of light”. In: *Physical review letters* 81.26, p. 5800 (cited on pages 22, 115).
- [Schott et al. 2015] Schott, Sam, Jacopo Bertolotti, Jean-Francois Léger, Laurent Bourdieu, and Sylvain Gigan (2015). “Characterization of the angular memory effect of scattered light in biological tissues”. In: *Optics express* 23.10, pp. 13505–13516 (cited on page 213).
- [Sebbah 2001] Sebbah, Patrick (2001). *Waves and imaging through complex media*. Springer Science & Business Media (cited on page 30).
- [Senior et al. 2009] Senior, John M and M Yousif Jamro (2009). *Optical fiber communications: principles and practice*. Pearson Education (cited on page 206).
- [Shack 1971] Shack, Roland V (1971). “Production and use of a lecticular hartmann screen”. In: *J. Opt. Soc. Am.* 61, pp. 656–661 (cited on page 87).
- [Shapiro 1986] Shapiro, B (1986). “Large intensity fluctuations for wave propagation in random media”. In: *Physical review letters* 57.17, p. 2168 (cited on pages 22, 23).
- [Sheng et al. 2007] Sheng, Ping and Bart van Tiggelen (2007). *Introduction to Wave Scattering, Localization and Mesoscopic Phenomena*. (Cited on page 69).
- [Sheppard 2002] Sheppard, Colin JR (2002). “Three-dimensional phase imaging with the intensity transport equation”. In: *Applied optics* 41.28, pp. 5951–5955 (cited on page 86).
- [Shnerb et al. 1991] Shnerb, N and M Kaveh (1991). “Non-Rayleigh statistics of waves in random systems”. In: *Physical Review B* 43.1, p. 1279 (cited on page 115).
- [Shu 1982] Shu, Frank (1982). *The physical universe: an introduction to astronomy*. University science books (cited on page xxi).
- [Sines et al. 1987] Sines, George and Yannis A Sakellarakis (1987). “Lenses in antiquity”. In: *American Journal of Archaeology*, pp. 191–196 (cited on page 205).
- [Small et al. 2012] Small, Eran, Ori Katz, Yefeng Guan, and Yaron Silberberg (2012). “Spectral control of broadband light through random media by wavefront shaping”. In: *Optics letters* 37.16, pp. 3429–3431 (cited on page 69).
- [Smith 1999] Smith, A Mark (1999). “Ptolemy and the foundations of ancient mathematical optics: A source based guided study”. In: *Transactions of the American Philosophical Society* 89.3, pp. 1–172 (cited on page 205).

- [Smith 1960] Smith, Felix T (1960). “Lifetime matrix in collision theory”. In: *Physical Review* 118.1, p. 349 (cited on page 65).
- [Snyder et al. 2012] Snyder, Allan W and John Love (2012). *Optical waveguide theory*. Springer Science & Business Media (cited on page 207).
- [Sprik et al. 2008] Sprik, Rudolf, Arnaud Tourin, Julien de Rosny, and Mathias Fink (2008). “Eigenvalue distributions of correlated multichannel transfer matrices in strongly scattering systems”. In: *Physical Review B* 78.1, p. 012202 (cited on pages 58, 163).
- [Strudley et al. 2013] Strudley, Tom, Tilman Zehender, Claire Blejean, Erik PAM Bakkers, and Otto L Muskens (2013). “Mesoscopic light transport by very strong collective multiple scattering in nanowire mats”. In: *Nature photonics* 7.5, pp. 413–418 (cited on page 115).
- [Strudley et al. 2014] Strudley, Tom, Duygu Akbulut, Willem L Vos, Ad Lagendijk, Allard P Mosk, and Otto L Muskens (2014). “Observation of intensity statistics of light transmitted through 3D random media”. In: *Optics letters* 39.21, pp. 6347–6350 (cited on pages 115, 116).
- [Sylvester 1867] Sylvester, James Joseph (1867). “LX. Thoughts on inverse orthogonal matrices, simultaneous signsuccessions, and tessellated pavements in two or more colours, with applications to Newton’s rule, ornamental tile-work, and the theory of numbers”. In: *The London, Edinburgh, and Dublin Philosophical Magazine and Journal of Science* 34.232, pp. 461–475 (cited on page 94).
- [Syurik et al. 2018] Syurik, Julia, Gianni Jacucci, Olimpia D Onelli, Hendrik Hölscher, and Silvia Vignolini (2018). “Bio-inspired highly scattering networks via polymer phase separation”. In: *Advanced Functional Materials* 28.24, p. 1706901 (cited on page 69).
- [Tao 2012] Tao, Terence (2012). *Topics in random matrix theory*. Vol. 132. American Mathematical Soc. (cited on page 278).
- [Teague 1983] Teague, Michael Reed (1983). “Deterministic phase retrieval: a Green’s function solution”. In: *JOSA* 73.11, pp. 1434–1441 (cited on page 86).
- [Thompson et al. 1997] Thompson, Charles A, Kevin J Webb, and Andrew M Weiner (1997). “Diffusive media characterization with laser speckle”. In: *Applied optics* 36.16, pp. 3726–3734 (cited on page 25).
- [Thouless 1977] Thouless, DJ (1977). “Maximum metallic resistance in thin wires”. In: *Physical Review Letters* 39.18, p. 1167 (cited on pages 25, 83).
- [Tourin et al. 1999] Tourin, A, A Derode, and M Fink (1999). “Dynamic time reversal of randomly backscattered acoustic waves”. In: *EPL (Europhysics Letters)* 47.2, p. 175 (cited on page 68).
- [Tran et al. 2019] Tran, Vinh, Sujit K Sahoo, and Cuong Dang (2019). “Fast 3D movement of a laser focusing spot behind scattering media by utilizing optical memory effect and optical conjugate planes”. In: *Scientific reports* 9.1, pp. 1–8 (cited on page 37).
- [Turtaev et al. 2017] Turtaev, Sergey, Ivo T Leite, Kevin J Mitchell, Miles J Padgett, David B Phillips, and Tomáš Čížmár (2017). “Comparison of nematic liquid-crystal and DMD based spatial light modulation in complex photonics”. In: *Optics express* 25.24, pp. 29874–29884 (cited on page 34).
- [Turunen et al. 1991] Turunen, Jari, Antti Vasara, and Ari T Friberg (1991). “Propagation invariance and self-imaging in variable-coherence optics”. In: *JOSA A* 8.2, pp. 282–289 (cited on page 126).
- [Tyndall 1870] Tyndall, John (1870). *Notes of a Course of Nine Lectures on Light: Delivered at the Royal Institution of Great Britain, April 8-June 3, 1869*. Longmans, Green (cited on page 205).
- [Tyson 2015] Tyson, Robert K (2015). *Principles of adaptive optics*. CRC press (cited on page 32).
- [Van Beijnum et al. 2011] Van Beijnum, Frerik, Elbert G Van Putten, Ad Lagendijk, and Allard P Mosk (2011). “Frequency bandwidth of light focused through turbid media”. In: *Optics letters* 36.3, pp. 373–375 (cited on page 37).

- [Van Putten et al. 2008] Van Putten, EG, Ivo Micha Vellekoop, and AP Mosk (2008). “Spatial amplitude and phase modulation using commercial twisted nematic LCDs”. In: *Applied optics* 47.12, pp. 2076–2081 (cited on pages 80, 81, 241).
- [Van Tiggelen et al. 1999] Van Tiggelen, BA, P Sebbah, M Stoytchev, and AZ Genack (1999). “Delay-time statistics for diffuse waves”. In: *Physical Review E* 59.6, p. 7166 (cited on page 65).
- [Vellekoop et al. 2005] Vellekoop, IM, P Lodahl, and A Lagendijk (2005). “Determination of the diffusion constant using phase-sensitive measurements”. In: *Physical Review E* 71.5, p. 056604 (cited on page 26).
- [Vellekoop 2015] Vellekoop, Ivo M (2015). “Feedback-based wavefront shaping”. In: *Optics express* 23.9, pp. 12189–12206 (cited on pages 25, 38).
- [Vellekoop et al. 2007] Vellekoop, Ivo M and AP Mosk (2007). “Focusing coherent light through opaque strongly scattering media”. In: *Optics letters* 32.16, pp. 2309–2311 (cited on pages 36, 38, 68, 143).
- [Vellekoop et al. 2010] Vellekoop, Ivo M, Aart Lagendijk, and AP Mosk (2010). “Exploiting disorder for perfect focusing”. In: *Nature photonics* 4.5, pp. 320–322 (cited on page 68).
- [Vellekoop et al. 2012] Vellekoop, Ivo M, Meng Cui, and Changhuei Yang (2012). “Digital optical phase conjugation of fluorescence in turbid tissue”. In: *Applied physics letters* 101.8, p. 081108 (cited on page 39).
- [Vellekoop et al. 2008a] Vellekoop, Ivo Micha, EG Van Putten, A Lagendijk, and AP Mosk (2008a). “Demixing light paths inside disordered metamaterials”. In: *Optics express* 16.1, pp. 67–80 (cited on page 39).
- [Vellekoop et al. 2008b] Vellekoop, Ivo Micha and AP Mosk (2008b). “Phase control algorithms for focusing light through turbid media”. In: *Optics communications* 281.11, pp. 3071–3080 (cited on page 143).
- [Vellekoop et al. 2008c] Vellekoop, Ivo Micha and AP Mosk (2008c). “Universal optimal transmission of light through disordered materials”. In: *Physical review letters* 101.12, p. 120601 (cited on pages 56, 64).
- [Vesga et al. 2019] Vesga, Arturo G, Matthias Hofer, Naveen Kumar Balla, Hilton B De Aguiar, Marc Guillon, and Sophie Brasselet (2019). “Focusing large spectral bandwidths through scattering media”. In: *Optics express* 27.20, pp. 28384–28394 (cited on page 214).
- [Vesperinas 2006] Vesperinas, Manuel Nieto (2006). *Scattering and diffraction in physical optics*. World Scientific Publishing Company (cited on page 20).
- [Vo-Dinh 2014] Vo-Dinh, Tuan (2014). *Biomedical photonics handbook: biomedical diagnostics*. CRC press (cited on page 31).
- [Volpe et al. 2014] Volpe, Giorgio, Giovanni Volpe, and Sylvain Gigan (2014). “Brownian motion in a speckle light field: tunable anomalous diffusion and selective optical manipulation”. In: *Scientific reports* 4.1, pp. 1–6 (cited on page 119).
- [Wang et al. 2011] Wang, Jing and Azriel Z Genack (2011). “Transport through modes in random media”. In: *Nature* 471.7338, pp. 345–348 (cited on page 40).
- [Wang et al. 2012] Wang, Ying Min, Benjamin Judkewitz, Charles A DiMarzio, and Changhuei Yang (2012). “Deep-tissue focal fluorescence imaging with digitally time-reversed ultrasound-encoded light”. In: *Nature communications* 3.1, pp. 1–8 (cited on page 39).
- [Ward et al. 2009] Ward, Jennifer E, Damien P Kelly, and John T Sheridan (2009). “Three-dimensional speckle size in generalized optical systems with limiting apertures”. In: *JOSA A* 26.8, pp. 1855–1864 (cited on pages 18, 19).
- [Weihs et al. 1996] Weihs, Gregor, Michael Reck, Harald Weinfurter, and Anton Zeilinger (1996). “Two-photon interference in optical fiber multiports”. In: *Physical Review A* 54.1, p. 893 (cited on page 210).

- [Weiner 2011] Weiner, Andrew M (2011). “Focusing through scattering media”. In: *Nature Photonics* 5.6, pp. 332–334 (cited on page 27).
- [Wiersma 2008] Wiersma, Diederik S (2008). “The physics and applications of random lasers”. In: *Nature physics* 4.5, pp. 359–367 (cited on page 69).
- [Wiersma 2013] Wiersma, Diederik S (2013). “Disordered photonics”. In: *Nature Photonics* 7.3, pp. 188–196 (cited on page 69).
- [Wigner 1955] Wigner, Eugene P (1955). “Lower limit for the energy derivative of the scattering phase shift”. In: *Physical Review* 98.1, p. 145 (cited on page 65).
- [Wigner 1993] Wigner, Eugene P (1993). “Characteristic vectors of bordered matrices with infinite dimensions i”. In: *The Collected Works of Eugene Paul Wigner*. Springer, pp. 524–540 (cited on page 54).
- [Wright et al. 2017] Wright, Logan G, Demetrios N Christodoulides, and Frank W Wise (2017). “Spatiotemporal mode-locking in multimode fiber lasers”. In: *Science* 358.6359, pp. 94–97 (cited on page 207).
- [Xiong et al. 2016] Xiong, Wen, Philipp Ambichl, Yaron Bromberg, Brandon Redding, Stefan Rotter, and Hui Cao (2016). “Spatiotemporal control of light transmission through a multimode fiber with strong mode coupling”. In: *Physical review letters* 117.5, p. 053901 (cited on pages 66, 172, 211).
- [Xiong et al. 2017] Xiong, Wen, Philipp Ambichl, Yaron Bromberg, Brandon Redding, Stefan Rotter, and Hui Cao (2017). “Principal modes in multimode fibers: exploring the crossover from weak to strong mode coupling”. In: *Optics express* 25.3, pp. 2709–2724 (cited on pages 66, 210, 211).
- [Xiong et al. 2018] Xiong, Wen, Chia Wei Hsu, Yaron Bromberg, Jose Enrique Antonio-Lopez, Rodrigo Amezcua Correa, and Hui Cao (2018). “Complete polarization control in multimode fibers with polarization and mode coupling”. In: *Light: Science & Applications* 7.1, pp. 1–10 (cited on pages 209, 211).
- [Xiong et al. 2019] Xiong, Wen, Chia Wei Hsu, and Hui Cao (2019). “Long-range spatio-temporal correlations in multimode fibers for pulse delivery”. In: *Nature communications* 10.1, pp. 1–7 (cited on pages 52, 65, 141, 150, 163, 210–212).
- [Xiong et al. 2020] Xiong, Wen, Shai Gertler, Hasan Yilmaz, and Hui Cao (2020). “Multimode-fiber-based single-shot full-field measurement of optical pulses”. In: *Optics letters* 45.8, pp. 2462–2465 (cited on page 207).
- [Yang et al. 2014] Yang, Xin, Ye Pu, and Demetri Psaltis (2014). “Imaging blood cells through scattering biological tissue using speckle scanning microscopy”. In: *Optics express* 22.3, pp. 3405–3413 (cited on page 213).
- [Yaqoob et al. 2008] Yaqoob, Zahid, Demetri Psaltis, Michael S Feld, and Changhuei Yang (2008). “Optical phase conjugation for turbidity suppression in biological samples”. In: *Nature photonics* 2.2, pp. 110–115 (cited on page 35).
- [Yariv et al. 1979] Yariv, Amnon, Dan Fekete, and David M Pepper (1979). “Compensation for channel dispersion by nonlinear optical phase conjugation”. In: *Optics Letters* 4.2, pp. 52–54 (cited on page 35).
- [Yaskov 2016] Yaskov, Pavel (2016). “Necessary and sufficient conditions for the Marchenko-Pastur theorem”. In: *Electronic Communications in Probability* 21, pp. 1–8 (cited on page 59).
- [Yilmaz et al. 2015] Yilmaz, Hasan, Elbert G van Putten, Jacopo Bertolotti, Ad Lagendijk, Willem L Vos, and Allard P Mosk (2015). “Speckle correlation resolution enhancement of wide-field fluorescence imaging”. In: *Optica* 2.5, pp. 424–429 (cited on page 171).

- [Yilmaz et al. 2019] Yilmaz, Hasan, Chia Wei Hsu, Alexey Yamilov, and Hui Cao (2019). “Transverse localization of transmission eigenchannels”. In: *Nature Photonics* 13.5, pp. 352–358 (cited on page 57).
- [Yilmaz et al. 2021] Yilmaz, Hasan, Matthias Kühmayer, Chia Wei Hsu, Stefan Rotter, and Hui Cao (2021). “Customizing the angular memory effect for scattering media”. In: *Physical Review X* 11.3, p. 031010 (cited on pages 67, 172–174).
- [Yu et al. 2013] Yu, Hyeonseung, Timothy R Hillman, Wonshik Choi, Ji Oon Lee, Michael S Feld, Ramachandra R Dasari, and YongKeun Park (2013). “Measuring large optical transmission matrices of disordered media”. In: *Physical review letters* 111.15, p. 153902 (cited on pages 44, 56, 58, 64).
- [Zhao et al. 2004] Zhao, Donghui, Xianfeng Chen, Kaiming Zhou, Lin Zhang, Ian Bennion, William N MacPherson, James S Barton, and Julian DC Jones (2004). “Bend sensors with direction recognition based on long-period gratings written in D-shaped fiber”. In: *Applied optics* 43.29, pp. 5425–5428 (cited on page 207).
- [Zhou et al. 2014] Zhou, Edward Haojiang, Haowen Ruan, Changhui Yang, and Benjamin Judkewitz (2014). “Focusing on moving targets through scattering samples”. In: *Optica* 1.4, pp. 227–232 (cited on page 40).
- [Zhu et al. 2014] Zhu, Long and Jian Wang (2014). “Arbitrary manipulation of spatial amplitude and phase using phase-only spatial light modulators”. In: *Scientific reports* 4.1, pp. 1–7 (cited on page 80).
- [Zhu et al. 2020] Zhu, Longdi, Jacques Boutet de Monvel, Pascal Berto, Sophie Brasselet, Sylvain Gigan, and Marc Guillon (2020). “Chromato-axial memory effect through a forward-scattering slab”. In: *Optica* 7.4, pp. 338–345 (cited on pages xix, xxv, 214, 221).
- [Zyczkowski et al. 2000] Zyczkowski, Karol and Hans-Jürgen Sommers (2000). “Truncations of random unitary matrices”. In: *Journal of Physics A: Mathematical and General* 33.10, p. 2045 (cited on pages 233, 273).